

ADVERTIMENT. L'accés als continguts d'aquesta tesi queda condicionat a l'acceptació de les condicions d'ús establertes per la següent llicència Creative Commons:  http://cat.creativecommons.org/?page_id=184

ADVERTENCIA. El acceso a los contenidos de esta tesis queda condicionado a la aceptación de las condiciones de uso establecidas por la siguiente licencia Creative Commons:  <http://es.creativecommons.org/blog/licencias/>

WARNING. The access to the contents of this doctoral thesis it is limited to the acceptance of the use conditions set by the following Creative Commons license:  <https://creativecommons.org/licenses/?lang=en>

A Thesis submitted in the fulfillment of the requirements for the degree of Doctor
of Philosophy in Electrical and Telecommunications Engineering

Heat transport in binary semiconductor polytypes and devices based on 2D materials: an *ab initio* study

Author:

Martí Raya Moreno

Supervisor:

Prof. Xavier Cartoixa Soler

Submitted in:

May 2022

Departament d'Enginyeria Electrònica
Universitat Autònoma de Barcelona

Abstract

In this thesis we calculate, using first principles and solving the Phonon Boltzmann Transport Equation, the lattice thermal conductivity (κ) for binary semiconductor polytypes. First, we present results for the nanoscale-metastable hexagonal diamond (lonsdaleite) Si, showing a reduction of 40% in comparison with the common cubic diamond polytype of Si, finding a similar reduction in nanowires. Building onto this, we extend those results to binary semiconductors, calculating the κ for cubic (zinc-blende) and hexagonal (wurtzite) phases for 8 binary semiconductors, explaining the different behavior of the ratio $\kappa_{\text{hex}}/\kappa_{\text{cub}}$ between the two phases. Contrary, to silicon we found that this cannot be explained by classical conditions for a high κ ; indeed, we show that this behavior depends on the relative importance of two antagonistic factors: anharmonicity, which we find to be always higher in the cubic phase; and the accessible phase space, which is higher for the less symmetric hexagonal phase. Based on that, we develop a method that predicts the most conducting phase—cubic or hexagonal—where other more heuristic approaches fail. We also present results for nanowires made of the same materials, showing the possibility to tune $\kappa_{\text{hex}}/\kappa_{\text{cub}}$ over a wide range by modifying their diameter, thus making them attractive materials for complex phononic and thermoelectric applications/systems. We also briefly comment on

Abstract

the differences between binary alloys cubic and hexagonal phases, as well as the phase and twin boundary resistance for some of the semiconductors.

Moreover, we present BTE-Barna (Boltzmann Transport Equation - Beyond the Rta for NAnosystems), a software package that extends the Monte Carlo (MC) module of the `almaBTE` solver of the Peierls-Boltzmann transport equation for phonons (PBTE) to work with nanosystems based on 2D materials with complex geometries. To properly capture how the phonon occupations evolve in momentum space as a result of scattering, we have supplemented the relaxation-time approximation with an implementation of the propagator for the full linearized version of the PBTE. The code can now find solutions for finite and extended devices under the effect of a thermal gradient, with isothermal reservoirs or with an arbitrary initial temperature distribution in space and time, writing out the temperature and heat flux distributions as well as their spectral decompositions. Besides the full deviational MC solver, an iterative solver of the linearized PBTE for highly symmetric systems confined along some direction, namely nanoribbons and nanowires, is also included. Finally, we use these new tools to investigate the features arising from hydrodynamic effects in graphene and phosphorene devices with finite heat sources. We explain the mechanisms that create these hydrodynamic features, showing that boundary scattering and geometry are determinant factors, and that the length scales at which they can appear depend solely on the ability of intrinsic scattering to randomize the heat flux. We relate this last point to the non-local lengths and mean free paths, additionally providing an insight into how the scattering operator must be treated to obtain a proper description of the hydrodynamic behavior.

Acknowledgments

First, I would like to thank my supervisor Prof. Xavier Cartoixà Soler for his trust during these years, which allowed me to start pursuing a scientific career, as well as his guidance, reflected in useful discussions that have contributed to increase the overall quality of my work and this thesis.

Second, I really appreciate the kind hospitality of the Theoretical Materials Chemistry group of Prof. Georg K. H. Madsen at the Institute of Materials Chemistry (TU Wien), especially for hosting me during the pandemic. I would like to particularly thank my supervisor there, Dr. Jesús Carrete Montaña, for all the interesting talks about but not limited to my research. Not only that, but I want to thank both him and Ana Diaz Roca for the good moments we shared: the nice walks, glühwein (without alcohol of course), small bites, ice-skating, lunches, and so on; you made me feel less alone in quite a complex situation far away from home. Indeed, science aside meeting you both was one of the best outputs of my stay there in Wien.

Moreover, I would like to thank the financial support of the Ministerio de Educación, Cultura y Deporte program of Formación de Profesorado Universitario under Grant No. FPU2016/02565, the Ministerio de Economía y Competitividad (MINECO) under Grant No. TEC2015-67462-C2-1-R (MINECO/FEDER), and

Acknowledgments

the Ministerio de Ciencia, Innovación y Universidades under Grant No. RTI2018-097876-B-C21 (MCIU/AEI/FEDER, UE); without which this thesis wouldn't have been possible. Moreover, I would also like to thank the financial support of the Ministerio de Universidades under grant EST19/00655 during my short-term stay at the Institute of Materials Chemistry (TU Wien).

Finally, I cannot ignore all other people that have also contributed not from a scientific point but from a human point of view. My colleagues during all these four years in the department of electronic engineering: Alvaro, Emili, Ertugrul, Ferran, Jona, Laura, Matteo, and Marta. Especial mention here to Ana Ruiz Flores, thank you for all those special shared moments and for making all those years much more entertaining, with all travels, lunches, and those necessary procrastination coffees; you made me better. I would also like to thank my combat mates, Daniel and Ivan, for those sometimes needed shouts and punches. I am also quite grateful to Noemí Contreras Pereda for her kind and sincere support and wise advice not only for those years but since we met in the Bachelor's degree, as well as for our friendship which resisted a non-negligible number of coffees dropped on top of her. Neither I can forget all my family, particularly my parents who always supported pursuing my dreams and who have been always an example of determination. Certainly, I cannot forget my dog, Blanqueta, who has been a great emotional support to me.

Contents

Abstract	i
Acknowledgments	iii
Introduction	1
1 Solids from first-principles: the electronic problem in a crystalline lattice	6
1.1 Quantum description of a material	7
1.1.1 The Born-Oppenheimer approximation and the electronic problem	8
1.2 Density functional theory	9
1.2.1 Approaches to the exchange-correlation functional . . .	12
1.2.2 Periodic boundary conditions: lattices and reciprocal space	13
1.2.3 Basis set	15
1.2.4 Pseudopotential method	16
1.2.5 London's dispersion forces in DFT	16
1.3 Time independent perturbation theory	17
1.3.1 First-order corrections	18
1.3.1.1 Hellman-Feynman theorem: atomic forces . .	19
1.3.1.2 1 st -order correction to the wave functions: the Sternheimer equation	19

Contents

1.3.2	Higher order corrections: the $2n+1$ theorem	20
1.3.3	Multiple perturbations	21
1.4	Density functional perturbation theory	21
1.4.1	The case of homogeneous electric field	22
1.5	Time dependent perturbation theory: Fermi's golden rule	23
2	Lattice dynamics, phonons, and their interactions	26
2.1	Lattice dynamics: the harmonic approximation	27
2.1.1	Harmonic approximation and normal modes of vibration	29
2.1.1.1	Polar materials	31
2.1.2	Quantum theory and phonons	34
2.1.2.1	Quantum theory of lattice dynamics and lattice vibrational energy	36
2.1.2.2	Phonons and normal modes	38
2.1.3	Phonon specific heat and density of states for general lattice	39
2.1.4	Phonon calculations from first principles	40
2.1.4.1	Finite difference method	40
2.1.4.2	Linear response theory	41
2.1.4.3	Molecular dynamics method	42
2.2	Anharmonicity	43
2.2.1	Three-phonon processes	45
2.2.1.1	Umklapp and normal scattering	47
2.2.2	Performing integrals containing three-phonon processes	49
2.2.3	Frequency shift, thermal expansion and Grüneisen param- eter	51
2.2.4	Anharmonic calculations from first principles	52
2.3	Mass disorder effect over atomic vibrations: isotopic scattering .	54
2.4	Phonons in alloys: the virtual crystal approximation	55
2.5	Electron-phonon interaction	56

3	Thermal transport modeling	58
3.1	Mesoscopic Modeling and Fourier's law	59
3.1.1	Fourier's law failure and beyond-Fourier mesoscopic models	59
3.1.1.1	Generalized hydrodynamics	61
3.2	Semiclassical modeling: the PBTE	62
3.2.1	Approaches to collision term	64
3.2.1.1	Four and higher-order phonon processes	67
3.2.2	Solution for the homogeneous system with an applied thermal gradient	68
3.2.3	Size effects and solution for highly symmetric systems	71
3.2.4	General solution of the PBTE for arbitrary geometries and boundary conditions	75
3.2.5	Electron-phonon coupling and thermoelectric properties	76
3.2.5.1	Solution of the homogeneous coupled phonon-electron BTE	78
3.2.6	Software packages solving the PBTE based on first-principles	81
3.3	Other methodologies	84
4	Thermal simulation of devices: the Monte Carlo method	86
4.1	The basics and limits of the phonon-based Monte Carlo methods	87
4.2	Energy-based deviational formulations	90
4.2.1	Deviational energy sources	91
4.2.1.1	Initial temperature profile	92
4.2.1.2	Isothermal boundaries	92
4.2.1.3	Applied thermal gradients	93
4.2.2	Interaction with boundaries	94
4.2.2.1	Specular scattering	94

Contents

4.2.2.2	Diffusive boundaries	95
4.2.3	Interaction with interfaces: the diffusive mismatch model	96
4.2.4	Periodic boundary conditions	98
4.2.5	Particle termination and canceling	98
4.3	Scattering within energy-based deviational MC methods	99
4.3.1	RTA scattering	99
4.3.2	Beyond the RTA scattering	100
4.4	Properties sampling	101
4.5	The ensemble energy-based deviational MC algorithm	102
4.6	Steady-state and RTA efficient algorithms	103
4.6.1	Trajectory sampling and steady-state properties	106
4.6.2	Extended systems with applied gradients	107
5	Thermal conductivity in nanoscale-emerging crystal phases	109
5.1	Cubic and hexagonal phases	111
5.2	Lonsdaleite silicon	112
5.3	III-V and II-VI semiconductors	119
5.3.1	Interatomic Force Constants test	120
5.3.2	Bulk	130
5.3.2.1	Standard analysis of $\kappa_{\text{hex}}/\kappa_{\text{cub}}$	132
5.3.2.2	Effective anharmonicity and accessible phase space	135
5.3.2.3	The ratio of effective anharmonicity and accessible phase space product	142
5.3.2.4	Four-phonon scattering for GaN	147
5.3.3	Nanowires	148
5.3.4	Alloys	158
5.4	Phase boundary thermal resistance	159
5.5	Summary and conclusions	164

6	BTE-Barna: An extension of almaBTE for thermal simulation of devices based on 2D materials	166
6.1	BTE-Barna structure	168
6.2	Effective thermal conductivity in simple nanosystems	171
6.3	RTA Monte Carlo	172
6.3.1	Interface model for stacked layered systems: localized diffuse mismatch model	173
6.4	Beyond RTA Monte Carlo	176
6.4.1	B_{ij} calculation and enforcement of conservation laws . .	177
6.4.2	Efficient propagator calculation	178
6.4.2.1	Linear interpolation of the propagator for sys- tems with multiple reference temperatures . .	179
6.4.3	RTA-bRTA	180
6.5	Code validation	181
6.5.1	RTA code validation	182
6.5.2	Beyond RTA: B -matrix validation	183
6.5.3	Beyond RTA: Propagator and bRTA validation	184
6.6	Results	185
6.6.1	Phosphorene devices	185
6.6.1.1	Nanoribbons	187
6.6.1.2	RTA, bRTA and Fourier heat equation comparison	190
6.6.1.3	Finite device examples	197
6.6.2	Results: Example of material junction	199
6.7	Summary and conclusions	208
7	Hydrodynamic signatures in thermal transport in devices based on 2D materials from first-principles	209
7.1	Hydrodynamics and 2D materials: the role of normal and umk- lapp processes	212

Contents

7.2	Methodology	214
7.3	Bulk properties and size effects	216
7.4	Results	220
7.4.1	Quasiballistic devices	221
7.4.1.1	Vortex formation	230
7.4.2	Non-ballistic devices	231
7.4.2.1	Phosphorene	231
7.4.2.2	Graphene	238
7.5	Summary and conclusions	241
Conclusions		243
Appendix A Description of the BTE–Barna executables, inputs, and outputs		246
A.1	kappa_Tsweep_nanos	246
A.2	Monte Carlo simulators and analyzers: inputs, outputs and executables	247
A.2.1	Geometry files	247
A.2.2	RTAMC2D	250
A.2.2.1	input.xml	250
A.2.2.2	Output files	253
A.2.3	PropagatorBuilder	255
A.2.4	beRTAMC2D	256
A.2.4.1	Line command inputs	257
A.2.4.2	input.xml	257
A.2.4.3	Outputs: standard output	259
A.2.4.4	Outputs: properties.msgpack.bin	259
A.2.5	dist_reader	260
A.2.5.1	input.xml	260

Contents

A.2.5.2	Output files	261
---------	------------------------	-----

Bibliography		262
---------------------	--	------------

Introduction

Over the last decades, the continuous development of micro- and nanofabrication techniques has allowed for ever-increasing integration levels in electronic devices [1, 2]. A deep understanding of the thermal transport in those systems is fundamental to optimize their operation since, if not carefully managed, heat can severely hinder their efficiency and/or durability [3–6].

Indeed, heat management has already introduced limitations to processor design. In particular, the ever-higher integration levels, following Moore’s law trend (see the exponential evolution in time of the number of transistors in processors at Fig. I.1), mean ever-shrinking devices, which has increased the sub-threshold (off state) and gate leakage currents of the transistors. These increments have translated to rather high-density powers; for instance, a large soccer field, $\sim 8000\text{ m}^2$, full of typical 2006’s chip with power densities in the order of 100 W cm^{-2} [3, 4] dissipates approximately the equivalent of the combined generation power of all the 7 active Spanish nuclear reactors, 7.4 GW [7]. Consequently, the clock rate—the rate at which the processor’s transistors switch—has stagnated during the last 15 years (see clock-rate and thermal power design in Fig. I.1) to prevent processors from melting by their self-generated heat. This forced the industry to move to multi-core processors to maintain the performance increase (see the

Introduction

number of logical cores in Fig. I.1), so that each core is able to run at a lower frequency resulting in lower dissipation but still allowing an increment in the performance [6]. Notwithstanding this paradigm change, heat management still remains as one of the key problems for electronics. Furthermore, this continuous shrinking not only causes heat issues but pushes the materials of those devices to their fundamental limits, i.e. atomic size. In that context two-dimensional materials (2DMs), thanks to their excellent physical properties [8], together with the possibility of creating stackings with the desired electrical and/or chemical properties, as well as their compatibility with current fabrication technology, are quite promising candidates to replace traditional materials in transistors [9, 10].

Moreover, those advances in semiconductor synthesis and fabrication techniques at the micro- and nanoscale have lead to a development of more efficient thermoelectric systems (i.e. systems that can convert thermal to electric energy) [15, 16], which are interesting for energy-harvesting applications. To detail, they allow not only to give a practical use to thermal waste of all our devices and/or buildings—something quite interesting in the current situation of climate crisis—but to generate energy for wearable devices, thus removing the necessity of external batteries [17]. However, traditionally those systems offered quite a low efficiency, therefore creating a need to enhance their energy conversion ratio [18]. This last has brought into the spotlight the importance of phonon engineering or phononics for such a purpose, namely the use of nanostructuration to manipulate the vibrational properties of materials. Nanostructuration provides an effective way of reducing the lattice thermal conductivity without deteriorating electrical properties (i.e. obtaining a phonon-glass while keeping an electron-crystal) [16, 17, 19], thereby obtaining conversion ratios unachievable using more classical approaches, such as alloying [19]. Here, it is interesting to evaluate the new metastable phases found in group-IV, III-V, and II-VI semiconductor nanowires [20–30] for thermoelectric applications, as they normally show a lower

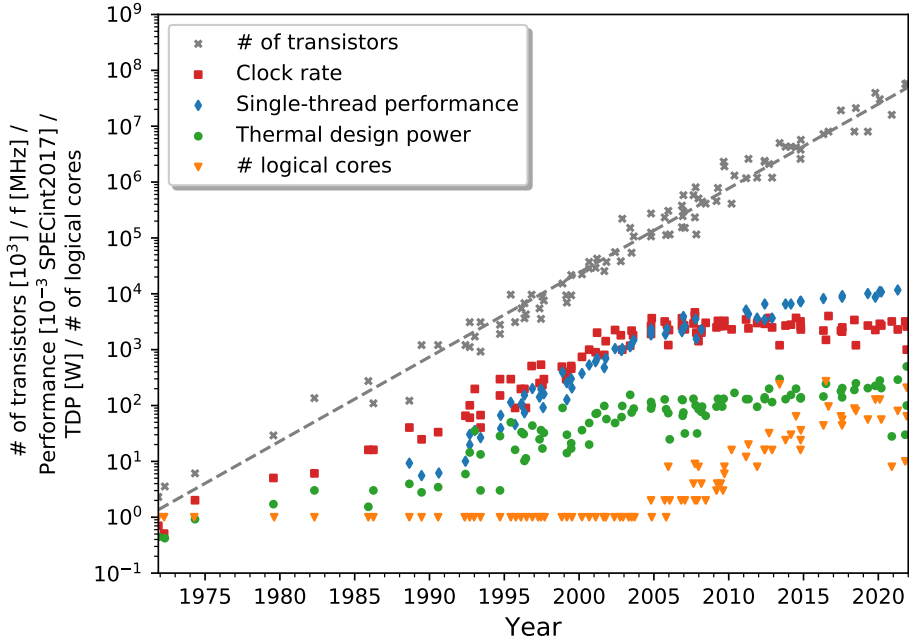


Figure I.1.: Number of thousands of transistors, clock rate, single-thread performance, thermal power design (i.e. the average power the processor dissipates when operating at the base frequency with all cores active), and the number of logical cores of several processors as a function of their release date. Data has been collected by Rupp [11] from the original work of Danowitz *et al.* [12] up to 2010, and from AMD, Intel and IBM data-sheets henceforth to 2022. We note that the original data from Ref. [12] provides performance in terms of SPECint 2006 [13], which is approximately 9 times larger than SPECint 2017 [14] (i.e. such factor is obtained by comparing results for Xeon Platinum 8180 for both standards). The dashed gray line provides Moore's law [1] trend.

thermal conductivity than their more stable counterparts while maintaining similar electronic properties. Moreover, it is worth mentioning that such reduction and control over thermal properties are also interesting for energy-saving applications, for instance, they can offer more effective and eco-friendly thermal insulators for buildings than classical alternatives [31].

Introduction

Classically, heat has been modeled with Fourier’s law [32]; however, this mesoscopic equation is known to fail in times and sizes that are not rare in nanodevices [33–38], and thus it becomes necessary to resort to microscopic-based models. In the case of semiconductors, where the main heat carriers are collective bundles of phonons (i.e. vibrational quanta of a crystalline lattice), incoherent heat transport, including non-Fourier features, can be described using the semiclassical Peierls-Boltzmann transport equation (PBTE) with the appropriate boundary conditions [39, 40].

Originally, the microscopic properties required to solve the former equation were computed using simplified models, like Debye, and/or parameterizations for the atomic interactions, i.e. force fields [41, 42]. However, such models and/or parameterizations lacked the transferability to investigate novel materials. Moreover, in most cases, they cannot properly describe the thermal properties of the materials they are parameterized for; an illustrative case of the last is the failure of the Tersoff force field to reproduce Si thermal conductivity [43]. Consequently, it was not until the inclusion of phonon properties calculated from first-principles that those methods gained popularity, as it allowed to predict the thermal properties of materials where those simpler models are lacking or directly erroneous [44, 45]. Indeed, the advent of several open-source packages solving the PBTE for the community such as *ShengBTE* [46], *almaBTE* [47] or *Phono3py* [48], has increased even more the popularity of the first-principles-based PBTE for the description of the thermal properties.

In this thesis, we discuss the thermal conductivity (κ) for nanoscale emerging crystal phases for group-IV, III-V, and II-VI semiconductors using first-principles-based PBTE, explaining the microscopic origin of κ difference between these nanoscale-metastable and the bulk-stable phases. Moreover, we have developed efficient computational tools for the solution of the PBTE in nanodevices based on 2D materials and used those new tools to discuss the hydrodynamic features in

Introduction

such devices from an *ab initio* perspective.

This thesis is structured as follows: Chapters 1-4 describe in detail the theoretical framework and methodologies used in this thesis. First, in Chapter 1 we introduce the quantum description of crystals, focusing on its practical solution using density functional theory. In Chapter 2 we introduce phonons, their interactions, and practical ways to calculate them using first principles. Then in Chapter 3 we discuss the different heat transport models ranging from mesoscopic to microscopic models, focusing on the Peierls-Boltzmann transport equation, its solution for several boundary conditions, and the different approaches to the scattering operator. To finish with the theoretical introduction, in Chapter 4, we review the Monte Carlo methods for the solution of the PBTE equation for complex geometries and/or boundary conditions. Afterwards in Chapter 5 we discuss the use of such methodologies to compute the thermal properties in nanoscale-emerging crystal phases unstable in bulk under normal conditions. In Chapter 6, we present BTE-Barna a package, including iterative and Monte Carlo solvers of the PBTE, for nanodevices based on 2D materials. Finally, in Chapter 7 we present a practical example in which BTE-Barna has been used to investigate hydrodynamic signature in 2D-based nanodevices from first principles. A general summary, conclusions and future perspective are given in Conclusions. The Appendix provides a detailed documentation of BTE-Barna executables, inputs, and outputs.

CHAPTER 1

Solids from first-principles: the electronic problem in a crystalline lattice

In this Chapter we discuss the quantum description of a material focusing on crystals, as they offer a parameter-free way of accurately computing the properties of the different materials, thus allowing to model novel materials for which other simpler descriptions are lacking. First, we present the general problem in Section 1.1, focusing on the common approaches on how to simplify the problem in Subsection 1.1.1. We follow, with an explanation on one of the most widespread methodologies to solve this problem, the density functional theory, in Section 1.2, centering on the case of crystals. Finally, we present ways of computing, using perturbation theory, the static and dynamic response of materials to several kinds of perturbations like a homogeneous electric field, in Sections 1.3-1.5.

1.1. Quantum description of a material

Materials are composed of nuclei and electrons, so that given a set of N atoms, with l electrons, the Hamiltonian describing this system will be [49]

$$\begin{aligned}
 H_{\text{MB}} = T_{\text{N}} + T_{\text{e}} + V_{\text{ee}} + V_{\text{eN}} + V_{\text{NN}} = \\
 - \sum_I^N \frac{\hbar^2}{2M_I} \nabla_{\mathbf{R}_I}^2 - \sum_i^l \frac{\hbar^2}{2m_e} \nabla_{\mathbf{r}_i}^2 + \frac{1}{2} \sum_{I \neq J}^N \frac{Z_I Z_J}{4\pi\epsilon_0} \frac{1}{|\mathbf{R}_I - \mathbf{R}_J|} + \\
 \frac{1}{2} \sum_{i \neq j}^l \frac{e^2}{4\pi\epsilon_0} \frac{1}{|\mathbf{r}_i - \mathbf{r}_j|} - \sum_I^N \sum_i^l \frac{e Z_I}{4\pi\epsilon_0} \frac{1}{|\mathbf{r}_i - \mathbf{R}_I|}, \quad (1.1)
 \end{aligned}$$

where T_{N} and T_{e} are the kinetic energy operator for nuclei and electrons, V_{ee} , V_{NN} and V_{eN} are the electron-electron, nucleus-nucleus and electron-nucleus potential energy operator, I, J, \dots refer to nuclei, i, j, \dots refer to electrons, \hbar is the reduced Planck constant, M_I is the mass of the I -th nucleus, $\nabla_{\mathbf{R}_I}^2$ and $\nabla_{\mathbf{r}_i}^2$ are the Laplace operator for the nuclei and electrons, respectively, m_e is the mass of an electron, \mathbf{R}_I and \mathbf{r}_i are nuclear and electronic coordinates, e is the elementary charge (without sign), Z_I is the I -th nucleus charge, ϵ_0 is the vacuum permittivity. We note that for simplicity Eq. 1.1 is the non-relativistic version of the Hamiltonian, so that effects like spin-orbit coupling are neglected. Moreover, it treats nuclei as charged point particles disregarding its constituents.

Therefore, the many-body time-independent Schrödinger equation is

$$H_{\text{MB}} \Psi_{\text{MB}} = E_{\text{total}} \Psi_{\text{MB}}, \quad (1.2)$$

where E_{total} is the system energy, and Ψ_{MB} is the many-body wave function, which depends on both nuclear and electronic coordinates. In general Eq. 1.2 is rather too complex to be solved except for extremely simple systems like small atoms or tiny molecules.

1.1.1. The Born-Oppenheimer approximation and the electronic problem

A simplification of the many-body problem can be achieved by assuming the following ansatz for the many-body wave function

$$\Psi_{\text{MB}}(\mathbf{r}, \mathbf{R}) = \Xi(\mathbf{R})\Psi_{\mathbf{R}}(\mathbf{r}), \quad (1.3)$$

i.e. the total wave function is a product of the nuclear wave function, $\Xi(\mathbf{R})$, which only depends on nuclei coordinates, and the electronic wave function for a given nuclear coordinates, i.e. supposing that the nuclear coordinates are fixed at \mathbf{R} , so its dependence on them is parametric. Effectively, this latter means that any change in the nuclear coordinates is instantly followed by the electrons. Such a crude assumption is justified by the fact that the nuclear mass is much larger than the electronic one so that the nuclear dynamics is much slower than the electronic one, effectively decoupling their dynamics. Moreover, this great difference in mass also implies that the nuclear wave function is very well localized around the classical positions when compared to the electronic counterpart.

This approach was developed by Born and Oppenheimer, and thus is known as the Born-Oppenheimer approximation (BOA). In their original work [50], they used perturbation theory to obtain the energy in a molecule including the atomic vibrations. To do so, they have considered the electronic movement for an arbitrary but fixed nuclear configuration, so T_{N} is introduced perturbatively; thus obtaining Eq. 1.3 as the 0th order correction wave function.

Hence, in BOA the electronic Schrödinger equation is

$$H_{\text{el}}\Psi_{\mathbf{R}}(\mathbf{r}) = [T_{\text{e}} + V_{\text{ee}} + V_{\text{eN}} + V_{\text{NN}}]\Psi_{\mathbf{R}}(\mathbf{r}) = E_{\text{el}}\Psi_{\mathbf{R}}(\mathbf{r}), \quad (1.4)$$

1. Solids from first-principles: the electronic problem in a crystalline lattice

where V_{eN} is usually referred as an external potential, $V_{\text{ext}}(\mathbf{r}; \mathbf{R})$, influencing the electrons. Moreover, we note that V_{NN} only introduces a rigid shift as it depends parametrically on \mathbf{R} . Hereafter, we use Ψ to refer to the BOA many-body electronic wave function.

Consequently, within BOA, the solution of Eq. 1.4 for several \mathbf{R} gives the energy surface in which the nuclei are moving. Furthermore, it allows to separate the electronic and nuclear degrees of freedom highly reducing the complexity of Eq. 1.2.

1.2. Density functional theory

Despite BOA, a formal solution to the quantum problem is still a Herculean task. Although there exist a variety of methods to solve Eq. 1.4 like Hartree-Fock based methods [51] (e.g. Hartree-Fock with Møller-Plesset to account for the electronic correlation), or multi-configurational self-consistent field theory [52], those methods require the calculation of the rather complex electron-electron interactions—including Coulomb, exchange (i.e. Pauli repulsion) and correlation—which highly complicates its solution. Moreover, those methods rely on the wave function, which despite containing all the information is a quite unintuitive object that provides no clear picture except when asked by an operator [52].

Alternatively, Hohenberg and Kohn (HK) demonstrated via *reductio ad absurdum* that the ground-state density, $\rho_0(\mathbf{r})$, uniquely determines the external potential (i.e. nuclei positions and characteristics), V_{ext} , acting on the electrons [51–53]. Consequently, as V_{ext} determines the Hamiltonian, it follows that the many-body wave function—for all states, i.e. excited (Ψ') and ground (Ψ_0) states—is determined from it, from which the ground-state wave function and

1. Solids from first-principles: the electronic problem in a crystalline lattice

density ($\rho_0 \rightarrow V_{\text{ext}} \rightarrow \Psi \rightarrow \Psi_0 \rightarrow \rho_0$) can be computed. This last relation means that the ground state density also determines all excited states. Moreover, since the energy (E_{el}) is a function of the Hamiltonian, which is determined by ρ_0 , it must exist a functional that maps ρ_0 into E_{el} . Indeed, that functional must be minimized by the ground-state density as it is the state of minimal energy for a given atomic configuration [49, 51, 52].

Although the HK theorems state that must exist an energy functional of the density, it gives no hint of how to obtain it, and thus it provides no benefit with respect to Eq. 1.4. Indeed the real utility of the HK theorems is after Kohn and Sham (KS) [54], who proposed an ansatz to practically exploit those theorems. KS proposed to build an auxiliary system of non-interacting electrons acted upon by an effective potential (V_{eff}), thereby coupling the electrons through a mean-field. These single-particle wave functions, or KS orbitals, are defined in such a way that the resulting density is equal to the ground state one, and thus the HK theorems hold for the auxiliary system [51].

Hence, the total density for this fictitious system of N non-interacting electrons is

$$\rho_0(\mathbf{r}) = 2 \sum_i^N f_i |\phi_i(\mathbf{r})|^2, \quad (1.5)$$

where the 2 is due to spin degeneracy, f_i is the Fermi-Dirac distribution—henceforth we suppose a temperature of 0 K, which reduces f_i to a step-function, leaving only empty and doubly occupied states, so that the summations can be restricted to those occupied states—and ϕ_i is a KS orbital, and its energy functional is

$$E_{\text{el}}[\rho] = T_0[\rho] + \int \left(\frac{1}{2} V_{\text{H}}(\mathbf{r}) + V_{\text{ext}}(\mathbf{r}) \right) \rho(\mathbf{r}) d\mathbf{r} + E_{\text{XC}}[\rho] + E_{\text{NN}}, \quad (1.6)$$

where T_0 , $V_{\text{H}}(\mathbf{r})$, E_{XC} and E_{NN} are the single-particle kinetic energy operator,

1. Solids from first-principles: the electronic problem in a crystalline lattice

the Hartree potential (i.e. classic electrostatic repulsion, $V_H(\mathbf{r}) = e^2 \int \frac{\rho(\mathbf{r}')}{|\mathbf{r}-\mathbf{r}'|} d\mathbf{r}'$), the exchange-correlation functional which contains all the many-body corrections to the independent-particle ansatz, namely the exchange and correlation effects plus the kinetic energy correction accounting for the difference between its value in the independent-particle and many-body pictures, and the energy due to the electrostatic interaction between the different nuclei, respectively.

Therefore, there are only two unknown terms in Eq. 1.6, $T_0[\rho]$ and $E_{XC}[\rho]$. The former is usually calculated in terms of the KS orbitals,

$$T_0[\rho] \rightarrow T_0[\phi] = \sum_i^N \langle \phi_i | \frac{-\hbar^2}{2m_e} \nabla^2 | \phi_i \rangle, \quad (1.7)$$

as the exact relation with density is unknown, and any functional should be of high quality because of the importance of this contribution. Before discussing in detail the latter term, we found it important to discuss the consequences of treating the kinetic term in this way.

Albeit within the DFT and HK spirit it should be possible to obtain E_{el} by direct minimization of a trial density, i.e. without the need of the explicit computation of ϕ_i , the practical way of computing T_0 presented in Eq. 1.7 requires of them. To do so, one needs to note that the KS orbitals must obey the single-electron Schrödinger equation,

$$\left(\frac{-\hbar^2}{2m_e} \nabla^2 + V_{\text{eff}}(\mathbf{r}) \right) \phi_i(\mathbf{r}) = \varepsilon_i \phi_i(\mathbf{r}), \quad (1.8)$$

and its solution,

$$\sum_i^N \varepsilon_i = T_0[\rho] + \int V_{\text{eff}}(\mathbf{r}) \rho(\mathbf{r}) d\mathbf{r}. \quad (1.9)$$

Introducing Eq. 1.9 into Eq. 1.6 and minimizing with respect to ρ , leads

1. Solids from first-principles: the electronic problem in a crystalline lattice

to [55, 56]

$$V_{\text{eff}}(\mathbf{r}) = V_{\text{KS}}(\mathbf{r}) = V_{\text{H}}(\mathbf{r}) + V_{\text{ext}}(\mathbf{r}) + V_{\text{XC}}(\mathbf{r}) \quad (1.10)$$

where V_{KS} is the Kohn-Sham potential, and $V_{\text{XC}}(\mathbf{r}) = \frac{\delta E_{\text{XC}}[\rho]}{\delta \rho(\mathbf{r})}$. Consequently, Eqs. 1.8-1.10 together with Eq. 1.5 present a set of equations, known as the Kohn-Sham equations, that can be solved self-consistently. It is also worth mentioning that the KS eigenvalues, ε_i , are mathematical objects void of physical meaning, which surprisingly tend to provide a good/acceptable first approximation to the many-body spectra [57].

Finally, for the latter of the unknown functionals (i.e. E_{XC}) there is, unfortunately, no knowledge of its exact form, at least for the correlation part, and thus all DFT error lies in the approximation to this term, which includes not only the exchange and correlation effects but the kinetic energy correction because of the use of the KS orbitals in its computation; indeed quoting Kohn [58]

“The practical usefulness of ground-state DFT depends entirely on whether approximations for the functional $E_{\text{XC}}[\rho]$ could be found, which are at the same time sufficiently simple and sufficiently accurate.”

1.2.1. Approaches to the exchange-correlation functional

As we have noted, DFT is in principle an exact theory, however, the ignorance of the exact exchange-correlation term for general complex systems forces us to rely on approximations to this term, thus making its practical implementation approximate.

The most common and simple approaches to $E_{\text{XC}}[\rho]$ are the local density approximation (LDA) and the generalized gradient approximation (GGA). Within the LDA the exchange-correlation term is approximated at each point by the

1. Solids from first-principles: the electronic problem in a crystalline lattice

energy of a homogeneous electron gas (HEG, jellium) of the same density,

$$E_{\text{XC}}^{\text{LDA}}[\rho] = \int \rho(\mathbf{r}) \varepsilon_{\text{XC}}^{\text{HEG}}[\rho(\mathbf{r})] d\mathbf{r}, \quad (1.11)$$

where $\varepsilon_{\text{XC}}^{\text{HEG}}$ is the exchange-correlation energy per particle of a HEG of density $\rho(\mathbf{r})$. This $\varepsilon_{\text{XC}}^{\text{HEG}}$ is commonly parametrized to quantum Monte Carlo solutions of the HEG problem, for instance, the parametrization of Perdew and Zunger [59] to Ceperley and Alder [60] quantum Monte Carlo data; other common parametrizations to the Ceperley and Alder data are those of Perdew and Wang [61], and Vosko, Wilk, and Nusiar [62].

On the other hand the GGA generalizes LDA by introducing an enhancement factor $F_{\text{XC}}[\rho(\mathbf{r}), \nabla\rho(\mathbf{r})]$ as [63]

$$E_{\text{XC}}^{\text{GGA}}[\rho] = \int \rho(\mathbf{r}) \varepsilon_{\text{XC}}^{\text{HEG}}[\rho(\mathbf{r})] F_{\text{XC}}[\rho(\mathbf{r}), \nabla\rho(\mathbf{r})] d\mathbf{r}. \quad (1.12)$$

Commonly used GGA functionals are the Perdew-Wang-95 (PW95) [63] or the Perdew-Burke-Ernzerhof (PBE) [64].

1.2.2. Periodic boundary conditions: lattices and reciprocal space

Although the application of the BOA together with the DFT highly reduces the complexity of solving the quantum mechanics problem for a given set of atoms, this problem is still of high complexity. Eq. 1.4 and the Kohn-Sham equations are valid for all kinds of materials, ranging from gases to ordered solids (i.e. crystals). However, its complexity still makes its solution unpractical out of relatively small systems (i.e. few thousands of atoms), and thus bulk materials would *a priori* be out of its scope.

1. Solids from first-principles: the electronic problem in a crystalline lattice

Nevertheless, for ordered bulk materials, i.e. crystals, one can exploit the symmetry of the system to fully reduce the problem to a repetitive unit, known as the unit cell, defined by three lattice vectors, $L = (\mathbf{a}_1, \mathbf{a}_2, \mathbf{a}_3)$, with a volume $V_{\text{uc}} = \det(L)$. Therefore, the Hamiltonian for the independent electrons has the crystal symmetry, $V_{KS}(\mathbf{r} + \mathbf{R}) = V_{KS}(\mathbf{r})$, where \mathbf{R} is a translation vector ($\mathbf{R} = \sum_{\alpha} n_{\alpha} \cdot \mathbf{a}_{\alpha}$, where α runs over lattice vectors and $n_{\alpha} \in \mathbb{Z}$) [65]. Following this, it is obvious that translation operators, $T_{\mathbf{R}}$, must commute with the Hamiltonian, be additive and form an Abelian group. These last properties restrict the KS eigenfunctions to functions satisfying $\phi_j(\mathbf{r} + \mathbf{R}) = e^{i\mathbf{k}\mathbf{R}}\phi_j(\mathbf{r})$, such as Bloch's waves [65, 66],

$$\phi_{n\mathbf{k}}(\mathbf{r}) = e^{i\mathbf{k}\cdot\mathbf{r}}u_{n\mathbf{k}}(\mathbf{r}) \quad (1.13)$$

where \mathbf{k} is a wave vector of the reciprocal lattice (B) and $u_{n\mathbf{k}}(\mathbf{r})$ is a function with the periodicity of the lattice

$$\mathbf{k} = B\mathbf{k}_{\beta} = (\mathbf{b}_1, \mathbf{b}_2, \mathbf{b}_3)k_{\beta}, \quad (1.14)$$

$$B = 2\pi(L^{-1})^T. \quad (1.15)$$

Here, \mathbf{k}_{β} is a vector in the B basis. These \mathbf{k} are restricted to a cell in the reciprocal lattice, being the most common choice the Brillouin zone (BZ), by means of system's periodicity (i.e. $\phi_{n(\mathbf{k}+\mathbf{G})} = \phi_{n\mathbf{k}}$, where \mathbf{G} is a reciprocal lattice vector) [65, 66]. Moreover, crystal symmetry also relates the different \mathbf{k} points through point-group operations, and thus allows further restricting the calculation to a quotient group of \mathbf{k} points—usually named as the irreducible BZ—; so the properties in a general \mathbf{k} point can be recovered through rotations and inversions from this irreducible set of points [67].

1. Solids from first-principles: the electronic problem in a crystalline lattice

1.2.3. Basis set

The solution of the KS equations can be achieved by discretizing the unit cell using a real space mesh, so that Eq. 1.8 can be solved through finite differences or discontinuous Galerkin method [49, 51]; however, in most cases the mesh size required for an accurate description renders those methods unpractical for an efficient solution of the KS equations.

Alternatively, it is possible to expand the KS orbitals in terms of a linear combination of basis functions. Maybe the most natural choice for those basis functions are the atomic orbitals φ_μ (i.e. modified or solutions of hydrogen-like atoms),

$$\phi_{n\mathbf{k}} = \sum_{A\mu} c_{n\mathbf{k}\mu} \varphi_\mu(\mathbf{r} - \mathbf{R}_A), \quad (1.16)$$

where A runs over all the unit cells. We note that in general the Hamiltonian terms will contain $\langle \varphi_\mu(\mathbf{r} - \mathbf{R}_A) | H | \varphi_{\mu'}(\mathbf{r} - \mathbf{R}_{A'}) \rangle$ terms, which vanish for separated orbitals. In contrast, as $u_{n\mathbf{k}}(\mathbf{r})$ has the periodicity of the system, it is possible to expand it as Fourier series,

$$u_{n\mathbf{k}}(\mathbf{r}) = \sum_{\mathbf{G}} c_{n\mathbf{k}}(\mathbf{G}) e^{i\mathbf{G} \cdot \mathbf{r}}. \quad (1.17)$$

In principle, this expansion requires an infinite number of plane waves. However, in practice, one needs to introduce a cutoff. In general, only smaller \mathbf{G} are required to properly reproduce the wave function. Therefore, $c_{n\mathbf{k}}(\mathbf{G})$ will become small for larger \mathbf{G} s, so that one can define the so-called plane wave kinetic energy cutoff, E_{cut} ,

$$|\mathbf{k} + \mathbf{G}| \leq \sqrt{\frac{2m_e}{\hbar^2} E_{\text{cut}}} \quad (1.18)$$

as the variable controlling the upper limit of the expansion. Overall, when compared to the orbital-based expansion, the plane-wave expansion offers several

1. Solids from first-principles: the electronic problem in a crystalline lattice

advantages, as it allows for a systematic improvement of the basis by merely increasing the cutoff and allows for an easier evaluation of atomic forces (see Subsection 1.3.1.1). On the other hand, within the plane-wave framework vacuum regions and atomic vicinity have the same computational cost, contrary to the orbital-based expansions in which vacuum regions are almost free.

1.2.4. Pseudopotential method

The complexity of the KS equations can be highly reduced by noting that the inner KS states are tightly-bound states highly located around the nucleus, and thus they remain almost unaffected by changes in the chemical environment. Hence, it becomes possible to separate the electronic density between valence states, which take part in the chemical bonding and are therefore affected by atoms in the vicinity, and core states, which remain frozen and unaltered by this vicinity [49].

The practical way to do it is to remove the core states, and to modify the resulting wave functions of the valence states, so near the nucleus they present a smooth node-less behavior while providing the same electronic charge as the full, i.e. all-electron, wave function in that region. Moreover, the V_{ext} is modified to provide the pseudo-wave function near the nucleus, while outside the nuclear region it becomes a screened ionic potential (i.e. Z_I is replaced by the number of valence electrons) [49, 51].

1.2.5. London's dispersion forces in DFT

London's dispersion forces, which in the condensed-matter community are usually a synonym of van der Waals forces (vdW), arise from quantum fluctuations caused by long-range electronic correlations, generating instantaneous dipoles.

1. Solids from first-principles: the electronic problem in a crystalline lattice

The local or semi-local character of LDA and GGA disregards these long-range and non-local correlations generating the vdW interaction [68–70].

Such a shortcoming of these common XC functionals hinders the accuracy of DFT calculations for systems in which these interactions are important, like it would be the case of graphite or other layered materials. To overcome this limitation, the most common approach is to add the missing interaction as a first-principles-based pair-wise interatomic potential [68], for instance, Grimme's D2 [71] and D3 [72] parameterizations. Alternatively, it is possible to properly treat vdW interactions by using a non-local XC functional [73–76].

1.3. Time independent perturbation theory

Several quantities of interest for physics, engineering, or chemistry, like optical and electrical responses, depend on the response of the system to some kind of perturbation [51]. Given a small enough perturbations, it is possible to expand any quantity (X) around its reference unperturbed value, $X^{(0)}$, using a Taylor series [51, 77]:

$$X(\lambda) = X^{(0)} + \lambda X^{(1)} + \lambda^2 X^{(2)} + \dots \quad (1.19)$$

being λ a small parameter and $X^{(n)}$ is the n -th order correction to X (i.e.: $X^{(n)} = \frac{1}{n!} \frac{d^n X^{(0)}}{d\lambda^n} \Big|_{\lambda=0}$). Consequently, by inserting that expansion into the Schrödinger equation one obtains:

$$H_i^{(0)} \left| \Psi_i^{(0)} \right\rangle = \varepsilon_i^{(0)} \left| \Psi_i^{(0)} \right\rangle \quad (1.20)$$

$$(H_i^{(0)} - \varepsilon_i^{(0)}) \left| \Psi_i^{(1)} \right\rangle = -(H_i^{(1)} - \varepsilon_i^{(1)}) \left| \Psi_i^{(0)} \right\rangle, \quad (1.21)$$

$$(H_i^{(0)} - \varepsilon_i^{(0)}) \left| \Psi_i^{(2)} \right\rangle = -(H_i^{(1)} - \varepsilon_i^{(1)}) \left| \Psi_i^{(1)} \right\rangle - (H_i^{(2)} - \varepsilon_i^{(2)}) \left| \Psi_i^{(0)} \right\rangle, \quad (1.22)$$

1. *Solids from first-principles: the electronic problem in a crystalline lattice*

$$\begin{aligned}
 (H_i^{(0)} - \varepsilon_i^{(0)}) \left| \Psi_i^{(3)} \right\rangle = \\
 - (H_i^{(1)} - \varepsilon_i^{(1)}) \left| \Psi_i^{(2)} \right\rangle - (H_i^{(2)} - \varepsilon_i^{(2)}) \left| \Psi_i^{(1)} \right\rangle - (H_i^{(3)} - \varepsilon_i^{(3)}) \left| \Psi_i^{(0)} \right\rangle
 \end{aligned} \tag{1.23}$$

and so on for higher orders. It is important to notice that wave functions appearing in Eqs. 1.20-1.23 must comply with the normalization constraint (i.e. $\langle \Psi_i | \Psi_i \rangle = 1$), and thus

$$\left\langle \Psi_i^{(0)} \left| \Psi_i^{(0)} \right\rangle = 1 \tag{1.24}$$

$$\left\langle \Psi_i^{(0)} \left| \Psi_i^{(1)} \right\rangle + \left\langle \Psi_i^{(1)} \left| \Psi_i^{(0)} \right\rangle = 0 \tag{1.25}$$

$$\left\langle \Psi_i^{(0)} \left| \Psi_i^{(2)} \right\rangle + \left\langle \Psi_i^{(1)} \left| \Psi_i^{(1)} \right\rangle + \left\langle \Psi_i^{(2)} \left| \Psi_i^{(0)} \right\rangle = 0 \tag{1.26}$$

$$\left\langle \Psi_i^{(0)} \left| \Psi_i^{(3)} \right\rangle + \left\langle \Psi_i^{(1)} \left| \Psi_i^{(2)} \right\rangle + \left\langle \Psi_i^{(2)} \left| \Psi_i^{(1)} \right\rangle + \left\langle \Psi_i^{(3)} \left| \Psi_i^{(0)} \right\rangle = 0 \tag{1.27}$$

1.3.1. First-order corrections

The first order correction to energy (ε) due to λ , can be obtained by multiplying Eq. 1.21 by $\left\langle \Psi_i^{(0)} \right|$, so that

$$\varepsilon_i^{(1)} = \left\langle \Psi_i^{(0)} \left| H^{(1)} \right| \Psi_i^{(0)} \right\rangle. \tag{1.28}$$

This result is the well-known Hellman-Feynman theorem [77, 78], which is usually used to compute the atomic forces.

1. Solids from first-principles: the electronic problem in a crystalline lattice

1.3.1.1. Hellman-Feynman theorem: atomic forces

Within the DFT framework, the force acting on the I -th atom is [78]

$$\mathbf{F}_I = -\frac{\partial E}{\partial \mathbf{R}_I} = -\left\langle \Psi^{(0)} \left| \frac{\partial H_{\text{el}}}{\partial \mathbf{R}_I} \right| \Psi^{(0)} \right\rangle = -\int n(\mathbf{r}) \frac{\partial V_{\text{ext}}(\mathbf{r}; \mathbf{R})}{\partial \mathbf{R}_I} d\mathbf{r} - \frac{\partial E_{\text{NN}}}{\partial \mathbf{R}_I}. \quad (1.29)$$

It is important to notice, that the last term in Eq. 1.29 is only valid for a complete basis set. However, this constraint can indeed be relaxed, so that the Hellman-Feynman theorem also holds for basis functions without dependence on nuclear positions, like plane-waves [56, 79]; otherwise it becomes necessary to add the so-called Pulay corrections [51, 56]. Although Eq. 1.29 is based on the exact eigenfunctions of the Hamiltonian, it can be demonstrated that Hellman-Feynman holds for any stationary wave function satisfying the Schrödinger equation (i.e. Kohn-Sham eigenstates). Consequently, the theorem also holds for the KS eigenstates of a pseudopotential Hamiltonian [56, 80].

1.3.1.2. 1st-order correction to the wave functions: the Sternheimer equation

The first-order correction to the wave functions, $\Psi^{(1)}_i$ for a set of non-degenerate states is [51]

$$\left| \Psi^{(1)}_i \right\rangle = \sum_{j \neq i} \frac{\left\langle \Psi^{(0)}_j \left| H^{(1)} \right| \Psi^{(0)}_i \right\rangle}{\varepsilon_i - \varepsilon_j} \left| \Psi^{(0)}_j \right\rangle. \quad (1.30)$$

Alternatively, it can be obtained as a linear solution of Eq. 1.21, which is usually known as the Sternheimer equation. A more detailed description of how this calculation is performed within the DFT framework can be found in Subsection 1.4.

1.3.2. Higher order corrections: the $2n+1$ theorem

Analogously to the first-order correction, the second-order correction to energy is

$$\begin{aligned} \varepsilon_i^{(2)} = & \langle \Psi_i^{(0)} | H_i^{(2)} | \Psi_i^{(0)} \rangle + \langle \Psi_i^{(0)} | H_i^{(1)} - \varepsilon_i^{(1)} | \Psi_i^{(1)} \rangle = \\ & \langle \Psi_i^{(0)} | H_i^{(2)} | \Psi_i^{(0)} \rangle + \frac{1}{2} \left[\langle \Psi_i^{(0)} | H_i^{(1)} | \Psi_i^{(1)} \rangle + \langle \Psi_i^{(0)} | H_i^{(1)} | \Psi_i^{(1)} \rangle \right], \end{aligned} \quad (1.31)$$

where we used the normalization condition of Eq. 1.25 and combined it with its Hermitian conjugate. In a similar way, the third-order correction to energy is given by

$$\begin{aligned} \varepsilon_i^{(3)} = & \langle \Psi_i^{(0)} | H_i^{(3)} | \Psi_i^{(0)} \rangle + \langle \Psi_i^{(1)} | H_i^{(2)} - \varepsilon_i^{(2)} | \Psi_i^{(1)} \rangle + \\ & \langle \Psi_i^{(2)} | H_i^{(1)} - \varepsilon_i^{(1)} | \Psi_i^{(2)} \rangle, \end{aligned} \quad (1.32)$$

requiring the second order correction to wave function to obtain $\varepsilon_i^{(3)}$. Nevertheless, it is possible to obtain an expression that does only require wave function corrections up to first order. Expanding $\langle \Psi_i | H_i - \varepsilon_i | \Psi_i \rangle$ to third order and making use of Eqs. 1.20-1.27 one gets:

$$\begin{aligned} \varepsilon_i^{(3)} = & \langle \Psi_i^{(0)} | H_i^{(3)} | \Psi_i^{(0)} \rangle + \langle \Psi_i^{(1)} | H_i^{(1)} - \varepsilon_i^{(1)} | \Psi_i^{(1)} \rangle + \\ & \langle \Psi_i^{(0)} | H_i^{(2)} | \Psi_i^{(1)} \rangle + \langle \Psi_i^{(1)} | H_i^{(2)} | \Psi_i^{(0)} \rangle. \end{aligned} \quad (1.33)$$

Therefore, it becomes possible to calculate the second and third-order corrections to energy with only the knowledge of $\Psi_i^{(1)}$. This last is nothing but a practical consequence of the well-known $2n + 1$ theorem, which states that the correction to energy up to the $2n + 1$ order can be determined by the knowledge of the n -th order correction to the wave function, or in the DFT case the Kohn-Sham orbitals [51, 77, 78].

1.3.3. Multiple perturbations

Up until now, we have only addressed single perturbations; nonetheless, it is possible to perform a similar derivation for multiple perturbations. For instance, the second-order correction to total energy can be easily derived by deriving Eq. 1.28 with respect to a second perturbation, so [78]

$$\frac{\partial^2 E}{\partial \lambda_j \partial \lambda_l} = \sum_i^{occ} \left\langle \Psi_i^{(0)} \left| \frac{\partial^2 H}{\partial \lambda_j \partial \lambda_l} \right| \Psi_i^{(0)} \right\rangle + \left\langle \frac{\partial \Psi_i^{(0)}}{\partial \lambda_j} \left| \frac{\partial H}{\partial \lambda_l} \right| \Psi_i^{(0)} \right\rangle + \left\langle \Psi_i^{(0)} \left| \frac{\partial H}{\partial \lambda_l} \right| \frac{\partial \Psi_i^{(0)}}{\partial \lambda_j} \right\rangle. \quad (1.34)$$

Examples of the third-order correction to energy for multiple perturbations can be found in Ref. [81].

1.4. Density functional perturbation theory

As indicated in Section 1.3, several quantities of interest as it could be the response of the system to an electric field or atomic vibrations can be defined in terms of perturbation theory. Although in principle it is possible to calculate the responses to a perturbation by building a supercell with the applied perturbation and getting the desired quantities through numerical derivatives, this method is tedious and in the case of periodic perturbations, it would require unpractical enormous cells for small wave vectors, as the perturbation must be commensurate with the supercell [77, 78, 82]. A more affordable alternative, named density functional perturbation theory (DFPT), is to make use of perturbation theory within the DFT framework to obtain those properties.

1. Solids from first-principles: the electronic problem in a crystalline lattice

Within the DFT, $H^{(1)}$ can be defined as

$$H^{(1)}(\mathbf{r}) = V_{\text{ext}}^{(1)}(\mathbf{r}) + e^2 \int \frac{\rho^{(1)}(\mathbf{r}')}{|\mathbf{r} - \mathbf{r}'|} d\mathbf{r}' + \int \frac{\delta V_{XC}}{\delta \rho(\mathbf{r}')} \rho^{(1)}(\mathbf{r}') d\mathbf{r}' \quad (1.35)$$

where we have supposed that the perturbation does not affect the kinetic energy, and $\rho^{(1)}$ is the first-correction to density defined as

$$\rho^{(1)}(\mathbf{r}) = \sum_i^{\text{occ}} \left[\Psi_i^{(1)*}(\mathbf{r}) \Psi_i^{(0)}(\mathbf{r}) + \Psi_i^{(0)*}(\mathbf{r}) \Psi_i^{(1)}(\mathbf{r}) \right]. \quad (1.36)$$

Therefore, the Sternheimer equation (see Eq. 1.21) can be solved self-consistently in combination with Eqs. 1.28, 1.35, and 1.36 [77].

Alternatively, it is also possible to set up a variational problem in terms of the perturbed quantities, so that its minimization results in the perturbed wave functions [83].

1.4.1. The case of homogeneous electric field

Given a solid with an applied homogeneous constant electric field, the perturbation Hamiltonian is $V(\mathbf{r}) = e\mathbf{E} \cdot \mathbf{r}$, which for a periodic solid is an ill-defined operator. However, in the perturbation theory one is only interested in non-diagonal terms (i.e. $\langle \Psi_m | \mathbf{r} | \Psi_j \rangle$ with $i \neq j$) which are well defined through the Hamiltonian commutator [78]

$$\langle \Psi_m | \mathbf{r} | \Psi_j \rangle = \frac{\langle \Psi_m | [H, \mathbf{r}] | \Psi_j \rangle}{\varepsilon_m - \varepsilon_j} = -\frac{\hbar^2}{m_e} \frac{\langle \Psi_m | \nabla | \Psi_j \rangle}{\varepsilon_m - \varepsilon_j}. \quad (1.37)$$

Following Eq. 1.37 it is possible to define several quantities that provide information about the system's response to a homogeneous electric field; for instance, the electronic contribution to the dielectric constant (ϵ^∞) or the Born charges (i.e. the

1. Solids from first-principles: the electronic problem in a crystalline lattice

change in the polarization due to an atomic displacement), Z^* , are [84, 85]

$$\epsilon_{\alpha\beta}^\infty = \delta_{\alpha\beta} - 2\pi^2 \int_{BZ} \sum_j^{occ} \langle u_{j\mathbf{k}0}^{(1),\mathbf{E}_\alpha} | i u_{j\mathbf{k}0}^{(1),\mathbf{k}_\beta} \rangle d\mathbf{k}, \quad (1.38)$$

$$Z_{I\alpha\beta}^* = Z_I \delta_{\alpha\beta} + \frac{V_{uc}}{2\pi^3} \int_{BZ} \sum_j^{occ} \langle u_{j\mathbf{k}0}^{(1),\mathbf{R}_{I\alpha}} | i u_{j\mathbf{k}}^{(1),\mathbf{k}_\beta} \rangle d\mathbf{k} \quad (1.39)$$

where α and β refer to the Cartesian axis, I refers to atomic indices, j refers to electronic bands, Z_I is the ionic charge of the I -th atom, and

$$u_{j\mathbf{k}\mathbf{q}}^{(1),\lambda}(\mathbf{r}) = \sqrt{NV_{uc}} e^{-i(\mathbf{k}+\mathbf{q})\cdot\mathbf{r}} \Psi_{j\mathbf{k}}^{(1),\lambda}(\mathbf{r}). \quad (1.40)$$

In the last expression, N is the number of cells in the crystal, λ is the perturbation and q is the periodic perturbation wave vector.

1.5. Time dependent perturbation theory: Fermi's golden rule

In some cases, it becomes of interest the time evolution of the states due to a perturbation. For instance, the semiclassical transport theory is fully based on the transition rates due to several interactions of the carriers (i.e. interactions with those perturbations). Given a small time-dependent perturbation, the Hamiltonian can be split into [86]

$$H(t) = H_0 + H_I(t) \quad (1.41)$$

where H_0 is the unperturbed time-independent Hamiltonian—with eigenstates ψ_k , and eigenvalues ε_k , i.e. $H_0\psi_k = \varepsilon_k\psi_k$ —and $H_I(t)$ is the time-dependent perturbation. We make now use of the interaction picture, so that the wave

1. *Solids from first-principles: the electronic problem in a crystalline lattice*

function, $\bar{\Psi}$, and the operators, \bar{A} , are defined as:

$$|\bar{\Psi}(t)\rangle = \exp\left(\frac{iH_0t}{\hbar}\right) |\Psi(t)\rangle, \quad (1.42)$$

$$\bar{A}(t) = \exp\left(\frac{iH_0t}{\hbar}\right) A(t) \exp\left(\frac{-iH_0t}{\hbar}\right). \quad (1.43)$$

Therefore, by taking the time derivative of $\bar{\Psi}$ we arrive to the Schrödinger equation in the interaction picture

$$i\hbar \frac{\partial \bar{\Psi}(t)}{\partial t} = \bar{H}_I(t) \bar{\Psi}(t) \quad (1.44)$$

and

$$i\hbar \frac{\partial \bar{U}(t, t_0)}{\partial t} = \bar{H}_I(t) \bar{U}(t, t_0) \quad (1.45)$$

where $\bar{U}(t, t_0)$ is the Dyson or time evolution operator that evolves the eigenstate from t_0 to t , i.e. $|\bar{\Psi}(t)\rangle = \bar{U}(t, t_0) |\bar{\Psi}(t_0)\rangle$. The solution of Eq. 1.45, $\bar{U}(t, t_0) = \bar{U}(t_0, t_0) - \frac{i}{\hbar} \int_{t_0}^t \bar{H}_I(t') \bar{U}(t', t_0) dt'$, leads to the Dyson series [86]

$$\bar{U}(t, t_0) = \mathbb{1} - \frac{i}{\hbar} \int_{t_0}^t dt' \bar{H}_I(t') + \left(-\frac{i}{\hbar}\right)^2 \int_{t_0}^t \int_{t_0}^{t'} dt' dt'' \bar{H}_I(t') \bar{H}_I(t'') + \dots \quad (1.46)$$

Now if we expand the wave function in terms of the unperturbed time-independent eigenstates, $|\bar{\Psi}(t)\rangle = \sum_k c_k(t) |\psi_k\rangle$, we arrive to

$$c_k(t) = \langle \psi_k | \bar{U}(t, t_0) | \bar{\Psi}(t_0) \rangle. \quad (1.47)$$

This last equation can be further simplified by assuming that $\bar{\Psi}(t_0) = \psi_l$, so $c_k(t) = \langle \psi_k | \bar{U}(t, t_0) | \psi_l \rangle$. Following, Eq. 1.46 and restricting ourselves to the first-order and assuming a harmonic perturbation, namely $H_I(t) = V_I \exp(i\omega t)$

1. *Solids from first-principles: the electronic problem in a crystalline lattice*

and $t_0 = 0$, we arrive to [87]

$$c_k(t) = \delta_{kl} - \frac{i}{\hbar} \langle k|V_I|l \rangle \int_0^t \exp\left(\frac{i}{\hbar}(\varepsilon_k - \varepsilon_l + \hbar\omega)t'\right) dt' =$$

$$\delta_{kl} - \frac{i}{\hbar} \langle k|V_I|l \rangle \exp\left(\frac{i}{2\hbar}[\varepsilon_k - \varepsilon_l + \hbar\omega]t\right) \frac{\sin\left(\frac{\varepsilon_k - \varepsilon_l + \hbar\omega}{2\hbar}t\right)}{\frac{\varepsilon_k - \varepsilon_l + \hbar\omega}{2\hbar}} t, \quad (1.48)$$

so if $l \neq k$, the scattering rate, $\Gamma_{lk} = \lim_{t \rightarrow +\infty} \frac{|c_k(t)|^2}{t}$, is

$$\Gamma_{lk} = \frac{2\pi}{\hbar} |\langle k|V_I|l \rangle|^2 \delta(\varepsilon_k - \varepsilon_l + \hbar\omega). \quad (1.49)$$

This expression is the celebrated Fermi's Golden Rule (FGR), which is also valid for a constant perturbation, although the energy conservation delta is only between the initial and final state, as well as for other particles and their combinations, as it would be the case of phonons (see Subsection 2.1.2.2).

CHAPTER 2

Lattice dynamics, phonons, and their interactions

In the previous Chapter, we have discussed static crystalline lattice, in which each atom lies in its equilibrium position so that the lattice is in its ground state. However, even at 0 K, the lattice does not remain static but its atoms oscillate around those equilibrium positions. Concerning heat transport, the atomic vibrations—including but not limited to the zero-point oscillation—are of key importance as they affect one of the main heat carriers for metals, the electrons. Namely, those vibrations modify the potential affecting those electrons in a way that can alter their quantum state. Moreover, those atomic vibrations carry energy by themselves, and thus they can also carry heat [39].

In this chapter, we discuss vibrations in solids. First, we present the harmonic approximation (Section 2.1), staying within classical mechanics to solve the lattice dynamics problem (Subsection 2.1.1), presenting the normal modes of vibration. We continue by translating the problem to quantum mechanics, introducing the concept of phonon (Subsection 2.1.2), following a discussion of their several interactions (Sections 2.2, 2.3 and 2.5). Additionally, several methods to compute

phonons and their interactions and other aspects of those calculations are also discussed in this Chapter.

2.1. Lattice dynamics: the harmonic approximation

In principle, an exact description of atomic vibrations would require describing the movement of the nuclei together with that of their electrons. Certainly, this task is insurmountable even for the most simple crystals. However, one can again use the Born-Oppenheimer approximation (see 1.1.1), so that the problem is simplified to describe the motion of the nuclei. For further simplification, and owing to the high localization of nuclei wave functions, one can suppose that they are fully localized around single points, and thus can be represented by classical particles.

Therefore, the equation of movement for nuclei around their equilibrium positions can be obtained through the unconstrained Lagrange's equation of motion:

$$\frac{d}{dt} \frac{\partial L}{\partial \dot{\mathbf{u}}} = \frac{\partial L}{\partial \mathbf{u}} \quad (2.1)$$

where \mathbf{u} is the generalized coordinate corresponding to the atomic displacements with respect to the equilibrium positions and L is the Lagrangian, which for this system is defined as:

$$L = \frac{1}{2} \sum_{A i \alpha} m_i \dot{\mathbf{u}}_{\alpha}^2(A, i) - \Phi(\mathbf{u}), \quad (2.2)$$

where A represents the unit cell index, i is the atom index inside the given cell, α refers to the Cartesian axis, m_i is the atomic mass of i^{th} atom, and $\Phi(\mathbf{u})$ is the potential energy for given deviations from equilibrium.

2. Lattice dynamics, phonons, and their interactions

Given a static array of atoms located at their equilibrium positions (\mathbf{r}_0) – i.e. the positions that minimize the total energy of the system for a given conditions – one can make the Taylor expansion of the potential energy ($\Phi(\mathbf{u})$) around those equilibrium position as [56, 67]:

$$\begin{aligned} \Phi(\mathbf{u}) = & \Phi_0 + \frac{1}{2} \sum_{AB} \sum_{ij} \sum_{\alpha\beta} \Phi_{\alpha\beta}(A, i, B, j) \mathbf{u}_\alpha(A, i) \mathbf{u}_\beta(B, j) + \\ & \frac{1}{6} \sum_{ABC} \sum_{ijk} \sum_{\alpha\beta\gamma} \Phi_{\alpha\beta\gamma}(A, i, B, j, C, k) \mathbf{u}_\alpha(A, i) \mathbf{u}_\beta(B, j) \mathbf{u}_\gamma(C, k) + \dots \end{aligned} \quad (2.3)$$

where A, B, C, \dots are the unit cell indices, i, j, k, \dots are atom indices inside the given unit cell and $\alpha, \beta, \gamma, \dots$ refer to the Cartesian axes, and Φ_0 is the potential energy with atoms at their \mathbf{r}_0 s. $\Phi_{\alpha\beta}(A, i, B, j)$ terms are usually known as harmonic force constants and are defined as

$$\Phi_{\alpha\beta}(A, i, B, j) = \left. \frac{\partial^2 \Phi}{\partial \mathbf{u}_\alpha(A, i) \partial \mathbf{u}_\beta(B, j)} \right|_{\mathbf{r}_0}, \quad (2.4)$$

namely, they are second derivatives of the potential energy with respect to displacement of two atoms around equilibrium. In a similar manner, the $\Phi_{\alpha\beta\gamma}(A, i, B, j, C, k)$ terms are third derivatives of the potential energy with respect to displacement of three atoms around equilibrium

$$\Phi_{\alpha\beta\gamma}(A, i, B, j, C, k) = \left. \frac{\partial^3 \Phi}{\partial \mathbf{u}_\alpha(A, i) \partial \mathbf{u}_\beta(B, j) \partial \mathbf{u}_\gamma(C, k)} \right|_{\mathbf{r}_0}, \quad (2.5)$$

and are commonly known as third order forces constants or anharmonic force constants. The term corresponding to the first derivative has been not included in Eq. 2.3 as it is null by construction due to fact that we are in a minimum of energy. Higher-order terms are defined analogously to second and third order terms.

2.1.1. Harmonic approximation and normal modes of vibration

Within the Born-Oppenheimer approximation, our equations are until now exact. However, it is unpractical to solve Eq. 2.1 without cutting off the Taylor expansion of the potential. Usually, the displacements are small enough that one can make use of harmonic approximation [56, 67], which consists in considering only quadratic terms of Eq. 2.3 and adding the additional terms through perturbation theory [67].

Thus, combining Eq. 2.3 up to second-order with Eq. 2.2, and introducing it into Eq. 2.1 leads to:

$$m_i \ddot{\mathbf{u}}_\alpha(A, i) = - \sum_{Bj\beta} \Phi_{\alpha\beta}(A, i, B, j) \mathbf{u}_\beta(B, j) \quad (2.6)$$

which is the equation of motion for the ion i^{th} at cell A . Harmonic oscillation are proposed as ansatz for last equation.

$$\mathbf{u}(A, i, q, t) = \frac{1}{\sqrt{m_i}} \boldsymbol{\xi}_i e^{i\mathbf{q} \cdot \mathbf{R}_A - i\omega t} \quad (2.7)$$

where $\boldsymbol{\xi}_i$ is the polarization vector that provides information about the vibration direction, \mathbf{q} is the wave vector of the oscillating wave, \mathbf{R}_A is the A -th cell origin, ω is the oscillation frequency and t is time. $\mathbf{u}(A, i)$ is related to atomic displacement through its real part. Then, introducing Eq. 2.7 into Eq. 2.6 one arrives to:

$$\omega^2 \boldsymbol{\xi}_{i\alpha} = \sum_{Bj\beta} \frac{\Phi_{\alpha\beta}(A, i, B, j)}{\sqrt{m_i m_j}} e^{iq(\mathbf{R}_B - \mathbf{R}_A)} \boldsymbol{\xi}_{j\beta} \quad (2.8)$$

2. Lattice dynamics, phonons, and their interactions

defining now the dynamical matrix as:

$$D_{ij}^{\alpha\beta}(\mathbf{q}) = \sum_{B'} \frac{\Phi_{\alpha\beta}(0, i, B', j)}{\sqrt{m_i m_j}} e^{i\mathbf{q} \cdot \mathbf{R}'_B}, \quad (2.9)$$

where we have made use of translational symmetry to bring all the problem to the unit cell located at the origin (i.e. $\mathbf{R}_{A'} = 0$ and $\mathbf{R}_{B'} = \mathbf{R}_B - \mathbf{R}_A$). Introducing Eq. 2.9 into Eq. 2.8 we arrive to an eigenvalue problem.

$$[\omega(q, \nu)]^2 \xi_{i\alpha}(\mathbf{q}, \nu) = \sum_{Bj} D_{ij}^{\alpha\beta}(\mathbf{q}) \xi_{j\beta}(\mathbf{q}, \nu) \quad (2.10)$$

where ν is the index identifying one of the $3N_{\text{atoms}}$ (being N_{atoms} the number of atoms in the unit cell) solutions for a given q -point. Those solutions, called normal modes of vibrations, are usually divided into two types: acoustic and optical bands; strictly, speaking in a solid there can only exist three acoustic brands (those that for the Γ -point—i.e. $\mathbf{q} = (0, 0, 0)$ —have a null frequency and correspond to rigid translations along the three axes) being the rest optical (not null at Γ ($\omega \neq 0$) and with phase shift movements) [56]. Hence, those vibrational modes or normal modes, are well characterized by the wave vector \mathbf{q} and the band index ν . Furthermore, normal modes spectra, namely $\omega(\mathbf{q}, \nu)$, comply with both crystal symmetry, because of Φ_0 respecting crystal's symmetry, and time reversal symmetry [i.e. $\omega(\mathbf{q}, \nu) = \omega(-\mathbf{q}, \nu)$], because of $D(-\mathbf{q}) = D^*(\mathbf{q})$. To summarize, atoms of a crystalline lattice are not static but oscillate around their equilibrium positions with frequencies and directions given by the solution of Eq. 2.10.

In addition to a normal mode's frequency and eigenvector, it is also possible to define a group velocity for a given mode $\left[\mathbf{v}_\alpha(\mathbf{q}, \nu) = \frac{\partial \omega(\mathbf{q}, \nu)}{\partial \mathbf{q}_\alpha} \right]$ as:

$$\frac{\partial}{\partial \mathbf{q}_\alpha} [\omega(\mathbf{q}, \nu)]^2 = \frac{\partial}{\partial \mathbf{q}_\alpha} \langle \xi(\mathbf{q}, \nu) | D(\mathbf{q}) | \xi(\mathbf{q}, \nu) \rangle \quad (2.11)$$

2. Lattice dynamics, phonons, and their interactions

$$\mathbf{v}_\alpha(\mathbf{q}, \nu) = \frac{1}{2\omega(\mathbf{q}, \nu)} \langle \xi(\mathbf{q}, \nu) | \frac{\partial D(\mathbf{q})}{\partial \mathbf{q}_\alpha} | \xi(\mathbf{q}, \nu) \rangle \quad (2.12)$$

where

$$\frac{\partial D(\mathbf{q})}{\partial \mathbf{q}_\alpha} = i \sum_{B'} \mathbf{R}_{B'} \frac{\Phi_{\alpha\beta}(0, i, B, j)}{\sqrt{m_i m_j}} e^{i\mathbf{q} \cdot \mathbf{R}_B}. \quad (2.13)$$

Finally, it is illustrative to make a small remark on the limits of harmonic theory to describe atomic vibrations. Since this approach is based on the assumption of small displacements, and thus it breaks down for systems with large displacements, as it is the case of systems with light atoms, like H, or at high temperature [67].

2.1.1.1. Polar materials

In polar materials, the atomic vibrations give rise to a non-negligible electric field, which gives rise to additional force terms; so that the equation of motion becomes [82, 88]:

$$m_i \ddot{\mathbf{u}}_\alpha(A, i, q) = - \sum_{Bj\beta} \Phi_{\alpha\beta}(A, i, B, j) \mathbf{u}_\beta(B, j, q) + e[Z_i^* \cdot \mathbf{E}(A, i, q)]_\alpha, \quad (2.14)$$

where Z_i^* is the Born-charge tensor of the i -th atom (i.e. $Z_{i,\alpha\beta}^* = -\frac{\partial^2 E_{\text{BOA}}}{\partial \mathbf{E}_\beta \partial \mathbf{R}_{i\alpha}}$), e is the elementary charge, and $\mathbf{E}(A, i, \mathbf{q})$ is the electric field generated by the atomic displacement. This last term can be defined in terms of the polarization— $\mathbf{P}(A, i, \mathbf{q}) = \frac{e}{V} Z_i \mathbf{u}(A, i, q)$, where V is the volume in which $\mathbf{P}(A, i, \mathbf{q})$ is computed—induced by lattice vibration $\mathbf{u}(A, i, \mathbf{q})$, using the Poisson equation as

$$-\nabla \cdot [\epsilon^\infty \cdot \mathbf{E}(A, i, \mathbf{q})] = \nabla \cdot \mathbf{P}(A, i, \mathbf{q}), \quad (2.15)$$

where ϵ^∞ is the high-frequency static dielectric function (i.e. the electronic contribution to the static dielectric tensor). We note that the high-frequency (∞) in ϵ^∞ refers to the fact that for high enough frequencies the nuclei cannot

2. Lattice dynamics, phonons, and their interactions

follow the perturbation, and thus remain clamped at \mathbf{r}_0 without contributing to the dielectric function. Therefore ∞ does only mean the electronic contribution not an actual frequency, indeed in our case we are calculating it for an static electric field.

This equation is then solved under periodic boundary conditions for all directions, giving

$$\mathbf{E}(A, i, \mathbf{q}) = -\frac{4\pi e}{V} \sum_{Bj} \frac{[\mathbf{q} \cdot Z_j^*]}{\mathbf{q} \cdot \epsilon^\infty \cdot \mathbf{q}} \mathbf{u}(B, j, \mathbf{q}) \mathbf{q}. \quad (2.16)$$

Thus, the force that the (A, i) atom experience due to the electric field generated by the atomic displacements, $\mathbf{F}(A, i, \mathbf{q})$, is

$$\mathbf{F}(A, i, \mathbf{q}) = e\mathbf{E}(A, i, \mathbf{q}) \cdot Z_i^* = -\frac{4\pi e^2}{V} \sum_{Bj} \frac{[\mathbf{q} \cdot Z_j^*][\mathbf{q} \cdot Z_i^*]}{\mathbf{q} \cdot \epsilon^\infty \cdot \mathbf{q}} \mathbf{u}(B, j, \mathbf{q}). \quad (2.17)$$

Therefore, in analogy with $\Phi_{\alpha\beta}(0, i, B, j)$ one can define the second order non-analytic interatomic force constants $[\Phi_{\alpha\beta}(0, i, B, j)]$ as [48]

$$\Phi_{\alpha\beta}^{\text{NA}}(0, i, B, j, \mathbf{q}) = -\frac{\partial \mathbf{F}_\alpha(A, i, \mathbf{q})}{\partial \mathbf{u}_\beta(B, j, \mathbf{q})} = \frac{4\pi e^2}{V} \frac{[\mathbf{q} \cdot Z_j^*]_\beta [\mathbf{q} \cdot Z_i^*]_\alpha}{\mathbf{q} \cdot \epsilon^\infty \cdot \mathbf{q}}. \quad (2.18)$$

Consequently, dynamical matrix becomes a summation of two contributions; a short-range one defined in Eq. 2.9 and a non-analytic one $D^{\text{NA}\alpha\beta}_{ij}(\mathbf{q})$ coming from the electric field arising from atomic vibrations. This term is defined as

$$D^{\text{NA}\alpha\beta}_{ij}(\mathbf{q}) = \sum_B \frac{\Phi_{\alpha\beta}^{\text{NA}}(0, i, B, j, \mathbf{q})}{\sqrt{m_i m_j}} e^{i\mathbf{q} \cdot \mathbf{R}_B}, \quad (2.19)$$

Equivalently, to short-range we can define the contribution of non-analytic term

2. Lattice dynamics, phonons, and their interactions

to velocity via Eq. 2.12, where $\frac{\partial D_{ij}^{\text{NA}\alpha\beta}(\mathbf{q})}{\partial \mathbf{q}}$ is defined as

$$\begin{aligned} \frac{\partial D_{ij}^{\text{NA}\alpha\beta}(\mathbf{q})}{\partial \mathbf{q}_\gamma} = & i \sum_B \mathbf{R}_{B\gamma} \frac{\Phi_{\alpha\beta}^{\text{NA}}(0, i, B, j, \mathbf{q})}{\sqrt{m_i m_j}} e^{i\mathbf{q} \cdot \mathbf{R}_B} + \\ & \sum_B \frac{1}{\sqrt{m_i m_j}} e^{i\mathbf{q} \cdot \mathbf{R}_B} \frac{\partial \Phi_{\alpha\beta}^{\text{NA}}(0, i, B, j, \mathbf{q})}{\partial \mathbf{q}_\gamma}, \end{aligned} \quad (2.20)$$

where

$$\begin{aligned} \frac{\partial \Phi_{\alpha\beta}^{\text{NA}}(0, i, B, j, \mathbf{q})}{\partial \mathbf{q}_\gamma} = & \frac{4\pi e^2}{V} \frac{(Z_i^*)_{\alpha\gamma} (\mathbf{q} \cdot Z_j^*)_\beta + (\mathbf{q} \cdot Z_i^*)_\alpha (\cdot Z_j^*)_{\beta\gamma}}{\mathbf{q} \cdot \epsilon^\infty \cdot \mathbf{q}} - \\ & \frac{8\pi e^2}{V} \frac{(\mathbf{q} \cdot Z_i^*)_\alpha (\mathbf{q} \cdot Z_j^*)_\beta (\mathbf{q} \cdot \epsilon_\gamma^\infty)}{(\mathbf{q} \cdot \epsilon^\infty \cdot \mathbf{q})^2} \end{aligned} \quad (2.21)$$

In terms of the solution—i.e.: frequencies—the introduction of the non-analytic term becomes much more relevant for small \mathbf{q} , being for instance the origin of the LO-TO splitting in polar materials; moreover, it causes discontinuity in Γ for non-cubic systems.

On the other hand, regarding the validity of derived corrections, it should be noticed that they are only valid for 3D systems as when solving the Poisson equation we have supposed periodic conditions in all directions, which is not valid for 2D-polar materials like boron nitride. In Ref. [88], Sohler *et al.* discussed and derived the non-analytic correction for 2D polar systems; showing that, contrary to bulk-materials, for such kind of systems there is no LO-TO splitting at Γ , being this point being experimentally demonstrated by De Luca *et al* using Raman spectroscopy on few-layer WSe₂ [89].

2.1.2. Quantum theory and phonons

Hitherto we have supposed a classical lattice. Before starting with the quantum description of lattice dynamics, it is useful to express classical dynamics in terms of the eigenvalues and eigenvectors of Eq. 2.9, as it would rather facilitate such a transition from the classical to the quantum picture.

Therefore, we express a general atomic displacement, $\mathbf{u}(A, i, t)$, and its time derivative, $\dot{\mathbf{u}}(A, i, t)$, using the eigensolutions of Eq. 2.9 [67, 90, 91]:

$$\mathbf{u}(A, i, t) = \frac{1}{\sqrt{Nm_i}} \sum_{\mathbf{q}, \nu} \boldsymbol{\pi}(\mathbf{q}, \nu) \boldsymbol{\xi}_i(\mathbf{q}, \nu) e^{i\mathbf{q} \cdot \mathbf{R}_A - i\omega(\mathbf{q}, \nu)t} \quad (2.22)$$

and

$$\dot{\mathbf{u}}(A, i, t) = \frac{i\omega(\mathbf{q}, \nu)}{\sqrt{Nm_i}} \sum_{\mathbf{q}, \nu} \dot{\boldsymbol{\pi}}(\mathbf{q}, \nu) \boldsymbol{\xi}_i(\mathbf{q}, \nu) e^{i\mathbf{q} \cdot \mathbf{R}_A - i\omega(\mathbf{q}, \nu)t}, \quad (2.23)$$

where $\boldsymbol{\pi}(\mathbf{q}, \nu)$ is an expansion coefficient related to a generalized coordinate $\boldsymbol{\Pi}(\mathbf{q}, \nu, t)$ and N is the number of cells in the crystal. The generalized coordinate, $\boldsymbol{\Pi}(\mathbf{q}, \nu, t)$, is defined as

$$\boldsymbol{\Pi}(\mathbf{q}, \nu, t) = \boldsymbol{\pi}(\mathbf{q}, \nu) e^{i\omega(\mathbf{q}, \nu)t}. \quad (2.24)$$

2. Lattice dynamics, phonons, and their interactions

Using Eqs. 2.23 and 2.24 the kinetic energy (T) can be rewritten as:

$$\begin{aligned}
 T &= \frac{1}{2} \sum_{A i \alpha} \sum_{\mathbf{q} \mathbf{q}', \nu \nu'} \dot{\Pi}(\mathbf{q}, \nu, t) \dot{\Pi}(\mathbf{q}', \nu', t) \xi_{i \alpha}(\mathbf{q}, \nu) \xi_{i \alpha}(\mathbf{q}', \nu') e^{i \mathbf{q} \cdot \mathbf{R}_A} e^{i \mathbf{q}' \cdot \mathbf{R}_A} = \\
 &\frac{1}{2} \sum_{i \alpha} \sum_{\mathbf{q} \mathbf{q}', \nu \nu'} \dot{\Pi}(\mathbf{q}, \nu, t) \dot{\Pi}(\mathbf{q}', \nu', t) \xi_{i \alpha}(\mathbf{q}, \nu) \xi_{i \alpha}(\mathbf{q}', \nu') \delta_{\mathbf{q} + \mathbf{q}', 0} = \\
 &\frac{1}{2} \sum_{i \alpha} \sum_{\mathbf{q}, \nu \nu'} \dot{\Pi}(\mathbf{q}, \nu, t) \dot{\Pi}(-\mathbf{q}, \nu', t) \xi_{i \alpha}(\mathbf{q}, \nu) \xi_{i \alpha}(-\mathbf{q}, \nu') = \\
 &\frac{1}{2} \sum_{\mathbf{q}, \nu} \dot{\Pi}(\mathbf{q}, \nu, t) \dot{\Pi}(-\mathbf{q}, \nu, t) \quad (2.25)
 \end{aligned}$$

where we have used the plane wave and the eigenvector orthonormality. On the other hand, inserting Eqs. 2.23 and 2.24 into the harmonic crystalline potential (Φ^{Harm}) gives:

$$\begin{aligned}
 \Phi^{\text{Harm}} &= \frac{1}{2} \sum_{A B i j \alpha \beta} \Phi_{\alpha \beta}(A, i, B, j) \mathbf{u}_{\beta}(B, j, t) = \\
 &\frac{1}{2} \sum_{\mathbf{q} \mathbf{q}', \nu \nu'} \Pi(\mathbf{q}, \nu, t) \Pi(\mathbf{q}', \nu', t) \sum_{A B i j \alpha \beta} \frac{\Phi_{\alpha \beta}(A, i, B, j)}{\sqrt{m_i m_j}} \times \\
 &\quad [\xi_{i \alpha}(\mathbf{q}, \nu) \xi_{j \beta}(\mathbf{q}', \nu') e^{i(\mathbf{q} \cdot \mathbf{R}_A + \mathbf{q}' \cdot \mathbf{R}_B)}] = \\
 &\frac{1}{2} \sum_{\mathbf{q} \mathbf{q}', \nu \nu'} \Pi(\mathbf{q}, \nu, t) \Pi(\mathbf{q}', \nu', t) \sum_{A' B' i j \alpha \beta} \frac{\Phi_{\alpha \beta}(0, i, B', j)}{\sqrt{m_i m_j}} \xi_{i \alpha}(\mathbf{q}, \nu) \xi_{j \beta}(\mathbf{q}', \nu') \times \\
 &\quad \left[e^{i(\mathbf{q} + \mathbf{q}') \cdot (\mathbf{R}_A + \mathbf{R}_C)} e^{i \mathbf{q}' \cdot (\mathbf{R}_B - \mathbf{R}_C)} \right] = \\
 &\frac{1}{2} \sum_{\mathbf{q}, \nu \nu'} \Pi(\mathbf{q}, \nu, t) \Pi(-\mathbf{q}, \nu', t) \sum_{i j \alpha \beta} D_{ij}^{\alpha \beta}(\mathbf{q}) \xi_{i \alpha}(\mathbf{q}, \nu) \xi_{j \beta}(-\mathbf{q}, \nu') = \\
 &\frac{1}{2} \sum_{\mathbf{q}, \nu} [\omega(\mathbf{q}, \nu)]^2 \Pi(\mathbf{q}, \nu, t) \Pi(-\mathbf{q}, \nu, t) \quad (2.26)
 \end{aligned}$$

Using Eqs. 2.25 and 2.26, the conjugate momentum, $\Lambda(\mathbf{q}, \nu, t)$, can be defined

2. Lattice dynamics, phonons, and their interactions

as:

$$\Lambda(\mathbf{q}, \nu, t) = \frac{\partial L}{\partial \dot{\Pi}(\mathbf{q}, \nu, t)} = \dot{\Pi}(-\mathbf{q}, \nu, t). \quad (2.27)$$

Then, the harmonic Hamiltonian ($\mathcal{H}^{\text{Harm}} = T + \Phi^{\text{Harm}}$) can be written in terms of $\Pi(\mathbf{q}, \nu, t)$ and $\Lambda(\mathbf{q}, \nu)$ as

$$\mathcal{H}^{\text{Harm}} = \frac{1}{2} \sum_{\mathbf{q}\nu} \{ \Lambda(\mathbf{q}, \nu, t) \Lambda(-\mathbf{q}, \nu, t) + [\omega(\mathbf{q}, \nu)]^2 \Pi(\mathbf{q}, \nu, t) \Pi(-\mathbf{q}, \nu, t) \}, \quad (2.28)$$

which is the Hamiltonian for a set of uncoupled harmonic oscillators each of which corresponds to a normal mode of vibration [67, 90]. The equation of motion, namely $\Lambda(\mathbf{q}, \nu, t) = -\frac{\partial \mathcal{H}^{\text{Harm}}}{\partial \Pi(\mathbf{q}, \nu, t)}$, of each vibrational mode is then

$$\ddot{\Pi}(\mathbf{q}, \nu, t) = -[\omega(\mathbf{q}, \nu)]^2 \Pi(\mathbf{q}, \nu, t), \quad (2.29)$$

which is in fact that of a harmonic oscillator.

2.1.2.1. Quantum theory of lattice dynamics and lattice vibrational energy

Now, the transition to quantum mechanics can be easily done by simply letting $\Pi(\mathbf{q}, \nu, t)$ and $\Lambda(\mathbf{q}, \nu, t)$ become operators $\hat{\Pi}(\mathbf{q}, \nu)$ and $\hat{\Lambda}(\mathbf{q}, \nu)$. These operators do not commute, because as their classical counterparts they derive from the non-commuting position and momentum operators, and are subject to the commutator relationships [56, 67, 90]

$$[\hat{\Pi}(\mathbf{q}, \nu), \hat{\Lambda}(\mathbf{q}', \nu')] = i\hbar \delta_{\mathbf{q}\mathbf{q}'} \delta_{\nu\nu'}, \quad (2.30)$$

$$[\hat{\Pi}(\mathbf{q}, \nu), \hat{\Pi}(\mathbf{q}', \nu')] = [\hat{\Lambda}(\mathbf{q}, \nu), \hat{\Lambda}(\mathbf{q}', \nu')] = 0. \quad (2.31)$$

2. Lattice dynamics, phonons, and their interactions

As in the quantum harmonic oscillator case, it is useful to define the creation and annihilation operators, which rise or decrease the excited state in which the harmonic oscillator is located. These operators, which are denoted by $\hat{A}^\dagger(\mathbf{q}, \nu)$ for the creation operator and $\hat{A}(\mathbf{q}, \nu)$ for annihilation one, are

$$\hat{A}^\dagger(\mathbf{q}, \nu) = \frac{1}{2\hbar\omega(\mathbf{q}, \nu)} \left[\omega(\mathbf{q}, \nu)\hat{\Pi}(-\mathbf{q}, \nu) - i\hat{\Lambda}(\mathbf{q}, \nu) \right] \quad (2.32)$$

$$\hat{A}(\mathbf{q}, \nu) = \frac{1}{2\hbar\omega(\mathbf{q}, \nu)} \left[\omega(\mathbf{q}, \nu)\hat{\Pi}(\mathbf{q}, \nu) + i\hat{\Lambda}(\mathbf{q}, \nu) \right]. \quad (2.33)$$

If we now define the harmonic oscillator eigenstate $|n(\mathbf{q}, \nu)\rangle$, which is a normal mode with wave vector \mathbf{q} and branch ν in its n -th excited state, the action of these operators on these states is:

$$\hat{A}^\dagger |n(\mathbf{q}, \nu)\rangle = \sqrt{n(\mathbf{q}, \nu) + 1} |n(\mathbf{q}, \nu) + 1\rangle \quad (2.34)$$

$$\hat{A} |n(\mathbf{q}, \nu)\rangle = \sqrt{n(\mathbf{q}, \nu)} |n(\mathbf{q}, \nu) - 1\rangle \quad (2.35)$$

$$\hat{A}^\dagger(\mathbf{q}, \nu)\hat{A}(\mathbf{q}, \nu) |n(\mathbf{q}, \nu)\rangle = n(\mathbf{q}, \nu) |n(\mathbf{q}, \nu)\rangle \quad (2.36)$$

where $n(\mathbf{q}, \nu)$ is the excitation state of $|n(\mathbf{q}, \nu)\rangle$ and $|n(\mathbf{q}, \nu) + 1\rangle$ ($|n(\mathbf{q}, \nu) - 1\rangle$) is the state $|n(\mathbf{q}, \nu)\rangle$ in the nearest-higher (nearest-lower) excitation state to $|n(\mathbf{q}, \nu)\rangle$.

Using Eqs. 2.32 and 2.33, it is possible to obtain $\hat{\Pi}(\mathbf{q}, \nu)$ and $\hat{\Lambda}(\mathbf{q}, \nu)$ in terms of the creation and annihilation operators

$$\hat{\Pi}(\mathbf{q}, \nu) = \sqrt{\frac{\hbar}{2\omega(\mathbf{q}, \nu)}} \left[\hat{A}^\dagger(-\mathbf{q}, \nu) + \hat{A}(\mathbf{q}, \nu) \right], \quad (2.37)$$

$$\hat{\Lambda}(\mathbf{q}, \nu) = i\sqrt{\frac{\hbar\omega(\mathbf{q}, \nu)}{2}} \left[\hat{A}^\dagger(\mathbf{q}, \nu) - \hat{A}(-\mathbf{q}, \nu) \right] \quad (2.38)$$

2. Lattice dynamics, phonons, and their interactions

Finally, putting Eq. 2.37 and Eq. 2.38 into the Hamiltonian one arrives to [56]:

$$\hat{\mathcal{H}}^{\text{Harm}} = \sum_{\mathbf{q}\nu} \left\{ \hbar\omega(\mathbf{q}, \nu) \left[\hat{A}^\dagger(\mathbf{q}, \nu) \hat{A}(\mathbf{q}, \nu) + \frac{1}{2} \right] \right\}, \quad (2.39)$$

which applied over $|n(\mathbf{q}, \nu)\rangle$ gives the following expression for lattice energy due to vibrations

$$E^{\text{Harm}} = \sum_{\mathbf{q}, \nu} \hbar\omega(\mathbf{q}, \nu) \left[n(\mathbf{q}, \nu) + \frac{1}{2} \right]. \quad (2.40)$$

2.1.2.2. Phonons and normal modes

In our derivation of quantum mechanical theory for lattice vibrations we have used the wave picture (normal modes), namely we stated that given state (normal mode) is in its $n(\mathbf{q}, \nu)$ -th excited state. However, one can make use of corpuscular picture, and say that a given state is populated with $n(\mathbf{q}, \nu)$ quanta of vibration with energy $\hbar\omega_{\mathbf{q}, \nu}$ and quasi-momentum $\hbar\mathbf{q}$ [92, 93]. Those quanta are called phonons in analogy with photons. Opposite to those, their (quasi)momentum is not a real momentum as it complies with crystal symmetry, i.e. shifting it by \mathbf{G} , where \mathbf{G} is a reciprocal lattice vector, retrieves the same phonon mode [$\omega(\mathbf{q}, \nu) = \omega(\mathbf{q} + \mathbf{G}, \nu)$, $v_\alpha(\mathbf{q}, \nu) = v_\alpha(\mathbf{q} + \mathbf{G}, \nu)$, etc.]. Since each normal mode satisfies the equations of a quantum harmonic oscillator, their corpuscular counterparts, phonons, are bosons [91]. Thus, the expected value of $n(\mathbf{q}, \nu)$ in equilibrium at given temperature, $n^0(\mathbf{q}, \nu, T)$, is determined by the Bose-Einstein statistics [90]:

$$n^0(\mathbf{q}, \nu, T) = \frac{1}{e^{\frac{\hbar\omega(\mathbf{q}, \nu)}{k_B T}} - 1} \quad (2.41)$$

where T is the lattice temperature and k_B is the Boltzmann constant. It is worth noting that in Eq. 2.41 the chemical potential (μ) is zero, as phonons in equilibrium do not have a fixed number but are constantly created and destroyed by

2. Lattice dynamics, phonons, and their interactions

their interactions, thus their number (n) takes in average the value that minimizes the free energy (F) for fixed temperature and volume, i.e. $(\frac{\partial F}{\partial n})_{V,T} = \mu = 0$.

2.1.3. Phonon specific heat and density of states for general lattice

Since we have determined the dynamics and properties of the lattice vibrations as well as other important quantities like phonon occupation number, we can define some important properties based on the harmonic approximation.

Maybe the most important harmonic properties, as it is one of most used quantities to characterize the phonon spectra is the density of states, $\text{DOS}(\omega)$, which indicates the number of available phonon states at given frequency per unit of volume

$$\text{DOS}(\omega) = \frac{1}{V_{\text{uc}}} \sum_{\lambda} \delta(\omega - \omega_{\lambda}), \quad (2.42)$$

where V_{uc} is the volume of the unit cell, λ is the phonon mode, viz. (\mathbf{q}, ν) , and ω_{λ} is equivalent to $\omega(\mathbf{q}, \nu)$

Another quite important harmonic quantity is the volumetric heat capacity (C_v):

$$C_v = \frac{1}{V_{\text{uc}}} \frac{\partial E^{\text{Harm}}}{\partial T} = \frac{1}{N_{\text{q}} V_{\text{uc}}} \sum_{\lambda} C_{\lambda}(T) = \frac{1}{N_{\text{q}} V_{\text{uc}}} \sum_{\lambda} \hbar \omega_{\lambda} \frac{\partial n_{\lambda}^0(T)}{\partial T} = \frac{1}{N_{\text{q}} V_{\text{uc}}} \sum_{\lambda} n_{\lambda}^0(T) [n_{\lambda}^0(T) + 1] \frac{\hbar^2 \omega_{\lambda}^2}{k_B T^2} \quad (2.43)$$

where C_{λ} is the heat capacity of the λ -th phonon mode.

2.1.4. Phonon calculations from first principles

Following Eq. 2.10, lattice dynamics—i.e. phonon properties—can be simply determined through the knowledge of atomic types, positions, and harmonic force constants. From the first principles point of view, the former quantities are readily and quickly calculated from relaxation to ground-state. Indeed, all the complexity is in the calculation of the latter, namely the harmonic force constants. Here we shortly review some methodologies to obtain harmonic force constants: the finite difference method, the linear response theory, and using molecular dynamics. It should be noted, that in the case of polar materials an additional DFPT step is required to obtain Born charges and dielectric constants (see Subsection 1.4.1) necessary for the non-analytic term of the dynamical matrix.

2.1.4.1. Finite difference method

This approach is based on the approximation of $\Phi_{\alpha\beta}(A, i, B, j)$ through finite-differences

$$\begin{aligned} \Phi_{\alpha\beta}(A, i, B, j) &= - \left. \frac{\partial \mathbf{F}_\beta(B, j)}{\partial \mathbf{u}_\alpha(A, i)} \right|_{\mathbf{r}_0} \approx \\ &- \frac{1}{2h} [\mathbf{F}_\beta(B, j)(\mathbf{u}_\alpha(A, i) = h) - \mathbf{F}_\beta(B, j)(\mathbf{u}_\alpha(A, i) = -h)] \quad (2.44) \end{aligned}$$

where $\mathbf{F}_\beta(B, j)$ is the β component of the force acting on the j -th atom in the B -th unit cell, h is a small displacement from the equilibrium position and $\mathbf{F}_\beta(B, j)(\mathbf{u}_\alpha(A, i) = h)$ states for the the β component of the force acting on the j -th atom in the B -th unit cell when the i -th atom in the A -th cell has a displacement h in the α direction from its equilibrium position.

The calculation of the Eq. 2.44 is usually conducted within supercells, being those big enough for the perturbation effect to vanish, i.e. to prevent self-

2. Lattice dynamics, phonons, and their interactions

interaction between the displaced atoms in the periodic images of the cell.

Consequently, the number of harmonic force constants required to construct the dynamical matrix is equal to $9n_{\text{uc}}^2 N_{\text{sc}}$, for a supercell made of N_{sc} unit cells of n_{uc} atoms. Naively, one would need to run $6n_{\text{uc}}$ DFT ground-state calculation, one for each displacement, as each DFT run computes the forces in the whole system. To illustrate the sizes we are talking about; a supercell of $4 \times 4 \times 4$ build from unit cell of 2 atoms, as it would be the case of cubic silicon, would require 12 ground-state calculations in a cell of 128 atoms. These calculations are demanding from a computational point of view, especially taking into account that the involved displacements reduce crystal symmetry, which further increases the cost of the ground-state calculations. However, it is possible to exploit crystal symmetries, so that symmetry-related displacements are only done once, to reduce the number of calculations to a more manageable number [94].

2.1.4.2. Linear response theory

Harmonic force constants are derivatives of energy with respect to atomic displacements, thus we can make use of perturbation theory (see 1.3) to obtain them. Within DFPT framework, the harmonic IFCs in the reciprocal space can be computed to be [78]

$$\Phi_{\alpha\beta}(i, j, \mathbf{q}) = \Phi_{\alpha\beta}^{el}(i, j, \mathbf{q}) + \Phi_{\alpha\beta}^{ion}(i, j, \mathbf{q}), \quad (2.45)$$

where $\Phi_{\alpha\beta}^{el}(i, j, \mathbf{q})$ is the electronic contribution to the force constant and $\Phi_{\alpha\beta}^{ion}(i, j, \mathbf{q})$ is the contribution due to nuclei-nuclei interaction, which is easily evaluated using Ewald's summation (see B2 of Ref. [78]). On the other hand the

2. Lattice dynamics, phonons, and their interactions

electronic contribution is

$$\Phi_{\alpha\beta}^{el}(i, j, \mathbf{q}) = \int \left(\frac{\partial \rho(\mathbf{r})}{\partial \mathbf{u}_\alpha(i, \mathbf{q})} \right)^* \frac{\partial V_{KS}(\mathbf{r})}{\partial \mathbf{u}_\beta(j, \mathbf{q})} d\mathbf{r} + \int \frac{\partial^2 V_{KS}(\mathbf{r})}{\partial \mathbf{u}_\alpha(i, \mathbf{q}) \partial \mathbf{u}_\beta(j, \mathbf{q})} \rho(\mathbf{r}) d\mathbf{r} \quad (2.46)$$

where $\rho(\mathbf{r})$ is the electronic density and V_{KS} is the Kohn-Sham potential, $\mathbf{u}_\alpha(i, \mathbf{q})$ terms are the Fourier transforms of atomic displacements. The derivative of the potential with respect to displacements is

$$\frac{\partial V_{KS}(\mathbf{r})}{\partial \mathbf{u}_\beta(j, \mathbf{q})} = \sum_B \frac{\partial V_{KS}(\mathbf{r})}{\partial \mathbf{r}_\beta(j)} e^{-i\mathbf{q} \cdot \mathbf{R}_B} \quad (2.47)$$

and derivatives of $\rho(\mathbf{r})$ can be obtained through the solution of the Sternheimer equation (see 1.3.1.2).

2.1.4.3. Molecular dynamics method

An intuitive picture of the basic idea behind the method can be obtained through a simple 1D classic harmonic oscillator [95]. The equipartition theorem states that

$$\frac{1}{2} K \langle u^2 \rangle = \frac{1}{2} k_B T, \quad (2.48)$$

where K is the force constant, $\langle u^2 \rangle$ is the expected value of the squared deviations from equilibrium position. From Eq. 2.48 it follows that we can describe force constant as function of $\langle u^2 \rangle$

$$K = \frac{k_B T}{\langle u^2 \rangle}. \quad (2.49)$$

2. Lattice dynamics, phonons, and their interactions

Despite our model simplicity, such relation can be proven for more complex systems like lattice vibrations [96]. Indeed, Kong *et al.* demonstrated that

$$\Phi_{\alpha\beta}(i, j, \mathbf{q}) = k_B T \langle \mathbf{u}(i, \mathbf{q}) \mathbf{u}^*(j, \mathbf{q}) \rangle^{-1} \quad (2.50)$$

where $\Phi_{\alpha\beta}(i, j, \mathbf{q})$ is the Fourier transform of $\Phi_{\alpha\beta}(0, i, B, j)$, and $\mathbf{u}(i, \mathbf{q})$ is the Fourier transform of the atomic displacements with respect to their equilibrium positions. Thus, Eq. 2.50 offers a theoretical framework to obtain the harmonic IFCs from molecular dynamics runs, either classical or quantum. Contrary to other methods, this one naturally accounts for finite temperature effects into the IFCs, namely finite-difference and linear response methods provide IFCs calculated at 0 K, needing alternative methods to account for such effects [95].

2.2. Anharmonicity

We have discussed the lattice dynamics using the harmonic approximation, in which we have obtained that crystal dynamics is that of an uncoupled set of harmonic oscillators (see Eqs. 2.28 and 2.39). Although in general the harmonic approximation gives an accurate description of several important crystal properties like the phonon frequencies and velocities or the heat capacity, it fails to describe a plethora of other properties, for instance: the thermal dependence of crystal volume or phonon frequencies, or the finite thermal conductivity [97]. Such a failure has its origin in the fact that atomic vibrations are not purely harmonic but have some degree of anharmonicity, which couples the different vibrational modes [56]. For a proper description of those properties, the anharmonicity can be introduced as a perturbation to the harmonic approximation. To that end, it is useful to express the atomic displacement operator (\hat{u}) and its time derivative (\hat{v})

2. Lattice dynamics, phonons, and their interactions

in terms of the creation and annihilation operators [67, 98],

$$\hat{u}_\alpha(A, i) = \sqrt{\frac{\hbar}{2Nm_j}} \sum_\lambda \frac{1}{\sqrt{\omega_\lambda}} \xi_{i\alpha\lambda} e^{iqR_A} \left(\hat{A}_\lambda + \hat{A}_{-\lambda}^\dagger \right), \quad (2.51)$$

$$\hat{v}_\alpha(A, i) = i \sqrt{\frac{\hbar}{2Nm_j}} \sum_\lambda \frac{1}{\sqrt{\omega_\lambda}} \xi_{i\alpha\lambda} e^{iqR_A} \left(\hat{A}_{-\lambda}^\dagger - \hat{A}_\lambda \right), \quad (2.52)$$

where N is the number of cells of the crystal, λ is the phonon mode, viz. (\mathbf{q}, ν) , so ω_λ and $\xi_{i\alpha\lambda}$ are equivalent to $\omega(\mathbf{q}, \nu)$ and $\xi_{i\alpha}(\mathbf{q}, \nu)$, respectively, and $-\lambda$ is equivalent to $(-\mathbf{q}, \nu)$. Therefore, using Eq. 2.51, the third-order perturbation term can be written using the creation and annihilation operators as

$$\begin{aligned} \hat{\mathcal{H}}^{\text{Anh-3}} &= \frac{1}{6} \left(\frac{\hbar}{2N} \right)^{\frac{3}{2}} \sum_{\lambda\lambda'\lambda''} \frac{1}{\sqrt{\omega_\lambda\omega_{\lambda'}\omega_{\lambda''}}} \\ &\sum_{ABC} \sum_{ijk} \sum_{\alpha\beta\gamma} \Phi_{\alpha\beta\gamma}(A, i, B, j, C, k) \frac{\xi_{i\alpha\lambda} \xi_{j\beta\lambda'} \xi_{k\gamma\lambda''}}{\sqrt{m_i m_j m_k}} \left(e^{i\mathbf{q}\cdot\mathbf{R}_A} e^{i\mathbf{q}'\cdot\mathbf{R}_B} e^{i\mathbf{q}''\cdot\mathbf{R}_C} \right) \\ &\left[\left(\hat{A}_\lambda + \hat{A}_{-\lambda}^\dagger \right) \left(\hat{A}_{\lambda'} + \hat{A}_{-\lambda'}^\dagger \right) \left(\hat{A}_{\lambda''} + \hat{A}_{-\lambda''}^\dagger \right) \right], \quad (2.53) \end{aligned}$$

which can be reduced by using translational invariance and plane wave orthonormality to

$$\begin{aligned} \hat{\mathcal{H}}^{\text{Anh-3}} &= \frac{1}{6\sqrt{N}} \left(\frac{\hbar}{2} \right)^{\frac{3}{2}} \sum_{\lambda\lambda'\lambda''} \frac{V_{\lambda\lambda'\lambda''}}{\sqrt{\omega_\lambda\omega_{\lambda'}\omega_{\lambda''}}} \left[\left(\hat{A}_\lambda + \hat{A}_{-\lambda}^\dagger \right) \right. \\ &\left. \left(\hat{A}_{\lambda'} + \hat{A}_{-\lambda'}^\dagger \right) \left(\hat{A}_{\lambda''} + \hat{A}_{-\lambda''}^\dagger \right) \right] \delta(\mathbf{q} + \mathbf{q}' + \mathbf{q}'' + \mathbf{G}), \quad (2.54) \end{aligned}$$

where \mathbf{G} is a reciprocal lattice vector and we have defined $V_{\lambda\lambda'\lambda''} = \sum_{B'C'} \sum_{ijk} \sum_{\alpha\beta\gamma} \Phi_{\alpha\beta\gamma}(0, i, B', j, C', k) \frac{\xi_{i\alpha\lambda} \xi_{j\beta\lambda'} \xi_{k\gamma\lambda''}}{\sqrt{m_i m_j m_k}} \left(e^{i\mathbf{q}'\cdot\mathbf{R}_{B'}} e^{i\mathbf{q}''\cdot\mathbf{R}_{C'}} \right)$.

2.2.1. Three-phonon processes

From the expansion of creation and annihilation term in Eq. 2.54,

$$\begin{aligned} \hat{A}_\lambda \hat{A}_{\lambda'} \hat{A}_{\lambda''} + \hat{A}_\lambda \hat{A}_{\lambda'} \hat{A}_{-\lambda''}^\dagger + \hat{A}_\lambda \hat{A}_{-\lambda'}^\dagger \hat{A}_{\lambda''} + \\ \hat{A}_\lambda \hat{A}_{-\lambda'}^\dagger \hat{A}_{-\lambda''}^\dagger + \hat{A}_{-\lambda}^\dagger \hat{A}_{\lambda'} \hat{A}_{\lambda''} + \hat{A}_{-\lambda}^\dagger \hat{A}_{\lambda'} \hat{A}_{-\lambda''}^\dagger + \\ \hat{A}_{-\lambda}^\dagger \hat{A}_{-\lambda'}^\dagger \hat{A}_{\lambda''} + \hat{A}_{-\lambda}^\dagger \hat{A}_{-\lambda'}^\dagger \hat{A}_{-\lambda''}^\dagger, \quad (2.55) \end{aligned}$$

is it possible to see what effect causes the anharmonic perturbation in the harmonic system. Following Eq. 2.55, it is easy to see that the action of third-order anharmonic potential over phonons causes them to interact in triplets (analogously fourth-order would cause phonons to interact in quartets) [56]. We can also discard some of these processes, namely those which create or annihilate three-phonons as those processes cannot conserve energy, and thus are unimportant out of time scales related to the violation of the conservation of energy via the uncertainty principle [97]. Therefore, we see that there are only two kinds of allowed processes, those in which a phonon is annihilated and two are created—henceforth called emission processes—and the ones annihilating two phonons and creating a third-one—henceforth called absorption processes. Furthermore, such interaction between phonons, which are now created and destroyed through it, causes phonons to gain a finite lifetime. We note that here this lifetime needs to be understood as the fact that a phonon does not remain in a given state indefinitely but transition to other states through absorbing or emitting another phonon.

Moreover, $\delta(\mathbf{q} + \mathbf{q}' + \mathbf{q}'' + \mathbf{G})$ implies that only those processes conserving the quasi-momentum up to an arbitrary reciprocal lattice vector are allowed. Therefore combining Eq. 2.55 with this condition one obtains that the three-

2. Lattice dynamics, phonons, and their interactions

phonon processes must satisfy

$$\omega_\lambda \pm \omega_{\lambda'} - \omega_{\lambda''} = 0, \quad (2.56)$$

$$\mathbf{q} \pm \mathbf{q}' - \mathbf{q}'' = \mathbf{G}, \quad (2.57)$$

where “+ (−)” refers to absorption (emission) process.

Finally, it is possible to obtain the rate at which a phonon transitions to other states due to emission or absorption process by inserting Eq. 2.54 into the Fermi's golden rule (see Section 1.5). Thus the transition rate (Γ) for emission and absorption are [39, 56]

$$\Gamma_{\lambda \rightarrow \lambda' \lambda''} = \frac{2\pi}{\hbar} \left| \langle n_\lambda - 1, n_{\lambda'} + 1, n_{\lambda''} + 1 | \hat{\mathcal{H}}^{\text{Anh}-3} | n_\lambda, n_{\lambda'}, n_{\lambda''} \rangle \right|^2 = P_{\lambda \rightarrow \lambda' \lambda''}^{\text{3ph}} [n_\lambda (n_{\lambda'} + 1) (n_{\lambda''} + 1)] \quad (2.58)$$

and

$$\Gamma_{\lambda \lambda' \rightarrow \lambda''} = \frac{2\pi}{\hbar} \left| \langle n_\lambda - 1, n_{\lambda'} - 1, n_{\lambda''} + 1 | \hat{\mathcal{H}}^{\text{Anh}-3} | n_\lambda, n_{\lambda'}, n_{\lambda''} \rangle \right|^2 = P_{\lambda \lambda' \rightarrow \lambda''}^{\text{3ph}} [n_\lambda n_{\lambda'} (n_{\lambda''} + 1)], \quad (2.59)$$

respectively; where the intrinsic transition rate are $P_{\lambda \rightarrow \lambda' \lambda''}^{\text{3ph}} = \frac{\hbar\pi}{4N} \frac{|V_{\lambda\lambda'\lambda''}|^2}{\omega_\lambda \omega_{\lambda'} \omega_{\lambda''}} \delta(\omega_\lambda - \omega_{\lambda'} - \omega_{\lambda''})$ and $P_{\lambda \lambda' \rightarrow \lambda''}^{\text{3ph}} = \frac{\hbar\pi}{4N} \frac{|V_{\lambda\lambda'\lambda''}|^2}{\omega_\lambda \omega_{\lambda'} \omega_{\lambda''}} \delta(\omega_\lambda + \omega_{\lambda'} - \omega_{\lambda''})$. Following microscopic reversibility we have that $P_{\lambda \rightarrow \lambda' \lambda''}^{\text{3ph}} = P_{\lambda' \lambda'' \rightarrow \lambda}^{\text{3ph}}$, and because of detailed balance we have that in equilibrium $\Gamma_{\lambda \lambda' \rightarrow \lambda''} = \Gamma_{\lambda'' \rightarrow \lambda \lambda'}$ [39].

2.2.1.1. Umklapp and normal scattering

Usually, three-phonon processes are classified in function of whether the quasi-momentum is fully conserved (i.e. $\mathbf{G} = \mathbf{0}$ in Eq. 2.57) or not; namely, it is conserved but within a reciprocal lattice vector \mathbf{G} , so $\mathbf{G} \neq \mathbf{0}$ in Eq. 2.57. The former processes are referred to as normal processes or \mathcal{N} processes [99], whilst the latter are referred to as umklapp processes or \mathcal{U} processes [99, 100]. Therefore, this distinction between \mathcal{N} and \mathcal{U} processes is solely a \mathbf{G} vector. However, as \mathbf{G} depends on the chosen cell, the distinction between \mathcal{N} and \mathcal{U} is somehow artificial [101, 102]; indeed, this was already noted by Peierls [92]:

“Physically there is no important difference between processes in which the sum $\mathbf{q} + \mathbf{q}'$ just remains within the basic cell, and those in which it falls just outside and has to be brought back by adding a suitable \mathbf{G} , and indeed the distinction between the two depends on our convention in choosing the basic cell.”

Consequently, the underlying theory and quantities derived from it, as it could be thermal conductivity (see Section 3.2) cannot be dependent on this distinction.

We find it worth commenting on this last point, as it is a common approach in the field of thermal transport to make such distinction because of approximations, like the Callaway model [99]. Indeed, this last model is fully based on such distinction so that umklapp processes relax the distribution to its equilibrium value, while normal processes relax it to a displaced one. However, such a strict classification is known to yield thermal conductivities with, at best, a 30% error [103, 104] at room temperature in the case of graphene. Indeed, to obtain more accurate results it has been proved that one needs to perform a more careful analysis of umklapp scattering in thermal resistivity, in a way that not all umklapp processes are resistive [103, 105]. For instance, this redefinition of the umklapp role on thermal transport yields improved results for the thermal conductivity

2. Lattice dynamics, phonons, and their interactions

of graphene, reducing its error to 3%. However, such an improvement is not guaranteed *a priori*. For example, in the case of black phosphorous the error in the zigzag thermal conductivity, even with such a correction, is of 15% [103].

This necessity of redefining the role of umklapp processes, but also normal ones, on thermal transport is rooted in a general misconception which relates \mathcal{N} with non-resistive processes, namely those in which the flux ($\mathbf{J} = \sum_i \mathbf{v}_i \hbar \omega_i n_i$) is conserved (i.e. $\mathbf{v}'' = \mathbf{v} \pm \mathbf{v}'$) and \mathcal{U} with resistive ones. In line with the Peierls statement, this is in general false, out of the simplistic single band Debye model; so that to determine if a single process is resistive or not, one needs to check whether $\mathbf{v}'' = \mathbf{v} \pm \mathbf{v}'$ holds (i.e. non-resistive) or not (i.e. resistive) [102]. In fact, the distinction only makes sense beyond the individual processes, i.e. from a statistical point of view, where Peierls demonstrated by a mathematical analysis of solution of the homogeneous Boltzmann Transport Equation that, in the absence of \mathcal{U} processes for the chosen cell, thermal equilibrium cannot be established [92, 102]. Indeed, a more rigorous mathematical treatment leads to the exact solution for such a case, namely a displaced Bose-Einstein distribution [102, 106], which is in general capable of supporting a collective phonon flux *ad infinitum*:

$$n(\mathbf{q}, \nu, T) = \frac{1}{e^{\frac{\hbar \omega(\mathbf{q}, \nu) - \mathbf{q} \cdot \mathbf{v}_n}{k_B T}} - 1}, \quad (2.60)$$

where v_n is the velocity of the whole phonon distribution.

However, we note that this last result is a consequence of limiting the processes within the arbitrarily chosen reciprocal cell, and thus holds for any unit cell, while \mathcal{U} - \mathcal{N} classification depends on the chosen cell. Consequently, statistically speaking a strict distinction between \mathcal{U} and \mathcal{N} cannot be made, but only in a general sense for small temperatures [102], and for the natural/traditional choice of the reciprocal cell, i.e. one centered in Γ [102]. In such a case, most of the processes are normal, limited to low frequencies in the vicinity of Γ , leading to

the collective behavior of the phonons (see Subsection 3.1.1.1).

2.2.2. Performing integrals containing three-phonon processes

Within transport theory it is common to have integrals containing three-phonon scattering rates [46, 107] (see Subsection 3.2.1). Such expressions can in principle seem simple; however, recall that one usually works with regular reciprocal space meshes, and thus the energy conservation would not be satisfied for almost any of the possible combinations for the given mesh. To overcome this limitation there are several strategies:

1. *Gaussian quadrature*: the integral is solved by finding, given an initial mesh, the explicit points that fulfill the energy and momentum conservation constraints [98, 108]. However, this method is computationally inefficient as it requires a search and interpolation over all the search space [98].
2. *Linear tetrahedron method*: the BZ is divided into tetrahedra so that all functions (frequencies, velocities,...) are calculated at each of the tetrahedron vertices. The interest quantities for the integral evaluation are then linearly interpolated inside the corresponding tetrahedron [107, 109]. We note that linear interpolation might be inappropriate for materials with quadratic bands without an appropriate correction [110]—notice that Blöchl corrections are not valid for phonon frequencies and other response functions [110, 111]—or by using quadratic, higher-order interpolants or hybrid methods (i.e. combining quadratic polynomials for interpolation and linear ones for the integrals) [112].
3. *Gaussian smearing method*: The delta function is replaced by a Gaussian

2. Lattice dynamics, phonons, and their interactions

function [40, 46],

$$\delta(\omega_\lambda \pm \omega_{\lambda'} - \omega_{\lambda''}) \simeq \frac{1}{\sqrt{2\pi}\sigma} \exp\left(-\frac{[\omega_\lambda \pm (\omega_{\lambda'} - \omega_{\lambda''})]^2}{2\sigma^2}\right), \quad (2.61)$$

where σ is the smearing factor, determining the degree in which a process can deviate from the strict energy conservation.

From all the three methods, the smearing one is conceptually the most simple. Moreover, it is more suited than the other two especially for complex systems and/or band structures; although it also requires denser \mathbf{q} -meshes to converge [107]. However, the principal drawback of this methodology, is the introduction of σ , as it allows for tuning to fit the experimental results, breaking with the parameter-free spirit of the first-principles calculations.

To solve this, it is possible to use an adaptive smearing scheme based on the properties of the phonons taking part on the scattering process to calculate the smearing of each process [40, 113]. Hence, the smearing factor for a given three-phonon process, $\sigma_{\lambda\lambda'\lambda''}$, is [46]

$$\sigma_{\lambda\lambda'\lambda''} = \frac{a}{\sqrt{12}} \|(G_{\mu\alpha}^T N_{\mu\mu}^{-1})^T \cdot (\mathbf{v}_{\lambda'} - \mathbf{v}_{\lambda''})_\alpha\|, \quad (2.62)$$

where μ indicates a reciprocal-space lattice vector, $N_{\mu\mu}$ is a diagonal matrix with the \mathbf{q} -grid size, and a is the scalebroad factor, i.e. a scaling factor for the smearing parameter. This last is ideally 1, but it is usually reduced to speed up calculations as one usually only takes into account processes whose energy deviation is not larger than $n \times \sigma$ [46, 47].

We note that Eq. 2.62 breaks the microscopic reversibility. This is that given a transition $\lambda \rightarrow \lambda' + \lambda''$ and its reverse process $\lambda' + \lambda'' \rightarrow \lambda$, $\sigma_{\lambda\lambda'\lambda''} \neq \sigma_{\lambda'\lambda''\lambda}$ as in general $\mathbf{v}_{\lambda'} - \mathbf{v}_{\lambda''} \neq \mathbf{v}_{\lambda''} - \mathbf{v}_{\lambda}$; indeed for the absorption process we also have that the same physical process to occur at different rate as $\sigma_{\lambda'\lambda''\lambda} \neq \sigma_{\lambda''\lambda'\lambda}$. Moreover,

2. Lattice dynamics, phonons, and their interactions

the way smearing is constructed, as products of velocities over reciprocal lattice vectors, breaks crystal symmetry as it can cause symmetry equivalent triplets (i.e. triplets of phonons related by symmetry operations) to give different smearing values.

It is also important to notice that since we are not strictly imposing energy conservation, the smearing method will also break the detailed balance principle. Notwithstanding those conceptual flaws, the smearing methods, and in special the ones with an adaptive smearing scheme have succeeded in predicting thermal properties of different materials [46, 47].

2.2.3. Frequency shift, thermal expansion and Grüneisen parameter

In addition to finite lifetimes, anharmonicity also gives rise to other interesting phenomena such as thermal expansion or frequency shift. A common approach to tackle that problem is the so-called quasi-harmonic approximation, in which the harmonic properties—i.e. $\omega(V)$ and electron energy $E_{\text{el}}(V)$ —at different volumes are used to build the Gibbs free energy, $G(V, T)$, at different V and T [114], so that its minimum at fixed T gives $V_{\text{eq}}(T)$, from which it becomes possible to define the thermal expansion coefficient, α , as

$$\alpha(T) = \frac{1}{V_{\text{eq}}} \frac{\partial V_{\text{eq}}}{\partial T}. \quad (2.63)$$

Moreover, as $\omega(V)$ and $V_{\text{eq}}(T)$ we have a shift in frequencies due to the volumetric change of the thermal expansion. Such a change, which is a direct indicative of the crystal anharmonicity, is usually defined in terms of the Grüneisen parameter, γ_i , as

$$\gamma_i = - \frac{V_{\text{eq}}^0}{\omega_i(V_{\text{eq}}^0)} \left. \frac{\partial \omega_i(V)}{\partial V_{\text{eq}}} \right|_{V_{\text{eq}}=V_{\text{eq}}^0}, \quad (2.64)$$

2. Lattice dynamics, phonons, and their interactions

where $V_{\text{eq}}^0 = V_{\text{eq}}(T = 0 \text{ K})$. This last can be computed by numerical differentiation of frequencies at different equilibrium volumes [108]. Alternatively, it can be computed directly from the third-order force constants at V_{eq}^0 as [108]

$$\gamma_i = -\frac{1}{6\omega_i^2} \sum_{BC} \sum_{ijk} \sum_{\alpha\beta\gamma} \Phi_{\alpha\beta\gamma}(0, i, B, j, C, k) \frac{\xi_{i\alpha\lambda}^* \xi_{j\beta\lambda'}}{\sqrt{m_i m_j}} e^{i\mathbf{q} \cdot \mathbf{R}_B \mathbf{r}_{Ck\gamma}}, \quad (2.65)$$

where $\mathbf{r}_{Ck\gamma}$ is γ -component of the position of the k -th atom inside the C cell.

We note that in addition to the shift because of this volume change, there is an additional shift to phonon frequencies coming from the several phonon interactions. Paradigmatically, in contrast with scattering terms, the shift caused by third-order terms is lower than those caused by four-order terms in the potential expansion [115].

2.2.4. Anharmonic calculations from first principles

Like in the case of the harmonic properties, anharmonic ones are fully determined by anharmonic force constants, usually calculated up to the third-order. It is possible to calculate these anharmonic force constants either using finite differences [46] or linear response theory [83, 116]. In the former, the anharmonic third-order force constants can be computed as

2. Lattice dynamics, phonons, and their interactions

$$\begin{aligned}
\Phi_{\alpha\beta\gamma}(A, i, B, j, C, k) &= \frac{\partial^3 E}{\partial \mathbf{u}_\alpha(A, i) \partial \mathbf{u}_\beta(B, j) \partial \mathbf{u}_\gamma(C, k)} \approx \\
&- \frac{1}{2h} \left[\frac{\partial \mathbf{F}_\gamma(C, k)}{\partial \mathbf{u}_\beta(B, j)}(\mathbf{u}_\alpha(A, i) = h) - \frac{\partial \mathbf{F}_\gamma(C, k)}{\partial \mathbf{u}_\beta(B, j)}(\mathbf{u}_\alpha(A, i) = -h) \right] \approx \\
&\frac{1}{4h} [-\mathbf{F}_\gamma(B, j)(\mathbf{u}_\alpha(A, i) = h, \mathbf{u}_\beta(B, j) = h) + \\
&\mathbf{F}_\gamma(B, j)(\mathbf{u}_\alpha(A, i) = h, \mathbf{u}_\beta(B, j) = -h) - \\
&\mathbf{F}_\gamma(B, j)(\mathbf{u}_\alpha(A, i) = -h, \mathbf{u}_\beta(B, j) = h) + \\
&\mathbf{F}_\gamma(B, j)(\mathbf{u}_\alpha(A, i) = -h, \mathbf{u}_\beta(B, j) = -h)]. \quad (2.66)
\end{aligned}$$

We note that because of the additional derivative the number of DFT runs increases significantly from the harmonic calculation, namely $4 \times 9n_{\text{uc}}^2 N_{\text{sc}}$ versus the $6n_{\text{uc}}$ of the harmonic ones. Therefore, in addition, to make use of crystal symmetry to reduce the computational burden, a distance cut-off is usually defined so that if the involved atoms are further away than it, they are considered non-interacting (viz. $\Phi_{\alpha\beta\gamma}(A, i, B, j, C, k) \approx 0$).

Alternatively, it is also possible to reconstruct the leading terms of the third-order force constants from Grüneisen parameters, either calculated experimentally or using the quasi-harmonic approximation [117].

In the case of polar materials, equivalently to the harmonic case, the electric field caused by the atomic vibrations gives rise to non-analytic terms in the third-order force constants [118, 119]. However, in contrast with its harmonic counterparts, these non-analytic terms are usually assumed to be negligible [120], and thus it is customary to ignore them. We note that such approximation is valid for common semiconductors like GaAs, but can be inappropriate for highly polar materials [118].

2.3. Mass disorder effect over atomic vibrations: isotopic scattering

We have supposed up until now that a given atom has an uniform mass in the whole crystal, such assumption is false for most of atomic species, as naturally one encounters all the different stable isotopes within a crystal. The problem of how this affects phonons can be tackled using perturbation theory. First, all masses appearing in the previous equations are supposed to be the mean weighted mass of the atomic species (\bar{m}_i), i.e. the one in which the mass of each isotope is weighted by its natural occurrence ($\bar{m}_i = \sum_j w_j m_j$, where j is an isotope of i with atomic mass m_j and natural occurrence of w_j). Hence, one can introduce the effect of mass variation (Δm_i) as a perturbation term to the harmonic Hamiltonian as [121]

$$\hat{\mathcal{H}}^{\text{mass}} = \frac{1}{2} \sum_{iA\alpha} \Delta m_i(A) |\hat{v}_\alpha(A, i, t)|^2, \quad (2.67)$$

where $\hat{v}_\alpha(A, i, t)$ is the atomic velocity operator (see Eq. 2.52). Introducing Eq. 2.51 into Eq. 2.67 allows to express this last in terms of the creation and annihilation operators [121]:

$$\begin{aligned} \hat{\mathcal{H}}^{\text{mass}} = & -\frac{\hbar}{4N} \sum_{\lambda\lambda'} \sum_{iA\alpha} \frac{\Delta m_i}{\bar{m}_i} \sqrt{\omega_\lambda \omega_{\lambda'}} \boldsymbol{\xi}_{i\alpha\lambda'}^* \boldsymbol{\xi}_{i\alpha\lambda} e^{i(\mathbf{q}-\mathbf{q}')\mathbf{R}_A} \\ & \left[\hat{A}_{-\lambda'} \hat{A}_{-\lambda}^\dagger - \hat{A}_{-\lambda'} \hat{A}_\lambda - \hat{A}_\lambda^\dagger \hat{A}_{-\lambda}^\dagger + \hat{A}_\lambda^\dagger \hat{A}_\lambda \right]. \end{aligned} \quad (2.68)$$

Following Eq. 2.68, we can observe that mass disorder causes phonons to change their state. As for three-phonon, we can eliminate those processes that only create or destroy phonons as they cannot conserve energy; hence we only keep $\hat{A}_{-\lambda'} \hat{A}_{-\lambda}^\dagger + \hat{A}_\lambda^\dagger \hat{A}_\lambda$. Thus, interaction with isotopes causes phonons to change its state.

2. Lattice dynamics, phonons, and their interactions

The transition rate from λ to λ' due to isotopes can be calculated using the Fermi's golden rule to be [46, 47, 121]

$$\Gamma_{\lambda \rightarrow \lambda'}^{\text{iso}} = P_{\lambda \rightarrow \lambda'}^{\text{iso}} n_{\lambda} (n_{\lambda'} + 1) = \frac{\pi \omega_{\lambda} \omega_{\lambda'}}{2} n_{\lambda} (n_{\lambda'} + 1) \sum_i \frac{\sigma^2(m_i)}{\bar{m}_i} |\xi_{i\lambda'} \xi_{i\lambda}|^2 \delta(\omega_{\lambda} - \omega_{\lambda'}) \quad (2.69)$$

where we assumed that mass disorder is randomly distributed along the lattice and $P_{\lambda \rightarrow \lambda'}^{\text{iso}}$ is the intrinsic transition probability due to a isotopic scattering process. Following microscopic reversibility we have that $P_{\lambda \rightarrow \lambda'}^{\text{iso}} = P_{\lambda' \rightarrow \lambda}^{\text{iso}}$, and because of detailed balance we have that in equilibrium $\Gamma_{\lambda \rightarrow \lambda'}^{\text{iso}} = \Gamma_{\lambda' \rightarrow \lambda}^{\text{iso}}$ [39].

Concerning the first-principles calculation of the Eq. 2.69, as this only requires harmonic properties, it can be done through techniques explained in Subsection 2.1.4 of this Chapter. Finally, regarding the allowed isotopic processes and the integrals containing them; we note that Eq. 2.62 remains valid but with $v_{\lambda'}$ instead of $v_{\lambda''} - v_{\lambda'}$. Moreover, it is possible to build a smearing respectful with the microscopic reversibility for isotopic processes. We observe that since momentum is not conserved, the frequencies are uncorrelated random variables, and thus the total smearing, which respects the reversibility, can be obtained as the quadratic sum of direct and reverse processes.

2.4. Phonons in alloys: the virtual crystal approximation

Alloys, which are mixtures of two or more crystals, are usually treated within the virtual crystal approximation (VCA). This consists on treating the alloy as an effective crystal whose properties (lattice constants, masses, Born Charges, dielectric constants, IFCs,...) are calculated using Vegard's law, i.e. a weighted linear

2. Lattice dynamics, phonons, and their interactions

combination of the pure compounds properties forming the alloy, for instance for the harmonic force constants: $\Phi_{\alpha\beta}^{\text{VCA}}(0, i, B, j) = \sum_m w_m \Phi_{\alpha\beta}^m(0, i, B, j)$, where m is one of the alloy's constituents with weight w_m [47, 122, 123]. Concerning the effect of alloying over the virtual crystal phonons, the compositional disorder in alloys acts like isotopic disorder scattering, and thus it can be tackled identically, treating the mass disorder with respect to Vegard's masses. Despite the VCA has proven its accuracy and improvement with respect more simple modes such as the mass-defect model [124] in describing the thermal properties of alloys [40, 47, 123], it has some inherent limitations as it cannot account for local relaxations of the structure, changes to the electronic structure, local ordering or localized vibrational states (i.e. without plane-wave character) [47, 123, 124]. In addition to quantitative deviations from the experimental results [122], these failures can even cause a qualitative fail on the behavior of thermal conductivity with temperature, which in some cases differ from the one of a pure material as predicted by the VCA [125, 126].

2.5. Electron-phonon interaction

Besides interacting with other vibrations and isotopes, it is not difficult to see that any change in the atomic coordinates (i.e. vibrations) will affect electron density and vice versa. Within the BOA framework, such interaction between atomic vibrations and the electronic system can be treated perturbatively. Therefore, within DFT the KS potential can be expanded up to first-order in terms of phonon displacements [127]:

$$V_{\text{KS}}(\mathbf{u}_\lambda) = V_{\text{KS}}(0) + \sum_{iA\alpha} \frac{\partial V_{\text{KS}}}{\partial \mathbf{R}_{iA\alpha}} \sqrt{\frac{\hbar}{2NM_i\omega_\lambda}} e^{i\mathbf{q}\cdot\mathbf{R}_A} \boldsymbol{\xi}_\lambda (\hat{A}_{\lambda'} + \hat{A}_{-\lambda}^\dagger) \quad (2.70)$$

2. Lattice dynamics, phonons, and their interactions

where we have expanded atomic displacements due λ phonon using phonon creation and annihilation operators. Thus the electron-phonon Hamiltonian is

$$\hat{H}_{\text{ep}} = \sum_{ij\lambda} g_{i\lambda j} (\hat{A}_{\lambda'} + \hat{A}_{-\lambda}^\dagger) \hat{C}_i \hat{C}_j^\dagger = \sum_{ij\lambda} \langle \phi_j | \sum_{iA\alpha} \frac{\partial V_{\text{KS}}}{\partial \mathbf{R}_{iA\alpha}} \sqrt{\frac{\hbar}{2NM_i\omega_\lambda}} e^{i\mathbf{q} \cdot \mathbf{R}_A} \boldsymbol{\xi}_\lambda | \phi_i \rangle (\hat{A}_{\lambda'} \hat{C}_i \hat{C}_j^\dagger + \hat{A}_{-\lambda}^\dagger \hat{C}_i \hat{C}_j^\dagger) \quad (2.71)$$

where $g_{i\lambda j}$ is the electron-phonon matrix element coupling the i and j electronic states due to λ phonon mode, \hat{C}_i and \hat{C}_i^\dagger are the electronic annihilation and creation operators, respectively. Following Eq. 2.71 we can see that electron-phonon interaction can cause either transition between electronic states due to a phonon emission or absorption, the scattering rates of which can be computed through the FGR [127].

The calculation of such matrix elements can be done using first principles within the DFPT framework. However, owing to the high computational cost associated with these calculations, they are usually restricted to small \mathbf{k} and \mathbf{q} -meshes. Therefore, interpolation schemes such as Fourier or Wannier interpolation are usually required to obtain those quantities on larger meshes necessary for the computation of related quantities [127, 128]. We note that for polar materials, one needs to take into account the coupling with the electric field caused by the atomic vibrations [127–130].

CHAPTER 3

Thermal transport modeling

The continuous development of micro- and nanofabrication techniques has allowed for higher integration levels in electronic devices and more efficient thermoelectric systems, or better thermal insulators for improved energy saving in buildings [1, 2, 15, 16, 31]. Indeed, the reduction in size [1] and the required increment in operating speeds of devices in electronics, or the necessity to enhance the energy conversion ratio for thermoelectrics have increased the importance of phonon engineering or phononics[131]. Therefore, a proper understanding of the thermal transport in those systems becomes essential to optimize their operation, as if not managed carefully, heat can severely hinder their efficiency and/or durability [3–6].

In this chapter we discuss thermal transport modeling ranging from the more simple mesoscopic models to more complex models, focusing on the solution of the semiclassical linearized Peierls-Boltzmann transport equation (PBTE) as well as making a brief description of some software packages solving it. Finally, we briefly comment on other methodologies for the modeling and thermal properties calculation.

3.1. Mesoscopic Modeling and Fourier's law

Thermal modeling has its roots back into the 19th century Fourier's original work [32]. Therein, Fourier concluded that thermal flux was proportional to minus the thermal gradient:

$$\mathbf{J} = -\kappa \nabla T \quad (3.1)$$

where \mathbf{J} is the heat flux, κ is the thermal conductivity rank-2 tensor and T is the local equilibrium temperature. When Eq. 3.1 is combined with the energy-balance equation one gets the time-dependent heat equation [33]:

$$\frac{\partial T}{\partial t} = -\alpha \nabla^2 T \quad (3.2)$$

where α is the thermal diffusivity, which is defined as the ratio between the thermal conductivity and the volumetric heat capacity (κ/C_v). Therefore, using Eqs. 3.1 and 3.2 together with the appropriate boundary conditions, it becomes possible to determine the full heat mechanics in mesoscopic systems using only a small set of materials properties (i.e. κ and C_v). This last makes these kinds of models attractive when compared to more complex ways of modeling thermal transport, as they are fast, efficient, and offer a clear physical picture of the phenomena [132, 133]. However, these models per se do not provide any information on how to compute those thermal properties other than experimental fitting or as solutions of more complex microscopic models.

3.1.1. Fourier's law failure and beyond-Fourier mesoscopic models

Eq. 3.2 is a parabolic partial differential equation the solution of which leads to the evolution of the temperature in space and time. Nevertheless, its solution has

3. Thermal transport modeling

the particularity, that any kind of thermal perturbation is instantaneously felt by the whole system. This “paradox” in which a thermal disturbance propagates at infinite speed is a very well-known flaw of Fourier’s theory, thus forbidding memory effects or the proper description of the heat pulse dynamics, e.g. the second-sound [33, 134]. One of the first attempts to overcome such limitation was by Cattaneo [135], who based on the kinetic theory introduced a lag term accounting for the thermal inertia [132]. Thus,

$$\tau_J \frac{\partial \mathbf{J}}{\partial t} + \mathbf{J} = -\kappa \nabla T , \quad (3.3)$$

which is known as the Maxwell-Cattaneo-Vernotte equation, where τ_J is the relaxation time of heat flux. Notwithstanding the great improvement to Fourier’s law, the Eq. 3.3 is still unable to properly reproduce the other important Fourier deviation found in the nanoscale, non-local effects. A prototypical non-local effect is the Poiseuille heat flux profile found in nanowires and nanoribbons [136, 137]. Although such a feature can be described through the Fourier’s law by imposing a position-dependent κ —with lower values nearby to the edges due to the boundary scattering—, it can be more easily described using a single effective κ (lower than bulk one due to the boundary scattering) and a non-local term. Other examples of the Fourier failure due to the presence of memory and/or non-local effects can be found in the literature; for instance, it has been observed that Fourier’s law fails to correctly reproduce several thermoreflectance [34–36] and thermal grating [37, 38] experiments. Indeed, for most of those cases, not even a modified Fourier can accurately reproduce the experimental results [35].

In such systems and situations, the heat dynamics is better modeled as a viscous fluid by means of the hydrodynamic equation (named in that way because of its similarity with the Navier-Stokes equation describing the dynamics in

3. Thermal transport modeling

viscous liquids):

$$\tau_J \frac{\partial \mathbf{J}}{\partial t} + \mathbf{J} = -\kappa \nabla T + \ell^2 (\nabla^2 \mathbf{J} + 2 \nabla \nabla \cdot \mathbf{J}) , \quad (3.4)$$

where ℓ is the non-local length rank-2 tensor and is related to the distance that heat can conserve its inertia [33, 136, 137]. The earliest derivation of this hydrodynamic equation for heat transport was by Guyer and Krumhansl (GK) [138]. In their work, they derived an equivalent expression by expanding the phonon distribution on the eigenvectors of the PBTE normal collision operator—i.e. the operator accounting for the change in the populations of the microscopic heat carriers because of the interaction between each other, impurities, boundaries,...—under the condition that normal (\mathcal{N}) scattering is dominant over umklapp (\mathcal{U}) and extrinsic (\mathcal{E}) scattering. Indeed, within the GK framework, hydrodynamic features are only possible when \mathcal{N} processes dominate over all other kinds of scattering [132, 139, 140]. Similarly, Simoncelli *et al.* [141] have derived an alternative set of coupled mesoscopic equations describing both the Fourier and hydrodynamic regime using the PBTE and relaxons—i.e. the eigenvectors of the full collision operator— [142]. Nonetheless, they have still relied on the separation of scattering operator between the \mathcal{N} , the \mathcal{U} and the \mathcal{E} contributions.

3.1.1.1. Generalized hydrodynamics

It is worth noting that the role of \mathcal{U} and \mathcal{N} processes in phonon hydrodynamics is more nuanced than the widespread belief, rooted in the GK derivation, that \mathcal{N} processes must dominate [139, 140]. That is a sufficient but not necessary condition, since the hydrodynamic regime is possible even in the case where \mathcal{N} and \mathcal{U} scattering are comparable or when \mathcal{E} dominates over the intrinsic scattering [132, 143]. Moreover, as discussed in Subsection 2.2.1.1 such classification might be inappropriate, as it is subject to the specific choice of the primitive

3. Thermal transport modeling

cell [101, 102], and even if one takes the primitive cell centered around the Γ point, \mathcal{N} process are not ensured to conserve the heat flux out of the single band Debye's model [102].

A more general hydrodynamic theory, not relaying on \mathcal{N} dominance or on the classification of three-phonon processes into \mathcal{N} and \mathcal{U} , has been recently proposed by Sendra *et al.* [143]. In their work, they derived Eq. 3.4 by projecting the PBTE over energy and quasimomenta, and by expanding phonon distribution on macroscopic variables like flux. This generalizes the hydrodynamic regime to materials where both resistive and non-resistive processes are comparable—i.e. out of the range of applicability of the RTA (see Subsection 3.2.1)—, as in the case of diamond or 2D materials [132], but also to materials like room-temperature silicon in which intrinsic resistive scattering is the dominant mechanism [143].

3.2. Semiclassical modeling: the Peierls-Boltzmann transport equation

Despite their utility, mesoscopic models do not provide any information about the elements carrying the heat. From a microscopic point of view in solids, heat is carried by electrons and atomic vibrations, i.e. phonons. Indeed, for materials with small free-electron densities, like the insulators, semiconductors, and semimetals which are generally used in the electronic devices, heat is mainly carried by phonons; so the electronic contribution to heat transport for those materials is usually deemed negligible and thus discarded [39, 144]. Therefore, any microscopic heat modeling for semiconductors requires somehow describing the evolution of the phonon populations both in time and space. One of the earliest attempts to do so is after Peierls [100]. Analogously to Boltzmann's kinetic theory of gases, Peierls's proposed that phonons diffuse and scatter, and that all the information is contained within a continuous phonon distribution function,

3. Thermal transport modeling

both in real and phase space [92]. Thus, the phonon distribution function evolves accordingly to

$$\frac{\partial n_i(\mathbf{r}, t)}{\partial t} + \mathbf{v}_i \cdot \nabla n_i(\mathbf{r}, t) = \left. \frac{\partial n_i(\mathbf{r}, t)}{\partial t} \right|_{\text{collision}}, \quad (3.5)$$

where $n_i(\mathbf{r}, t)$ is the phonon distribution function for the i phonon mode, \mathbf{r} is the position, t is the time, \mathbf{v}_i is the velocity of a phonon in the i mode, $\left. \frac{\partial n_i(\mathbf{r}, t)}{\partial t} \right|_{\text{collision}}$ represents the change in the distribution due to phonon interactions. For thermal transport problems is customary to expand diffusion term—i.e. $\mathbf{v}_i \nabla n_i(\mathbf{r}, t)$ —in terms of the thermal gradient $\left[\frac{\partial n_i(\mathbf{r}, t)}{\partial T} \mathbf{v}_i \cdot \nabla T(\mathbf{r}, t) \right]$.

As noted, the thermal properties of the system are fully determined by $n_i(\mathbf{r}, t)$, namely energy density, $\rho(\mathbf{r}, t)$, temperature, $T(\mathbf{r}, t)$, and heat flux, $\mathbf{J}(\mathbf{r}, t)$, can defined in terms of the distribution function as:

$$\rho(\mathbf{r}, t) = \frac{1}{N_q V_{\text{uc}}} \sum_i \hbar \omega_i n_i(\mathbf{r}, t), \quad (3.6)$$

$$T(\mathbf{r}, t) = \frac{\rho(\mathbf{r}, t)}{C_v}, \quad (3.7)$$

$$\mathbf{J}(\mathbf{r}, t) = \frac{1}{N_q V_{\text{uc}}} \sum_i \mathbf{v}_i \hbar \omega_i n_i(\mathbf{r}, t), \quad (3.8)$$

where N_q is the number of \mathbf{q} -points in the summation, V_{uc} is the volume of the unit cell, \hbar is reduced Planck constant, C_v is the volumetric heat capacity (see Eq. 2.43), and ω_i is the frequency of the i -th phonon mode. It is worth mentioning that in Eq. 3.8 only out-of-equilibrium contributions can lead to a non-zero flux.

Finally, before starting a depth discussion about the PBTE and its solutions, we find it worth commenting that although it has been widely used to model lots of materials, PBTE is known to break down for some systems, specifically when branch spacing is lower than the phonon linewidths. For instance, this happens for large energy broadenings caused by strong phonon interactions (i.e.

3. Thermal transport modeling

high anharmonicity), or in large unit cells [145]. In those cases (e.g. lanthanum zirconate [146]) one needs to rely on alternatives like, the Wigner-Boltzmann framework derived by Simoncelli *et al.* [145, 146].

3.2.1. Approaches to collision term

Considering only the three-phonon and the isotopic scattering, the collision term of Eq. 3.5 can be defined as:

$$\begin{aligned} \left. \frac{\partial n_i(\mathbf{r}, t)}{\partial t} \right|_{\text{collision}} = & - \sum_{jk} P_{i+j \rightarrow k}^{3\text{ph}} [n_i n_j (n_k + 1) - \\ & (n_i + 1)(n_j + 1)n_k] - \frac{1}{2} \sum_{jk} P_{i \rightarrow j+k}^{3\text{ph}} [n_i (n_j + 1)(n_k + 1) - (n_i + 1)n_j n_k] - \\ & \sum_j P_{i \rightarrow j}^{\text{iso}} [n_i (n_j + 1) - (n_i + 1)n_j], \quad (3.9) \end{aligned}$$

where $P_{\text{init} \rightarrow \text{final}}^{\text{mechanism}}$ indicates the intrinsic scattering rate (i.e. the one without occupation factors) from a set of initial states to a set of final states due to a given mechanism, indicating “iso” isotopic, “3ph” three-phonon processes (see Subsections 2.2.1 and 2.3), and i, j, k, \dots state for phonon modes. Moreover, we recall that within semiclassical theory scattering is strictly local. From Eq. 3.9 it follows that collision is indeed a complex nonlinear operator, complicating the solution of the PBTE.

The easiest approach to simplify Eq. 3.9 into a more tractable form is to linearize it. To do so, the phonon distribution is split between a reference equilibrium distribution (i.e. a Bose-Einstein one), n_i^0 , and a deviation from it, n_i^d , so $n_i = n_i^0 + n_i^d$. If one considers only small deviations from the equilibrium part of the distribution ($n_i^d \ll n_i^0$), one can disregard any non-linear term with respect

3. Thermal transport modeling

to the deviations. Therefore, Eq. 3.9 reduces to

$$\left. \frac{\partial n_i^d}{\partial t} \right|_{\text{collision}} = A_{ij} n_j^d \quad (3.10)$$

where

$$\begin{aligned} A_{ij} = & \sum_{sml} P_{s+m \rightarrow l}^{\text{3ph}} [(n_l^0 - n_s^0) \delta_{is} \delta_{jm} + \\ & (n_s^0 + n_m^0 + 1) \delta_{is} \delta_{jl} + (n_l^0 - n_m^0) \delta_{is} \delta_{ji}] \\ & + \frac{1}{2} \sum_{sml} P_{s \rightarrow n+l}^{\text{3ph}} [(n_l^0 - n_s^0) \delta_{is} \delta_{jm} + (n_m^0 - n_s^0) \delta_{is} \delta_{jl} \\ & - (n_l^0 + n_m^0 + 1) \delta_{is} \delta_{ji}] + \\ & \sum_{sm} P_{s \rightarrow m}^{\text{iso}} [\delta_{is} \delta_{jm} - \delta_{is} \delta_{ji}] . \quad (3.11) \end{aligned}$$

where we have used detailed balance [i.e. $\left. \frac{\partial n_i^0}{\partial t} \right|_{\text{collision}} = 0$, so for each individual process like three-phonon absorption we have that $n_i^0(n_j^0 + 1)(n_k^0 + 1) = n_i^0(n_j^0 + 1)(n_k^0 + 1)$].

This last equation is still quite complex, thus it is customarily simplified into a more friendly form, using the the so-called (single mode) relaxation time approximation (SMRTA or RTA), where it is assumed that each phonon mode relaxes to equilibrium independently. This translates to supposing that only the involved mode (i) is slightly out of equilibrium while the other modes remain in equilibrium (i.e. $n_j = n_j^0 \forall j \neq i$). Hence, Eq. 3.10 reduces to

$$\begin{aligned} \left. \frac{\partial n_i(\mathbf{r}, t)}{\partial t} \right|_{\text{collision}} = & - \sum_{jk} P_{i+j \rightarrow k}^{\text{3ph}} (n_j^0 - n_k^0) n_i^d - \\ & \frac{1}{2} \sum_{jk} P_{i \rightarrow j+k}^{\text{3ph}} (n_k^0 + n_j^0 + 1) n_i^d - \sum_j P_{i \rightarrow j}^{\text{iso}} n_i^d = - \frac{n_i^d}{\tau_i}, \quad (3.12) \end{aligned}$$

3. Thermal transport modeling

where we have defined the mode RTA lifetime, τ_i , as

$$\tau_i = \left[\sum_{jk} P_{i+j \rightarrow k}^{3\text{ph}} (n_j^0 - n_k^0) + \frac{1}{2} \sum_{jk} P_{i \rightarrow j+k}^{3\text{ph}} (n_k^0 + n_j^0 + 1) + \sum_j P_{i \rightarrow j}^{\text{iso}} \right]^{-1}. \quad (3.13)$$

The simplicity of this approach, which fully decouples the phonon modes (i.e. the linear operator is diagonal, indeed it is defined in terms of the full linearized operator as $A_{ij}\delta_{ij}$), has taken the RTA to a prominent place in the resolution of the PBTE, describing prototypical semiconductors like silicon with high accuracy [46]. However, it is easy to see that such a collision operator does not conserve heat flux to any degree, deeming all the three-phonon processes as resistive. Such a flaw causes the RTA to fail for cases in which the processes that are not directly resistive but indirectly so through population redistribution, are dominant or of similar importance as resistive ones. This is the case of all materials for low enough temperatures or materials like diamond and 2D materials, for which the RTA has been observed to provide quite a poor description of thermal properties [44, 139, 147]. Furthermore, we can see that the RTA scattering operator violates energy conservation. For instance, let us imagine an isolated homogeneous system well described by an equilibrium distribution at 300.1 K; if one sets the reference distribution at 300 K and applies the RTA-scattering operator to these “deviations” it would incorrectly lead to its disappearance, effectively cooling down the isolated system. Therefore, an RTA-operator-based solution of the PBTE requires additional conditions to satisfy the energy conservation constraint.

Therefore, for a proper description of the scattering working even in materials dominated by the non-resistive processes, we need to go beyond the RTA (i.e. return to Eq. 3.10). Contrary to its RTA counterpart, A_{ij} conserves energy without

3. Thermal transport modeling

any addition to the formalism, as long as the constitutive processes conserve it. Additionally, because it allows for the redistribution of the phonon population, scattering does not necessarily fully destroy heat flux but allows for some degree of inertia even under the effect of a significant scattering.

Finally, we find it worth mentioning differences regarding hydrodynamic effects for both approaches. Despite deeming all processes resistive, i.e. flux randomizing, this does not mean that the RTA does not permit any degree of inertia, namely hydrodynamics, but that it heavily underestimates it. Indeed, in materials/situations for which the RTA yields poor results, the hydrodynamic features are expected to be strong, as due to a large number of non-resistive processes the phonon distribution can keep its inertia over large distances [139, 140]. Therefore, the beyond-RTA operator is necessary to obtain an accurate description of those hydrodynamic features, in those materials and/or situations.

3.2.1.1. *Four and higher-order phonon processes*

Experimentally, for most materials, thermal conductivity temperature dependence is very well captured by $(aT + bT^2)^{-1}$. Such a linear term is due to three-phonon processes, while the quadratic behavior is due to the higher-order processes. For common materials is observed that $a \gg b$ up to higher temperatures, to the point that $\kappa(T)$ is very well described by only $\frac{1}{aT}$. Certainly, this indicates from an experimental point of view that in most materials at intermediate or low temperatures, three-phonon processes are enough to obtain accurate thermal properties [148, 149].

Although this is the most common behavior, there are cases in which three-phonon processes are highly restricted because of large gaps in the spectrum and/or bunched bands [150]. However, those features do not restrict the allowed four-phonon processes, increasing in those cases their contribution to the thermal

3. Thermal transport modeling

properties to a significant level, even at room temperature.

Therefore, it is safe to suppose that for most materials, in which the commented features are not important, especially the large gap, the four-phonon processes can be safely ignored.

3.2.2. Solution for the homogeneous system with an applied thermal gradient

Maybe, the most simple system that can be described through the PBTE is a homogeneous system under an applied thermal gradient. Definitely, the solution of the PBTE in this system is of great interest as it allows obtaining the thermal conductivity and non-local lengths from a microscopic perspective. The RTA-PBTE for those systems reduces to

$$\frac{\partial n_i^0}{\partial T} \mathbf{v}_i \cdot \nabla T = -\frac{n_i^d}{\tau_i}, \quad (3.14)$$

so that $n_i^d = -\tau_i \frac{\partial n_i^0}{\partial T} \mathbf{v}_i \cdot \nabla T$ and the heat flux is therefore

$$\mathbf{J} = -\frac{1}{N_q V_{uc}} \sum_i \mathbf{v}_i \hbar \omega_i \left(\tau_i \frac{\partial n_i^0}{\partial T} \mathbf{v}_i \cdot \nabla T \right). \quad (3.15)$$

Thus, through Fourier's law κ^{RTA} is defined as

$$\kappa^{\text{RTA}} = \frac{1}{N_q V_{uc}} \sum_i \mathbf{v}_i \otimes \mathbf{v}_i \hbar \omega_i \tau_i \frac{\partial n_i^0}{\partial T} \quad (3.16)$$

Moreover, by projecting the isotropic RTA-PBTE over energy and quasimomenta, and by expanding phonon distribution on macroscopic variables like the flux, it is

3. Thermal transport modeling

possible to obtain a microscopic description of the non-local length [143]

$$\ell_{\text{iso}}^{\text{RTA}} = \frac{1}{5} \frac{\int_{BZ} \hbar q_i v_i^2 \tau_i^2 \frac{\partial n_i^0}{\partial T} di}{\int_{BZ} \hbar q_i v_i \frac{\partial n_i^0}{\partial T} di}, \quad (3.17)$$

where q_i is the wave vector of the i mode in the first Brillouin Zone.

On the other hand, for the full linearized operator PBTE we have

$$\frac{\partial n_i^0}{\partial T} \mathbf{v}_i \cdot \nabla T = \sum_j A_{ij} n_j^d, \quad (3.18)$$

the solution of which is

$$n_i^d = -\tau_i \frac{\partial n_i^0}{\partial T} \mathbf{v}_i \cdot \nabla T + \sum_{j \neq i} \tau_i A_{ij} n_j^d, \quad (3.19)$$

where we have used that $A_{ii} = -\tau_i^{-1}$. Therefore, the solution of Eq. 3.19 depends on itself making its direct solution unpractical. The usual approach, originally developed by Omini and Sparavigna[41], is to iteratively solve it starting from the RTA solution. Omini's approach slightly differs from ours, as they have expanded the phonon distribution as linear function of the applied field (∇T), $n_i = n_i^0 + \frac{\partial n_i^0}{\partial(\hbar\omega_i)} \mathbf{F}_i \cdot \nabla T$ where \mathbf{F}_i is a deviation function. Therefore, the PBTE can be recast in terms of the α^{th} -component of the deviation function [98] as

$$\begin{aligned} \mathbf{v}_{i\alpha} \frac{\partial n_i^0}{\partial T} &= \sum_{jk} P_{i+j \rightarrow k}^{\text{3ph}} [n_i^0 n_j^0 (n_k^0 + 1)] (\mathbf{F}_{k\alpha} - \mathbf{F}_{j\alpha} - \mathbf{F}_{i\alpha}) + \\ &\quad \frac{1}{2} \sum_{jk} P_{i \rightarrow j+k}^{\text{3ph}} [n_i^0 (n_j^0 + 1) (n_k^0 + 1)] (\mathbf{F}_{k\alpha} + \mathbf{F}_{j\alpha} - \mathbf{F}_{i\alpha}) + \\ &\quad \sum_j P_{i \rightarrow j}^{\text{iso}} [n_i^0 (n_j^0 + 1)] (\mathbf{F}_{j\alpha} - \mathbf{F}_{i\alpha}), \end{aligned} \quad (3.20)$$

3. Thermal transport modeling

so $\mathbf{F}_{i\alpha}$ can be obtained through the solution of

$$\begin{aligned} \mathbf{F}_{i\alpha} = & \frac{\hbar\omega_i \mathbf{v}_{i\alpha} \tau_i}{T} + \frac{\tau_i}{n_i^0(n_i^0 + 1)} \left[\sum_{jk} P_{i+j \rightarrow k}^{3\text{ph}} [n_i^0 n_j^0 (n_k^0 + 1)] (\mathbf{F}_{k\alpha} - \mathbf{F}_{j\alpha}) + \right. \\ & \frac{1}{2} \sum_{jk} P_{i \rightarrow j+k}^{3\text{ph}} [n_i^0 (n_j^0 + 1) (n_k^0 + 1)] (\mathbf{F}_{k\alpha} + \mathbf{F}_{j\alpha}) + \\ & \left. \sum_j P_{i \rightarrow j}^{\text{iso}} [n_i^0 (n_j^0 + 1)] \mathbf{F}_{j\alpha} \right]. \quad (3.21) \end{aligned}$$

From the computational point of view there are two ways to solve Eq. 3.21, the first is to use iterative procedure developed by Omini and Sparavigna [41] by using the RTA solution ($\mathbf{F}_{i\alpha}^0 = \frac{\hbar\omega_i \mathbf{v}_{i\alpha} \tau_i}{T}$) as the 0th-iteration and iterating until convergence. However, as discussed by Fugallo *et al.* [120] its convergence is not ensured. An alternative solution is to notice that Eq. 3.21 is a linear system with $\mathbf{F}_{i\alpha}$ as its unknowns, thus it can be iteratively solved with variational solvers with RTA as initial guess [120]. Moreover, this variational methodology has better stability than Omini's one, providing solutions even when the former fails to converge.

Analogously to the RTA one can define the κ as a function of the deviation functions:

$$\kappa_{\alpha\beta} = \frac{1}{k_B V_{\text{uc}} N_q T^2} \sum_{\lambda} n_i^0 (n_i^0 + 1) (\hbar\omega_i)^2 \mathbf{v}_{i\alpha} \mathbf{F}_{i\beta}. \quad (3.22)$$

where k_B is the Boltzmann constant.

Consequently, it becomes possible to obtain thermal properties through those equations either within or beyond the RTA.

Although the iterative solution of the PBTE is by far the most common way to go beyond the RTA in the homogeneous case, there are alternative methods to solve the PBTE and obtain the κ . Here, we shortly review some of them:

3. Thermal transport modeling

- *Kinetic Collective Model*: This model, which generalizes the GK framework, is based on two opposite limiting behaviors [151]. The kinetic regime in which \mathcal{U} processes are dominant so that modes are completely unmixed. On the contrary, we find the collective regime in which \mathcal{N} processes are important so that they mix modes making distribution relax globally. Finally, the κ is calculated as a weighted mix of both regimes.
- *Relaxons*: The PBTE is solved by recasting it in terms of relaxons, i.e. the eigenvectors of the scattering operator representing collective phonon excitations. Each of these relaxons represents a deviational distribution of several phonon modes so that the scattering operator eigenvalues describe how the phonon distribution relaxes to equilibrium [152].
- *Direct solution of the LBTE*: The homogeneous PBTE is directly solved by pseudo-inverting the scattering operator in the Fourier space [153]. In addition to static κ this methodology also provides the frequency-dependent κ . The main drawback of this method is the computational cost of the pseudo-inversion of the scattering operator.

3.2.3. Size effects and solution for highly symmetric systems

Until now we have only tackled the PBTE for infinite systems, nevertheless the treatment of boundaries becomes essential to describe thermal transport in real devices, especially at the nanoscale. The most basic approach to get a grasp of boundary effects is to consider that phonons with large mean free paths (i.e. $|\mathbf{v}_i|\tau_i$) than the system's characteristic length (L) do not contribute to thermal properties as they are blocked by boundaries. Thus we define the cumulative quantities as a function of the phonon mean free path, for instance, the cumulative

3. Thermal transport modeling

thermal conductivity is

$$\kappa_{\text{cum}}(L) = \frac{1}{N_{\text{q}} V_{\text{uc}}} \sum_{\{i : \tau_i |\mathbf{v}_i| < L\}} \mathbf{v}_i \otimes \mathbf{v}_i \hbar \omega_i \tau_i \frac{\partial n_i^0}{\partial T}. \quad (3.23)$$

Although Eq. 3.23 provides an approximate idea of the size effects over thermal properties, the effect of boundaries over the phonons cannot be an abrupt cut-off but some sort of partial suppression depending on their mean free paths. Moreover, these cumulative curves do not take into account the system's geometry which might lead to an erroneous description for some modes; for example, given an infinite nanowire of radius R , the cumulative function will predict all the phonon modes with mean free paths larger than R to be fully suppressed, even those with a velocity parallel to the unbound axis of the nanowire. A more refined approach to the boundary scattering is to consider an extra term in the scattering rate coming from the interaction with boundaries, and the use the Mathiessen's rule to obtain the total rate [99, 107]:

$$\tau_{i,\text{total}}^{-1} = \tau_i^{-1} + \frac{|\mathbf{v}_i|}{L(p)} \quad (3.24)$$

where L is the system's effective characteristic length, depending on the diffusivity of the boundaries [107]

$$L(p) = \frac{1+p}{1-p} L, \quad (3.25)$$

where p ranges from 0 for purely diffusive boundaries to 1 for fully reflective ones. Although this model is an improvement to the cumulative one, as it does not consider an abrupt cut-off but a smooth one, it is still incapable of considering system's geometry. Moreover, Wang *et al.* [154] demonstrated Mathiessen's rule breakdown for boundary scattering in 2D ribbons, thus making this solution inadequate for those systems.

Indeed, the appropriate way to tackle boundaries is to go beyond the homoge-

3. Thermal transport modeling

neous case, as the inclusion of physical boundaries breaks the crystal symmetry, and hence the homogeneity. Consequently, it becomes necessary to resort to the non-homogeneous PBTE,

$$\frac{\partial n_i^0}{\partial T} \mathbf{v}_i \cdot \nabla T(\mathbf{r}) + \mathbf{v}_i \cdot \nabla n_i^d(\mathbf{r}) = \sum_j A_{ij} n_j^d(\mathbf{r}), \quad (3.26)$$

with the appropriate boundary condition for phonons arriving to a boundary at \mathbf{r}_B ,

$$\left\{ n_j^d(\mathbf{r}_B) = \frac{1}{N_q} \sum_{\{i: \mathbf{v}_i \cdot \hat{\mathbf{e}}_\perp^{in} > 0\}} P_{i \rightarrow j}^B n_i^d(\mathbf{r}_B) : \mathbf{v}_j \cdot \hat{\mathbf{e}}_\perp^{in} < 0 \right\}. \quad (3.27)$$

Here, $P_{j \rightarrow i}^B$ is the probability of a phonon in mode i to be scattered to j mode and $\hat{\mathbf{e}}_\perp^{in}$ is a the normal vector to boundary pointing into the material. This last equation can be further simplified by noting that from all phonons arriving to the boundary, only a fraction p is specularly reflected whilst the rest are diffusively scattered, so that in the steady-state they will only contribute to the equilibrium distribution [39]. In other words, a perfect diffuse boundary absorbs all phonons arriving to it, which are then reemitted from such a boundary at rate and distribution depending on the temperature of that boundary [155]. This allows to simplify boundary scattering to

$$\left\{ n_j^d(\mathbf{r}_B) = p n_i^d(\mathbf{r}_B) : \mathbf{v}_j \cdot \hat{\mathbf{e}}_\perp^{in} < 0 \text{ and } \mathbf{v}_i = \mathbf{v}_j - 2(\mathbf{v}_j \cdot \hat{\mathbf{e}}_\perp^{in}) \hat{\mathbf{e}}_\perp^{in} \right\}. \quad (3.28)$$

Thus, then we can solve Eq. 3.26 under the appropriate boundary conditions, embodied in Eq. 3.28 arriving to [39, 40]

$$n_i^0(\mathbf{r}) = \tau_i \left[-\frac{\partial n_i^0}{\partial T} \mathbf{v}_i \cdot \nabla T(\mathbf{r}) + \sum_{j \neq i} A_{ij} n_j^d \right] \left(1 - e^{-\frac{|\mathbf{r} - \mathbf{r}_B|}{\tau_i \mathbf{v}_B}} \right), \quad (3.29)$$

3. Thermal transport modeling

where \mathbf{v}_B is the magnitude of the component of the velocity normal to the boundary, and we have further supposed fully diffusive boundaries (i.e. $p = 0$). Despite in principle the solution of the Eq. 3.29 provides an accurate and correct description of size effects, its solution would require a discretization in space. This is from a computational point of view impractical, owing to the enormous required memory resources and computational time for its solution. However, for highly symmetric systems, like nanowires or nanoribbons, it is possible to obtain an approximate solution by using averages [40]. In such a way, it becomes possible to obtain an effective thermal conductivity (κ_{nano}) along the periodic direction by simply introducing suppression factors in the lifetimes ($\tau_i^{\text{nano}} = \tau_i S_i^{\text{nano}}$) and then iteratively solving the PBTE like in the bulk case. Those suppression factors are calculated as the mean of the exponential factors in Eq. 3.29 over the cross section [40]:

$$S_i^{\text{nano}} = \frac{1}{A_c} \int_{A_c} 1 - e^{-\frac{|\mathbf{r}-\mathbf{r}_B|}{\tau_i \mathbf{v}_B}} dA \quad (3.30)$$

where A_c is the area cross-section normal to system periodic direction. For nanoribbons contained in the XY plane, the suppression factors (S_i^{nr}) are calculated to be:

$$S_i^{\text{nr}} = 1 + \left[\frac{M_i^{\text{nr}}}{L} \left(e^{-\frac{L}{M_i^{\text{nr}}}} - 1 \right) \right] \quad (3.31)$$

$$M_i^{\text{nr}} = \left| \left[\begin{pmatrix} \mathbf{u}_y & \mathbf{u}_x \\ -\mathbf{u}_x & \mathbf{u}_y \end{pmatrix}^{-1} \mathbf{v}_i \right] \cdot \mathbf{e}_1 \right| \tau_i, \quad (3.32)$$

where \mathbf{u} is a normalized vector pointing along the unbounded direction of the system, L is the nanoribbon width and \mathbf{e}_1 is the first column of identity matrix. In the case of cylindrical nanowires, the suppression factors (S_λ^{nw}) can be calculated, analogously to the case nanoribbons, by evaluating the integral in modified

3. Thermal transport modeling

cylindrical coordinates with the z -axis pointing to the periodic direction, yielding:

$$S_i^{\text{nw}} = 1 - \frac{2M_i^{\text{nw}}}{R^2} \left[M_i^{\text{nw}} \left(e^{-\frac{R}{M_i^{\text{nw}}}} - 1 \right) + R \right] \quad (3.33)$$

$$M_i^{\text{nw}} = \|\mathbf{v}_i - (\mathbf{v}_i \cdot \mathbf{u})\mathbf{u}\| \tau_i, \quad (3.34)$$

where R is the nanowire radius.

As opposed to the previous methodologies this one allows for the correct description of the boundary effect, depending on each phonon projected mean free path over a vector normal to boundaries, while taking into account system geometry. For instance, for nanoribbons we have the proper geometrical limits:

$\lim_{L \rightarrow +\infty} S_i^{\text{nr}} = 1$, $\lim_{M_i^{\text{nr}} \rightarrow 0} S_i^{\text{nr}} = 1$ and $\lim_{M_i^{\text{nr}} \rightarrow +\infty} S_i^{\text{nr}} = 0$, which correspond to the bulk, the mode propagating parallel to a periodic-direction, and the fully incident mode with infinite mean free path limits, respectively.

3.2.4. General solution of the PBTE for arbitrary geometries and boundary conditions

We now seek the general solution of the PBTE in both space and time, not only valid for highly symmetric systems but for arbitrary geometries, as well as all types of boundary conditions not only limited to diffusive borders or gradients but isothermal reservoirs, initial temperature profiles, and so on. Solving such a general problem is not an easy task, as the PBTE (see Eq. 3.5) is a six-dimensional time-dependent problem, thus suffering from the so-called “curse of dimensionality”. Therefore, any attempt of directly/or iteratively solving it is rendered impractical due to the excessive memory resources and computation time required to solve it [40, 47, 87]. An alternative and easier approach is to generate phonons accordingly to sources (isothermal boundaries, initial temperature profiles,...) and simulate their trajectories in time and space inside the given system, whilst they

3. Thermal transport modeling

interact with boundaries, interfaces, other phonons, or mass disorders; obtaining through the summation of all the trajectories, the time and space evolution of the distribution function. As phonon generation and scattering outcome are fully based on random numbers, those methods of solving the PBTE are known collectively as Monte Carlo methods [87]. For a more in-depth discussion on the subject, we direct the reader to Chapter 4, where the use of Monte Carlo methods for the resolution of PBTE is discussed in detail.

3.2.5. Electron-phonon coupling and thermoelectric properties

Although we have ignored it until now, the effect of the electron-phonon scattering in the thermal properties might be essential for some materials, specially in determining of the thermoelectric parameters [156–158]. Introducing the electron-phonon scattering adds a new term into the PBTE collision term

$\left(\frac{\partial n_i}{\partial t}\right)\Big|_{\text{e-ph, collision}} = -2 \sum_{\Pi\Lambda} P_{\Pi+i\rightarrow\Lambda}^{\text{e-ph}} [f_{\Pi} n_i (1 - f_{\Lambda}) - (1 - f_{\Lambda}) (n_i + 1) f_{\Lambda}]$, where 2 is due to spin degeneracy, “ $e - ph$ ” stands for the electron-phonon interaction, $P_{\Pi+i\rightarrow\Lambda}^{\text{e-ph}}$ is the intrinsic transition rate due to the electron-phonon interaction, $\Lambda, \Pi \dots$ indicate electronic states and f is the electron distribution function); which when linearized and inserted into Eq. 3.11 leads to:

$$\frac{\partial n_i^d}{\partial t}\Big|_{\text{collision}} = A_{ij} n_j^d + B_{ij} n_j^d + C_{i\Omega} f_{\Omega}^d \quad (3.35)$$

where

$$B_{ij} = 2 \sum_{\Pi s \Lambda} P_{\Pi+s\rightarrow\Lambda}^{\text{e-ph}} (f_{\Lambda}^0 - f_{\Pi}^0) \delta_{is} \delta_{ji} \quad (3.36)$$

3. Thermal transport modeling

and

$$C_{i\Omega} = 2 \sum_{\Pi s \Lambda} P_{\Pi+s \rightarrow \Lambda}^{\text{e-ph}} [(-f_{\Lambda}^0 - n_s^0) \delta_{is} \delta_{\Omega \Pi} + (-f_{\Pi}^0 + n_{\Lambda}^0 + 1) \delta_{is} \delta_{\Omega \Lambda}], \quad (3.37)$$

where f_{Λ}^0 is the equilibrium part equal to a Fermi-Dirac distribution at system's reference temperature and chemical potential.

Thus, the operator mixes both electron and phonon distribution functions through the so-called drag terms ($C_{i\Omega}$). Consequently, we need to couple the PBTE to its electronic counterpart (BTE),

$$\frac{\partial f_{\Pi}(r, t)}{\partial t} + \mathbf{v}_{\Pi} \cdot \nabla_r f_{\Pi}(r, t) - e \mathbf{E} \cdot \nabla_q f_{\Pi}(r, t) = \left. \frac{\partial f_{\Pi}(r, t)}{\partial t} \right|_{\text{collision}}, \quad (3.38)$$

$$\begin{aligned} \left. \frac{\partial f_{\Pi}(r, t)}{\partial t} \right|_{\text{collision}} = & - \sum_{i \Lambda} P_{\Pi+i \rightarrow \Lambda}^{\text{e-ph}} [f_{\Pi} n_i (1 - f_{\Lambda}) - (1 - f_{\Lambda}) (n_i + 1) f_{\Lambda}] - \\ & \sum_{i \Lambda} P_{\Pi \rightarrow \Lambda+i}^{\text{e-ph}} [f_{\Pi} (n_i + 1) (1 - f_{\Lambda}) - (1 - f_{\Lambda}) n_i f_{\Lambda}], \end{aligned} \quad (3.39)$$

by linearizing this last term we obtain:

$$\left. \frac{\partial f_{\Pi}^d}{\partial t} \right|_{\text{collision}} = D_{\Pi \Omega} f_{\Omega}^d + M_{\Pi j} n_j^d \quad (3.40)$$

where

$$\begin{aligned} D_{\Pi \Omega} = & \sum_{\Upsilon s \Lambda} P_{\Upsilon \rightarrow \Lambda+s}^{\text{e-ph}} [(f_{\Lambda}^0 - n_s^0 - 1) \delta_{\Upsilon \Pi} \delta_{\Omega \Pi} + [(f_{\Upsilon}^0 + n_s^0) \delta_{\Upsilon \Pi} \delta_{\Omega \Lambda}] + \\ & \sum_{\Upsilon s \Lambda} P_{\Upsilon+s \rightarrow \Lambda}^{\text{e-ph}} [-(f_{\Lambda}^0 + n_s^0) \delta_{\Upsilon \Pi} \delta_{\Omega \Pi} + (-f_{\Upsilon}^0 + n_s^0 + 1) \delta_{\Upsilon \Pi} \delta_{\Omega \Lambda}] \end{aligned} \quad (3.41)$$

3. Thermal transport modeling

and

$$M_{\Pi j} = \sum_{\Omega s \Lambda} P_{\Omega \rightarrow \Lambda+s}^{\text{e-ph}} (f_{\Lambda}^0 - f_{\Omega}^0) \delta_{\Pi \Omega} \delta_{js} + \sum_{\Omega s \Lambda} P_{\Omega+s \rightarrow \Lambda}^{\text{e-ph}} (f_{\Lambda}^0 - f_{\Omega}^0) \delta_{\Pi \Omega} \delta_{js}. \quad (3.42)$$

Consequently, in order to describe a material in which both electrons and phonons contribute to the desired property, as it can be the case of Seebeck coefficient affected by the phonon drag [156, 157], one needs to solve the coupled linearized BTE-PBTE system, i.e.

$$\begin{pmatrix} \frac{\partial n_i(\mathbf{r}, t)}{\partial t} + \mathbf{v}_i \cdot \nabla_{\mathbf{r}} n_i(\mathbf{r}, t) \\ \frac{\partial f_{\Pi}(\mathbf{r}, t)}{\partial t} + \mathbf{v}_i \cdot \nabla_{\mathbf{r}} f_{\Pi}(\mathbf{r}, t) - e \mathbf{E} \nabla_{\mathbf{q}} f_{\Pi}(\mathbf{r}, t) \end{pmatrix} = \begin{pmatrix} A_{ij} + B_{ij} & C_{i\Omega} \\ M_{\Pi j} & D_{\Pi \Omega} \end{pmatrix} \begin{pmatrix} n_i^d \\ f_{\Omega}^d \end{pmatrix} \quad (3.43)$$

3.2.5.1. Solution of the homogeneous coupled phonon-electron BTE

If the solution of PBTE or BTE is already complex, the solution of Eq. 3.43 is an Herculean task of such complexity that the examples in the literature are scarce, and are often limited to simple systems (e.g. bulk under applied homogeneous electric field and thermal gradient [158], or out-of-equilibrium isolated systems [159]) or have the coupling simplified to gross quantities [160]. Despite its limitations, the former solution is interesting as it provides a microscopic description of all thermoelectric variables with the appropriate drag terms. In their derivation, Protik *et al.* extended the iterative approach given in 3.2 to the coupled electron-phonon system; starting from deviation expanded as a function

3. Thermal transport modeling

of the applied electric field (\mathbf{E}) and temperature gradient:

$$f_{\Pi} = f_{\Pi}^0 - \frac{f_{\Pi}^0(1 - f_{\Pi}^0)}{k_B T} (\nabla T \cdot \mathbf{H}_{\Pi} + \mathbf{E} \cdot \mathbf{J}_{\Pi}) \quad (3.44)$$

$$n_i = n_i^0 - \frac{n_i^0(n_i^0 + 1)}{k_B T} (\nabla T \cdot \mathbf{F}_i + \mathbf{E} \cdot \mathbf{G}_i) \quad (3.45)$$

where $\mathbf{H}_{\Pi}(\mathbf{F}_i)$ and $\mathbf{J}_{\Pi}(\mathbf{G}_i)$ are the electron (phonon) deviation functions due to applied thermal gradient and electric fields, respectively. By inserting those inside the homogeneous PBTE and BTE one arrives to a set of equation for all α -components of each of the deviation functions:

$$\begin{aligned} \mathbf{F}_{i\alpha} = & \frac{\hbar\omega_i \mathbf{V}_{i\alpha} \tau_i}{T} + \frac{\tau_i}{n_i^0(n_i^0 + 1)} \left[\sum_{jk} P_{i+j \rightarrow k}^{3\text{ph}} [n_i^0 n_j^0 (n_k^0 + 1)] (\mathbf{F}_{k\alpha} - \mathbf{F}_{j\alpha}) + \right. \\ & \left. \frac{1}{2} \sum_{jk} P_{i \rightarrow j+k}^{3\text{ph}} [n_i^0 (n_j^0 + 1) (n_k^0 + 1)] (\mathbf{F}_{k\alpha} + \mathbf{F}_{j\alpha}) + \right. \\ & \left. \sum_j P_{i \rightarrow j}^{\text{iso}} [n_i^0 (n_j^0 + 1)] \mathbf{F}_{j\alpha} + 2 \sum_{\Pi\Lambda} P_{\Pi+i \rightarrow \Lambda}^{\text{e-ph}} [f_{\Pi}^0 n_i^0 (1 - f_{\Lambda}^0)] (\mathbf{H}_{\Lambda} - \mathbf{H}_{\Pi}) \right], \end{aligned} \quad (3.46)$$

$$\begin{aligned} \mathbf{G}_{i\alpha} = & \frac{\tau_i}{n_i^0(n_i^0 + 1)} \left[\sum_{jk} P_{i+j \rightarrow k}^{3\text{ph}} [n_i^0 n_j^0 (n_k^0 + 1)] (\mathbf{G}_{k\alpha} - \mathbf{G}_{j\alpha}) + \right. \\ & \left. \frac{1}{2} \sum_{jk} P_{i \rightarrow j+k}^{3\text{ph}} [n_i^0 (n_j^0 + 1) (n_k^0 + 1)] (\mathbf{G}_{k\alpha} + \mathbf{G}_{j\alpha}) + \right. \\ & \left. \sum_j P_{i \rightarrow j}^{\text{iso}} [n_i^0 (n_j^0 + 1)] \mathbf{G}_{j\alpha} + 2 \sum_{\Pi\Lambda} P_{\Pi+i \rightarrow \Lambda}^{\text{e-ph}} [f_{\Pi}^0 n_i^0 (1 - f_{\Lambda}^0)] (\mathbf{J}_{\Lambda} - \mathbf{J}_{\Pi}) \right], \end{aligned} \quad (3.47)$$

3. Thermal transport modeling

$$\begin{aligned} \mathbf{H}_{\Pi\alpha} = & \frac{\tau_{\Pi}(\varepsilon_{\Pi} - \mu)\mathbf{v}_{\Pi\alpha}}{T} + \frac{\tau_{\Pi}}{f_{\Pi}^0(1 - f_{\Pi}^0)} \left[\sum_{i\Lambda} P_{\Pi+i\rightarrow\Lambda}^{\text{e-ph}} [f_{\Pi}^0 n_i^0 (1 - f_{\Lambda}^0)] \mathbf{H}_{\Lambda\alpha} + \right. \\ & \sum_{i\Lambda} P_{\Pi\rightarrow\Lambda+s}^{\text{e-ph}} [f_{\Pi}^0 (n_i^0 + 1)(1 - f_{\Lambda}^0)] \mathbf{H}_{\Lambda\alpha} + \sum_{i\Lambda} P_{\Pi\rightarrow\Lambda+i}^{\text{e-ph}} [f_{\Pi}^0 (n_i^0 + 1)(1 - f_{\Lambda}^0)] \mathbf{F}_{i\alpha} - \\ & \left. \sum_{i\Lambda} P_{\Pi+i\rightarrow\Lambda}^{\text{e-ph}} [f_{\Pi}^0 n_i^0 (1 - f_{\Lambda}^0)] \mathbf{F}_{i\alpha} \right], \quad (3.48) \end{aligned}$$

and

$$\begin{aligned} \mathbf{J}_{\Pi\alpha} = & e\tau_{\Pi}(\varepsilon_{\Pi} - \mu)\mathbf{v}_{\Pi\alpha} + \frac{\tau_{\Pi}}{f_{\Pi}^0(1 - f_{\Pi}^0)} \left[\sum_{i\Lambda} P_{\Pi+i\rightarrow\Lambda}^{\text{e-ph}} [f_{\Pi}^0 n_i^0 (1 - f_{\Lambda}^0)] \mathbf{J}_{\Lambda\alpha} + \right. \\ & \sum_{i\Lambda} P_{\Pi\rightarrow\Lambda+i}^{\text{e-ph}} [f_{\Pi}^0 (n_i^0 + 1)(1 - f_{\Lambda}^0)] \mathbf{J}_{\Lambda\alpha} + \sum_{i\Lambda} P_{\Pi\rightarrow\Lambda+i}^{\text{e-ph}} [f_{\Pi}^0 (n_i^0 + 1)(1 - f_{\Lambda}^0)] \mathbf{G}_{i\alpha} - \\ & \left. \sum_{i\Lambda} P_{\Pi+i\rightarrow\Lambda}^{\text{e-ph}} [f_{\Pi}^0 n_i^0 (1 - f_{\Lambda}^0)] \mathbf{G}_{i\alpha} \right]; \quad (3.49) \end{aligned}$$

where ε_{Π} is the energy of the Π electronic state, μ is the chemical potential and $\tau_{\Pi} = f_{\Pi}^0(1 - f_{\Pi}^0) [\sum_{i\Lambda} P_{\Pi+i\rightarrow\Lambda}^{\text{e-ph}} f_{\Pi}^0 n_i^0 (1 - f_{\Lambda}^0) + \sum_{i\Lambda} P_{\Pi\rightarrow\Lambda}^{\text{e-ph}} f_{\Pi}(n_i + 1)(1 - f_{\Lambda})]^{-1}$ is the RTA lifetime of the Π electronic state.

This set of equations can be solved similarly to the homogeneous PBTE (see Sec. 3.2.2). Then, the thermoelectric properties can be defined in terms of those

3. Thermal transport modeling

deviations [158] as:

$$\sigma = \frac{2e}{N_k V_{uc} k_B T} \sum_{\Pi} f_{\Pi}^0 (1 - f_{\Pi}^0) \mathbf{v}_{\Pi} \otimes \mathbf{J}_{\Pi} \quad (3.50)$$

$$\sigma S = -\frac{2e}{N_k V_{uc} k_B T} \sum_{\Pi} f_{\Pi}^0 (1 - f_{\Pi}^0) \mathbf{v}_{\Pi} \otimes \mathbf{H}_{\Pi} \quad (3.51)$$

$$\alpha_{el} = -\frac{2}{N_k V_{uc} k_B T} \sum_{\Pi} (\varepsilon_{\Pi} - \mu) f_{\Pi}^0 (1 - f_{\Pi}^0) \mathbf{v}_{\Pi} \otimes \mathbf{J}_{\Pi} \quad (3.52)$$

$$\kappa_{el,0} = \frac{2}{N_k V_{uc} k_B T} \sum_{\Pi} (\varepsilon_{\Pi} - \mu) f_{\Pi}^0 (1 - f_{\Pi}^0) \mathbf{v}_{\Pi} \otimes \mathbf{H}_{\Pi} \quad (3.53)$$

$$\alpha_{ph} = -\frac{1}{N_q V_{uc} k_B T} \sum_i \hbar \omega_i n_i^0 (n_i^0 + 1) \mathbf{v}_i \otimes \mathbf{G}_i \quad (3.54)$$

$$\kappa_{ph} = \frac{1}{N_q V_{uc} k_B T} \sum_i \hbar \omega_i n_i^0 (n_i^0 + 1) \mathbf{v}_i \otimes \mathbf{F}_i \quad (3.55)$$

where σ is the electric conductivity, S is the Seebeck coefficient, α_{el} is the electronic thermal response to an electric field, $\kappa_{el,0}$ is the electronic thermal conductivity without applied electric field, α_{ph} is the phonon thermal response to an electric field and κ_{ph} is the phonon thermal conductivity. Therefore, the total thermal conductivity at zero-current can be calculated as $\kappa = \kappa_{ph} + \kappa_{el,0} - \alpha_{el} S$.

3.2.6. Software packages solving the PBTE based on first-principles

The first attempts to solve the PBTE were based on simplified models like Debye for phonon-mode description together with parametric models for scattering rates. This was later improved by the use of classical force fields to model phonons and their interactions [41, 42], i.e. parameterizations of the atomic interactions.

However, it was not until the inclusion of phonon properties calculated from first-principles (frequencies, scattering rates...) that those methods gained popu-

3. Thermal transport modeling

larity, as they removed the necessity of adjustable parameters thus granting access to the thermal properties of novel materials where simpler models to describe those properties are lacking [44, 45].

Here we shortly review some software packages offering first-principles-based PBTE solvers:

- `Phono3py` [48]: It is the extension of `Phonopy` [161], which is a phonon solver based on the finite-difference method interfaced with several first-principles codes, to calculate phonon-phonon interaction using the supercell approach. It can calculate the thermal conductivity using the direct solution of the LBTE [153]. The integrals containing conservation deltas can be solved using the linear tetrahedron method or Gaussian smearing with a constant smearing parameter.
- `ShengBTE` [46]: This software package iteratively solves the PBTE using Omini’s iterative approach for bulk. Additionally, it can provide effective thermal conductivity for nanowires using the approach of Sec. 3.2.3. The integrals containing conservation deltas are solved using the adaptive smearing method.
- `FourPhonon` [162]: This software extends `ShengBTE` to account four-phonon processes. However, due to memory limitations, four-phonon processes are introduced by supposing the RTA collision term for them.
- `elphbolt` [163]: This software extends `ShengBTE` to solve the coupled electron-phonon BTE. Contrary to `ShengBTE`, integrals are performed using the tetrahedron method.
- `almaBTE` [47]: The successor of `ShengBTE`, it includes all its capabilities, except for the nanowire’s thermal conductivities. It has an improved treatment of velocity in degenerate points and the iterative solution is done through iterative linear solvers, offering improved convergence with respect

3. Thermal transport modeling

to its predecessor. Additionally, it offers support for alloys and superlattices. Finally, it also allows to obtain: the solutions of the single pulse 1D-response of the RTA-PBTE, the steady-state in 1D-multilayered structures with isothermal boundary conditions using RTA energy-based Monte Carlo methods, and effective thermal conductivities of thin-films.

We find it worth commenting on the κ -values obtained through those codes, namely Phonopy, ShengBTE and almaBTE, as they are calculating the same problem. ShengBTE and almaBTE provide different thermal conductivities, because of the proper treatment of velocity degeneracies implemented in almaBTE, as well as the latter uses variational solver for the linear problem instead of Omini's method. Therefore, we expect almaBTE results to be more reliable than ShengBTE's ones.

Regarding Phonopy- κ and almaBTE- κ they have been observed to provide significantly different results [164]. The origin of such differences lies in the methodologies used in both the solution of the PBTE and the calculation of integrals with conservation deltas. The fact that Phonopy performs those integrals using the linear tetrahedron method, which interpolates linearly the function between given points, limits its accuracy out of non-linear bands, like those found in 2D materials (see Subsection 2.2.2). On the other hand, almaBTE approach to those integrals does not rely on any supposition, thus being more appropriate for those cases. Here, we have not considered the other option that Phonopy offers to perform those integrals, the Gaussian smearing with constant smearing, as it makes results dependent on the chosen smearing, thus removing the benefits of a parameter-free approach.

3.3. Other methodologies

The other common approaches to transport modeling are based on molecular dynamics (MD), either classical or *ab initio*, being the most common: the equilibrium molecular dynamics (EMD), the non-equilibrium molecular dynamics (NEMD) [144], and the approach to equilibrium molecular dynamic (AEMD) [165].

The first of those methods, EMD, allows to obtain the thermal transport properties through the fluctuation-dissipation theorem embodied in the Green-Kubo relations [144], which for thermal conductivity in 3D system reads as

$$\kappa(\tau) = \frac{V}{3k_B T^2} \int_0^\tau \langle \mathbf{J}(t) \bullet \mathbf{J}(0) \rangle dt, \quad (3.56)$$

where τ is the correlation time and V is the system's volume. Then, for large enough τ -values Eq. 3.56 converges to the system's thermal conductivity. This method was originally believed to be inapplicable to first-principles calculation as \mathbf{J} requires a unique decomposition the total energy into individual atomic contributions [166]. Nonetheless, this assumption was latter proven false by Marcolongo *et al.* [167], thus allowing for *ab initio* EMD calculations.

On the other hand, the NEMD method allows to study of the actual heat transport processes; so that temperature profiles and heat fluxes for a given system can be determined [144]. Indeed, the extraction of thermal properties is done, as experimentally, by fitting to the mesoscopic equations [165].

Despite their widespread success, both the EMD and NEMD suffer from the fact that large simulation times are needed for the convergence of Eq. 3.56 in the former, and the establishment of the steady-state in the latter. To overcome these limitations, Melis *et al.* [165] developed the faster AEMD method, which is based on calculating transport properties from the relaxation of thermal periodic

3. Thermal transport modeling

perturbations to equilibrium through its fitting to Fourier's law [165].

CHAPTER 4

Thermal simulation of devices: the Monte Carlo method

We have already introduced the problems of solving the linearized PBTE (LPBTE) for devices as those found in state-of-the-art electronic devices or systems for thermoelectric applications, in the Subsection 3.2.4. For those systems, a direct or iterative solution of the LPBTE becomes unfeasible. Thus, one needs to rely on the so-called Monte Carlo (MC) methods to solve the PBTE.

In this chapter we review the MC methods to solve the PBTE, we start by presenting some basic concepts of the phonon-based Monte Carlo methodology, indicating its limitations. Deviational energy-based Monte Carlo techniques are then presented as a way of overcoming the limitations of traditional Monte Carlo methods; we discuss the different events a particle can suffer in those energy-based Monte Carlo, being those events equivalent to the phonon-based ones with minimal changes to the governing equations, namely an energy factor. Furthermore, we discuss both approaches to scattering operator, the RTA and the full linearized operator, as well how the energy-based MC deals with it.

4.1. The basics and limits of the phonon-based Monte Carlo methods

The MC method aims in our case to produce a solution of the PBTE for general system and boundary conditions. This is done by simulating the trajectory of particles representing a single/bunch phonon in space, momentum, and time. Those particles evolve in a semiclassical manner, moving freely inside the device following Newton's laws of motion, and changing from time to time their state, thus velocity, because of the intrinsic (three-phonon and isotopic) and extrinsic scattering (boundaries and interfaces). The methodology is stochastic in the sense that particles' initial state and scattering outcomes are chosen based on random numbers [87].

The Monte Carlo methods splits the evolution of the ensemble of particles from an initial time t_0 to a final time $t_f = t_0 + \Delta t$, where Δt is a small time step, into two steps, the advection which solves the left-side of the PBTE:

$$\frac{\partial n_i(\mathbf{r}, t)}{\partial t} + \mathbf{v}_i \nabla n_i(\mathbf{r}, t) = 0 \quad (4.1)$$

where n_i and \mathbf{v}_i are the i -th phonon mode distribution function and velocity, respectively. Eq. 4.1 solves to a net diffusion from higher densities of phonons to lower ones, so that phonon trajectories evolve ballistically,

$$\mathbf{r}(t + \Delta t) = \mathbf{r}(t) + \mathbf{v}_i \Delta t. \quad (4.2)$$

If during such evolution the particle encounters a boundary or an interface, it stops its evolution and changes its state accordingly to the kind of element encountered, more details on those interactions are given in Subsections 4.2.2 and 4.2.3. Moreover, in case the particle arrives at an isothermal boundary, it is thermalized, thus it is removed from the simulation.

4. Thermal simulation of devices: the Monte Carlo method

Finally, the advection step is finalized by simulating the effect of boundary conditions, this is the insertion of new particles based on phonon sources, like isothermal boundaries. Phonon/particles sources are further discussed in Subsection 4.2.1.

The right-side of the PBTE is solved in the scattering substep, following the advection step. Namely, one solves the right-side of the LPBTE (see Eq. 3.10)

$$\frac{\partial n_i(\mathbf{r}, t)}{\partial t} = A_{ij} n_j(\mathbf{r}, t). \quad (4.3)$$

Here, we need to notice that most widely used scattering operator in MC methods is the RTA one [168–171], i.e. $A_{ij} = -\frac{\delta_{ij}}{\tau_i}$, or the RTA-Callaway methods to account for the momentum conserving character of the \mathcal{N} processes [172]. Consequently, the probability (\mathcal{P}) that a particle in the i mode has scattered after a time Δt is given by

$$\mathcal{P}_i(\Delta t) = 1 - e^{-\frac{\Delta t}{\tau_i}}, \quad (4.4)$$

which is usually implemented by generating a random number R in the range $[0, 1)$, so that if $R < \mathcal{P}_i(\Delta t)$ the particle is scattered, and resampled due to energy conservation constraints. Then the mechanism of scattering M is sampled from distribution $\sum_J \frac{\tau_{i,J}^{-1}}{\tau_i^{-1}}$, where $\tau_{i,J}$ is the relaxation time due to J mechanism. For isotopic scattering the energy is conserved, but the momentum is randomized [170]. On the other hand, if phonon-phonon scattering is selected, the phonon is resampled from a postscattering distribution [169–171].

We note, that this resampling does not ensure energy conservation, thus additional algorithms are required to ensure the energy-conservation constraint [168–172]. For instance, Mei *et al.* [170] kept the post-scattering energy conserved within a tolerance range by randomly adding/deleting particles until the energy was inside an accepted tolerated deviation from the strict energy conservation. Of special interest, is the work of Chen *et al.* [172], in which they used a genetic

4. Thermal simulation of devices: the Monte Carlo method

algorithm to select the output state after the three-phonon scattering events, not only imposing the energy conservation, but also moment one for the \mathcal{N} processes. Although it seems those algorithms solve the problem, this is far from the truth, as they can bias the distribution in unknown ways [171].

Going beyond the RTA is conceptually easy but computationally expensive, as it requires keeping the transition rate and the involved modes of each possible process [173]. So that, if isotopic scattering is selected the transition is done simply by flipping the initial state to the final one. In the case that a three-phonon emission process is selected, the initial particle is deleted and two new particles are generated with the corresponding states for such transition. Finally, the case of the three-phonon absorption process is done by deleting the involved particle and a random one with the absorbed phonon-state in the same spatial cell. Although this algorithm solves some of the RTA issues, it raises other questions, like what to do if after N scattering events a phonon-mode is empty but the chosen scattering mechanism is an absorption of a phonon in such a state. Although one can suppose that to happen so rarely that one can simply do nothing (i.e. ostrich algorithm), such action will make scattering dependent on the phonon ordering, thus affecting the distribution in unknown ways.

Additionally, the classical Monte Carlo methods, both the RTA and beyond the RTA, suffer from a high noise-signal ratio to the point that when simulating processes near the equilibrium, the thermal noise typically masks anything occurring there [47, 168, 171, 174–176]. Indeed, any attempt to reduce it beyond a level in which it does not mask any feature, would require such a big number of computational particles that it would be unpractical, as statistical noise scales proportionally to $\frac{1}{\sqrt{N_p}}$, where N_p is the number of particles in the simulation [168, 171, 174]. Moreover, these traditional methods waste most of the computational effort in finding the solution for the very well-known equilibrium part of the distribution, dampening in that way their scalability [47, 176].

4.2. Energy-based deviational formulations

An alternative approach to overcome these limitations was developed by Péraud and Hadjiconstantinou [175]. To reduce statistical variance they stated that distribution function can be divided into two contributions, a known equilibrium one (n^0)—i.e. a Bose-Einstein distribution at a given reference temperature (T_{ref})—and the deviation from it (n^d). Therefore, the LPBTE within the deviational formulation is

$$\frac{\partial n_i^d}{\partial t} + \mathbf{v}_i \cdot \nabla n_i^d + \frac{\partial n_i^0}{\partial t} \mathbf{v}_i \cdot \nabla T_{\text{ref}} = A_{ij} n_j^d, \quad (4.5)$$

where we n_i^d is position and time dependent, and the new source term $\left(\frac{\partial n_i^0}{\partial t} \mathbf{v}_i \cdot \nabla T_{\text{ref}}\right)$ is due to variation in reference temperature. So that by choosing an appropriate n^0 , n^d becomes small, both in value and in uncertainty. Furthermore, in such a formulation, all computational effort is used to describe those variations from equilibrium.

Moreover, to get rid of problems coming from energy conservation in the scattering part of the algorithm, they proposed that instead of using the usual phonon distribution function, to use the deviational energy distribution ($f_i = \hbar\omega_i n_i$). Thus we obtain the deviational-energy linearized PBTE,

$$\frac{\partial f_i^d}{\partial t} + \mathbf{v}_i \nabla f_i^d + \frac{\partial f_i^0}{\partial t} \mathbf{v}_i \cdot \nabla T_{\text{ref}} = B_{ij} f_j^d, \quad (4.6)$$

where $B_{ij} = \frac{\omega_i}{\omega_j} A_{ij}$. Therefore, in the deviational-energy MC the energy distribution is represented as

$$f_i^d(\mathbf{r}) = \varepsilon^d \sum_{J=0}^{N_p} \sigma_J \delta[\mathbf{r} - \mathbf{r}_J] \delta_{i,i_J}, \quad (4.7)$$

4. Thermal simulation of devices: the Monte Carlo method

where ε^d is the magnitude of deviation carried by each particle, N_p is the number of particles and σ_J is the sign of the contribution, as f_i^d can be a negative deviation. Consequently, the particles do not represent a bundle of a fixed number of deviational phonons of the i mode, but bundles of a deviational constant energy, so that the number of phonons forming that bundle is variable, and mode dependent.

We proceed now to first explain the different events that a bundle of energy can suffer during the MC simulation, except for intrinsic scattering, which is extensively discussed in Section 4.3. Henceforward in the following sections, we suppose that all phonon (particle) properties are calculated in a discrete regular \mathbf{q} -mesh and that real space is divided into computational boxes.

4.2.1. Deviational energy sources

In general, the computational particles are generated because of the boundary and/or initial conditions: the initial temperature profiles, the applied thermal gradients, and/or the isothermal boundaries. Here, it should be noted within the deviational scheme when referring to an initial temperature profile or gradient, these are relative to the reference temperature.

Moreover, we note that when calculating the number of particles (N) generated by a source, most of the time $N \notin \mathbb{Z}$. Hence owing to the impossibility of generating fractional particles, this fraction term must be treated in an average sense, so that the mean number of particles generated for an infinite number of samples equals N . To do so, one generates $\lfloor N \rfloor = \max\{m \in \mathbb{Z} \mid m \leq N\}$ particles, and then generates a random number $R \in (0, 1]$, thus if $R \leq N - \lfloor N \rfloor$ an additional particle is added.

In the cases of applied thermal gradients and isothermal boundaries, these generated particles are randomly distributed along the given time step, so they

4. Thermal simulation of devices: the Monte Carlo method

can advect for the remaining time; whereas, in the case of the initial temperature profile all particles are placed at $t = 0$ ps.

4.2.1.1. Initial temperature profile

Given an initial temperature profile $T(\mathbf{r}, 0)$ different than the reference one, an initial number of particles is generated to model the out-of-reference distributions at $t = 0$ ps. The number of particles (N^j) introduced due to an initial thermal profile in the j -th box is calculated as [171, 175, 176]:

$$N^j = \sum_i |N_i^j| = \sum_i \left| \frac{V_{j,\text{box}}}{N_q V_{\text{uc}} \varepsilon^d} [f_i^0(T_j) - f_i^0(T_{\text{ref}})] \right| \quad (4.8)$$

where $V_{j,\text{box}}$ is the volume of the j -th computational box. Then particles with mode i are generated at j with a probability $|N_i^j|/N^j$ and $\sigma = \text{sgn}(N_i)$.

4.2.1.2. Isothermal boundaries

Isothermal boundaries represent a boundary between the computational domain and thermal reservoirs, i.e. heat sources and sinks, which are usually assumed to be at thermal equilibrium. Therefore, all particles leaving the reservoir, i.e. entering the simulation domain, come from an equilibrium distribution, and any incoming particle arriving at it is instantly thermalized, i.e. eliminated from the simulation. Within the deviational energy formulation, the net flux crossing the boundary can be expressed as [171, 176]:

$$\mathbf{J}^{\text{iso}} = \sum_{\{i : \mathbf{v}_i \cdot \hat{\mathbf{e}}_{\perp}^{\text{in}} > 0\}} \mathbf{v}_i \cdot \hat{\mathbf{e}}_{\perp}^{\text{in}} \{f_i^0(T_{\text{iso}}, k) - f_i^0(T_{\text{ref}}, j)\} + \sum_{\{i : \mathbf{v}_i \cdot \hat{\mathbf{e}}_{\perp}^{\text{in}} < 0\}} \mathbf{v}_i \cdot \hat{\mathbf{e}}_{\perp}^{\text{in}} f_i^0(T_{\text{ref}}, j), \quad (4.9)$$

4. Thermal simulation of devices: the Monte Carlo method

where $\hat{\mathbf{e}}_{\perp}^{in}$ is a unitary vector normal to the boundary pointing into the material, and k and j refer to the reservoir and the computational box in contact with it, respectively. The term containing the condition $\mathbf{v}_i \cdot \hat{\mathbf{e}}_{\perp}^{in} < 0$ is captured by the particles arriving to the boundary, which are thermalized and erased from simulation upon contact. The other term of the flux is modeled by introducing

$$N^{\text{iso}} = \sum_i |N_i^{\text{iso}}| = \sum_{\{i: \mathbf{v}_i \cdot \hat{\mathbf{e}}_{\perp}^{in} > 0\}} \frac{A \Delta t}{N_q V_{\text{uc}} \varepsilon^d} \times \left| \{f_i^0(T_{\text{iso}}, k) - f_i^0(T_{\text{ref}}, j)\} \right| v_i \cdot \hat{\mathbf{e}}_{\perp}^{in} \quad (4.10)$$

particles each time step, where A is the the area of the isothermal boundary. The particles with mode i are generated at $k - j$ -th boundary, with a probability $|N_i^{\text{iso}}|/N^{\text{iso}}$ and $\sigma = \text{sgn}(N_i^{\text{iso}})$.

4.2.1.3. Applied thermal gradients

The deviational energy distribution due to an applied gradient (∇T_{ref}) in the j -th box for the i mode is [177]

$$f_i^{\text{grad}} = \mathbf{v}_i \cdot \nabla T_{\text{ref}} \frac{\partial f_i^0(T_{\text{ref}}, j)}{\partial T}. \quad (4.11)$$

Consequently, the number of deviational particles introduced due to the gradient term into the system (N^{grad}) is computed to be

$$N^{\text{grad}} = \sum_{i,j} |N_{i,j}^{\text{grad}}| = \frac{V_{j,\text{box}} \Delta t}{N_q V_{\text{uc}} \varepsilon^d} \sum_i |\mathbf{v}_i \cdot \nabla T_{\text{ref}}| \frac{\partial f_i^0(T_{\text{ref}}, j)}{\partial T}, \quad (4.12)$$

where j runs over the computational boxes. Then, the particles with mode i are generated at j -th box, with a probability $|N_i^{\text{grad}}|/N^{\text{grad}}$ and $\sigma = \text{sgn}(\mathbf{v}_i \cdot \nabla T_{\text{ref}})$.

4.2.2. Interaction with boundaries

Usually, interaction with physical boundaries is modeled as a combination of fully specular and diffusive boundaries, so that the chosen type of boundary scattering is controlled by a specularity parameter (p). Thus, when a particle arrives at a physical boundary, a random number ($R \in [0, 1)$) is generated, and if $R < (\geq)p$, specular (diffusive) mechanism is chosen. This p parameter can be computed by taking into account surface properties like roughness [39, 171].

4.2.2.1. Specular scattering

In specular scattering the parallel component quasi-momentum with respect to the border is conserved, and thus the final state after the scattering can be calculated as

$$\mathbf{q}' = \mathbf{q} - 2(\mathbf{q} \cdot \hat{\mathbf{e}}_{\perp}^{\text{in}})\hat{\mathbf{e}}_{\perp}^{\text{in}}, \quad (4.13)$$

$$\nu' = \nu \quad (4.14)$$

where (q, ν) and (q', ν') are the initial and final state, and $\hat{\mathbf{e}}_{\perp}^{\text{in}}$ is a unitary vector normal to the surface pointing into the material. Although its simplicity, Eq.4.13 can introduce important limitations to the allowed borders in a MC simulation, as not all the $\hat{\mathbf{e}}_{\perp}^{\text{in}}$ map the incident states (\mathbf{q}) to a valid state, i.e. a \mathbf{q}' contained in the mesh, but only those boundaries compatible with crystal symmetry.

4. Thermal simulation of devices: the Monte Carlo method

4.2.2.2. Diffusive boundaries

On the other hand, the diffusive scattering, do not conserve the momentum, with possible outcomes following Lambert's cosine law [173] defined by transition probabilities from a state i to f :

$$P_{i \rightarrow f} = \frac{\mathbf{v}_f \cdot \hat{\mathbf{e}}_{\perp}^{\text{in}} \delta(\omega_f - \omega_i)}{\sum_j \mathbf{v}_j \cdot \hat{\mathbf{e}}_{\perp}^{\text{in}} \delta(\omega_j - \omega_i)} \quad (4.15)$$

where $\delta(\omega_j - \omega_i)$ can be regularized using adaptive smearing [46] (see Subsection 2.2.2).

Alternatively, it is possible to properly reproduce the Casimir limit [155] by noting that the energy incident into the boundary (E_{in}) must be equal to the reemitted energy of such surface (E_{out}) [177, 178]. Therefore,

$$\mathbf{J}_{\text{out}} = \frac{1}{N_{\text{q}} V_{\text{uc}}} \sum_{\{i: \mathbf{v}_i \cdot \hat{\mathbf{e}}_{\perp}^{\text{in}} > 0\}} (\mathbf{v}_i \cdot \hat{\mathbf{e}}_{\perp}^{\text{in}}) \{f_i^0(T_{\text{wall}}) - f_i^0(T_{\text{ref}})\}, \quad (4.16)$$

where T_{wall} is the border temperature, is equal to $\frac{E_{\text{in}}}{A} \Delta t$, where $E_{\text{in}} = \varepsilon^d \sum_j^N \sigma_j$, N are the particles arriving at the boundary during a given time step (Δt), and A is the border area. Therefore, particles arriving at the boundary are used to compute E_{in} , and discarded. Then, E_{in} is used to calculate T_{wall} through inversion or interpolation of $\frac{E_{\text{in}}}{A} \Delta t = \mathbf{J}_{\text{out}}$. Afterwards, T_{wall} is used to create the distribution from which $\frac{|E_{\text{in}}|}{\varepsilon^d}$ particles are randomly drawn, during the given time step, with sign equal to $\text{sgn}(E_{\text{in}})$.

4.2.3. Interaction with interfaces: the diffusive mismatch model

Whenever a particle arrives at a boundary between two dissimilar materials it can be either transmitted or reflected, giving rise to a thermal resistance. Those processes can be elastic, inelastic, specular, or diffusive; or more generally a combination of all the previous kinds of scattering. This phenomenon is usually captured through the use of transmission and reflection probabilities.

The most common approaches to obtain those transmission probabilities are the acoustic mismatch model (AMM) and the diffusive mismatch model (DMM). In the former, the interface is supposed to be perfectly specular (i.e. no scattering occurs at the interface) and treated as a continuum. Therefore, the particle (phonon) can only specularly reflect, reflect and mode convert, refract, or refract and mode convert [179]. Thus, refraction angles and transmission probabilities are given by Snell's and Fresnel's phonon equivalent laws [179], respectively. It should be noted that the original model [179, 180] was limited to acoustic modes; being later expanded to full-band by Larroque *et al.* [181]. From an implementation point of view, the AMM suffers from the same drawbacks as specular boundary scattering (see Subsection 4.2.2.1).

On the other hand, the DMM supposes an interface that is rough and/or with many defects, hence all particles arriving at the interface scatter, losing their memory. Considering only elastic processes in an interface between A and B materials, the output state and side in a $A - B$ interface for a particle with mode

4. Thermal simulation of devices: the Monte Carlo method

k in the A side as [182]:

$$P_{k,A \rightarrow k',C} = \frac{8\pi^3}{V_{uc,C} N_{q,C}} |\mathbf{v}_k \cdot \mathbf{n}| \delta(\omega'_k - \omega_k) \times \\ (\Theta(\mathbf{v}_k \cdot \mathbf{n}) \delta_{BC} + \Theta(-\mathbf{v}_k \cdot \mathbf{n}) \delta_{AC}) \Bigg/ \\ \left[\sum_D^{A,B} \frac{8\pi^3}{V_{uc,D} N_{q,D}} \sum_j |\mathbf{v}_j \cdot \mathbf{n}| \times \right. \\ \left. \delta(\omega_j - \omega_k) (\Theta(\mathbf{v}_j \cdot \mathbf{n}) \delta_{BD} + \Theta(-\mathbf{v}_j \cdot \mathbf{n}) \delta_{AD}) \right] \quad (4.17)$$

where \mathbf{n} is the vector normal to the interface, pointing out of A into B , $C \in \{A, B\}$, and Θ is the Heaviside function. Of interest here is the work of Hopkins [183], which extended the DMM to inelastic processes, thus extending the validity of DMM to higher temperatures where those processes gain importance.

Despite those crude approaches, the DMM and AMM have been proven to qualitatively describe the interface thermal resistance (ITR) for several interfaces of bulk 3D materials such as Si/Ge [47, 181]. However, both approaches rely on the mismatch of the vibrational properties of the involved materials, and thus they are expected to fail in cases in which those are similar, as would be the case of twin boundaries in semiconductors [184]. Indeed in those cases, it is necessary to rely on methodologies that take into account the full atomistic description of the vibrational properties of the interface, as non-equilibrium Green function methods [184]. Moreover, due to the assumption of elastic scattering, those models fail to account for thermal rectification [185].

4.2.4. Periodic boundary conditions

For systems with some kind of periodicity, it is possible to conduct an MC simulation within a single periodic unit cell, so that when a particle enters into a periodic image it is immediately translated, entering the simulation domain by the opposite side along the given periodic direction.

4.2.5. Particle termination and canceling

Whenever a particle reaches a reservoir, it is absorbed by it, thus terminating it. However, in some cases, like larger systems, this deletion due to absorption at isothermal boundaries is not enough, and the number of particles can grow up to unmanageable values. Alternatively, it is possible to implement a cancellation scheme to keep the number of particles stable; in such a scheme, pairs of particles with the same mode but opposite signs, and in the same spatial cell are randomly selected and deleted. This scheme takes advantage of the fact that energy conservation, as well as the value of physical quantities only requires the net amount of particles. Notwithstanding, the speedup that the cancellation can introduce in the simulation, it is noteworthy that the cancellation scheme introduces a non-negligible error of second order with respect to the space mesh [171]. An example of this error is, for instance, the fact that for larger cells particles generated within that cell could be canceled before moving to another cell [177].

4.3. Scattering within energy-based deviational MC methods

During the scattering sub-step, the deviational energy distribution evolves accordingly to

$$\frac{\partial f_i^d(t)}{\partial t} = B_{ij} f_j^d(t), \quad (4.18)$$

$$f_i^d(t + \Delta t) = P(\Delta t) f_j^d(t) = e^{B_{ij} \Delta t} f_j^d(t), \quad (4.19)$$

where the propagator $P(\Delta t)$ is a non-Markovian transition matrix, as it has negative or higher than unity elements [177]. Moreover, we stress that $P(\Delta t)$ disregards any information about individual scattering mechanisms. Indeed, it does not indicate that a particle in the i mode is undergoing a given scattering mechanism to given state/s but how the distribution in the i mode is evolving, transferring or receiving energy from other modes.

4.3.1. RTA scattering

In the case of the RTA, B_{ij} reduces to a diagonal matrix $B_{ij} = -\frac{\delta_{ij}}{\tau_i}$, hence uncoupling the modes evolution, $f_i^d(t + \Delta t) = e^{-\frac{\Delta t}{\tau_i}} f_i^d(t)$. For each particle in a given state k , this last is modeled by generating a random number R in range $[0, 1)$ and if $R < 1 - e^{B_{kk} \Delta t}$ the particle is scattered and resampled from the postscattering distribution

$$\frac{C_{k'}(j)/\tau_{k'}(j)}{\sum_i C_i(j)/\tau_k(j)} \quad (4.20)$$

of the j -th computational box [171, 175, 176], where C_i is the volumetric heat capacity of the i mode. This resampling embodies the energy conservation constraints [169, 171], and is derived under the first-order expansion (i.e. we

4. Thermal simulation of devices: the Monte Carlo method

suppose small deviations of temperature with respect to reference one) of the distribution in terms of the temperature

$$f_i \approx f_i^0 + \frac{\partial f_i^0}{\partial T}(T - T_{\text{ref}}), \quad (4.21)$$

$$f_i^d \approx C_i \Delta T, \quad (4.22)$$

where we have used that $\frac{\partial f_i^0}{\partial T} = C_i$ and have defined the deviational temperature as $\Delta T = T - T_{\text{ref}}$. Here, it is important to stress that the linearization with respect to the temperature is not essential and in fact is possible to develop a resampling that is independent of it and its associated error [171, 175]. However, the benefits overcome the drawbacks, namely the necessity of calculating in each step the temperature and other quantities required for the resampling, as its associated cost and the coupling this introduces to different particles dynamics is removed. Moreover, by setting a spatially variable reference temperature the error associated to this linearization can be highly mitigated [171].

4.3.2. Beyond the RTA scattering

On the other hand using the full B_{ij} matrix (i.e. going beyond the RTA), is a tricky task, as the resulting propagator is, as already mentioned, a non-Markovian transition matrix, which makes its direct implementation difficult. A more implementation-friendly form can be obtained by using the power series [177, 178]:

$$f_i(t + \Delta t) = \sum_j \frac{P_{ij}(\Delta t)}{\mathcal{P}_j} \left(\sum_{n=0}^{\infty} \left(2 \frac{\mathcal{P}_j^-}{\mathcal{P}_j} \right)^n \right) f_j^d(t) \quad (4.23)$$

where $\mathcal{P}_j = \sum_k^{N_{\text{states}}} |P_{kj}|$ and $\mathcal{P}_j^- = \sum_{\{k: P_{kj} < 0\}}^{N_{\text{states}}} |P_{kj}|$. The recursive Eq. (4.23) can be implemented stochastically for a particle in state j with sign σ through the

4. Thermal simulation of devices: the Monte Carlo method

following strategy [177, 178]:

1. Sample a random number R in $[0, 1)$, and find the lower bound f of $\sum_k |P_{kj}(\Delta t)| / \mathcal{P}_j$ for R .
2. Set the new sign to $\sigma' = \text{sgn}(P_{fj}\sigma)$.
3. If $\sigma' \neq \sigma$, generate two particles with state j and time t .

It should be noticed that this algorithm generates additional particles, and thus it needs to be followed by a cancellation algorithm as discussed in Subsection 4.2.5 to prevent particles to grow exponentially to unmanageable levels.

4.4. Properties sampling

Finally, after the scattering substep, the instantaneous values of the deviational energy density ρ^d , the temperature T , and the heat flux J are obtained from the distribution in the i -th computational box as:

$$\rho^d(i) = \frac{\sum_{\{j: \mathbf{r}_j \in i\text{-th box}\}}^{N_{\text{particles}}} \varepsilon^d \sigma_j}{V_{i,\text{box}}}, \quad (4.24)$$

$$T(i) = \frac{\rho^d(i)}{C_v(i, T_{\text{ref}})} + T_{\text{ref}}(i), \quad (4.25)$$

$$\mathbf{J}(i) = \frac{\sum_{\{j: \mathbf{r}_j \in i\text{-th box}\}}^{N_{\text{particles}}} \mathbf{v}_j \varepsilon^d \sigma_j}{V_{i,\text{box}}}, \quad (4.26)$$

where $C_v(i, T_{\text{ref}})$ is the volumetric heat capacity of the i -th cell at T_{ref} . The spectral decomposition of those quantities deviational temperature, $\Delta T(\omega)$, and

4. Thermal simulation of devices: the Monte Carlo method

the α -component of the heat flux, $\mathbf{J}_\alpha(\omega)$, are computed as

$$\Delta T(i, \omega) = \frac{1}{V_{i,\text{box}}} \sum_{\{j: \mathbf{r}_j \in i\text{-th box}\}}^{N_{\text{particles}}} \frac{\varepsilon^d \sigma_j \delta(\omega - \omega_j)}{C_v(i, T_{\text{ref}})} \quad (4.27)$$

$$\mathbf{J}_\alpha(i, \omega) = \frac{1}{V_{i,\text{box}}} \sum_{\{j: \mathbf{r}_j \in i\text{-th box}\}}^{N_{\text{particles}}} \mathbf{v}_{j\alpha} \varepsilon^d \sigma_j \delta(\omega - \omega_j). \quad (4.28)$$

Finally, the deviational phonon distribution as function of the wave vector, $n^d(\mathbf{q}, i)$, is calculated as

$$n^d(\mathbf{q}, i) = \frac{\varepsilon^d V_{i,\text{uc}} N_{\mathbf{q}}}{V_{i,\text{box}} \hbar} \sum_j^{N_{\text{particles}}} \frac{\sigma_j}{\omega_j} \delta_{\mathbf{q}_j \mathbf{q}}, \quad (4.29)$$

4.5. The ensemble energy-based deviational MC algorithm

The algorithm of the ensemble energy-based deviational algorithm is for each time step (Δt) as follows

1. Generate particles accordingly to the particle sources for the given initial and boundary conditions (see Eqs. 4.8, 4.12 and 4.10). Place the particles generated by gradients and isothermal boundaries randomly along the time step and evolve them for the remaining time (see step 2).
2. Evolve particles ballistically from \mathbf{r}_0 ($\mathbf{r}_f = \mathbf{r}_0 + \mathbf{v}_i t_{\text{flight}}$) where t_{flight} is defined as $\min\{\Delta t, t_b\}$, where t_b is the time the particle needs to encounter a boundary or an isothermal wall.
3. If a particle encounters some physical boundary, thus finalizing its ballistic trajectory prematurely, track it and have its energy added to that boundary.

4. Thermal simulation of devices: the Monte Carlo method

4. Use the energies of the different boundaries to calculate their boundaries temperatures. Then, employ these temperature to generate the appropriate number of particles following Eq. 4.16. As in step 1, place those new particles along the time step and evolve them for the remaining time (see step 2).
5. Absorb and terminate particles that encounter an isothermal boundary, thus terminating their trajectory.
6. Intrinsically scatter (i.e. three-phonon, isotopic,...) all particles finishing their ballistic trajectory, following the algorithms of Section 4.3.
7. Cancel the particles following the cancellation scheme as detailed in Sub-section 4.2.5.
8. Sample the instantaneous properties at $t_0 + \Delta t$ following Eqs. 4.24-4.26.

Here, we have assumed adiabatic diffuse walls for physical boundaries.

4.6. Steady-state and RTA efficient algorithms

Given a system under the effect of time-independent sources, after a time t_{ss} it will reach a steady-state so that any initial condition (i.e. initial temperature profiles) effect has vanished. In such cases the properties can be obtained by time-averaging instead of the typical ensemble-average, so the steady-state property $A_{ss}(\mathbf{r})$ is calculated as [171, 176]

$$A_{ss}(\mathbf{r}) = \frac{1}{\tau} \int_{t_{ss}}^{t_{ss}+\tau} A(\mathbf{r}, t') dt' = \frac{\varepsilon^d}{\tau} \sum_j^{N_{\text{particles}}} \sigma_j \int_{\max\{t_j^{\text{emi}}, t_{ss}\}}^{t_{ss}+\tau} g_j(\mathbf{r}, t') dt' \quad (4.30)$$

4. Thermal simulation of devices: the Monte Carlo method

where $\sigma_j g_j(\mathbf{r}, t')$ is the contribution of the j -th particle to $A(\mathbf{r}, t')$, and t_j^{emi} is the time at which the j -th particle is emitted. By letting $\tau \rightarrow \infty$, and noting that within the steady-state any initial condition contribution would have vanished, one gets that the steady-state properties can be obtained by sampling the full trajectory of the emitted deviational power by the time-independent sources as

$$A(\mathbf{r}, t) = \varepsilon^d \sum_j^{N_{\text{particles}}} \sigma_j \int_{t_j^{\text{emi}}}^t g_j(\mathbf{r}, t') dt'. \quad (4.31)$$

Therefore, the contribution of the j -th particle, which now represents deviational power, to the steady-state can be obtained by simulating it from its emission up to its termination [176] or a maximum time. This last is justified as trajectories contributing to heat flux reach values in the order of the statistical deviation after a relatively small number of scattering events [171, 176]. Moreover, Eq. 4.31 also allows obtaining the contribution of that particle to the establishment of the steady-state by the time-independent sources, by sampling the trajectory at intermediate times.

Consequently, it is possible to perform N single-particle simulations from their emission to their termination to obtain the steady-state properties and its establishment. Although in principle it can be conducted within the RTA and beyond it, the fact that the scattering algorithm for the full linearized scattering operator creates additional particles, makes that method unpractical for beyond the RTA computations.

The simulation of the RTA-steady-state starts by calculating the total deviational power introduced in the system can be calculated as $|\dot{E}^{\text{tot}}| = |\dot{E}^{\text{grad}}| + |\dot{E}^{\text{iso}}|$ where $|\dot{E}^{\text{grad}}|$ and $|\dot{E}^{\text{iso}}|$ are the deviational power due to applied thermal

4. Thermal simulation of devices: the Monte Carlo method

gradients and isothermal walls, and are given by:

$$\left| \dot{E}^{\text{iso}} \right| = \sum_{i,j} |\dot{E}_{i,j}^{\text{iso}}| = \sum_{i,j} \varepsilon^d |N_{i,j}^{\text{iso}}| \Delta t, \quad (4.32)$$

where j is the isothermal wall index, i runs over modes at the wall, $N_{i,j}^{\text{iso}} \Delta t$ is the number of particles per unit of time introduced in the system due to the j -th isothermal wall (see Eq. 4.10),

$$\left| \dot{E}^{\text{grad}} \right| = \sum_{i,j} |\dot{E}_{i,j}^{\text{grad}}| = \sum_{i,j} \varepsilon^d |N_{i,j}^{\text{grad}}| \Delta t \quad (4.33)$$

where j runs over the computational boxes, and $N_{i,j}^{\text{grad}}$ is the contribution of the i mode to the number of deviational particles due to an applied thermal gradient in the j -th box (see Eq. 4.12). Then the desired number of particles ($N_{\text{particles}}$) carrying $\varepsilon^d = \frac{|\dot{E}^{\text{tot}}|}{N_{\text{particles}}}$ either negative or positive deviational power. These $N_{\text{particles}}$ particles are generated with mode i at j from source s with a probability $|\dot{E}_{i,j}^s|/|\dot{E}^{\text{tot}}|$ and sign $\sigma = \text{sgn}(\dot{E}_{i,j}^s)$.

Following the generation of deviational particles, the individual particle trajectories are computed as following the next algorithm:

1. Evolve particles ballistically from \mathbf{r}_0 ($\mathbf{r}_f = \mathbf{r}_0 + \mathbf{v}_i t_{\text{flight}}$) where t_{flight} is defined as $\min\{-\tau_i \ln(R), t_b\}$, where t_b is the time the particle needs to encounter a boundary, interface or an isothermal wall and R is random number in range $(0, 1]$.
2. Sample the properties for the ballistic trajectory following Eq. 4.31. Further details are given in Subsection 4.6.1.
3. Scatter the particles that have encountered physical boundaries or interfaces, finalizing their ballistic trajectory prematurely, and select the output state accordingly to Eqs. 4.15 and 4.17. Then, evolve those particles ballistically

4. Thermal simulation of devices: the Monte Carlo method

following the step 1.

4. Absorb and terminate particles that encounter an isothermal boundary, thus terminating their trajectory. Alternatively, if $t > t_{\max}$, also end the trajectory.
5. Intrinsically scatter (i.e. three-phonon, isotopic,...) all particles finishing their ballistic trajectory, and resample their properties from the post-scattering distribution (see Eq. 4.20). Then, evolve those particles ballistically following the step 1.

Here, we have supposed fully elastic diffusive scattering for both physical boundaries and interfaces.

4.6.1. Trajectory sampling and steady-state properties

Within this formalism, the trajectories are sampled on a time grid on top of an spatial grid (see Eq. 4.31), in such a way that the contribution from a trajectory path inside a computational box to deviational energy (e^d) and heat flux (j) grid point is:

$$e^d(k, i) = \frac{1}{V_k} \sigma \dot{\varepsilon}^d(t_f - t_0) [\Theta(t - t_i) - \Theta(t - t_{i+1})] \quad (4.34)$$

$$\mathbf{j}(k, i) = \frac{1}{V_k} \mathbf{v} \sigma \dot{\varepsilon}^d(t_f - t_0) [\Theta(t - t_i) - \Theta(t - t_{i+1})] \quad (4.35)$$

where k is the computational box id, V_k is the volume of the k -th box, and $(t_f - t_0) [\Theta(t - t_i) - \Theta(t - t_{i+1})]$ represents the interval between t_0 and t_f that belongs to the i -th point of the time grid, with Θ representing the Heaviside function. Here, we have supposed that the contribution is computed each time a particle changes its state or its spatial bin. Finally, by integrating Eqs. (4.34)-(4.35)

4. Thermal simulation of devices: the Monte Carlo method

one can obtain the evolution of temperature $T(k, t_i)$ and heat flux $J(k, t_i)$:

$$T(k, t_i) = T_{\text{ref}} + \frac{1}{C_v(T_{\text{ref}})} \sum_{l=0}^i e^d(k, l), \quad (4.36)$$

$$\mathbf{J}(k, t_i) = \sum_{l=0}^i \mathbf{j}(k, l). \quad (4.37)$$

4.6.2. Extended systems with applied gradients

For extended systems where no isothermal boundaries are present, e.g. an infinitely long nanoribbon with an applied thermal gradient, particles cannot exit the structure. It is, therefore, necessary to introduce an alternative way to collect them. For this purpose, and taking into account that transient to steady-state is normally not of interest for those cases, it is possible to use a modified version of the algorithm originally proposed by Randrianalisoa *et al.* [186, 187] and adapted to such cases by Péraud *et al.* [171].

We now list the modifications to the algorithm, to the previous one, for dealing with extended systems under applied gradients:

1. Generate particles from a gradient (source) generator, evolve them until they scatter (intrinsically or at borders or interfaces) and compute their contribution to steady-state.
2. Calculate the net number of particles that intrinsically scatter, at each computational box, $N_j = \sum_{\{i: \mathbf{r} \in j\}} N_i^{\text{intrinsic}} \sigma_i$, where j refers to box indexes. Then, delete those particles.
3. Generate $|N_j|$ particles with sign $\sigma = \text{sgn}(N_j)$ from the post-scattering distribution (see Eq. 4.20).

4. Thermal simulation of devices: the Monte Carlo method

4. If the number of particles is 0, no new particles are introduced or the properties have converged, end the simulation; otherwise repeat step 1.

It is noteworthy that as previously mentioned the cancellation scheme in step 2 introduces a non-negligible error of second order with respect to the space mesh [171].

CHAPTER 5

Thermal conductivity in nanoscale-emerging crystal phases

*This Chapter reproduces to a great extent the contents of [M. Raya-Moreno, H. Aramberri, J. A. Seijas-Bellido, X. Cartoixà, and R. Rurali, “Thermal conductivity of hexagonal Si and hexagonal Si nanowires from first-principle”, Appl. Phys. Lett., **111** 032107 (2017)] and [M. Raya-Moreno, R. Rurali, and X. Cartoixà, “Thermal conductivity for III-V and II-VI semiconductor wurtzite and zinc-blende polytypes: The role of anharmonicity and phase space”, Phys. Rev. Materials, **3** 084607 (2019)]. We note a partial reproduction of a few contents of the following collaborations [J. Carrete, M. López-Suárez, M. Raya-Moreno, A. S. Bochkarev, M. Royo, G. K. H. Madsen, X. Cartoixà, N. Mingo, and R. Rurali, “Phonon transport across crystal-phase interfaces and twin boundaries in semiconducting nanowires”, Nanoscale, **11** 16007–16016 (2019)] and [F. D. Santiago, M. Raya-Moreno, Á. Miranda, M. Cruz-Irisson, X. Cartoixà, and R. Rurali, “Tunable thermal conductivity of ternary alloy semiconductors from first-principles”, J. Phys. D: Appl. Phys., **54** 335302 (2021)].*

As already mentioned, heat management stands out as one of the key problems for several technologies. The reduction in size [1] and the required increase in

5. Thermal conductivity in nanoscale-emerging crystal phases

operating speeds of devices in electronics, or the necessity to enhance energy conversion ratio for thermoelectrics have brought into the spotlight the importance of phonon engineering or phononics [131]. For instance, for thermoelectric applications, a material with low thermal conductivity and high electrical conductivity, the so-called “phonon-glass and electron-crystal”, is desired to have a good efficiency, characterized by the ZT figure of merit. [18]. Historically, one of the preferred approaches to thermoelectric materials was alloying, as it introduces point-mass defects that strongly scatter phonons, significantly reducing lattice thermal conductivity [19]. A more recent approach to solve this problem is nanostructuration as an effective way of reducing the lattice thermal conductivity [16]—hereafter just referred to as thermal conductivity, κ —or a combination of both, namely nanostructuration and alloying [19].

At the same time, recent advances in semiconductor synthesis at the nanoscale have granted access to different phases that, in bulk, are only observed under extreme conditions. Namely, the wurtzite phase has theoretically been proved to be the most stable for several bulk-cubic [188] semiconductors when grown as nanowires (NWs) [189] provided their diameter is smaller than a given critical value, but it can also be obtained at larger sizes, though thermodynamically it is only metastable. Indeed, the wurtzite phase in NWs has been reported for a great range of bulk-cubic semiconductors: InP [20, 21], Si [22–24], InAs [25, 26], GaAs [27, 28] or GaP [29, 30] to name but a few.

It is in that context, that these new semiconductor phases can become a cornerstone for thermoelectricity and phononics in general, as they normally show a lower thermal conductivity than their more stable counterparts while maintaining similar electronic properties. For example, Togo *et al.* calculated thermal conductivity of wurtzite and zinc-blende phases for 33 different materials [48], Lindsay *et al.* [45] studied the zinc-blende/wurtzite thermal conductivity of GaN, and Li *et al.* addressed the thermal conductivity of bulk and nanowire InAs, AlN,

5. Thermal conductivity in nanoscale-emerging crystal phases

and BeO polymorphs [190]. However, none of these works explained in detail the origin of the reduction in thermal conductivity.

Concerning the qualitative behavior of the thermal conductivity of materials, Mukhopadhyay *et al.* [191], building on earlier work by Slack [192] and Lindsay *et al.* [193], have provided seven criteria to interpret the relative magnitude of the thermal conductivity between different materials.

In this Chapter, we study the thermal conductivity (κ) of several bulk and nanowire semiconductors for their cubic and hexagonal phases from first-principles. We begin presenting the two crystal phases, following with a discussion of the differences between the thermal conductivity of those phases for silicon and silicon nanowires. Then, we follow with a discussion of several III-V and II-VI semiconductors. After seeing that the seven criteria provided in Ref. [191] are unsuitable for rationalizing the bulk- $\kappa_{\text{hex}}/\kappa_{\text{cub}}$ value for these materials, we develop an approach that successfully addresses this issue, providing insight into the factors determining the thermal conductivity of the materials we have studied. Additionally, we present and discuss the thermal conductivity for nanowires and alloy for both phases, focusing our discussion on nanowires. Finally, we also discuss about the phase and twin interfaces that can be fabricated in experimental samples of those materials, for the case of Si, GaP, and InP.

5.1. Cubic and hexagonal phases

We find it worth commenting on the structural differences between cubic and hexagonal phases. As aforementioned, most of the used semiconductors for solid-state devices are naturally grown in a cubic crystal system, namely diamond—which belongs to the $Fd\bar{3}m$ (227) space group—for unary crystals (i.e. those made of a single atomic type) and zinc-blende (ZB) for binary ones, which belongs to the $F\bar{4}3m$ (216) space group. Nevertheless, the hexagonal phase is for most

5. Thermal conductivity in nanoscale-emerging crystal phases

of them metastable or even more stable than its cubic counterpart in a few cases. Although some of those materials can crystallize in different hexagonal lattices, like BN with its layered structure, we will focus on lonsdaleite—which belongs to the $P6_3/mmc$ (194) space group, and that takes its name from the carbon allotrope crystallizing in hexagonal diamond structure, named after the crystallographer Kathleen Lonsdale and firstly identified in Canyon Diablo meteorite [194]—for unary structures and wurtzite (WZ) for binary crystals; belonging this crystal lattice to the $P6_3mc$ (186) space group.

Interestingly, for a given set of atomic elements, the two crystal phases have the same sp^3 hybridization, which confers the characteristic tetrahedral bonding structure; even the 1st-, 2nd-, and higher order-neighbors distances are quite similar [43, 195, 196]. Indeed, the main difference is the atomic stacking along [111] (cubic) and [0001] (hexagonal) crystal axis, going from the ABCABC... in cubic crystal systems to the ABABAB... for the hexagonal ones (see Fig. 5.1).

5.2. Lonsdaleite silicon

Maybe the most paradigmatic example, owing to its importance for the semiconductor industry, of this new-old phase is the silicon one. In a recent example, we have reported and discussed a reduction of 40% in the thermal conductivity between the more stable 3C cubic-Si and 2H hexagonal-Si [43] (see Fig. 5.2). Harmonic and anharmonic IFCs, needed to calculate these thermal conductivities, were obtained using the supercell method, as implemented in `Phonopy` [161] for the harmonic IFCs and `thirdorder.py` [46] for anharmonic IFCs. They were calculated in diamond polytype in a 5x5x5 supercell for harmonic IFCs and 4x4x4 for the anharmonic IFCs. For the lonsdaleite, the used supercell was 4x4x3 for both types of IFC. The unit cells used to span the supercells were optimized until strict limits for stress (0.01 kbar) and forces

5. Thermal conductivity in nanoscale-emerging crystal phases

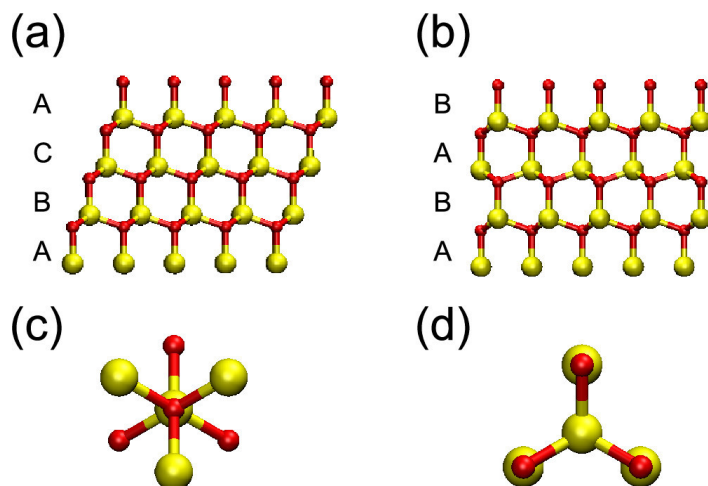


Figure 5.1.: Side view of (a) ZB and (b) WZ lattice structure where the ABCABC vs ABABAB stacking along the cubic $[111]$ axis can be appreciated. (c) Staggered and (d) eclipsed dihedral conformation of the ZB and WZ crystal phases. Reprinted with permission from [G. Giorgi, M. Amato, S. Ossicini, X. Cartoixà, E. Canadell, and R. Rurali, “Doping of III-V Arsenide and Phosphide Wurtzite Semiconductors”, *J. Phys. Chem. C* **124**, 27203–27212 (2020)]. Copyright 2020 American Chemical Society.

5. Thermal conductivity in nanoscale-emerging crystal phases

($5 \times 10^{-6} \text{ eV } \text{\AA}^{-1}$) were attained. These optimizations were conducted within DFT, using the plane-wave VASP [197–200] code with projector augmented-wave (PAW) potentials [201, 202] with a cutoff of 246 eV and a self-consistency tolerance of $1 \times 10^{-9} \text{ eV}$ for total energy and KS eigenvalues. LDA for the exchange-correlation as parametrized by Perdew and Zunger [59] to Ceperley-Alder [60] data was used. Then κ was obtained iteratively, for both Si bulk and nanowires, as implemented in ShengBTE [46] code using a Γ -centered $24 \times 24 \times 24$ \mathbf{q} -mesh which has been shown to yield a value of κ converged within 5% at room temperature [46].

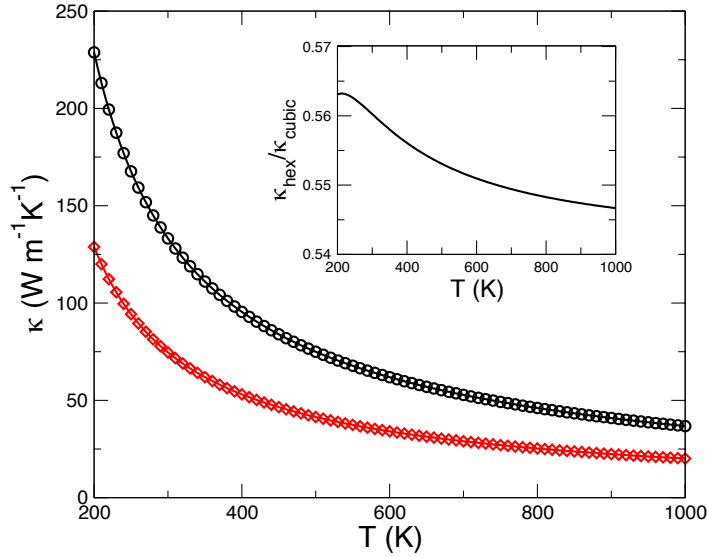


Figure 5.2.: Thermal conductivity of bulk cubic (circles) and hexagonal (diamonds) Si as a function of temperature. Reproduced from [M. Raya-Moreno, H. Aramberri, J. A. Seijas-Bellido, X. Cartoixà, and R. Rurali, “Thermal conductivity of hexagonal Si and hexagonal Si nanowires from first-principle”, Appl. Phys. Lett., **111** 032107 (2017)], with the permission of AIP Publishing.

This strong suppression of κ can be striking, owing to the similarities of both structures (see Section 5.1). Nonetheless, the symmetry reduction gives rise to

5. Thermal conductivity in nanoscale-emerging crystal phases

new low and medium-frequency optical phonons (see Fig. 5.3). Those optical modes reduce the acoustic-optical (a-o) gap, increasing in principle the probability of acoustic-acoustic-optical (a-a-o) scattering [192].

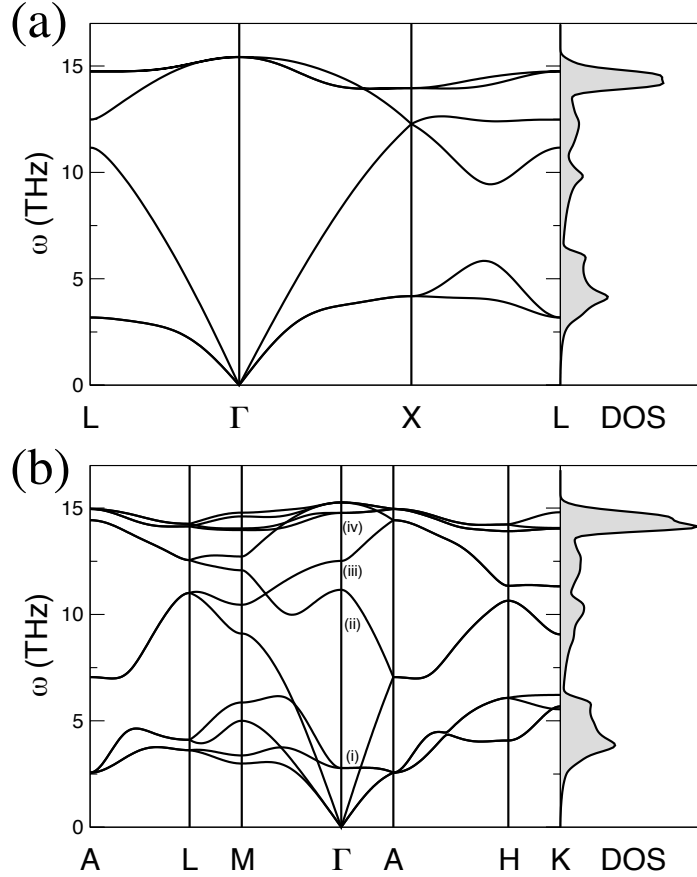


Figure 5.3.: Phonon band-structure of (a) cubic and (b) hexagonal Si. The eigenvectors of the low and mid-frequency optical modes at C, labeled (i)–(iv). The right hand-side panels show the vibrational density of states (DOS). Reproduced from [M. Raya-Moreno, H. Aramberri, J. A. Seijas-Bellido, X. Cartoixà, and R. Rurali, “Thermal conductivity of hexagonal Si and hexagonal Si nanowires from first-principle”, *Appl. Phys. Lett.*, **111** 032107 (2017)], with the permission of AIP Publishing.

5. Thermal conductivity in nanoscale-emerging crystal phases

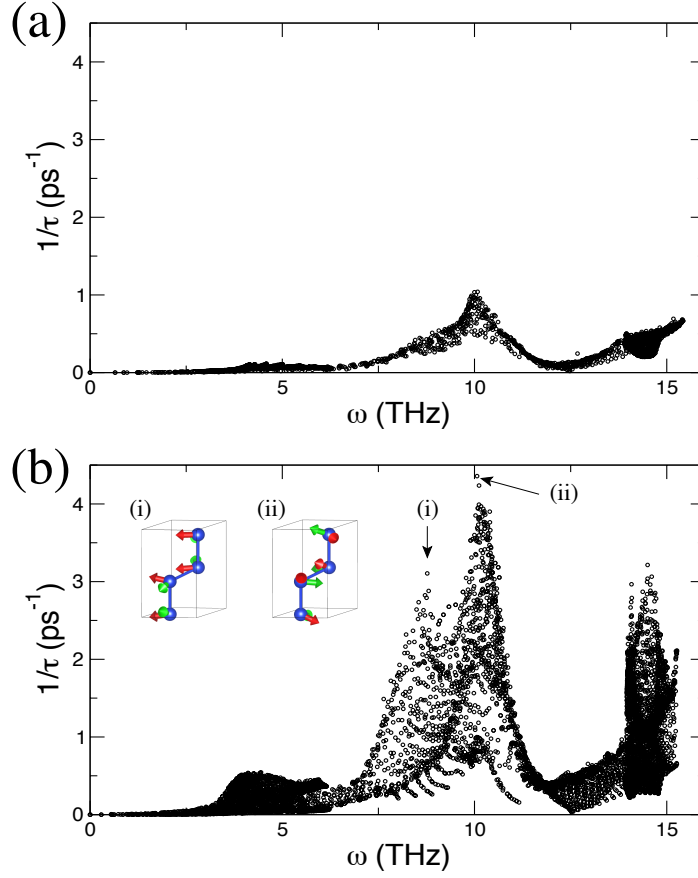


Figure 5.4.: Contribution of anharmonic three-phonon processes to the total scattering rate, for each q-point and each band for (a) cubic and (b) hexagonal Si. The inset in (b) shows the eigendisplacements of the modes that originate the two peaks at 8.7 and 10 THz; the red and green arrows indicate the real and the imaginary part of the eigenvector, i.e., the frozen phonon atomic displacement and atomic velocity, respectively. Reproduced from [M. Rayamoreno, H. Aramberri, J. A. Seijas-Bellido, X. Cartoixà, and R. Rurali, “Thermal conductivity of hexagonal Si and hexagonal Si nanowires from first-principle”, *Appl. Phys. Lett.*, **111** 032107 (2017)], with the permission of AIP Publishing.

5. Thermal conductivity in nanoscale-emerging crystal phases

To check to what extent these new modes result in the enormous reduction of κ , we have calculated the total RTA three-phonon scattering rates of each phonon mode as a function of the frequency (see Fig. 5.4). In cubic Si, a-a-o scattering and acoustic-optical-optical (a-o-o) scattering involving only transverse acoustic (TA) modes are largely suppressed because at most of the \mathbf{q} -points the a-o gap is larger than the acoustic bandwidth; thus, energy cannot be conserved in a three phonon process. The longitudinal acoustic (LA) mode, on the other hand, extends throughout a larger frequency range, and interaction with the optical phonons becomes possible. As a result, it is the latter that carries—with a peak at 10 THz, where the LA branch is closer to the optical bands—much of the total scattering rate. The picture changes drastically in hexagonal Si, where low and medium-frequency optical modes dominate the scattering rate, with up to a fourfold enhancement in the 8-11 THz range. Also, high-frequency scattering rates increase as a result of the additional optical phonons in the hexagonal lattice.

Consequently, the reduction in thermal conductivity between the cubic and the hexagonal phase is very well understood using some of the classical conditions for high thermal conductivity [192], namely the higher symmetry, and the larger a-o gap at most \mathbf{q} -points of the cubic phases, which results on a higher conductivity.

As previously mentioned, phases that are not thermodynamically stable at room temperature and atmospheric pressure in bulk form, like lonsdaleite, can naturally occur when the materials are grown as nanowires, and thus it is in nanowires that the cubic and hexagonal phases can both be easily accessed. Therefore, it is interesting to discuss the conductivity along the stacking direction, which is also the common growth direction ([111] for cubic and [0001] for hexagonal) for nanowires of different materials and diameters. Despite being one-dimensional structures, nanowire phonon dispersions can be approximated to the bulk ones for nanowires with diameters $\gtrsim 60$ -70 nm [40]. Hence, the PBTE can be solved using the methodology of Subsection 3.2.3 as implemented in ShengBTE [46].

5. Thermal conductivity in nanoscale-emerging crystal phases

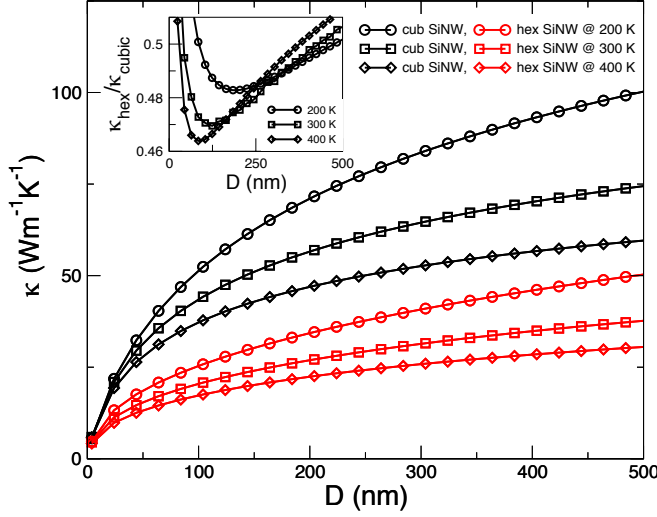


Figure 5.5.: Thermal conductivity of cubic (black lines) and hexagonal (red lines) Si NWs as a function of their diameter at $T = 200, 300$, and 400 K. Inset: ratio of the thermal conductivity, $\kappa_{\text{hex}}/\kappa_{\text{cub}}$, between hexagonal and cubic NWs. Reproduced from [M. Raya-Moreno, H. Aramberri, J. A. Seijas-Bellido, X. Cartoixà, and R. Rurali, “Thermal conductivity of hexagonal Si and hexagonal Si nanowires from first-principle”, *Appl. Phys. Lett.*, **111** 032107 (2017)], with the permission of AIP Publishing.

Therefore, in Fig. 5.5 we plot the thermal conductivity as a function of the nanowire diameter at three different temperatures for cubic and hexagonal Si NWs. Like their bulk counterparts, hexagonal Si NWs are considerably less conductive than cubic ones, with more pronounced reductions $\kappa_{\text{hex}}/\kappa_{\text{cub}}$ for diameters around 100-150 nm, depending on the temperature (inset of Fig. 5.5). For instance, a hexagonal Si NW with a typical diameter of 200 nm has a remarkably low thermal conductivity of $27 \text{ W m}^{-1} \text{ K}^{-1}$ at room temperature, making them an interesting candidate for thermoelectric applications.

5.3. III-V and II-VI semiconductors

Following the description of thermal conductivity in cubic and hexagonal phases for Si, we extend now such a discussion to other widely used III-V and II-VI semiconductors, namely: BN, AlAs, GaN, GaAs, GaP, InP, InAs, and ZnSe. To do so, the harmonic and anharmonic IFCs, needed to calculate the thermal conductivity, were obtained using the supercell method, as implemented in Phonopy [161] for the harmonic IFCs and `thirdorder.py` [46] for anharmonic IFCs. They were calculated in cubic polytypes in a $5 \times 5 \times 5$ supercell for harmonic IFCs and $4 \times 4 \times 4$ for the anharmonic IFCs. For hexagonal polytypes, the used supercell was $4 \times 4 \times 3$ for both types of IFC. To minimize the computational burden, anharmonic IFCs were computed from interactions up to fourth nearest neighbors, while it has been previously reported that including up to third nearest neighbors was sufficient to give a satisfactorily converged value of κ [46]. The unit cells used to span the supercells were optimized until strict limits for stress (3×10^{-3} GPa) and forces (5×10^{-4} eV Å⁻¹) were attained. These optimizations were conducted within DFT, using the plane-wave VASP [197–200] code with projector augmented-wave (PAW) potentials [201, 202]. LDA for the exchange-correlation as parametrized by Perdew and Zunger [59] to Ceperley-Alder [60] data was used. For each system, the k -point mesh size had been previously optimized, taking into account that the supercell used to calculate 3rd-order IFCs should be commensurate with the mesh in order not to introduce spurious forces. Therefore, the selected primitive cell k -mesh for cubic materials was a $16 \times 16 \times 16$ shifted mesh, and a $16 \times 16 \times 12$ Γ -centered mesh for hexagonal polytypes, which are converged meshes for all systems. After optimization, a DFPT run using VASP, with a doubled k -mesh was performed to obtain the Born charges (Z^*) and dielectric constant at high frequency (ϵ^∞), needed to calculate the non-analytic term correction for the dynamical matrix near Γ .

5. Thermal conductivity in nanoscale-emerging crystal phases

After obtaining the IFCs, the full linearized PBTE was solved iteratively, as implemented in the `almaBTE` [47] code for bulk and the `ShengBTE` code [46] for nanowires.

Regarding convergence with \mathbf{q} -mesh, we found (see Figs. 5.6-5.7 and 5.8-5.9) that for all materials but GaN and BN a q -mesh of $30 \times 30 \times 30$ (ZB) and $30 \times 30 \times 19$ (WZ) is enough to obtain converged values—less than 5% change with respect to a higher accuracy $34 \times 34 \times 34/21$ (ZB/WZ) mesh—of κ and κ_{pure} (i.e. without isotopes) for the 50–1000 K range. For GaN the converged \mathbf{q} -mesh is found to be $34 \times 34 \times 34$ (ZB) and $34 \times 34 \times 21$ (WZ) for κ and κ_{pure} , with respect to a $38 \times 38 \times 38/24$ (ZB/WZ) mesh. Finally, the harder phonon modes of BN translate into a more demanding convergence behavior. On one hand, \mathbf{q} -mesh convergence was only achieved for a $38 \times 38 \times 38$ and $38 \times 38 \times 24$ mesh, but only for the non-isotopically pure material, while the iterative calculation did not reach convergence for the isotopically pure material at low temperatures. Note that all these \mathbf{q} -mesh values are significantly denser than the $24 \times 24 \times 24$ mesh needed to achieve convergence in Si [46].

5.3.1. Interatomic Force Constants test

Owing to the computational cost required to obtain the anharmonic IFCs (168 and 208 DFT runs for cubic and hexagonal polytypes, respectively), prior to their calculation an accuracy test to the harmonic IFCs was done using Phonopy [48, 161, 203], by checking the optical phonon frequencies at the Γ point. These results, comparing calculated and experimental values, are shown in the phonon dispersion relations (see Figs. 5.10-5.13), exhibiting, despite small differences, a good agreement between our calculations and the experimental values for the TO modes. The non-analytical correction (NAC), needed in polar materials to get the LO-TO splitting, is underestimated because of it being inversely propor-

5. Thermal conductivity in nanoscale-emerging crystal phases

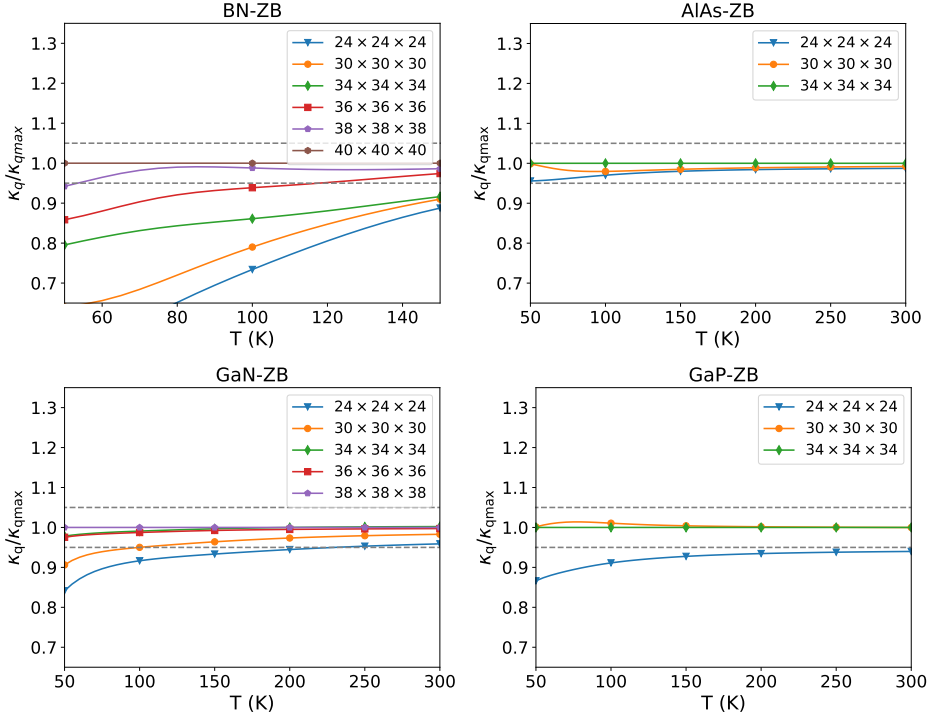


Figure 5.6.: Convergence of thermal conductivity with respect to the maximum q -mesh value for BN, AlAs, GaN, and GaP, as function of temperature for the zinc-blende phase. Dashed lines indicate the 5% threshold which we have taken as our convergence criterion. © American Physical Society. Reproduced with permission from Ref. [195].

5. Thermal conductivity in nanoscale-emerging crystal phases

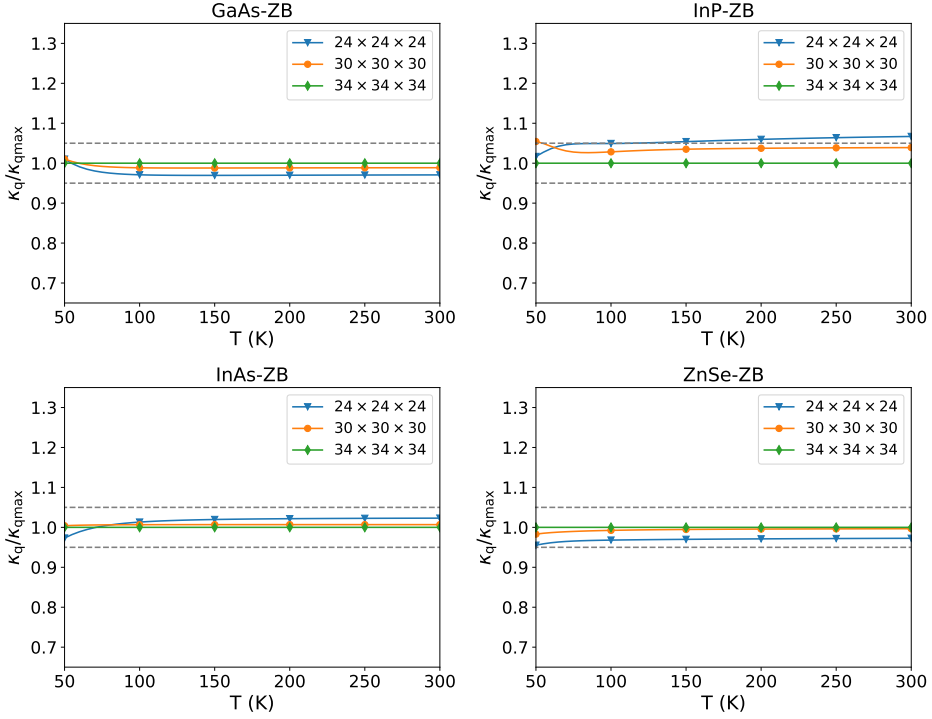


Figure 5.7.: Convergence of thermal conductivity with respect to the maximum q -mesh value for GaAs, InP, InAs and ZnSe, as function of temperature for the zinc-blende phase. Dashed lines indicate the 5% threshold which we have taken as our convergence criterion. © American Physical Society. Reproduced with permission from Ref. [195].

5. Thermal conductivity in nanoscale-emerging crystal phases

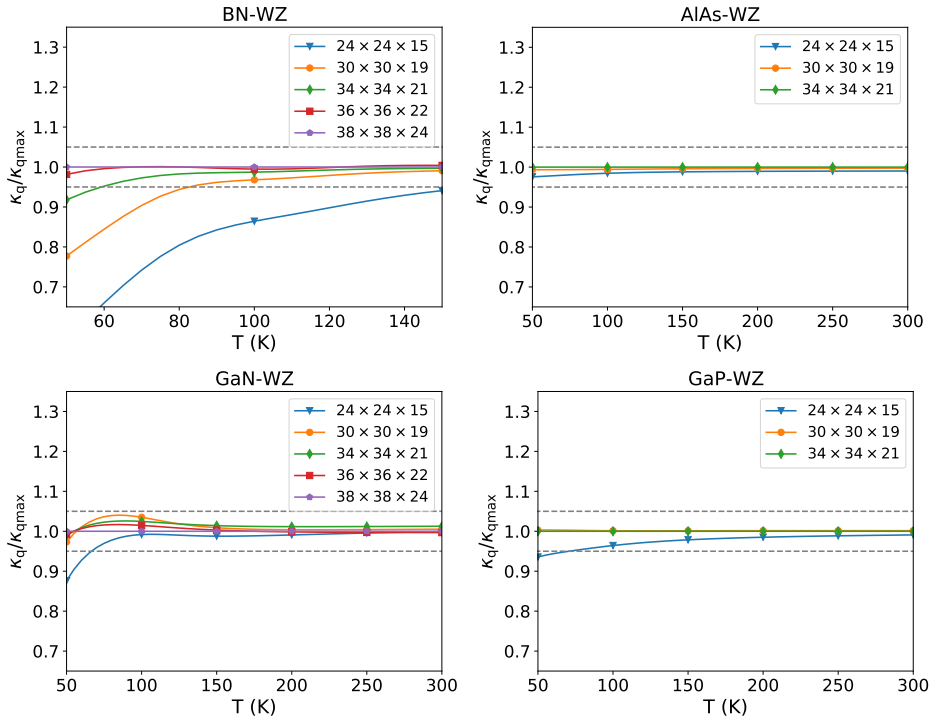


Figure 5.8.: Like Fig. 5.6, but for the wurtzite phase. © American Physical Society. Reproduced with permission from Ref. [195].

5. Thermal conductivity in nanoscale-emerging crystal phases

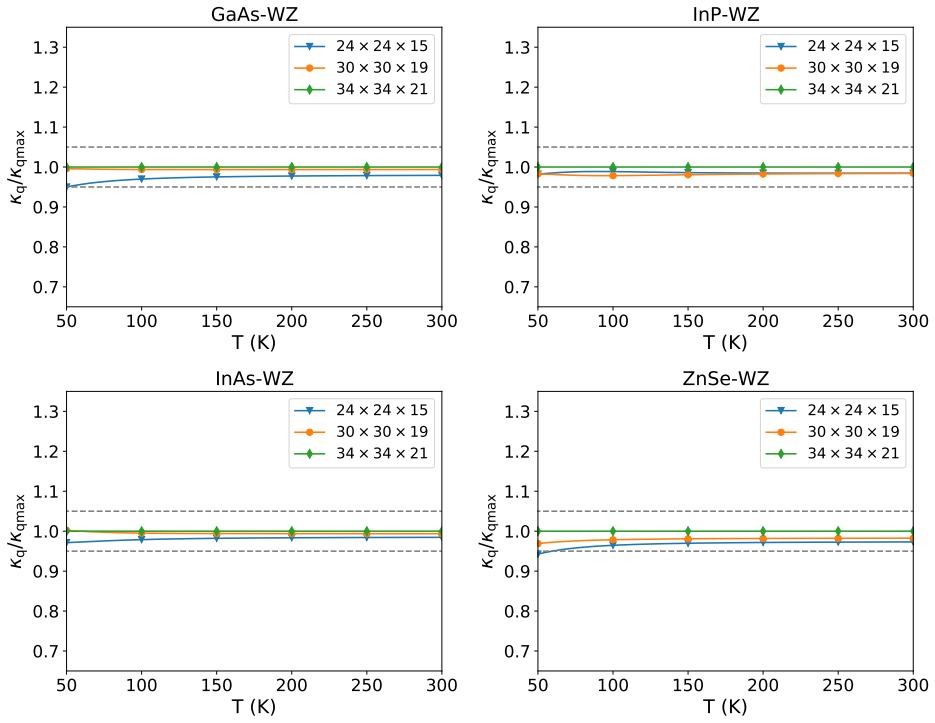


Figure 5.9.: Like Fig. 5.7, but for the wurtzite phase. © American Physical Society. Reproduced with permission from Ref. [195].

5. *Thermal conductivity in nanoscale-emerging crystal phases*

tional to ϵ^∞ (see Eq. 2.19 in Subsection 2.1.1.1), which is overestimated due to LDA inability to take into account the polarization dependence on the exchange-correlation functional under a field [204]. This leads to an underestimation of the LO frequency with respect to the experiments; nonetheless, we expect this discrepancy to have a nearly residual effect over thermal conductivity as it mostly affects high-frequency phonons near Γ the contribution of which to κ is small. It should be noted, nonetheless, that the effect of LDA and GGA shortcomings have been proven to have a smaller effect in the anharmonic properties than in the harmonic ones [205, 206].

5. Thermal conductivity in nanoscale-emerging crystal phases

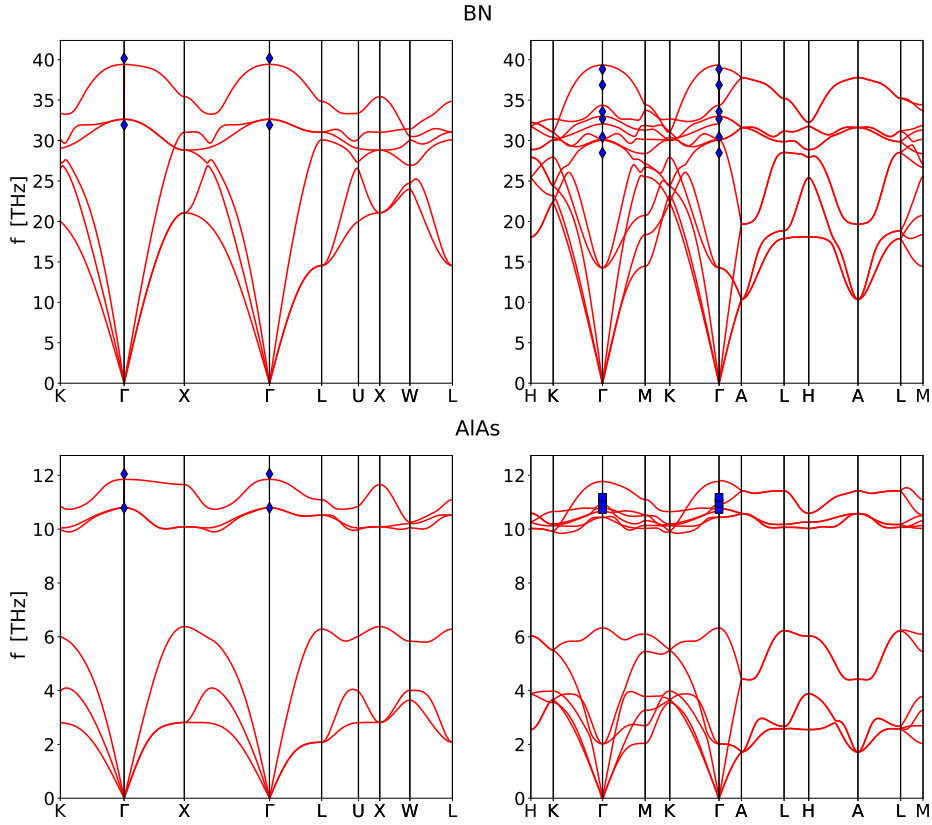


Figure 5.10.: Dispersion relation for BN (top) and AlAs (bottom) in the cubic (left) and hexagonal (right) phases. Experimental results for BN are from Ref. [207] (diamonds); and results for AlAs are from Ref. [208] (squares) and Ref. [209] (diamonds). © American Physical Society. Reproduced with permission from Ref. [195].

5. Thermal conductivity in nanoscale-emerging crystal phases

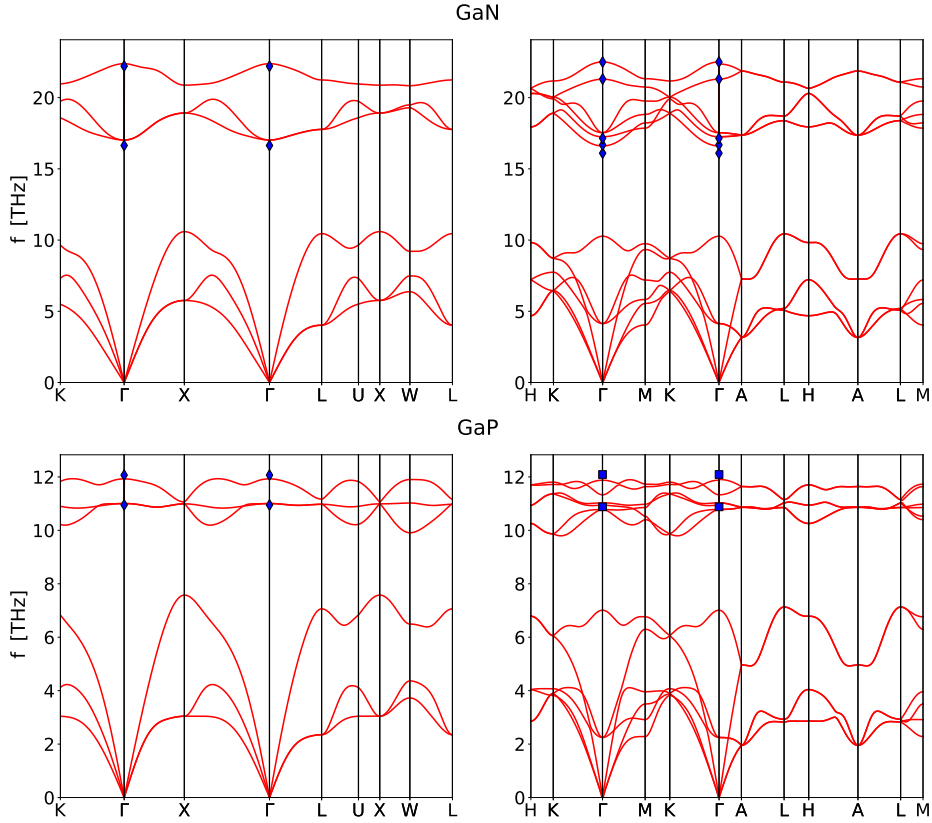


Figure 5.11.: Dispersion relation for GaN (top) and GaP (bottom) in the cubic (left) and hexagonal (right) phases. Experimental results for GaN are from Ref. [210] (diamonds), and the results for GaP are from Ref. [30] (squares) and Ref. [211] (diamonds). © American Physical Society. Reproduced with permission from Ref. [195].

5. Thermal conductivity in nanoscale-emerging crystal phases

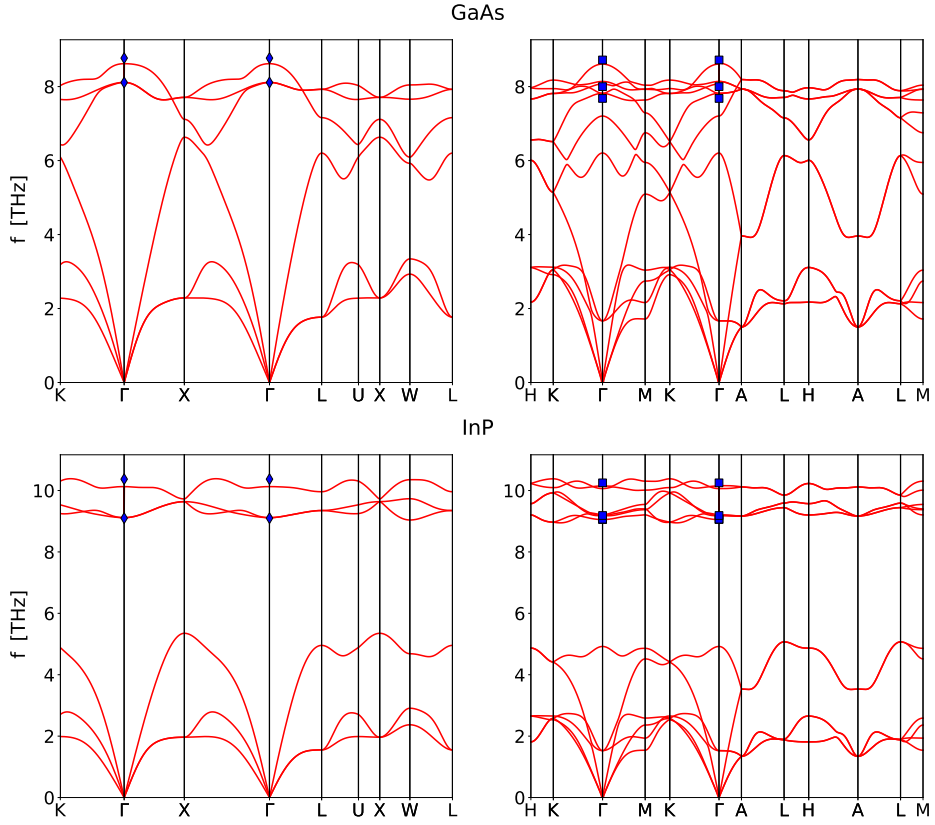


Figure 5.12.: Dispersion relation for GaAs (top) and InP (bottom) in the cubic (left) and hexagonal (right) phases. Experimental results for GaAs are from Ref. [28] (squares) and Ref. [212] (diamonds), and the results for InP are from Ref. [213] (squares) and Ref. [214] (diamonds). © American Physical Society. Reproduced with permission from Ref. [195].

5. Thermal conductivity in nanoscale-emerging crystal phases

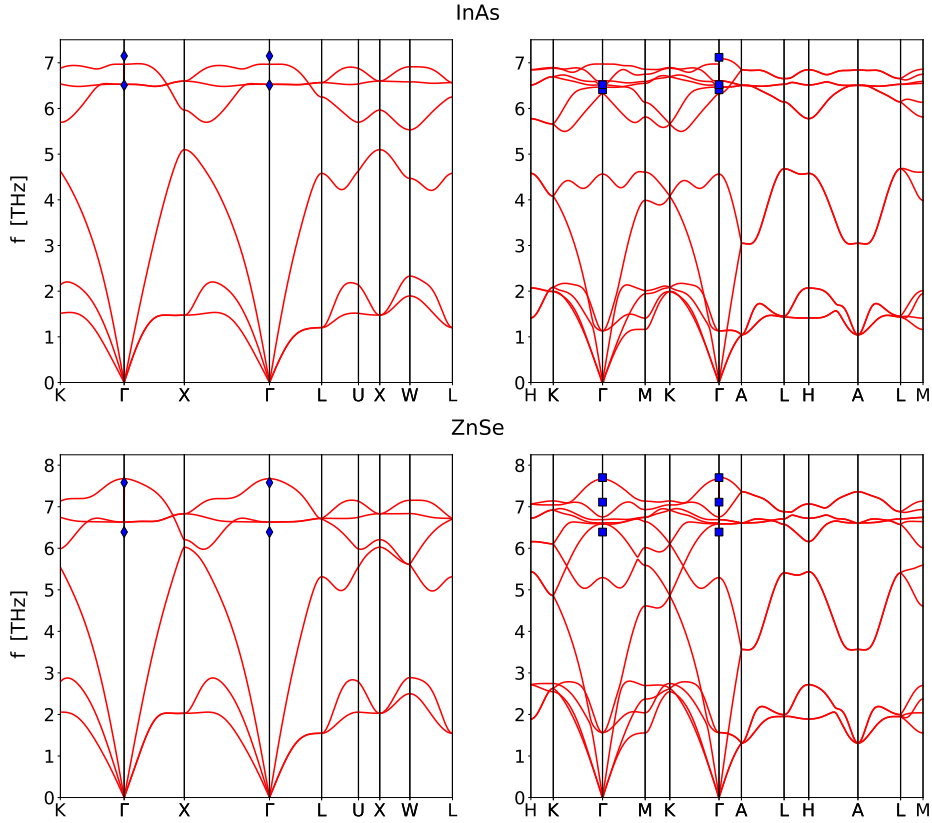


Figure 5.13.: Dispersion relation for InAs (top) and ZnSe (bottom) in the cubic (left) and hexagonal (right) phases. Experimental results for InAs are from Ref. [215] (squares) and Ref. [216] (diamonds), and the results for ZnSe are from Ref. [217] (squares) and Ref. [218] (diamonds). © American Physical Society. Reproduced with permission from Ref. [195].

5.3.2. Bulk

In this section, we study the thermal conductivities of cubic (ZB) and hexagonal (WZ) phases for different compound semiconductors. We further substantiate our results by comparing our calculated thermal conductivity to available experimental values (see Table 5.1). It is reasonable to expect that, for some materials, our results overestimate the experimental values, because samples used in such experiments might contain defects (impurities, vacancies, dislocations, etc), which can strongly suppress thermal conductivity, and they have not been considered in our simulations. Moreover, there might be a dependence of the measured value on the experimental technique, and it is quite challenging to obtain experimental thermal conductivity values with less than 5% error [219]. We note that our values are in excellent agreement with experimental results for GaAs and AlAs, while keeping a good agreement for InP, InAs, ZnSe, and GaP. In the nitrides, BN, and GaN, we obtain values within the dispersion of the experimentally reported magnitudes. Regarding comparison with other first-principles calculations, our results are in reasonable agreement with those of Lindsay et al. [45], while there is a stronger disagreement with the values of Togo et al. [48], which are obtained by a different approach to the LBTE. These two approaches are known to provide different values for the thermal conductivity in transition metal dichalcogenides as well [164].

We found (see Table 5.1 and Figs. 5.14-5.21) that most of the materials under study (GaAs, GaP, InP, InAs, ZnSe, and AlAs) follow the silicon behavior of reducing their κ with symmetry [43]. However, we observe that is possible for some materials (GaN) to have the opposite behavior, namely κ increases when symmetry is reduced, i.e. going from ZB to WZ. Moreover, as previously observed in other materials [190], BN can show these two opposite behaviors at different temperatures.

5. Thermal conductivity in nanoscale-emerging crystal phases

Table 5.1.: + Calculated κ and $\kappa_{\text{hex}}/\kappa_{\text{cub}}$ ratios at 300 K. The experimental κ at room temperature is also presented at normal conditions. The values for all κ 's are given in $\text{W m}^{-1} \text{K}^{-1}$. © American Physical Society. Reproduced with permission from Ref. [195].

	$\kappa_{\text{cub}}^{\text{calc}}$ Ref. [48]	$\kappa_{\text{hex}}^{\text{calc}}$ Ref. [48]	$\kappa_{\text{cub}}^{\text{calc}}$ Ref. [45]	$\kappa_{\text{hex}}^{\text{calc}}$ Ref. [45]	$\kappa_{\text{cub}}^{\text{calc}}$ This work	$\kappa_{\text{hex}}^{\text{calc}}$ This work	$\kappa_{\text{hex}}/\kappa_{\text{cub}}$	$\kappa^{\text{exp}\dagger}$
BN	726	592 (602/573) [§]	940 ^{††}	–	1071	887.7 (906.6/849.9) [§]	0.845	760 ^a (cub) 1200 ^b (cub)
AlAs	86.8	72.9 (73.9/71.0)	105	–	100.0	65.84 (65.54/66.45)	0.655	98 ^a (cub) 91 ^c (cub)
GaN	181	171 (171/172)	215	241 (242/239)	290.7	304.3 (293.8/325.3)	1.047	253 ^d (hex) 269 ^e (hex) 294 ^f (hex) 280 ^g (hex) 300 ^g (hex) 330 ^g (hex) 380 ^g (hex)
GaP	104	92.8 (96.5/85.4)	131	–	157.1	144.7 (148.8/136.4)	0.915	77 ^h (cub) 100 ^a (cub) 110 ⁱ (cub)
GaAs	32.1	27.2 (27.8/25.9)	54	–	47.23	39.52 (38.97/40.61)	0.837	45 ^a (cub) 45.5 ^j (cub) 46 ^k (cub)
InP	85.2	68.9 69.3/68.2	89	–	106.2	87.82 (85.46/92.55)	0.827	93 ^a (cub) 67 ^k (cub) 68 ^h (cub)
InAs	25.2	18.3 (18.5/18.0)	36	–	36.63	33.29 (33.13/33.61)	0.909	30 ^a (cub) 27.3 ^j (cub) 26.5 ^h (cub)
ZnSe	15.6	14.0 (13.8/14.5)	–	–	26.06	22.35 (21.65/23.76)	0.858	19 ^{a,l} (cub) 33 ^m (cub)

[†] Mean of κ trace (in-plane κ / out-of-plane κ , along c-crystallographic axis).

[‡] The material phase of the experimental measurement is indicated between brackets.

[§] The hexagonal phase refers to WZ, as opposed to the layered h-BN phase.

^{††} This value is from Ref. [193]

^a Ref. [220]

^b Refs. [221, 222]

^c Ref. [223]

^d Ref. [224]

^e Ref. [225]

^f Ref. [226]

^g Ref. [227]. Measurements are done at 298.15 K.

^h Ref. [228]

ⁱ Ref. [229]

^j Ref. [230]

^k Ref. [231]

^l Ref. [232]

^m Ref. [233]

5. Thermal conductivity in nanoscale-emerging crystal phases

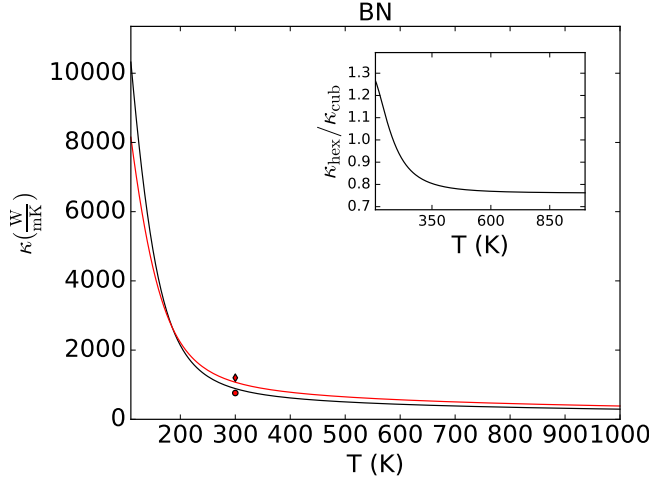


Figure 5.14.: Hexagonal(black) and cubic(red) BN thermal conductivity κ trace mean as a function of temperature. Experimental results for cubic phase are from Ref. [220] (circle) and Ref. [221, 222] (diamond). Inset: ratio between hexagonal and cubic thermal conductivity as a function of the temperature. © American Physical Society. Reproduced with permission from Ref. [195].

5.3.2.1. Standard analysis of $\kappa_{\text{hex}}/\kappa_{\text{cub}}$

Four conditions that a crystal must fulfill to have a high κ have been long established [192]: (I) to be structurally simple, (II) to be composed of light elements, (III) to have strong covalent bonds—represented normally by a high Debye temperature/frequency (f_D)—and (IV) to be harmonic, which is normally associated to a low Grüneisen parameter (γ).

Recently, three additional conditions for a high κ have been introduced by Lindsay *et al.* [193] and Mukhopadhyay *et al.* [191]. They demonstrated that, in addition to the four previous conditions, a higher κ is obtained if the material also has (V) a high “acoustic-optical” (a-o) gap, (VI) a high “acoustic bunching” and

5. Thermal conductivity in nanoscale-emerging crystal phases

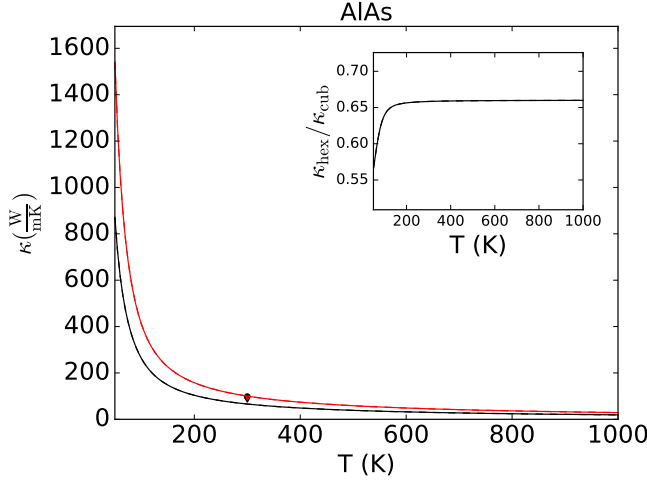


Figure 5.15.: Hexagonal(black) and cubic(red) AlAs thermal conductivity κ trace mean as a function of temperature. Experimental results for cubic phase are from Ref. [220](circle) and Ref. [223]. Since both constituting elements are isotopically pure, AlAs presents no isotopic scattering. Inset: ratio between hexagonal and cubic thermal conductivity as a function of the temperature. © American Physical Society. Reproduced with permission from Ref. [195].

(VII) low optical bandwidth.

We have collected those seven conditions for all materials under study, with values from our first-principles calculations, in Table 5.2. Interestingly, by observing those conditions together with the κ values, we see that they do not clarify which of the phases—cubic or hexagonal—is the most conductive: for instance if one looks at GaN four out of seven criteria suggest that zinc-blende phase should be the most conductive one, while one of them is neutral and only two of them predict a larger κ for the wurtzite. Yet, the calculations predict the latter to be more conductive. Additionally, those conditions cannot either explain the reason for some materials, like BN, to change their $\kappa_{\text{hex}}/\kappa_{\text{cub}}$ ratio behavior

5. Thermal conductivity in nanoscale-emerging crystal phases

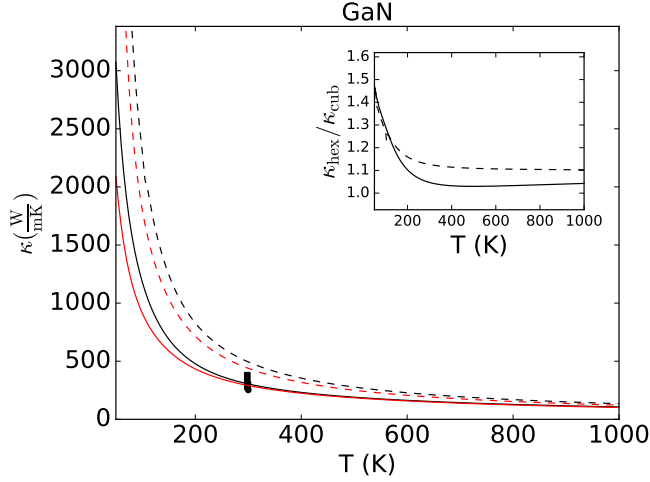


Figure 5.16.: Hexagonal(black) and cubic(red) GaN thermal conductivity κ (solid) and κ_{pure} (dashed) trace mean as a function of temperature. Experimental results for hexagonal phase are from: Ref. [224] (circle), Ref. [225] (diamond), Ref. [226] (triangle) and Ref. [227] (square). Inset: ratio between hexagonal and cubic thermal conductivity as a function of the temperature with (solid) and without (dashed) isotopic scattering. We notice that some numerical instabilities/noise were found in isotope free simulations at low temperature for wurtzite phase. © American Physical Society. Reproduced with permission from Ref. [195].

with temperature. Such a shortcoming is due to being based on arguments of a qualitative character that do not quantify the relative importance of each condition, thus the necessity of a more quantitative viewpoint to predict/understand which phase is the most conductive at a given temperature.

5. Thermal conductivity in nanoscale-emerging crystal phases

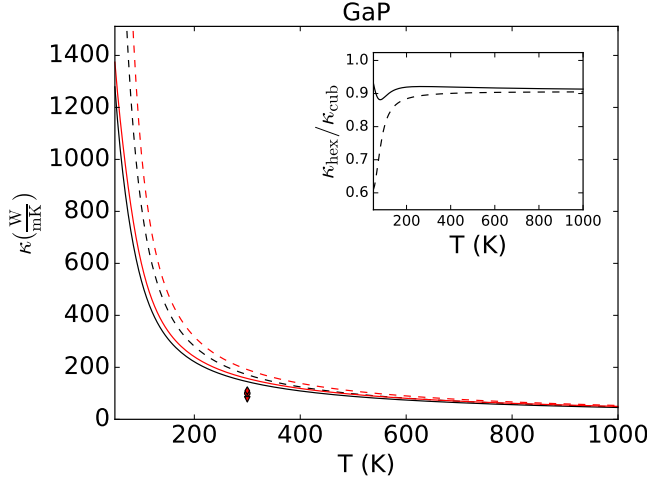


Figure 5.17.: Hexagonal(black) and cubic(red) GaP thermal conductivity κ (solid) and κ_{pure} (dashed) trace mean as a function of temperature. Experimental results for cubic phase are from Ref. [228] (triangle), Ref. [220](circle) and Ref. [229](diamond). Inset: ratio between hexagonal and cubic thermal conductivity as a function of the temperature with (solid) and without (dashed) isotopic scattering. © American Physical Society. Reproduced with permission from Ref. [195].

5.3.2.2. Effective anharmonicity and accessible phase space

To gain insight into the $\kappa_{\text{hex}}/\kappa_{\text{cub}}$ ratio at different temperatures, we focus our analysis on two quantities that together contain all conditions: the three-phonon scattering matrix elements or anharmonicity (high- κ conditions I, II, III and IV) and phase space, i.e. all the energy-conserving three-phonon combinations (high- κ conditions I, II, V, VI, and VII). In particular, the condition I, i.e. to be structural simple, leads to not only a lower number of bands, and thus available channels of scattering—namely phase space—but a decrease in the magnitude of the matrix elements, i.e. anharmonicity, due to the phase factors inside Eq. 2.54 [234]. Similarly, the mass effect is contained in both anharmonicity, through anharmonic

5. Thermal conductivity in nanoscale-emerging crystal phases

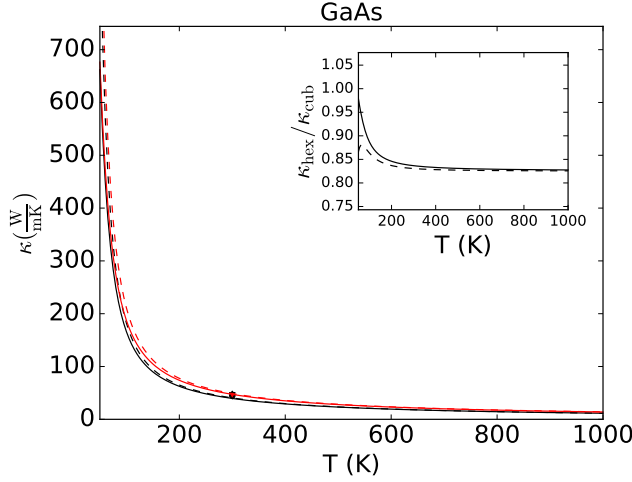


Figure 5.18.: Hexagonal(black) and cubic(red) GaAs thermal conductivity κ (solid) and κ_{pure} (dashed) trace mean as a function of temperature. Experimental results for cubic phase are from Ref. [220](circle) Ref. [230](triangle) and Ref. [231](diamond). Inset: ratio between hexagonal and cubic thermal conductivity as a function of the temperature with (solid) and without (dashed) isotopic scattering. © American Physical Society. Reproduced with permission from Ref. [195].

Hamiltonian dependence on mass (see Eq. 2.54), and the phase space, as the phonon spectrum indirectly depends on mass, through the dynamical matrix (see Eq. 2.9). Furthermore, condition III, i.e. strong bonding, is related to the potential, and thus to the anharmonic force constants (anharmonicity), as well as to the harmonic ones, so that the strong bonding leads to harder phonon modes, therefore affecting the phase space. As for condition IV, i.e. being harmonic, this is directly related to anharmonicity, keeping no relation to phase space. Finally, conditions V, VI, and VII lead to an increase in the available channels of scattering, namely they allow further acoustic-acoustic-optic (V), acoustic-acoustic-acoustic (VI), and acoustic-optic-optic processes, and are thus contained in the phase space.

5. Thermal conductivity in nanoscale-emerging crystal phases

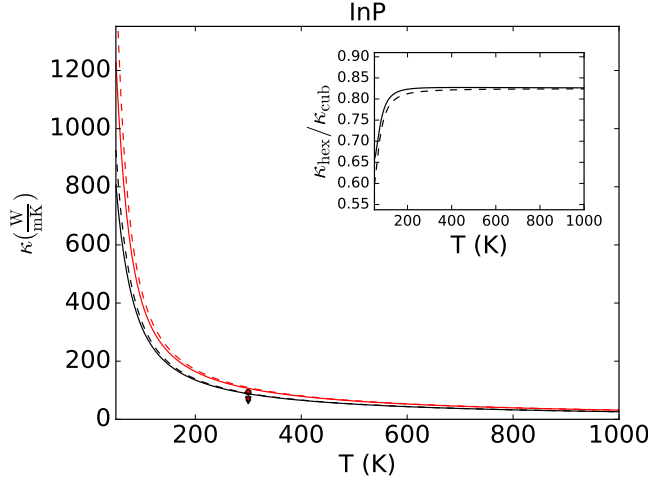


Figure 5.19.: Hexagonal(black) and cubic(red) InP thermal conductivity κ (solid) and κ_{pure} (dashed) trace mean as a function of temperature. Experimental results for cubic phase are from Ref. [228] (triangle), Ref. [220] (circle) and Ref. [231] (diamond). Inset: ratio between hexagonal and cubic thermal conductivity as a function of the temperature with (solid) and without (dashed) isotopic scattering. © American Physical Society. Reproduced with permission from Ref. [195].

In fact, anharmonicity and phase space directly contribute to κ via the three-phonon scattering rate [46] (see Eqs. 2.58, 2.59 and 3.12).

As it can be seen from Eqs. 2.58 and 2.59, an increment in anharmonicity ($V_{\lambda\lambda'\lambda''}^{\pm}$), where the superscript $- (+)$ refers to emission (absorption) three-phonon processes, produces an increment in the scattering rate, therefore a reduction in κ . In the same way, an increment in phase space, represented in the Eqs. 2.58 and 2.59 by the energy conservation delta $\delta(\omega_{\lambda} \pm \omega_{\lambda'} - \omega_{\lambda''})$, also reduces κ .

Comparing the phonon dispersion of both phases for all materials (see Figs. 5.10-5.13) it becomes obvious that similarly to the lonsdaleite the symmetry reduction, which causes the appearance of new low/medium optical eigenmodes with non-

5. Thermal conductivity in nanoscale-emerging crystal phases

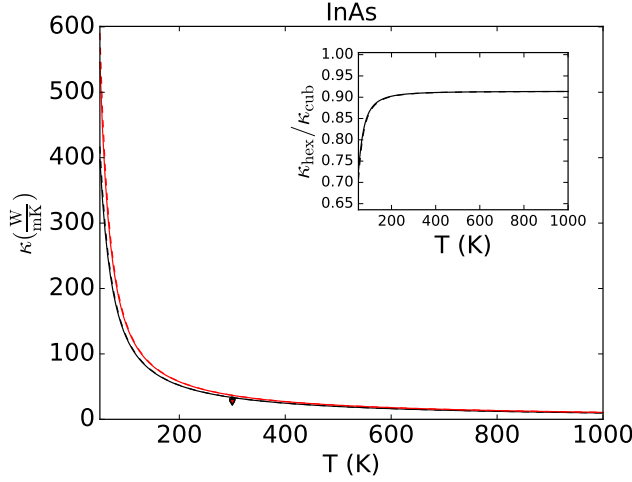


Figure 5.20.: Hexagonal(black) and cubic(red) InAs thermal conductivity κ (solid) and κ_{pure} (dashed) trace mean as a function of temperature. Experimental results for cubic phase are from Ref. [228] (triangle), Ref. [220] (circle) and Ref. [231] (diamond). Inset: ratio between hexagonal and cubic thermal conductivity as a function of the temperature with (solid) and without (dashed) isotopic scattering. © American Physical Society. Reproduced with permission from Ref. [195].

vanishing scattering matrix elements, also increases the phase space for transitions at a given temperature. In order to obtain an actual measurement of accessible phase space while taking into account the effect of temperature, we calculate it ($\delta_{\text{occ},T}$) defined as follows:

$$\delta_{\text{occ},T} = \frac{2}{3}(\delta_{\text{occ},T}^+ + \frac{1}{2}\delta_{\text{occ},T}^-) \quad (5.1)$$

5. Thermal conductivity in nanoscale-emerging crystal phases

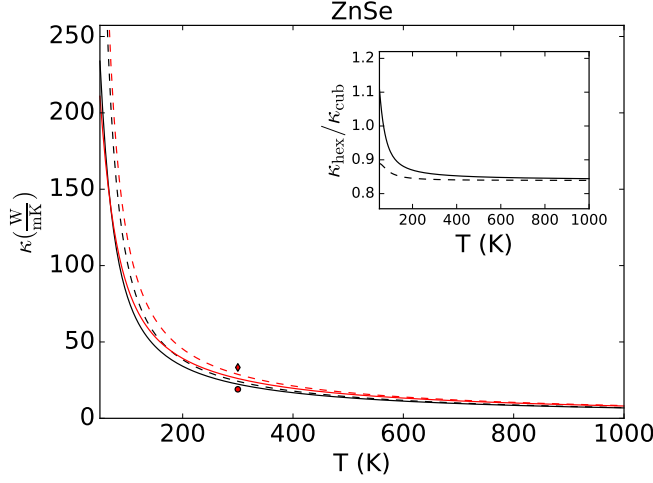


Figure 5.21.: Hexagonal(black) and cubic(red) ZnSe thermal conductivity κ (solid) and κ_{pure} (dashed) trace mean as a function of temperature. Experimental results for cubic phase are from Ref. [220, 232] (circle) and Ref. [233] (diamond). Inset: ratio between hexagonal and cubic thermal conductivity as a function of the temperature with (solid) and without (dashed) isotopic scattering. © American Physical Society. Reproduced with permission from Ref. [195].

$$\delta_{\text{occ},T}^+ = 2\pi \left[\frac{V_{\text{BZ}}}{(2\pi)^3} \right]^3 \sum_{ijk} \iiint_{\text{BZ}} \delta(\omega_\lambda + \omega_{\lambda'} - \omega_{\lambda''}) \times \\ n_{\mathbf{q},i}^0 n_{\mathbf{q}',j}^0 (1 + n_{\mathbf{q}'',k}^0) \delta_{\mathbf{q}+\mathbf{q}',\mathbf{q}''+\mathbf{G}} d\mathbf{q}'' d\mathbf{q}' d\mathbf{q}, \quad (5.2)$$

$$\delta_{\text{occ},T}^- = 2\pi \left[\frac{V_{\text{BZ}}}{(2\pi)^3} \right]^3 \sum_{ijk} \iiint_{\text{BZ}} \delta(\omega_\lambda - \omega_{\lambda'} - \omega_{\lambda''}) \times \\ n_{\mathbf{q},i}^0 (1 + n_{\mathbf{q}',j}^0) (1 + n_{\mathbf{q}'',k}^0) \delta_{\mathbf{q}-\mathbf{q}',\mathbf{q}''+\mathbf{G}} d\mathbf{q}'' d\mathbf{q}' d\mathbf{q}, \quad (5.3)$$

where $\delta_{\mathbf{q}\pm\mathbf{q}',\mathbf{q}''+\mathbf{G}}$ is the momentum conservation condition; $\delta_{\text{occ},T}^+$ and $\delta_{\text{occ},T}^-$

5. Thermal conductivity in nanoscale-emerging crystal phases

Table 5.2.: Seven standard conditions of high κ for all materials in both phases. Boldface indicates the characteristic more favorable to a higher κ . M_{avg} stands for the average atomic mass of the unit cell, f_D for the Debye frequency and $\gamma_{300\text{ K}}$ for the Grüneisen parameter at room temperature. © American Physical Society. Reproduced with permission from Ref. [195].

material	(I) crystal structure	(II) M_{avg} (amu)	(III) f_D (THz)	(IV) $\gamma_{300\text{ K}}$	(V) “a-o” gap (THz)	(VI) “acoustic” bunching (THz)	(VII) optical bandwidth (THz)
BN	WZ	12.41	39.15	0.67	0.00	30.11	11.41
	ZB	12.41	39.15	0.73	0.00	15.55	9.37
AlAs	WZ	50.95	5.44	0.29	3.54	6.32	1.93
	ZB	50.95	5.41	0.40	3.55	3.56	1.93
GaN	WZ	41.86	9.75	0.64	6.18	10.27	5.87
	ZB	41.86	9.71	0.70	6.50	6.43	5.36
GaP	WZ	50.35	6.66	0.51	2.67	7.01	2.10
	ZB	50.35	5.57	0.57	2.49	4.53	1.99
GaAs	WZ	72.32	4.53	0.55	0.00	6.21	2.89
	ZB	72.32	4.67	0.60	0.00	4.35	2.53
InP	WZ	72.90	3.51	0.38	3.88	4.92	1.42
	ZB	72.90	3.48	0.48	3.69	3.41	1.35
InAs	WZ	94.87	2.92	0.36	0.82	4.56	1.55
	ZB	94.87	3.07	0.38	0.51	3.62	1.39
ZnSe	WZ	72.17	4.70	0.67	0.00	5.29	2.03
	ZB	72.17	4.47	0.71	0.00	4.00	2.06

5. Thermal conductivity in nanoscale-emerging crystal phases

are the contribution to the accessible phase space of absorption and emission processes, i, j, \dots refer to phonon bands, $n_{i,\mathbf{q}}^0$ is the equilibrium Bose-Einstein distribution function of the $\lambda = (\mathbf{q}, i)$ phonon mode, and the $2/3$ and $1/2$ weighting factors ensure the normalization and non double counting of processes [235]. Therefore, $\delta_{\text{occ},T}$ gives an idea for a given temperature of the accessible part of the available phase space. Certainly, the attainable phase space for the different materials (see Table 5.3) confirms that, as inferred from dispersion relations, the hexagonal phase has a greater accessible phase space which contributes to reducing the $\kappa_{\text{hex}}/\kappa_{\text{cub}}$ ratio. This is a general feature of all the studied materials.

On the other hand, from the scattering matrix elements ($|V_{\lambda\lambda'\lambda''}^{\pm}|^2$) of energy-conserving three-phonon processes, one obtains direct information on the material anharmonicity. Notwithstanding that this bare anharmonicity is an interesting quantity by itself, it is not useful for us because it gives the same importance to processes in which the involved modes are occupied as those in which they are not. Therefore, analogously to what we did with the accessible phase space, we define the temperature-dependent mean effective anharmonicity as:

$$\overline{|V_{\lambda\lambda'\lambda''}|_{\text{occ},T}^2} = \frac{2}{3}(\overline{|V_{\lambda\lambda'\lambda''}^+}|_{\text{occ},T}^2 + \frac{1}{2}\overline{|V_{\lambda\lambda'\lambda''}^-}|_{\text{occ},T}^2) \quad (5.4)$$

where $\overline{|V_{\lambda\lambda'\lambda''}^+}|_{\text{occ},T}^2$ and $\overline{|V_{\lambda\lambda'\lambda''}^-}|_{\text{occ},T}^2$ are the arithmetic means of the population weighted three-phonon matrix elements squared modulus for absorption and emission processes:

$$|V_{\lambda\lambda'\lambda''}^+|_{\text{occ},T}^2 = |V_{\lambda\lambda'\lambda''}^+|^2 n_{\mathbf{q},i} n_{\mathbf{q}',j} (1 + n_{\mathbf{q}'',k}) \quad (5.5)$$

$$|V_{\lambda\lambda'\lambda''}^-|_{\text{occ},T}^2 = |V_{\lambda\lambda'\lambda''}^-|^2 n_{\mathbf{q},i} (1 + n_{\mathbf{q}',j}) (1 + n_{\mathbf{q}'',k}). \quad (5.6)$$

From the mean effective anharmonicity, it can be seen that, for all materials under study, the cubic phase is more anharmonic than the hexagonal phase both

5. Thermal conductivity in nanoscale-emerging crystal phases

at 77 K (a representative value of the low-temperature regime) and at 300 K (see Table 5.3).

Therefore, we have two antagonistic processes occurring when reducing the symmetry from cubic to hexagonal: an increment in the available phase space for phonon-phonon scattering events and a lowering of the anharmonicity, which makes the strength of those events weaker when compared to the cubic ones, with no indication of their relative importance as regards to κ .

5.3.2.3. *The ratio of effective anharmonicity and accessible phase space product*

As we already mentioned, despite being widely used to predict the relationship between thermal conductivity for different materials [191], the criteria listed in Subsection 5.3.2.1 lack the capacity to discern the relative importance of opposed processes.

To overcome such a limitation and owing to the fact that scattering rates are a product of the anharmonicity with phase space (see Eqs. 2.58 and 2.59), we represent in Fig. 5.22 $\kappa_{\text{hex}}/\kappa_{\text{cub}}$ versus the hexagonal-cubic ratio of the mean effective anharmonicity, Eq. 5.4, and the accessible phase space product, Eq. 5.1 at 77 and 300 K. We call this ratio, which is a central magnitude in our discussion, REAAPS, standing for Ratio of Effective Anharmonicity and Accessible Phase Space product. Isotopic scattering, despite being the clear mechanism determining the ratio at low temperature for some materials like GaP, is not accounted for in such analysis. To avoid the influence of the isotope effect, the same procedure, but with the ratios of isotopically pure materials, can be repeated (see Fig. 5.23).

By this analysis of the relative importance of the accessible phase space and effective anharmonicity at a given temperature, it can be observed from Fig. 5.23 that the $\kappa_{\text{hex}}^{\text{pure}}/\kappa_{\text{cub}}^{\text{pure}}$ ratio shows a strong correlation with the REAAPS, and that

5. Thermal conductivity in nanoscale-emerging crystal phases

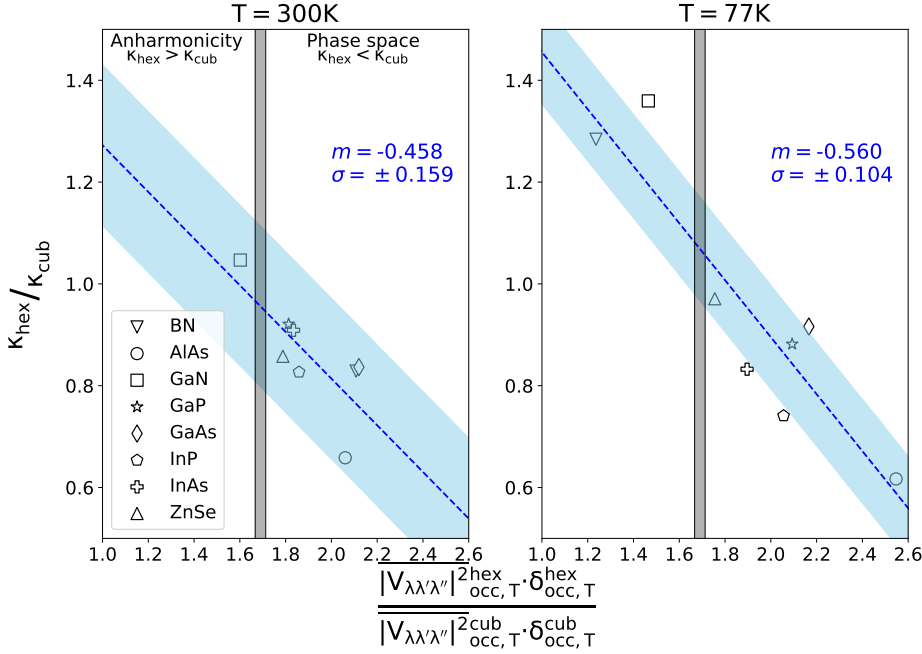


Figure 5.22.: $\kappa_{\text{hex}}/\kappa_{\text{cub}}$ ratio (with isotopic scattering) as a function of the hexagonal-cubic ratio of the mean effective anharmonicity and the accessible phase space product at 77 K (left) and 300 K (right) for different materials. The factor that controls the ratio $\kappa_{\text{hex}}/\kappa_{\text{cub}}$ (anharmonicity or phase space) for a given REAAPS is indicated together with which phase is the most conducting for that value. The gray-filled region corresponds to the limiting region. The dashed blue line corresponds to a linear regression of the data, with the corresponding slope m and standard deviation, σ provided in the figure. The cyan area corresponds to an interval $\pm\sigma$. © American Physical Society. Reproduced with permission from Ref. [195].

$\kappa_{\text{hex}}^{\text{pure}} > \kappa_{\text{cub}}^{\text{pure}}$ when REAAPS is lower than ~ 1.66 , indicating that in these cases the effective anharmonicity increment in the zinc-blende phase compensates the wurtzite accessible phase space increment, thus giving a higher conductivity in wurtzite phase. For higher values of REAAPS, the dominant factor is the increment in the accessible phase space of the wurtzite phase, hence the higher conductivity of the zinc-blende phase. Interestingly, the plots with (Fig. 5.22)

5. Thermal conductivity in nanoscale-emerging crystal phases

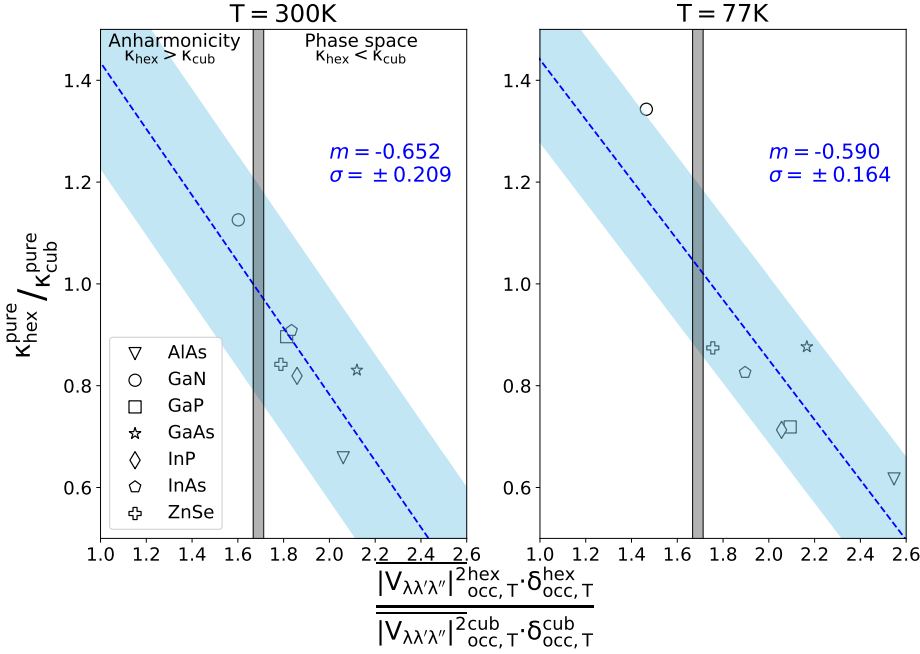


Figure 5.23.: $\kappa_{\text{hex}}^{\text{pure}} / \kappa_{\text{cub}}^{\text{pure}}$ ratio (without isotopic scattering) as a function of the hexagonal-cubic ratio of the mean effective anharmonicity and the accessible phase space product at 77 K (left) and 300 K (right) for different materials. The factor that controls the ratio $\kappa_{\text{hex}}^{\text{pure}} / \kappa_{\text{cub}}^{\text{pure}}$ (anharmonicity or phase space) for a given REAAPS is indicated together with which phase is the most conducting for that value. The gray-filled region corresponds to the limiting region. The dashed blue line corresponds to a linear regression of the data, with the corresponding slope m and standard deviation, σ provided in the figure. The cyan area corresponds to an interval $\pm\sigma$. © American Physical Society. Reproduced with permission from Ref. [195].

and without (Fig. 5.23) isotopic scattering are quite similar at both temperatures, indicating that three-phonon processes are the ones dominating the ratio behavior at the studied temperatures. We note that both the threshold of ~ 1.66 and the slopes of the linear regressions are independent, to a large extent, of temperature (see Fig. 5.24 for a plot at a high temperature, 700 K).

5. Thermal conductivity in nanoscale-emerging crystal phases

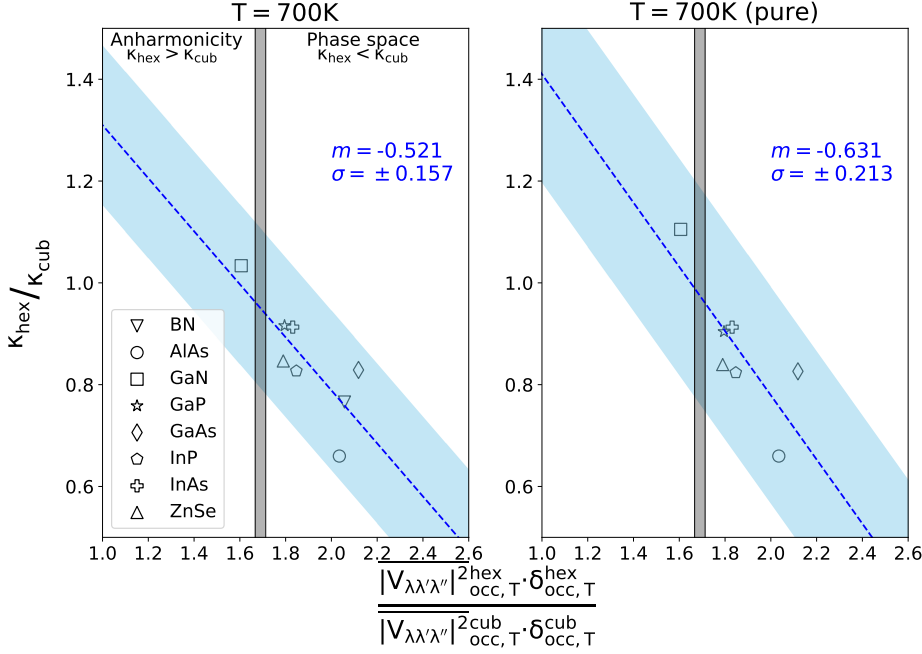


Figure 5.24.: $\kappa_{\text{hex}}/\kappa_{\text{cub}}$ ratio as a function of the hexagonal-cubic ratio of the mean effective anharmonicity and the accessible phase space product at 700 K for different materials with isotopic scattering (left) and without it (right). The factor that controls the ratio $\kappa_{\text{hex}}/\kappa_{\text{cub}}$ (anharmonicity or phase space) for a given REAAPS is indicated together with which phase is the most conducting for that value. The gray-filled region corresponds to the limiting region. The dashed blue line corresponds to a linear regression of the data, with the corresponding slope m and standard deviation, σ provided in the figure. The cyan area corresponds to an interval $\pm\sigma$. © American Physical Society. Reproduced with permission from Ref. [195].

Our analysis helps to explain some of the ratio behaviors such as in GaN, which has $\kappa_{\text{hex}} > \kappa_{\text{cub}}$ over all the temperature range considered. As observed in Table 5.3, the anharmonicity of the hexagonal phase is particularly small when compared to that of the cubic phase. Additionally, the ratio of the accessible phase space is somewhat lower than in other materials. Both factors favor a higher κ for the WZ phase, as it is indeed the case. This is in agreement with previous works

5. Thermal conductivity in nanoscale-emerging crystal phases

by Lindsay *et al.* [45] but in opposition to the results by Togo *et al.* [48], which, as mentioned before, are obtained by a different approach to the LBTE that yields different values for the thermal conductivity in other materials as well [164] (see Subsection 3.2.6 for a detailed discussion about the topic).

The case of BN is also interesting. Both Table 5.3 and Fig. 5.22 show that there is nothing particular to BN at 300 K, having $\kappa_{\text{hex}}^{300\text{ K}} < \kappa_{\text{cub}}^{300\text{ K}}$. However, when the temperature is lowered to 77 K, the accessible phase space decreases much more than in the other materials (a consequence of the hard phonon modes) and the ratio of accessible phase space takes a low value of 5.297, significantly different from the rest of the materials. From this it can be concluded that the change from $\kappa_{\text{hex}}^{300\text{ K}} < \kappa_{\text{cub}}^{300\text{ K}}$ to $\kappa_{\text{hex}}^{77\text{ K}} > \kappa_{\text{cub}}^{77\text{ K}}$ is due to the abnormally large increase of κ_{hex} as temperature is decreased because of the quicker decrease of the accessible phase space in the WZ phase.

Moreover, one can also see from Table 5.3 that for the vast majority of materials the behavior of the ratio with temperature is the opposite to the behavior of REAAPS with temperature. Therefore, when REAAPS decreases (increases) with the temperature, the ratio increases (decreases) for almost all materials, explaining the temperature dependence of $\kappa_{\text{hex}}^{\text{pure}} / \kappa_{\text{cub}}^{\text{pure}}$. However, this does not occur in the case of GaAs, where contrarily to the rest of the materials, the evolution of the REAAPS seems to indicate that the ratio should increase with temperature. This disagreement may show a limitation of our analysis, where we have not taken into account the correlations between anharmonicity and accessible phase space, which can play an important role in borderline cases. When isotopic scattering is added into consideration, it can significantly alter the monotonic dependence of the ratio vs. the temperature at very low temperatures, see the case of GaP for an example.

5.3.2.4. Four-phonon scattering for GaN

Feng *et al.* [150] have conducted a rigorous study of four-phonon scattering on three representative materials, showing that a significant reduction of κ is caused at high temperatures. This effect was shown to be particularly strong in BAs, a material with a large a-o gap, where the inclusion of four-phonon processes opened up scattering channels that were forbidden in a three-phonon event. GaN also presents a large a-o gap, and thus it is interesting to estimate how four-phonon scattering can affect the predicted values for κ .

Although a full study is out of the scope of this thesis, Ref. [150] provides some guidelines on how to estimate the effect of four-phonon scattering on thermal conductivity. We have followed the procedure there reported for the estimation, computing the anharmonicity ratio $|\Phi_4/\Phi_3|^2/|\Phi_2|$, where Φ_n is the n -th order on-site force constant for Ga along the stacking direction ([111] or [0001]), e.g. $\Phi_3 = \Phi_{0,\text{Ga},z;0,\text{Ga},z;0,\text{Ga},z}^{\text{WZ}}$, and comparing the cubic and hexagonal phases. These directions are chosen because (a) they correspond to the directions of the cation-anion bond, (b) they are the directions maximum structural difference between ZB and WZ, and (c) the IFCs do not take zero values. The results, shown in Table 5.4, indicate that the inclusion of four-order processes maintains that the anharmonicity of GaN-ZB is stronger than that of GaN-WZ. Also, those anharmonicity ratios, although the IFCs were computed along different directions than in Ref. [150] and we do not know up to what point they can be directly compared, have a higher numerical value than those provided for diamond, BAs, and Si [150]. Furthermore, given that GaN-ZB has a larger a-o gap than its WZ counterpart, we expect that at high temperatures ZB will be more affected by the inclusion of four-phonon processes than the hexagonal phase. From all these considerations, we can predict that $\kappa_{\text{hex}}/\kappa_{\text{cub}}$ will increase at high temperature once four-phonon processes are included in the analysis.

5.3.3. Nanowires

Like in the case of the hexagonal silicon, viz. lonsdaleite, the metastable phases that are not thermodynamically favored at room temperature and atmospheric pressure in bulk form can naturally occur when the materials are grown as nanowires, allowing access to both phases, ZB and WZ.

Consequently, κ along [111] (cubic) and [0001] (hexagonal) is plotted as function of the nanowire diameter for several temperatures in Figs. 5.25 and 5.26 together with $\kappa_{\text{hex}}/\kappa_{\text{cub}}$. In order to understand the ratio behavior in NWs, it becomes essential to obtain an insight of the size effects (boundary scattering). To do so, the cumulative thermal conductivity with the phonon mean free path (MFP) was plotted together with the nanowire κ for both phases at different temperatures (see Figs. 5.27 and 5.28). Thus, from Figs. 5.27 and 5.28 we can confirm that the ratio in NWs is mostly controlled by size effects. Although the cumulative thermal conductivity with MFP does not hold accurate predictive power [236], they overall reproduce the behavior of the ratios as a function of diameter (Figs. 5.29 and 5.30), especially at high temperatures¹. For instance, InAs having a ratio larger than 1 at small diameters is due to the behavior of the ratio of the cumulative functions. Notwithstanding its utility for determining size effects (i.e: boundary scattering) trends, it is also clear that the MFP plot cannot be used to perfectly predict the detailed ratio behavior as the cumulative and NW function differ, due to the cumulative function not accounting for phonon propagation axis or the expression of boundary scattering in NWs having an $\exp(-d/\lambda_{\text{MFP}})$ behavior—where d is the distance traveled by the phonon hitting the NW surface and λ_{MFP} is its MFP—as opposed to an abrupt cutoff [40] (see Subsection 3.2.3 for a detailed discussion on the topic).

¹The lack of agreement at 77 K might be due to the larger number of phonons (lower temperatures mean longer MFPs) affected by the different cutoff behaviors for a given MFP/diameter.

5. Thermal conductivity in nanoscale-emerging crystal phases

Moreover, from the nanowire κ s we can also observe that BN and GaN show a higher κ at 300 K than at 77 K, thus indicating a displacement in the $\kappa(T)$ peak to higher temperatures when compared to the bulk. Such results are coherent with experimental observations for silicon NWs [236], and they are associated with the domination of boundary scattering over three-phonon and isotopic resistive scattering in the NW geometry when compared to the bulk one. Finally, it is worth mentioning that the available tuning of κ ratios by modifying their diameter, especially for AlAs with a range between 0.7 and 1.1, makes these NWs interesting building blocks for complex thermoelectric and/or phononic systems.

5. Thermal conductivity in nanoscale-emerging crystal phases

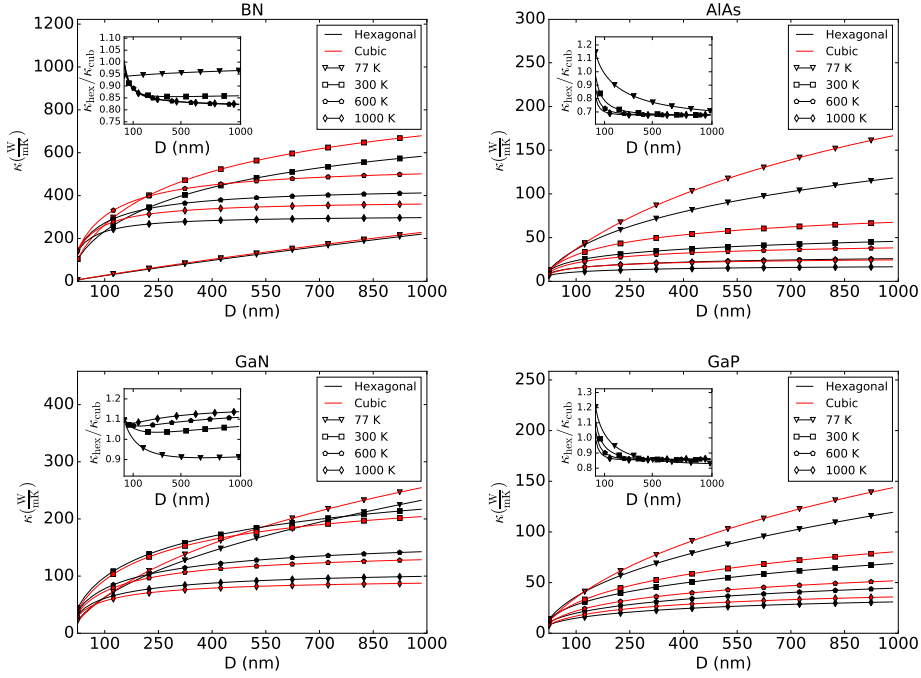


Figure 5.25.: Thermal lattice conductivity of BN, AlAs, GaN and GaP nanowires along [111] for cubic (red) and [0001] for hexagonal (black) at 77 K (triangles), 300 K (squares), 600 K (pentagons) and 1000 K (diamonds) as function of the nanowire diameter. Inset: hexagonal-cubic ratios for nanowires. © American Physical Society. Reproduced with permission from Ref. [195].

5. Thermal conductivity in nanoscale-emerging crystal phases

Table 5.3.: Mean of effective anharmonicity and accessible phase space for zinc-blende and wurtzite phases at 77 and 300 K, together with κ ratios. Boldface indicates the characteristic more favorable to a higher κ . Mean of effective anharmonicities and accessible phase spaces are given in $\text{eV}^2/(\text{amu}^3 \cdot \text{\AA}^6)$ and ps, respectively. © American Physical Society. Reproduced with permission from Ref. [195].

material	$ V_{\lambda\lambda'\lambda''} _{\text{occ},77\text{ K}}^2$	$\delta_{\text{occ},77\text{ K}}$	$\kappa_{\text{hex}}^{77\text{ K}}/\kappa_{\text{cub}}^{77\text{ K}}$	$ V_{\lambda\lambda'\lambda''} _{\text{occ},300\text{ K}}^2$	$\delta_{\text{occ},300\text{ K}}$	$\kappa_{\text{hex}}^{300\text{ K}}/\kappa_{\text{cub}}^{300\text{ K}}$
BN			1.284			0.829
ZB	3.387×10^{-10}	2.324×10^{-6}		1.350×10^{-4}	8.757×10^{-3}	
WZ	7.904×10^{-11}	1.231×10^{-5}		3.422×10^{-5}	7.284×10^{-2}	
WZ/ZB	0.233	5.297		0.253	8.318	
AlAs			0.617			0.658
ZB	1.538×10^{-7}	1.100×10^{-1}		4.378×10^{-5}	1.186×10^1	
WZ	4.457×10^{-8}	9.662×10^{-1}		1.051×10^{-5}	1.018×10^2	
WZ/ZB	0.290	8.784		0.240	8.583	
GaN			1.359			1.047
ZB	7.227×10^{-8}	5.877×10^{-3}		1.157×10^{-4}	1.217×10^0	
WZ	1.522×10^{-8}	4.088×10^{-2}		2.424×10^{-5}	9.302×10^0	
WZ/ZB	0.210	6.956		0.210	7.643	
GaP			0.882			0.921
ZB	1.631×10^{-7}	6.190×10^{-2}		7.073×10^{-5}	8.147×10^0	
WZ	3.797×10^{-8}	5.566×10^{-1}		1.471×10^{-5}	7.103×10^1	
WZ/ZB	0.233	8.992		0.208	8.719	
GaAs			0.916			0.837
ZB	1.914×10^{-7}	2.587×10^{-1}		3.777×10^{-5}	3.019×10^1	
WZ	4.817×10^{-8}	2.230×10^0		9.459×10^{-6}	2.559×10^2	
WZ/ZB	0.252	8.620		0.250	8.476	
InP			0.741			0.827
ZB	1.029×10^{-7}	3.581×10^{-1}		2.115×10^{-5}	3.114×10^1	
WZ	2.501×10^{-8}	3.030×10^0		4.692×10^{-6}	2.610×10^2	
WZ/ZB	0.243	8.461		0.222	8.382	
InAs			0.832			0.909
ZB	2.226×10^{-7}	8.224×10^{-1}		2.966×10^{-5}	6.909×10^1	
WZ	5.220×10^{-8}	6.651×10^0		6.776×10^{-6}	5.548×10^2	
WZ/ZB	0.235	8.087		0.228	8.030	
ZnSe			0.971			0.857
ZB	3.025×10^{-7}	4.817×10^{-1}		4.648×10^{-5}	4.902×10^1	
WZ	7.207×10^{-8}	3.548×10^0		1.105×10^{-5}	3.689×10^2	
WZ/ZB	0.238	7.366		0.238	7.25	

5. Thermal conductivity in nanoscale-emerging crystal phases

Table 5.4.: Anharmonicity ratio $|\Phi_4/\Phi_3|^2/|\Phi_2|$ to get an insight of the relative importance of four-phonon processes in GaN-ZB and GaN-WZ. IFCs have been calculated along the stacking direction ([111] or [0001]) using a $4 \times 4 \times 4$ ($4 \times 4 \times 3$) supercell for ZB (WZ) and central finite differences, and they are given in $\text{eV}/\text{\AA}^n$. © American Physical Society. Reproduced with permission from Ref. [195].

phase	Φ_2	Φ_3	Φ_4	$ \Phi_4/\Phi_3 ^2/ \Phi_2 $
GaN-ZB	20.1	70.0	244	0.604
GaN-WZ	19.7	69.3	184	0.358

5. Thermal conductivity in nanoscale-emerging crystal phases

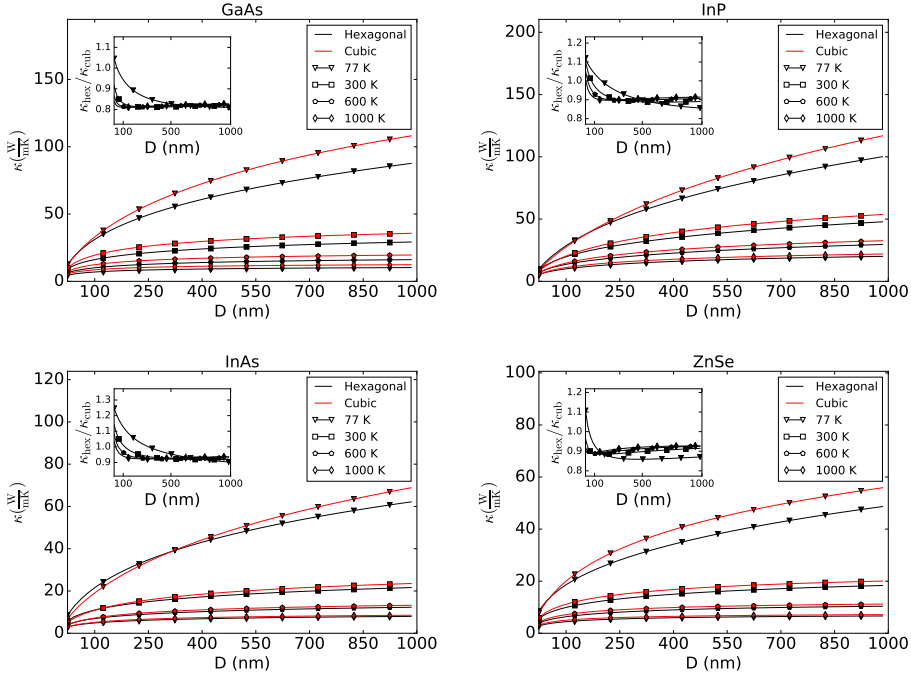


Figure 5.26.: Thermal lattice conductivity of GaAs, InP, InAs and ZnSe nanowires along [111] for cubic (red) and [0001] for hexagonal (black) at 77 K (triangles), 300 K (squares), 600 K (pentagons) and 1000 K (diamonds) as function of the nanowire diameter. Inset: hexagonal-cubic ratios for nanowires. © American Physical Society. Reproduced with permission from Ref. [195].

5. Thermal conductivity in nanoscale-emerging crystal phases

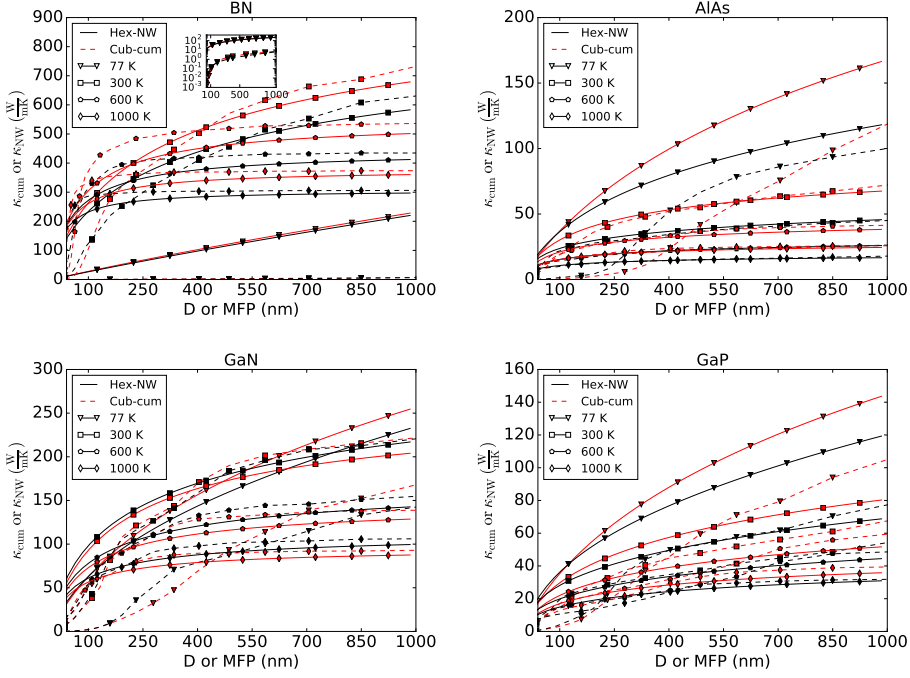


Figure 5.27.: Dashed lines: Bulk-cumulative thermal lattice conductivity for BN, AlAs, GaN and GaP at 77 K (triangles), 300 K (squares), 600 K (pentagons) and 1000 K (diamonds) as function of the phonons mean free path for zinc-blende (red) and wurtzite (black). Solid lines: Bulk normalized nanowire thermal lattice conductivity for BN, AlAs, GaN and GaP at 77 K (triangles), 300 K (squares), 600 K (pentagons) and 1000 K (diamonds) as function of nanowire diameter for zinc-blende (red) along [111] axis and wurtzite (black) along [0001] axis. BN-Inset: Zoom for 77 K. © American Physical Society. Reproduced with permission from Ref. [195].

5. Thermal conductivity in nanoscale-emerging crystal phases

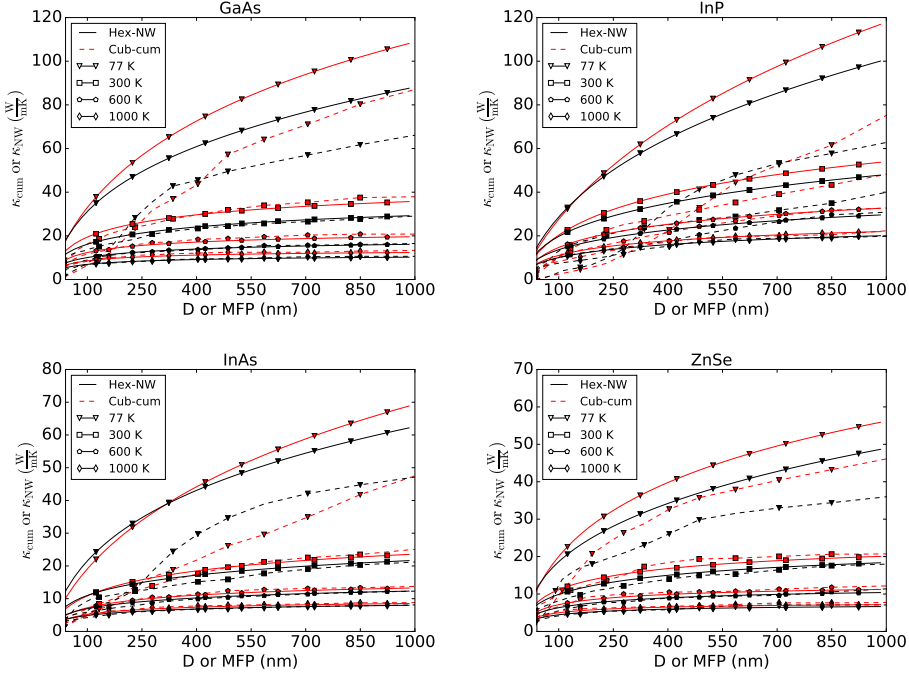


Figure 5.28.: Dashed lines: Bulk-cumulative thermal lattice conductivity for GaAs, InP, InAs and ZnSe at 77 K (triangles), 300 K (squares), 600 K (pentagons) and 1000 K (diamonds) as function of the phonons mean free path for zinc-blende (red) and wurtzite (black). Solid lines: Bulk normalized nanowire thermal lattice conductivity for GaAs, InP, InAs and ZnSe at 77 K (triangles), 300 K (squares), 600 K (pentagons) and 1000 K (diamonds) as function of nanowire diameter for zinc-blende (red) along [111] axis and wurtzite (black) along [0001] axis. © American Physical Society. Reproduced with permission from Ref. [195].

5. Thermal conductivity in nanoscale-emerging crystal phases

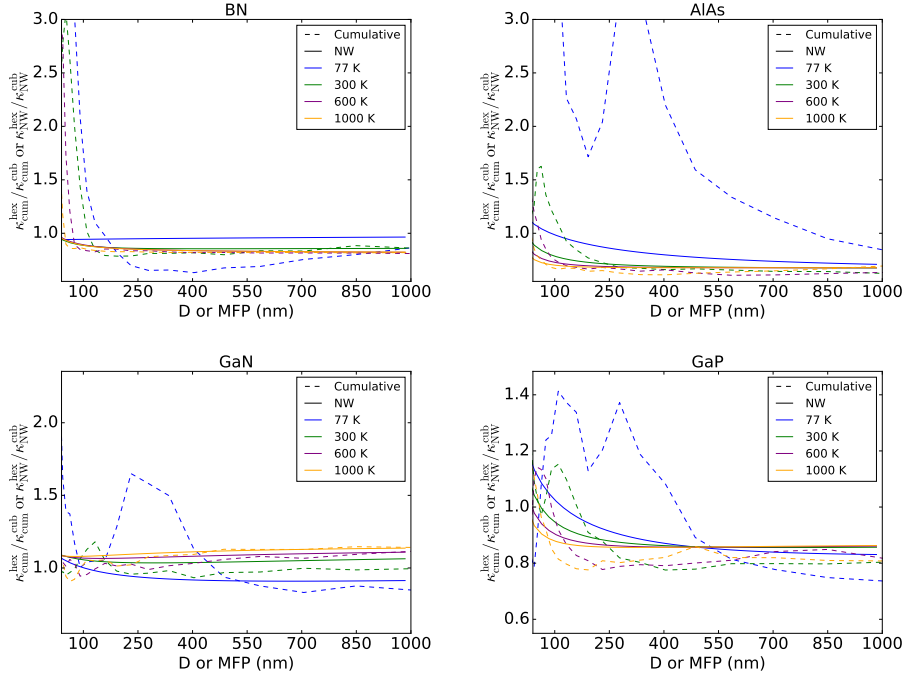


Figure 5.29.: Solid lines: Hexagonal-cubic thermal conductivity ratio for BN, AlAs, GaN and GaP nanowires at 77 K (blue), 300 K (green), 600 K (purple) and 1000 K (yellow) as function of diameter. Dashed lines: Hexagonal-cubic cumulative thermal conductivity ratio for BN, AlAs, GaN and GaP at 77 K (blue), 300 K (green), 600 K (purple) and 1000 K (yellow) as function of phonon MFP. © American Physical Society. Reproduced with permission from Ref. [195].

5. Thermal conductivity in nanoscale-emerging crystal phases

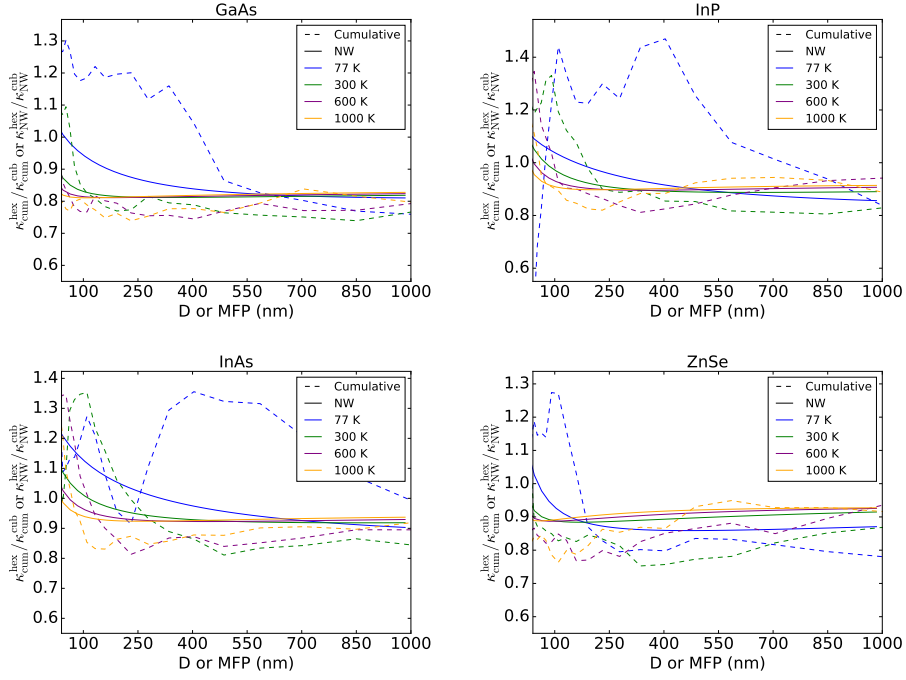


Figure 5.30.: Solid lines: Hexagonal-cubic thermal conductivity ratio for GaAs, InP, InAs and ZnSe nanowires at 77 K (blue), 300 K (green), 600 K (purple) and 1000 K (yellow) as function of diameter. Dashed lines: Hexagonal-cubic cumulative thermal conductivity ratio for GaAs, InP, InAs and ZnSe at 77 K (blue), 300 K (green), 600 K (purple) and 1000 K (yellow) as function of phonon MFP. © American Physical Society. Reproduced with permission from Ref. [195].

5.3.4. Alloys

The phase selection path to lowering thermal conductivity can be combined with more classical approaches such as alloying; indeed wurtzite $\text{In}_x\text{Ga}_{1-x}\text{As}$ [237, 238] and $\text{GaAs}_{1-x}\text{P}_x$ [123] NWs have been successfully synthesized. Therefore, it is interesting to understand the behavior of κ in such alloys, for both the bulk-stable ZB and the WZ. To do so, we have iteratively solved the homogeneous PBTE using the VCA together with mass-defect scattering, as detailed in Subsection 2.4, to model alloying [124]. The thermal conductivity for both materials and phases, i.e. zinc-blende and wurtzite, are given in Figs. 5.31 and 5.32, respectively.

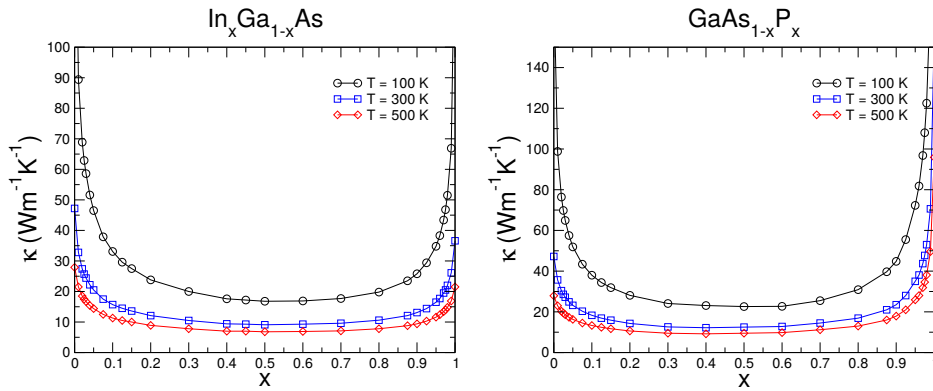


Figure 5.31.: Thermal conductivity as a function of composition at $T = 100\text{ K}$, 300 K , and 500 K for cubic $\text{In}_x\text{Ga}_{1-x}\text{As}$ and $\text{GaAs}_{1-x}\text{P}_x$. © IOP Publishing. Adapted with permission from [F. D. Santiago, M. Raya-Moreno, Á. Miranda, M. Cruz-Irisson, X. Cartoixà, and R. Rurali, “Tunable thermal conductivity of ternary alloy semiconductors from first-principles”, *J. Phys. D: Appl. Phys.*, **54** 335302 (2021)]. All rights reserved.

Contrary to their constituents, the thermal conductivity between the different crystal phases of alloys is almost the same, at least for the in-plane component of κ_{WZ} —i.e. xx and yy —and the κ_{ZB} . We note that Vegard’s combination is incapable of resulting in such an equalization. Hence, this last must have

5. Thermal conductivity in nanoscale-emerging crystal phases

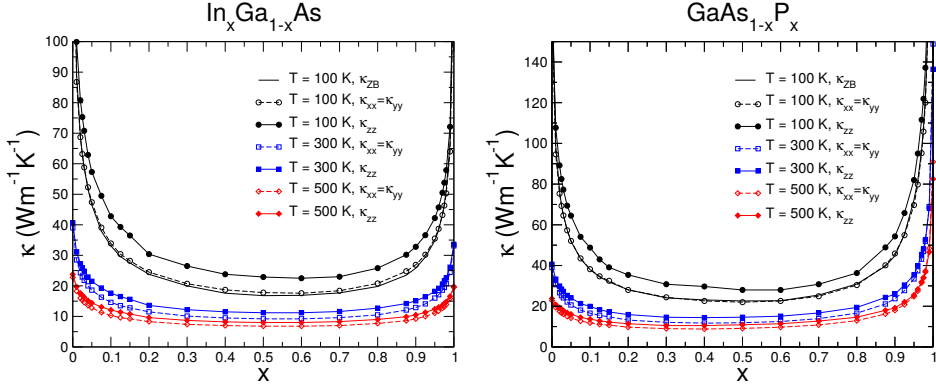


Figure 5.32.: Thermal conductivity as a function of composition at $T = 100\text{ K}$, 300 K , and 500 K for hexagonal $\text{In}_x\text{Ga}_{1-x}\text{As}$ and $\text{GaAs}_{1-x}\text{P}_x$. © IOP Publishing. Reproduced with permission from [F. D. Santiago, M. Raya-Moreno, Á. Miranda, M. Cruz-Irisson, X. Cartoixà, and R. Rurali, “Tunable thermal conductivity of ternary alloy semiconductors from first-principles”, *J. Phys. D: Appl. Phys.*, **54** 335302 (2021)]. All rights reserved.

its origin in the scattering caused by the compositional disorder of the alloy, which consequently is stronger in the ZB phase. Such results are in line with the differences in the $\kappa_{\text{hex}}/\kappa_{\text{cub}}$ ratio with and without the isotopic scattering found in the constituent pure bulk materials (see Figs. 5.18 and 5.17).

5.4. Phase boundary thermal resistance

As previously mentioned, both phases, namely diamond/zinc-blende and lonsdaleite/wurtzite, can be accessed in III-V and group-IV semiconductor nanowires. Indeed, for III-V materials the physical mechanism behind the formation of cubic or hexagonal phase is very well understood and controlled [239], in contrast with group-IV nanowires [184]. Such precise guidance over the synthesis outcome brings the opportunity to engineer nanowire-based devices or systems combining both phases, e.g. superlattices, for phononic and/or electronic applications. Nonetheless, while the process is very well controlled, it is not uncommon to

5. Thermal conductivity in nanoscale-emerging crystal phases

see stacking defects, like twin boundaries in cubic phases, which originate from a 60° rotation in one of the atomic planes resulting in an ABCABC|BACBAC stacking. Consequently, we have studied the thermal resistance of the phase (i.e. those between the hexagonal and the cubic phase) and twin boundaries (phase and twin TBRs), as these are essential quantities in the development of NW-semiconductor-based devices.

Unfortunately, as we noted in Subsection 4.2.3 the most common approaches to boundary scattering, namely AMM and DMM, are unsuited for the study of these TBRs since both sides have similar (phase) or identical vibrational properties (twin). Therefore, we have relied on state-of-the-art nonequilibrium Green's functions (NEGF) and NEMD (see Section 3.3) to compute TBR calculation. For reference, the former method calculates the TBR through the Landauer-Büttiker formalism [184], in which the frequency-dependent transmission coefficients are obtained through the Green's function, built using the IFCs and masses in the region of interest as well the semi-infinite thermal reservoirs. Further details on the NEGF for thermal transport can be found in Refs. [240] and [241]. Alternatively, it is also possible to obtain the transmission coefficient through the equivalent mode-matching formulation [242], which is based on directly matching the vibrational modes in the scattering region to the phonon modes of the semi-infinite leads.

It is important to notice that the used techniques, i.e. NEMD and NEGF, require that the perturbation causing the scattering, namely the interface, must not be felt at the connecting leads. Such a condition translates to relatively large systems—i.e. around 40 nm—with a considerable number of atoms, rendering DFT calculations unpractical, especially regarding the computation of third-order IFCs. Consequently, we have resorted to less intensive methods to compute atomic interactions, the classical force fields (i.e. parameterizations of the atomic interactions). For group III-V semiconductors, namely GaP and InP, we have used

5. Thermal conductivity in nanoscale-emerging crystal phases

the Vashishta *et al.* ansatz [243, 244] as parameterized in Refs. [245] (GaP) and [246] (InP), as they provide an acceptable description of the acoustic vibrational properties. For the silicon case, the available ansatzes and their parameterizations give rather poor vibrational properties; hence, we have built a neural-network force field, enabling a description of the phonon branches with an *ab initio* level of quality [184].

The TBRs for all materials and boundaries are given in Fig. 5.33, in general, the obtained values at room temperature, show lower resistance than conventional heterojunctions at room temperature, i.e. 300 K. Indeed, except for InP-phase which has comparable values, the obtained TBRs are approximately one order of magnitude lower than those of AlN-GaN ($3.33 \times 10^{-9} \text{ m}^2 \text{ K W}^{-1}$ [247]) or Si-Ge ($3.77 \times 10^{-9} \text{ m}^2 \text{ K W}^{-1}$ [248]) to name few of those conventional cases.

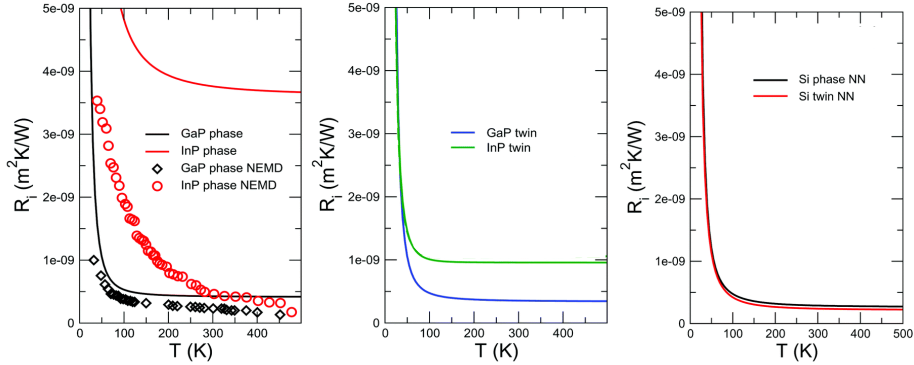


Figure 5.33.: TBR as a function of interface temperature for the two crystal-phase and twin interfaces obtained using NEGF. GaP-phase(twin) and InP-phase(twin) are depicted in the left (middle) panel. Right panel depict the results for both Si-twin and Si-phase. Data points in the left panel show the TBR computed from NEMD, which includes anharmonic effects at the interface. The uncertainty in the estimate of the TBR from NEMD, arising from the fluctuating character of the temperature profile, is $9.6 \times 10^{-11} \text{ m}^2 \text{ K W}^{-1}$ and $5.9 \times 10^{-10} \text{ m}^2 \text{ K W}^{-1}$ for GaP and InP, respectively. Adapted from Ref. [184] with permission from the Royal Society of Chemistry.

5. Thermal conductivity in nanoscale-emerging crystal phases

Regarding the differences between both kinds of boundaries, we observe lower TBRs for the twin interface. This is, however, nothing surprising as vibrational properties on both sides of the interface differ more in the crystal-phase case (see Figs. 5.11 and 5.12 for the dispersion relation of WZ and ZB GaP and InP, respectively); indeed, in the twin case the only difference is a C_6 rotation around the stacking direction, i.e. $[111]$ for the conventional primitive cell, of the phonon modes in each side. These lower TBRs for the twin case are further explained by looking at local interactions (see Fig. 5.34) which are again more dissimilar in the crystal-phase case, namely the IFCs, as the crystal-phase interface these magnitudes change from a ZB to a WZ bulk value with a transition giving a good estimate the effective thickness of the interface; whereas, in the twin case the bulk values on either side are the same, varying only at the interface, as a consequence of a small, but non-negligible relaxation of the atomic structure.

5. Thermal conductivity in nanoscale-emerging crystal phases

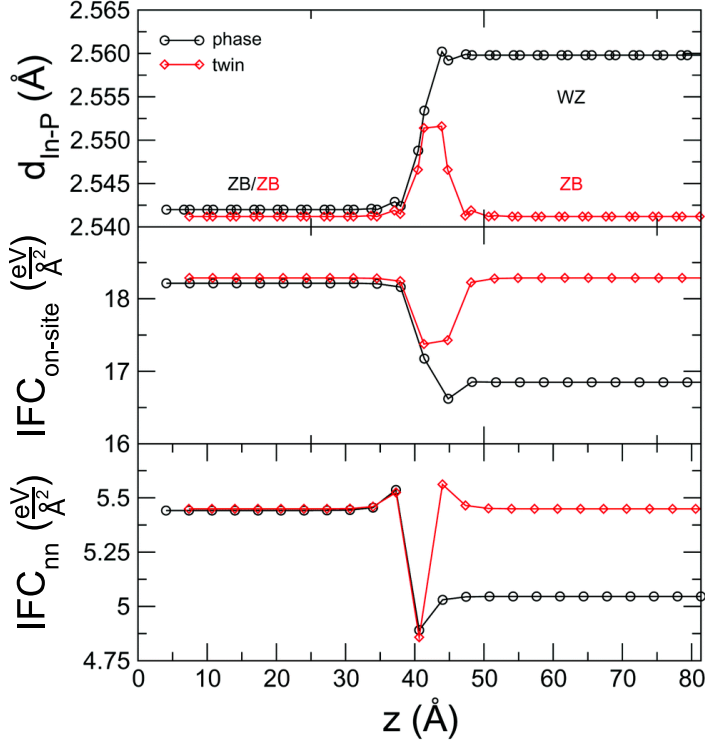


Figure 5.34.: Nearest-neighbor distance (top), on-site IFC (middle) and nearest-neighbor IFC (bottom) as a function of the position along the transport direction for a crystal-phase interface and a twin boundary in InP. The on-site IFC is computed as the Frobenius norm of the Jacobian of the forces of atom m with respect to its own displacement, $\left\| \frac{-\partial F_m}{\partial r_m} \right\|_F$, where m is an In atom; similarly, the nearest-neighbor IFC is defined as $\left\| \frac{-\partial F_m}{\partial r_n} \right\|_F$, where n is a P atom and a first neighbor of m such that $z_m < z_n$. Adapted from Ref. [184] with permission from the Royal Society of Chemistry.

5.5. Summary and conclusions

In this Chapter, we have presented *ab initio* calculations of the lattice thermal conductivity for the cubic and hexagonal phases of Si, GaAs, GaN, GaP, InAs, InP, AlAs, BN, and ZnSe using density functional theory and iteratively solving the phonon Boltzmann Transport Equation. For the Si case, we found a significant reduction of κ in lonsdaleite (hexagonal) with respect to the bulk-stable diamond cubic lattice, i.e. around 40%, having its origin in the substantially larger scattering rates of the new modes arising from the reduced symmetry of the hexagonal lattice. Such a great reduction of κ is related to the seven conditions for higher thermal conductivity. Contrary to Si, we found that for binary semiconductors those seven conditions do not provide any useful guideline to determine which of the crystal phases is the most conductive. For instance, for GaN we found that such conditions suggest that the zinc-blende phase should be the most conductive one, as one of them is neutral and only two of them predict a larger κ for the wurtzite. Yet, the calculations predict the latter to be more conductive. Additionally, those conditions cannot either explain the reason for some materials, like BN, to change their $\kappa_{\text{hex}}/\kappa_{\text{cub}}$ ratio behavior with temperature. Consequently, based on the theoretical expressions for the three-phonon scattering rate, we focused our analysis on two quantities that together contain all conditions and the finite temperature effects: the population-weighted three-phonon scattering matrix elements or anharmonicity and the phase space. Thereby, we found that which phase is the most conductive one depends on the relative strength between effective anharmonicity and accessible phase space. Such factors are shown to be antagonistic for all materials due to the higher effective anharmonicity of the cubic phase when compared to the hexagonal one, which, on the other hand, has a higher accessible phase space. Furthermore, we carry out an analysis of which factor is dominant when three phonon processes are the only ones present in each material

5. Thermal conductivity in nanoscale-emerging crystal phases

at 77 K and 300 K, showing that, when anharmonicity (phase space) dominates, it leads to a higher (lower) conductivity in the hexagonal phase compared to the cubic one. Moreover, we have observed that when the hexagonal-cubic ratio of temperature-weighted anharmonicity and accessible phase space product is less than ~ 1.66 , the dominating factor determining κ is anharmonicity ($\kappa_{\text{hex}} > \kappa_{\text{cub}}$). On the contrary, when that product is higher than ~ 1.66 , the dominating factor determining κ is the accessible phase space ($\kappa_{\text{hex}} < \kappa_{\text{cub}}$), thereby making such quantity an excellent tool to predict which is the most conductive phase at a given temperature when other more qualitative analyses fail. We have also presented results for NWs, showing the effect of boundary scattering on ($\kappa_{\text{hex}}/\kappa_{\text{cub}}$) and its relation to the phonon mean free paths. Moreover, we find that NWs, in particular the ones of binary semiconductors, have the ability to have their κ ratio tuned over a wide range with their diameter, hence making them appealing materials for phononic and thermoelectric applications. The case of AIAs, with a $\kappa_{\text{hex}}/\kappa_{\text{cub}}$ range between 0.7 and 1.1, is of special interest. Additionally, we briefly discuss the case of binary alloys based on III-V semiconductors, namely $\text{In}_x\text{Ga}_{1-x}\text{As}$ and $\text{GaAs}_{1-x}\text{P}_x$, showing that the differences between hexagonal and cubic phases are erased due to the compositional disorder scattering. Finally, we have also discussed the thermal boundary resistance of phase and twin interfaces usually found in NWs made of group-IV and III-V semiconductors, finding resistances of one order of magnitude lower than the ones of conventional heterojunctions.

CHAPTER 6

BTE–Barna: An extension of almaBTE for thermal simulation of devices based on 2D materials

This Chapter reproduces to a great extent the contents of [Raya-Moreno, M., Cartoixà, X., Carrete, J. (2022). BTE-Barna: An extension of almaBTE for thermal simulation of devices based on 2D materials. arXiv preprint arXiv:2202.00505.], which has been submitted for publication for publication to Computer Physics Communications.

As previously mentioned, the continuous shrinking of electronic components, following Moore’s Law [1], is pushing bulk semiconductor-based devices, such as silicon transistors, to their fundamental limits. Furthermore, this increase in the integration level leads to ever higher power densities and presents the Herculean challenge of dissipating the generated heat [2].

In this context, two dimensional materials (2DMs), thanks to their atomic thickness, low surface roughness and density of dangling bonds [8], together with the possibility of stacking them to create heterostructures with tuned properties and their compatibility with CMOS technology, are quite promising candidates to

replace III-V compounds and silicon in transistor channels [9, 10]. Understanding thermal transport in 2DMs is essential to optimize heat management in such devices.

As mentioned in Chapter 3, phonons are the main heat carriers in semiconductors, the evolution of which can be described through the semiclassical Peierls-Boltzmann Transport Equation (PBTE). For highly symmetric structures (e.g.: bulk systems, nanowires, thin-films...) the RTA and the full iterative solution of the PBTE is readily accessible. Indeed, the inclusion of phonon properties calculated from first-principles (frequencies, scattering rates...) makes it possible to obtain such a solution even for novel materials where simpler models to describe those properties are lacking [44, 45]. Examples of iterative first-principles-based PBTE solvers for those kind of systems has been extensively discussed in Subsection 3.2.6.

Among these, `almaBTE` is the only one allowing to go beyond highly symmetric structures. To do so, it uses the RTA-based deviational energy Monte Carlo methods (see Chapter 4), which have proven themselves as good alternatives to overcome the limitations [171, 175, 176] of more traditional methods. However, the validity of the RTA approach for 2D materials is questionable, and it has been shown to yield a very poor description of thermal properties for several of them [139, 147]. For those cases one might need to use an energy deviational Monte Carlo method based on the full collision operator (see Subsection 4.3.2).

Furthermore, `almaBTE`'s original implementation, `steady_montecarlo1d`, was designed to investigate one-dimensional steady-state situations in materials/heterostructures embedded between two isothermal reservoirs having the same cross section, which owing to finite thickness might not be true for 2D-material-based systems/devices. Moreover, it does not implement any kind of boundary scattering, nor allows for other boundary conditions (i.e. applied thermal gradients or an initial temperature profile); thus making the simulator

unsuited for thermal simulation of devices based on 2D materials.

In this Chapter we present the BTE-Barna (Boltzmann Transport Equation: Beyond Rta for NAnosystems) software package, an extension of `almaBTE` to tackle 2D systems both within and beyond the RTA, so that now it can address finite and/or periodic 2D materials and their heterojunctions under the effect of thermal gradients and isothermal reservoirs. We analyze a selection of test cases and discuss the validity of the RTA. Additionally, the iterative solver in `almaBTE` is extended to provide the effective thermal conductivity for nanoribbons and nanowires.

The Chapter is structured as follows: after displaying the general structure of BTE-Barna in Sec. 6.1 and discussing the implementation in Sections 6.2-6.4, we provide test cases of the implementation in Section 6.5 and present illustrative example applications of our package simulators in Section 6.6. The summary and conclusions for this Chapter are given in Section 6.7.

For a more practical example of the capabilities of the MC simulators included in the package, we direct the reader to Chapter 7, where we use these to investigate the features arising from hydrodynamic effects in graphene and phosphorene nanodevices at room temperature with finite heat sources/sinks.

6.1. BTE-Barna structure

Fig. 6.1 shows the different pieces of BTE-Barna package and how they relate to each other. The whole package heavily relies on `almaBTE` library routines, which have been extended to allow for the solution of PBTE in finite devices based on 2D materials. Moreover, all the executables use the mode-resolved phonon properties as inputs, which are read from `almaBTE`-generated HDF5 files. A more detailed explanation of all the executables, their inputs, and outputs

6. *BTE-Barna: thermal simulation of devices based on 2D materials*

can be found in the Appendix A.1 for the iterative solver, and in Appendix A.2 for the Monte Carlo solvers, their input generators, and post-processing tools.

BTE-Barna

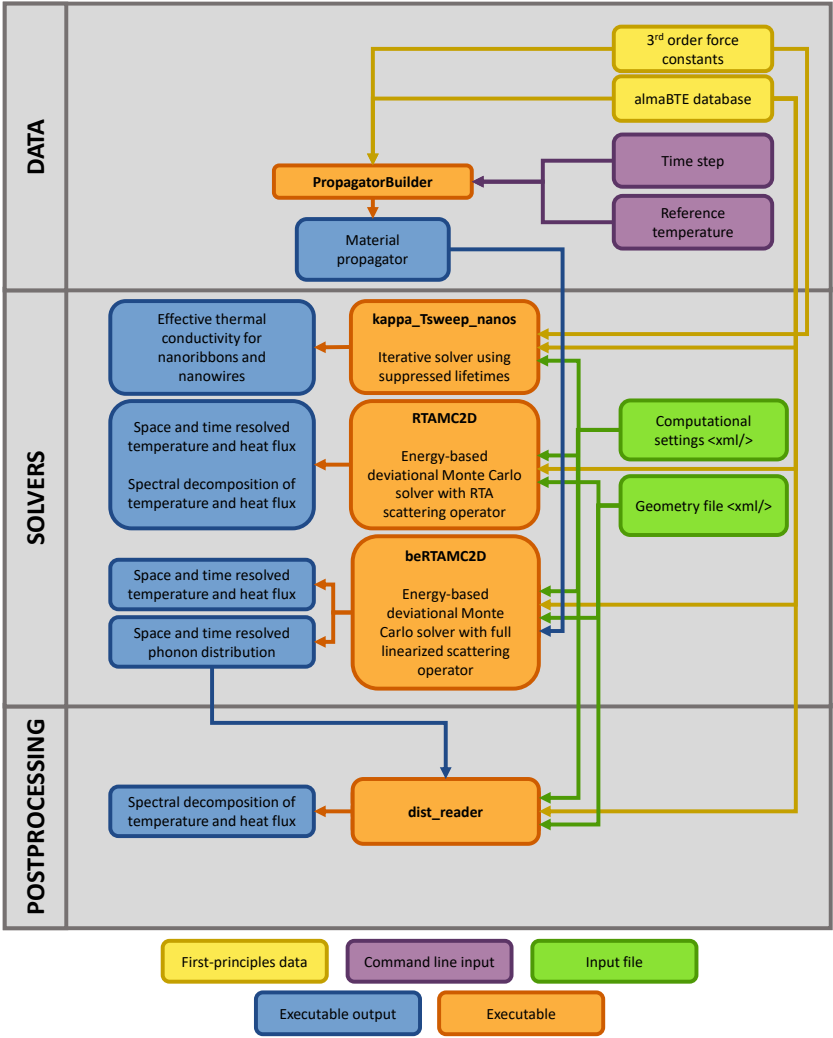


Figure 6.1.: General structure of BTE-Barna package.

6.2. Effective thermal conductivity in simple nanosystems

Despite the fact that an exact solution of the PBTE for highly symmetric systems like nanoribbons or nanowires would require a discretization in space, it is possible to obtain an approximate solution by using averages under the assumption of fully dispersive boundaries [40]. In such a way, it becomes possible to obtain an effective thermal conductivity (κ_{nano}) by simply introducing suppression factors in the lifetimes ($\tau_i^{\text{nano}} = \tau_i^0 S_{\lambda}^{\text{nano}}$) and then solving the PBTE like in bulk under homogeneous gradients [46] (see Subsection 3.2.3 for a detailed derivation and discussion of the methodology and the related equations).

For nanoribbons contained in the XY plane, the suppression factors (S_i^{nr}) are calculated using Eqs. 3.31 and 3.32:

$$S_i^{\text{nr}} = 1 + \left[\frac{M_i^{\text{nr}}}{L} \left(e^{-\frac{L}{M_i^{\text{nr}}}} - 1 \right) \right] \quad (3.31)$$

$$M_i^{\text{nr}} = \left| \left[\begin{pmatrix} \mathbf{u}_y & \mathbf{u}_x \\ -\mathbf{u}_x & \mathbf{u}_y \end{pmatrix}^{-1} \mathbf{v}_i \right] \cdot \mathbf{e}_1 \right| \tau_i, \quad (3.32)$$

where \mathbf{u} is a normalized vector pointing along the unbounded direction of the system, L is the nanoribbon width and \mathbf{e}_1 is the first column of identity matrix. In the case of cylindrical nanowires, the suppression factors (S_{λ}^{nw}) can be calculated using Eqs. 3.33 and 3.34:

$$S_i^{\text{nw}} = 1 - \frac{2M_i^{\text{nw}}}{R^2} \left[M_i^{\text{nw}} \left(e^{-\frac{R}{M_i^{\text{nw}}}} - 1 \right) + R \right] \quad (3.33)$$

$$M_i^{\text{nw}} = \|\mathbf{v}_i - (\mathbf{v}_i \cdot \mathbf{u})\mathbf{u}\| \tau_i, \quad (3.34)$$

where R is the nanowire radius.

Therefore, the calculation of effective thermal properties is performed as in `almaBTE`'s `kappa_Tsweep` [47], which solves the homogeneous PBTE using a variational solver for the irreducible linear system, i.e. the one defined in the irreducible set of \mathbf{q} -points determined symmetry. However, one must use $\tau_{\lambda}^{\text{nano}}$ in place of τ_{λ}^0 as detailed in Section 3.2.3. Moreover, since the boundaries break the crystal symmetry (i.e.: $S_{\lambda}^{\text{nano}}$ and consequently $\tau_{\lambda}^{\text{nano}}$ does not possess crystal symmetry) the related problem must be solved in the full Brillouin Zone; hence, requiring to recalculate and symmetrize the matrix elements and broadenings in the whole \mathbf{q} -mesh. Moreover, in the case that the full converged solution is required, one needs to solve a relatively big linear system (see Subsection 3.2.2).

To do so efficiently, we have parallelized the three-phonon lookup in the full BZ via `oneTBB`. Additionally, the linear system is solved using sparse matrices with the biconjugate gradient stabilized method (`BiCGSTAB`) combined with a symmetric scaling for improved numerical stability [249], as implemented in `Eigen3` [250].

6.3. RTA Monte Carlo

The implementation for 2D materials of the RTA Monte Carlo is based on code already in `almaBTE` [47], whose formulation was proposed by Péraud *et al.* [176]. The algorithm simulates the space and time evolution of deviational power (emitted by sources and absorbed by sinks) by splitting its distribution into discrete packets—the deviational particles—and tracking their trajectories in a linearized regime. The validity of the existing implementation rests on the assumption that differences in temperature are small enough that a single reference temperature can be defined for the whole system. We now take a look at the main improvements of our code upon that baseline; see Section 4.6 for a detailed explanation of the whole algorithm.

As previously commented, the original implementation, `steady_montecarlo1d`, was designed to investigate one-dimensional steady-state situations in materials/heterostructures embedded between two isothermal reservoirs having the same cross section, which owing to finite thickness might not be true for 2D-material-based systems/devices. Consequently, we extended the geometric algorithms to deal with 2D systems using the `boost::geometry` library [251]. In this implementation the system is composed of different computational boxes, which are defined by the user as convex hulls of points, therefore enabling the creation of complex geometries. Additionally, as the finiteness of real 2D devices requires dealing with boundary scattering, we implemented a full diffusive condition in which the out-state is randomly selected from a Lambert cosine law distribution (see Eq. 4.15).

Besides the steady-state, the code allows for the exploration of time evolution determined by boundary conditions. This is done by sampling the trajectories on a time grid on top of the spatial grid (see Subsection 4.6.1 for a detailed explanation of the trajectory sampling).

6.3.1. Interface model for stacked layered systems: localized diffuse mismatch model

The DMM (see Subsection 4.2.3) implemented for the treatment of interface scattering in `steady_montecarlo1d` is a purely elastic model, allowing the coupling between modes at each side of the interface with energy conservation as the sole requirement. As already commented, despite this crude approach, the DMM has been proven to qualitatively describe the interface thermal resistance (ITR) for several interfaces of bulk 3D materials such as Si/Ge [47]. However, for systems comprised of stacked layers, such as the interface between graphene and encapsulated graphene [252], energy matching as the single condition for trans-

mission is no longer a valid assumption. Under such conditions, well localized modes in unconnected layers—e.g.: encasing hBN layers vs. the bare monolayer at the graphene/encapsulated-graphene interface—would be predicted to be coupled, which is quite unrealistic and would lead to too low (or even negligible or negative) ITR values (see Fig. 6.2) [252]. Consequently, we developed the localized DMM (LDMM) to account for mode localization at layers. To that end,

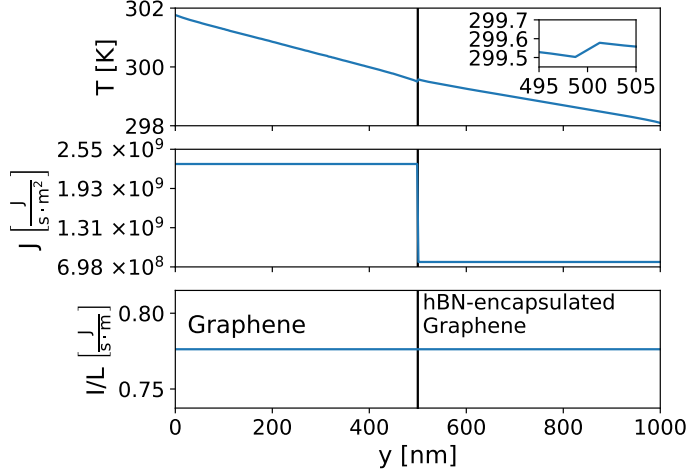


Figure 6.2.: Thermal profile, flux and heat intensity per unit of length in graphene/hBN-encapsulated graphene obtained using the RTA and the traditional DMM to model interface scattering. Inset: Zoom of thermal profile at the interface.

we define the localization vector at the I -th layer for a given mode ($\mathcal{L}_{I,\lambda}^A$) as:

$$\mathcal{L}_{I,\lambda}^A = \frac{\sum_{\{j:j \in I\}}^N \sum_{\alpha}^{x,y} |\xi_{\lambda,\alpha,j}|^2}{\sum_j^N \sum_{\alpha}^{x,y} |\xi_{\lambda,\alpha,j}|^2} \quad (6.1)$$

where I is the layer index of A side, λ is the phonon mode index, j is the atomic index, α is the Cartesian axis and $\xi_{\lambda,\alpha,j}$ is the eigenvector. Therefore, when calculating the coupling strength we multiply the classical DMM expression by

the coupling factor $\mathcal{C}_{\lambda,\lambda'}^{A,B}$:

$$\mathcal{C}_{\lambda,\lambda'}^{A,B} = 1 - \text{JSD}(\mathcal{L}_{\lambda}^A || \mathcal{L}_{\lambda'}^B) \quad (6.2)$$

where $\text{JSD}(\mathcal{L}_{\lambda}^A || \mathcal{L}_{\lambda'}^B) \in [0, 1]$ is the Jensen-Shannon divergence between localization functions. Therefore, $\mathcal{C}_{\lambda,\lambda'}^{A,B}$ is one for perfectly matching localization and zero for modes fully localized at different layers. As the Jensen-Shannon divergence requires both vectors to be of same length, for different materials the localization vectors are modified in such a way that connected layers remain untouched and paired while the remaining unconnected layers have their values summed up and added at the back of the localization vector; we provide an example for reference:

$$\mathcal{L}_{\lambda}^C = \begin{pmatrix} \mathcal{L}_{\lambda,i}^C \\ \mathcal{L}_{\lambda,j}^C \\ \sum_k \mathcal{L}_{\lambda,k}^C \end{pmatrix}, \quad \mathcal{L}_{\lambda'}^D = \begin{pmatrix} \mathcal{L}_{\lambda',\alpha}^D \\ \mathcal{L}_{\lambda',\beta}^D \\ \sum_{\mu} \mathcal{L}_{\lambda',\mu}^D \end{pmatrix} \quad (6.3)$$

In this example, layers i and j of C are connected to the α and β layers on the D side, and k and μ denote all unconnected layers on each side or a zero term if no additional layers exist. In Fig 6.3 we show results for the same case studied in Fig. 6.2 but using the LDMM, enabling us to obtain a non-negligible ITR as expected in this kind of system [252]. It should be noted that, despite the improvement in the results, the model is still incapable of describing the thermal rectification predicted in such systems [252, 253] because of the intrinsic symmetry of the DMM and the Jensen-Shannon divergence used to model the interface scattering.

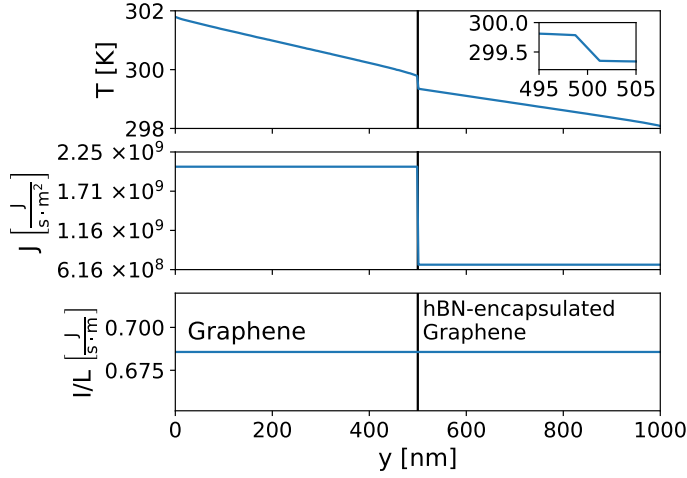


Figure 6.3.: Thermal profile, flux and heat intensity per unit of length in graphene/hBN-encapsulated graphene obtained using the RTA and the LDMM to model interface scattering. Inset: Zoom of thermal profile at the interface

6.4. Beyond RTA Monte Carlo

Given the RTA's failure to describe the thermal properties of 2DMs [139, 147], we implemented in `beRTAMC2D` (see Subsection A.2.4) a linearized ab initio phonon-low variance deviational simulation Monte Carlo (LAIP-LVDSMC) [178] simulator to overcome such limitation. This LAIP-LVDSMC algorithm, henceforth referred to as *beyond RTA* (bRTA), solves the deviational energy linearized PBTE (see Subsection 4.3.2 for a detailed explanation of the scattering substep, Section 4.5 for a general view of the whole algorithm, and Section 4.4 for an explanation on how the thermal properties are sampled each time step).

6.4.1. B_{ij} calculation and enforcement of conservation laws

As noted by Landon *et al.*, it is important for B_{ij} (see Subsection 4.3.2 for its definition) to respect crystal symmetries and microscopic reversibility [178]. The original almaBTE routines for calculating scattering amplitudes lead to violations of those constraints because the smearing method implemented there does not enforce the symmetry between emission and absorption processes [46] (see Subsection 2.2.2).

To enforce symmetry, matrix elements are built from a single representative of each equivalence class in the quotient group of q points using a new symmetric adaptive smearing scheme for energy conservation

$$\sigma_{ijk} = a\sqrt{\sigma_i^2 + \sigma_j^2 + \sigma_k^2} \quad (6.4)$$

$$\sigma_i = \frac{1}{\sqrt{12}} \|\{G_{\mu\alpha}^T \cdot N_{\mu\mu}^{-1}\}^T \cdot (\mathbf{v}_i)_\alpha\| \quad (6.5)$$

where i, j and k are the phonon modes taking part in the three-phonon process, μ indicates a reciprocal-space lattice vector, α indicates a Cartesian axis, $G_{\mu\alpha}$ is the reciprocal lattice basis matrix, $N_{\mu\mu}$ is a diagonal matrix whose elements are the size of the \mathbf{q} -point grid, and a is a broadening factor. The theoretically optimal value of a is 1, but it can often be decreased with significant gains in performance and little degradation in accuracy.

Next, those matrix elements are expanded using crystal symmetry and microscopic time reversibility and averaged to eliminate possible asymmetries. This lookup, together with matrix building, is parallelized via MPI and oneTBB, with stable summations following Neumaier's algorithm for matrix collapse and gathering [254].

Finally, it must be noted that B_{ij} requires a rather strict conservation of energy, which is violated by the broadening scheme. Therefore, we add a correction extracted from a Lagrange-multiplier approach [178] to our matrix to enforce it. On top of that, Landon *et al.* also discussed the necessity of including a momentum correction to make normal processes conserve the momentum. However, we found that including such correction was unnecessary and, in fact, results in spurious effects such as nonnegligible fluxes in directions perpendicular to the thermal gradient for homogeneous bulk systems.

6.4.2. Efficient propagator calculation

The scattering algorithm requires the explicit calculation of the propagator matrix $P(\Delta t) = e^{B\Delta t}$ [see Eq. (4.23)]. Although the matrix exponential is a well defined mathematical operation given by:

$$e^{B\Delta t} = \sum_{n=0}^{\infty} \frac{\Delta t^n}{n!} B^n, \quad (6.6)$$

its practical computation is cumbersome and still a topic under active research, with lots of methods available [255]. One of the most common approaches to computing e^A is the scaling-and-squaring method [256, 257], also chosen by Landon in his original work [177]. The method is based on squaring the matrix to reduce its norm, then computing the exponential using a Padé approximant and undoing the squaring, with an overall computational cost of at best $20N^3$ operations for dense matrices of size N [257]. For reference, the B -matrix of the prototypical 2DM, graphene, contains approximately 1.5×10^9 elements when a $80 \times 80 \times 1$ grid is used, so the scaling and squaring method is not suited for our problem.

In contrast, Krylov subspace methods are especially suited for big matrices,

where the action of the exponential matrix (e^A) on vector (\mathbf{b}) can be approximated using much more smaller matrices. The Krylov subspace $[\mathcal{K}_n(A, \mathbf{b})]$ of order n is a vector subspace spanned by $\{\mathbf{b}, A\mathbf{b}, A^2\mathbf{b}, \dots, A^{n-1}\mathbf{b}\}$, an orthonormal basis (S_n) of which can be build via Arnoldi iteration [258]. The problem can be then recast in terms of $\mathcal{K}_n(A, \mathbf{b})$ as [255, 259]:

$$e^A \mathbf{b} \approx \|\mathbf{b}\| S_n e^{H_n} \mathbf{e}_1 \quad (6.7)$$

where H_n is the projection of A on the basis S_n (of size $n \times n$) and \mathbf{e}_1 is the first column of the identity matrix. The Krylov subspace size and therefore the dimensions of H_n may be truncated down to a desired precision via the error bound $\|e^A \mathbf{b} - \|\mathbf{b}\| S_n e^{H_n} \mathbf{e}_1\| \leq 2\|\mathbf{b}\| \frac{\|A\|^n e^{\|A\|}}{n!}$ [260]. In fact, small values of n tend to give good approximations and enable a calculation of the small $n \times n$ sized e^{H_n} -matrix efficiently through the scaling and squaring method. Despite its efficiency and suitability for our case, the Krylov subspace method is limited to the calculation of arbitrary matrix-vector products $e^A \mathbf{b}$, not of e^A itself. Nevertheless, one can easily recover each column of e^A by using canonical basis vectors as \mathbf{b} -vectors. This way of calculating e^A has the added advantage of being straightforward to parallelize, as each column can be calculated independently.

6.4.2.1. *Linear interpolation of the propagator for systems with multiple reference temperatures*

From the linearized scattering operator (see Eq. 3.11) it becomes clear that different reference temperatures would require different propagators. This is not problematic per se, but the fact that each propagator occupies a big amount of RAM can be a problem for simulations with variable reference temperatures [171]. To relieve the memory burden for such simulations we use on-the-fly linear interpolation of $P(\Delta t)$ between pairs of temperatures, thus requiring memory storage

only for a few reference propagators. Linear interpolation was chosen because it ensures energy conservation at the interpolated temperatures. We tested the performance of these linear interpolants against the corresponding exact propagators by calculating the error per element between the phosphorene propagator at 305 K and the interpolated result using 300 K and 310 K as knots. We also did the same for 320 K using 300 K and 340 K as knots. In both cases, we obtained an error per element in the order of 10^{-6} .

6.4.3. RTA-bRTA

The RTA version of the bRTA algorithm is exactly equal to the full version, except that the scattering algorithm for each particle in a given state k is simplified to generate a random number R in range $[0, 1)$ and if $R < 1 - e^{B_{kk}\Delta t}$ the particle is scattered and resampled from the distribution $\frac{C_{k'}(j)/\tau_{k'}(j)}{\sum_i C_i(j)/\tau_i(j)}$ of the j -th computational box, where C_i and τ_i are the volumetric heat capacity and the RTA lifetime of the i mode, respectively (see Subsection 4.3 for further details on the differences between the scattering algorithms). Contrary to the RTAMC2D implementation, this implementation allows for multiple reference temperatures and initial temperature profiles. Owing to those advantages, we have implemented the RTA version of the algorithm in Section 4.5 in the `beRTAMC2D` executable. Despite the advantages of this implementation, we notice that the RTAMC2D one is much more efficient for steady-state calculations, with time-independent sources.

6.5. Code validation

As previously mentioned, 2DMs are being extensively studied as possible substitutes of silicon in MOSFET [261–263]. Amid all candidates to succeed silicon, the monolayer, also known as phosphorene, and few-layer black phosphorous (bP) have attracted lots of attention due to its electronic properties, such as its high mobility when compared to other candidates like transition metal dichalcogenides [264]. Indeed, is it possible to find several examples of fully functional MOSFETS based on few-layer bP [264–266]. The work of Wu *et al.* is of interest, presenting high-performance MOSFETs with reconfigurable polarities [267]. Furthermore, phosphorene has been proposed to be an important actor in the survival of Moore’s law down to atomic sizes [268] thus increasing the importance of controlling heat transport for phosphorene at the device level.

Therefore, in this section we present phosphorene-based test cases. To that end, we have used first-principles data—i.e.: atomic positions and interatomic force constants of second and third order—of Ref. [269] to obtain phonon properties (frequencies, eigenvectors, lifetimes, group velocities, etc.) alongside with the propagator. Second-order interatomic force constants were renormalized to enforce crystal symmetry, translational invariance and rotational invariance necessary for a proper description of quadratic acoustic bands [270], the broadening parameter was fixed to 1 for energy conservation and the layer thickness was set to 0.533 nm [271]. The phonon properties and the propagator were calculated on a Γ -centered \mathbf{q} -mesh of $50 \times 50 \times 1$ points, for which thermal bulk conductivity is found to be converged—with less than a 5% change with respect to a higher quality mesh of $100 \times 100 \times 1$ points—at 300 K. The propagator for the bRTA calculations was calculated using a time step of 0.25 ps.

6.5.1. RTA code validation

To validate the RTA code, we simulated an infinitely large piece of phosphorene with an applied thermal gradient represented as a source generator (see Subsection 4.2.1.3) as depicted in Fig. 6.4.

Table 6.1.: Calculated κ for phosphorene at 300 K along the armchair (AC) and zigzag (ZZ) directions using the RTA.

	AC $\left[\frac{\text{W}}{\text{m}\cdot\text{K}}\right]$	ZZ $\left[\frac{\text{W}}{\text{m}\cdot\text{K}}\right]$
κ_{almaBTE}	20.7	57.8
$\kappa_{\text{RTA}}^{\text{MC}}$	20.3 ± 0.1	56.2 ± 0.2

$\kappa_{\text{AC,RTA}}^{\text{MC}}$ and $\kappa_{\text{ZZ,RTA}}^{\text{MC}}$ were calculated via Fourier's law from fluxes ($J = -\kappa\nabla T$). The results are quite close to the ones obtained using `almaBTE`'s bulk thermal conductivity calculator, `kappa.Tsweep` (see Table 6.1); with the differences being less than the typical experimental error of 5% for thermal conductivities [219].

We conducted an additional test of this RTA algorithm by comparing it to an RTA version of `bRTA` (see 6.4.3). To do so we simulated an infinite nanoribbon (NR) in the AC direction with an applied gradient of 0.2 K nm^{-1} along the NR. The heat flux profiles from both methods, plotted in Fig. 6.5, are in excellent agreement.

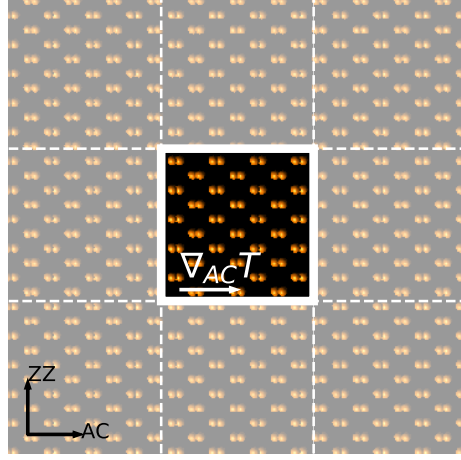


Figure 6.4.: Sketch of the simulation setup for perfect phosphorene with a thermal gradient applied in the AC direction. Replicas illustrating the periodic boundary conditions are depicted as off-color boxes.

6.5.2. Beyond RTA: B -matrix validation

To validate our B_{ij} construction algorithm we used the resulting matrix to obtain the lattice thermal conductivity (κ) by iteratively solving the linear system,

$$\left(\frac{\partial f_i^0}{\partial T} \mathbf{v}_i \cdot \nabla T \right)_i = \sum_j B_{ij} f_j^d, \quad (6.8)$$

i.e. Eq. 4.5 for an homogeneous system with an applied thermal gradient. using the RTA solution ($f_j^{d,RTA} = \frac{1}{B_{jj}} \frac{\partial f_j^0}{\partial T} \mathbf{v}_j \cdot \nabla T$) as an initial guess, and we then compared the results against `almaBTE`'s `kappa_Tsweep` for the case of phosphorene (see Table 6.2). The agreement between both methods and the fact that they are in line with other theoretical calculations provide support to our

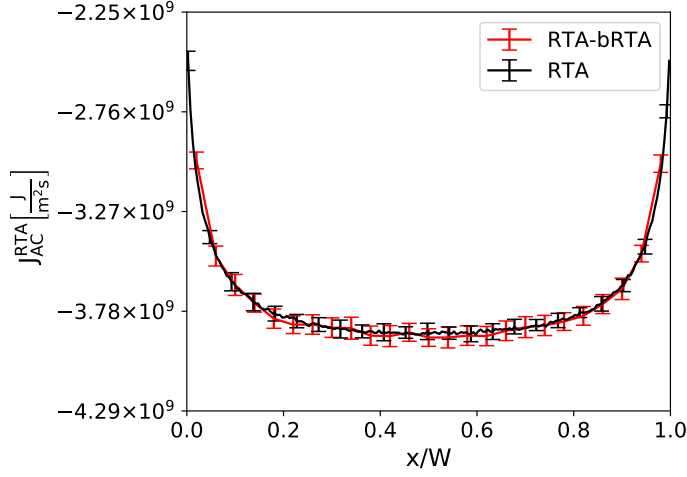


Figure 6.5.: Comparison of RTA (black) and RTA-bRTA (red) heat flux in AC direction as function of normalized position for a phosphorene nanoribbon of 400 nm of width with $\nabla_{AC}T = 0.2 \text{ K nm}^{-1}$.

methodology.

6.5.3. Beyond RTA: Propagator and bRTA validation

To validate $P(\Delta t)$ together with the rest of the bRTA implementation, we simulated an infinitely large piece of phosphorene with an applied thermal gradient represented as a source generator [see Eq. (4.33)], as shown in Fig. 6.4.

The MC heat fluxes for the infinite phosphorene under thermal gradients along the ZZ and AC directions are plotted in Fig. 6.6. κ_{AC}^{MC} and κ_{ZZ}^{MC} are calculated via Fourier's law ($J = -\kappa \nabla T$) to be $27.4 \pm 0.2 \text{ W}/(\text{m} \cdot \text{K})$ and $82.8 \pm 0.5 \text{ W}/(\text{m} \cdot \text{K})$ respectively. Those results show an excellent agreement between iterative and MC solutions, thus validating our bRTA implementation.

Table 6.2.: Calculated κ for phosphorene at 300 K for armchair (AC) and zigzag (ZZ) directions. Other theoretical results are provided for comparison.

	AC $\left[\frac{\text{W}}{\text{m}\cdot\text{K}}\right]$	ZZ $\left[\frac{\text{W}}{\text{m}\cdot\text{K}}\right]$
κ_{almaBTE}	27.501	82.878
κ_{B}	27.499	82.860
Ref. [272] [†]	23.9	82.1
Ref. [273] [†]	35.5	108.3
Ref. [269]	22.0	63.2

[†] These results are rescaled to take into account differences in assumed thickness.

6.6. Results

In this section we present illustrative example applications of our package simulators.

6.6.1. Phosphorene devices

In this section we present thermal transport results for different phosphorene-based configurations/devices using the simulators developed in previous sections.

6. *BTE-Barna: thermal simulation of devices based on 2D materials*

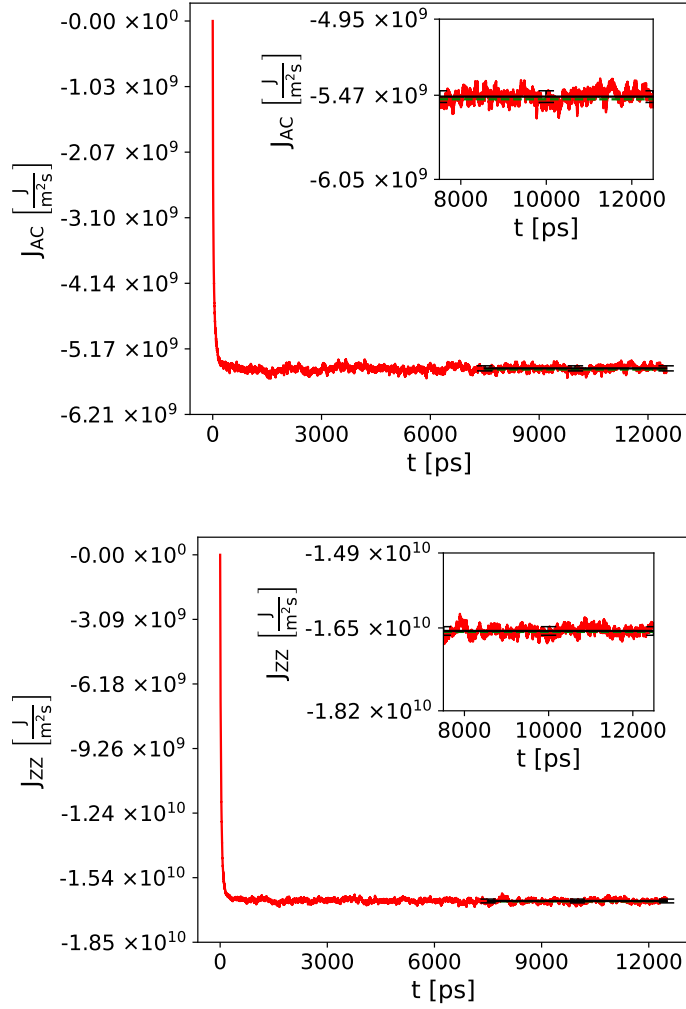


Figure 6.6.: bRTA heat flux as function of simulation time (red) and average steady-state flux (black) in AC (top) and ZZ (bottom) for infinitely large phosphorene at 300 K under an applied thermal gradient of 0.2 K nm^{-1} in the transport direction. The iterative result calculated via Fourier's law with κ^{almaBTE} is given in both cases for comparison (dashed green). Inset: zoomed view of the steady-state region used to compute the mean flux.

6.6.1.1. *Nanoribbons*

Among the simplest 2D-based systems used in devices are nanoribbons [262, 263]. We have calculated the heat transport in infinite phosphorene AC nanoribbons under the effect of a thermal gradient of 0.2 K nm^{-1} . The results of the normalized heat flux relative to the bulk value, together with an RTA rescaled version for three different widths are shown in Fig. 6.7.

As expected, boundary scattering increases and becomes dominant over other mechanisms in thinner nanoribbons. This is clearly seen in the reduction of heat flux with decreasing width and the fact that the difference between the RTA and beyond-RTA methods vanishes for smaller ribbons [see the 4 nm case in Fig. 6.7(a)], since boundary scattering is not dependent on the approach used to describe intrinsic anharmonic and isotopic scattering. Consequently, for wide nanoribbons in which anharmonic and isotopic scattering are dominant it should be possible to obtain a good approximation to bRTA results by simply using a $\kappa_{\text{almaBTE}}/\kappa_{\text{RTA}}$ -rescaled RTA [see Fig. 6.7(b)]. Indeed, the main differences between this estimate and bRTA for the 400 nm-ribbon are in the regions near the boundaries, in which the bRTA flux is lower than the rescaled version. Although also visible in other cases, this is more pronounced in the wider nanoribbon.

In view of the above, the RTA clearly overestimates the momentum destruction due to intrinsic scattering leading to more diffusive flux profiles when compared to bRTA results. The latter yields more Poiseuille-like profiles, with stronger hydrodynamic features, by properly capturing the coupling between phonon modes [139, 274].

To further explore those hydrodynamic signatures, we fitted our nanoribbon

results to a mesoscopic equation based on Sellitto *et al.*'s work [137]:

$$J(x) = -\kappa \left\{ 1 - \left[\frac{1}{1 + C \tanh\left(\frac{W}{2\ell}\right)} \right] \frac{\cosh\left(\frac{x}{\ell}\right)}{\cosh\left(\frac{W}{2\ell}\right)} \right\} \nabla T \quad (6.9)$$

where W is the nanoribbon width, x is the distance from the center of the nanoribbon, ℓ is the non-local length [143] and C is related to wall properties, taking a value of 2 in our case because we have assumed completely diffusive walls.

In Figs. 6.8 and 6.9 the fits of our RTA and bRTA simulator results to hydrodynamic mesoscopic equation for nanoribbons are shown; in both we obtain a set of parameters that accurately match the simulation results. The agreement afforded by the beyond-RTA method is, however, slightly better.

As for the fitted parameters, we can observe a relative fast convergence of thermal conductivity towards bulk values as the nanoribbon gets wider and boundary scattering effects become negligible in the middle of the strip (see Fig. 6.10). The value of the non-local length (ℓ) rises towards a converged value as the ribbon becomes wider (see Fig. 6.11), in agreement with what is expected from a microscopic description of the value [143]. The observed differences between RTA and the higher beyond-RTA ℓ values, especially for larger widths, can be easily interpreted by keeping in mind that in RTA all scattering processes are deemed as resistive and introduce artifactual modifications of the heat flux. It should be noted that the theoretical formulas used to obtain the $\ell^{\text{RTA,iso}}$ values are derived under the assumption of isotropy and are therefore expected to be useful only as approximations in our case. For reference, the results for ZZ-nanoribbons are also given in Figs. 6.12-6.15. We note that, these results do not provide any additional information regarding the analysis done for the AC nanoribbons, with the AC findings and conclusions being also valid for the ZZ nanoribbons.

Finally, we have also obtained κ_{nano} for nanoribbons of several widths with

6. BTE-Barna: thermal simulation of devices based on 2D materials

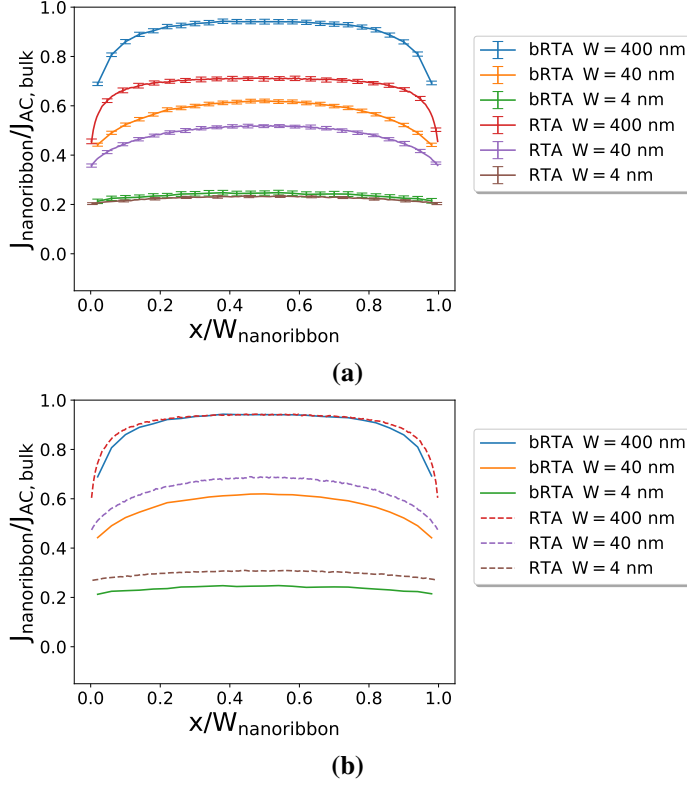


Figure 6.7.: Top: RTA and bRTA bulk-normalized heat flux in the AC direction as a function of the normalized position for a phosphorene nanoribbon with $\nabla_{\text{AC}}T = 0.2 \text{ K nm}^{-1}$. Bottom: Comparison of bulk-normalized bRTA and $\kappa_{\text{almabTE}}/\kappa_{\text{RTA}}$ -rescaled RTA heat fluxes.

both types of edges using the methodology described in Section 3.2.3 for solving the PBTE in systems with edges as detailed in Section 6.2 (see Fig. 6.16). For consistency check, we compared the effective flux obtained via Fourier using κ_{nano} with the flux average over width obtained from Monte Carlo simulators, obtaining, as can be seen in Fig.6.17, an excellent match between both methods.

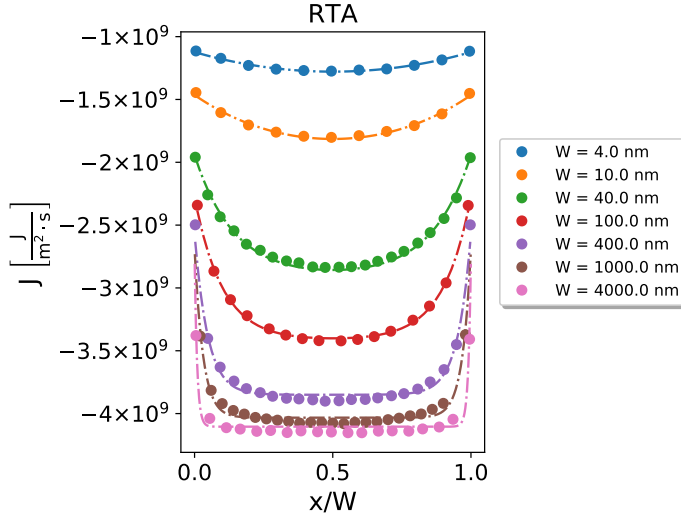


Figure 6.8.: Fitting to to Eq. 6.9 (lines) of RTA-MC calculated heat flux (points) as a function of normalized position for phosphorene AC nanoribbons of different widths under the effect of $\nabla_{AC}T = 0.2 \text{ K nm}^{-1}$.

6.6.1.2. *RTA, bRTA and Fourier heat equation comparison*

Taking into account that operational frequencies of microprocessors are limited to the GHz by cooling constraints [268, 275], it is of interest to be able to study heating dynamics at short times. As an example of capabilities to simulate short heating dynamics, we have studied the temperature time evolution for a piece of phosphorene initially at 300 K with periodic boundary conditions in the AC direction and sandwiched between two isothermal reservoirs, at 300 K and 302 K, in the ZZ direction (see Fig. 6.18).

Fig. 6.19 shows the RTA, bRTA and Fourier ($\frac{\partial T}{\partial t} = \alpha \nabla^2 T$, where α is the thermal diffusivity: $\alpha = \kappa / C_v$) heat profiles at two different times. The difference between the Fourier heat equation and BTE results at short times is a well known shortcoming of the former [276, 277]. Regarding PBTE solutions, bRTA and RTA

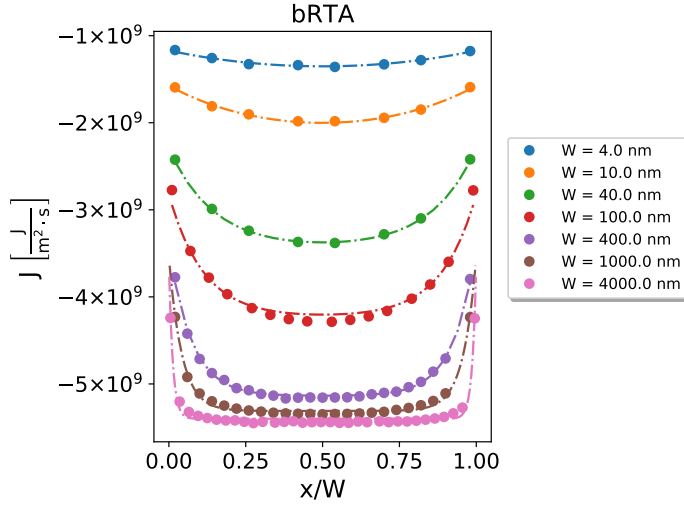


Figure 6.9.: Fitting to Eq. 6.9 formula (lines) of bRTA calculated heat flux (points) as a function of normalized position for phosphorene AC nanoribbons of different widths under the effect of $\nabla_{AC}T = 0.2 \text{ K nm}^{-1}$.

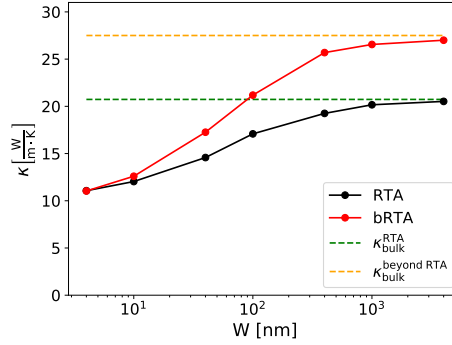


Figure 6.10.: Fitted thermal conductivity as a function of AC nanoribbon width for RTA (black) and bRTA (red) MC calculations. RTA (green) and beyond RTA (orange) bulk values are given for reference.

results clearly differ at this instance. The bRTA shows a faster heating, which is not surprising since RTA scattering completely randomizes momentum, thus dampening the fluxes and leading to a lower thermal conductivity.

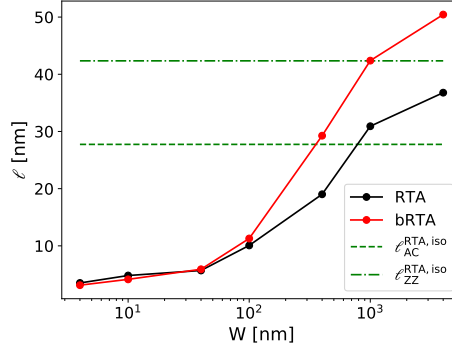


Figure 6.11.: Fitted non-local distance ℓ as a function of AC nanoribbon width for RTA (black) and bRTA (red) MC calculations. RTA bulk values of ℓ calculated using Sendra et. al.'s formula [143] are given for reference (green).

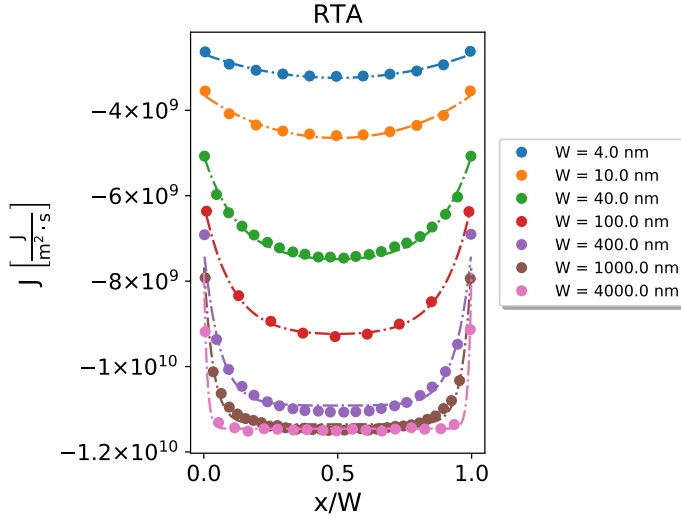


Figure 6.12.: Fitting to Eq. 6.9 (lines) of RTA-MC calculated heat flux (points) as a function of normalized position for phosphorene ZZ nanoribbons of different widths under the effect of $\nabla_{ZZ}T = 0.2 \text{ K nm}^{-1}$.

In Fig. 6.21 we plot the spectral decomposition of the contributions to the deviational temperature at the middle and near the hot edge of the beam. In

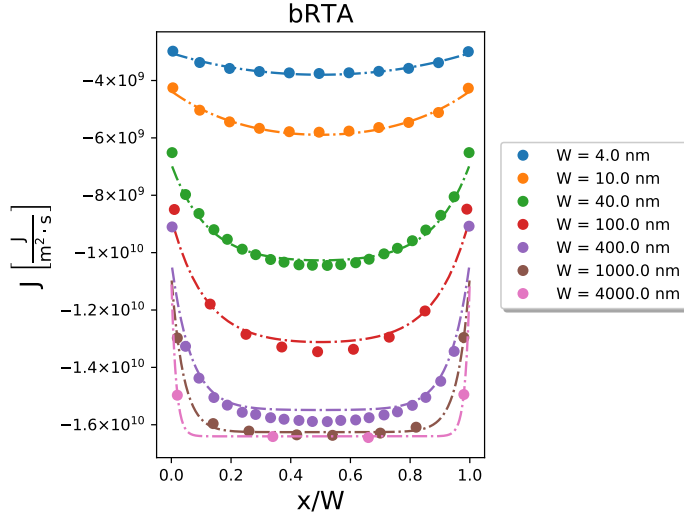


Figure 6.13.: Fitting to Eq. 6.9 (lines) of bRTA calculated heat flux (points) as a function of normalized position for phosphorene ZZ nanoribbons of different widths under the effect of $\nabla_{ZZ}T = 0.2 \text{ K nm}^{-1}$.

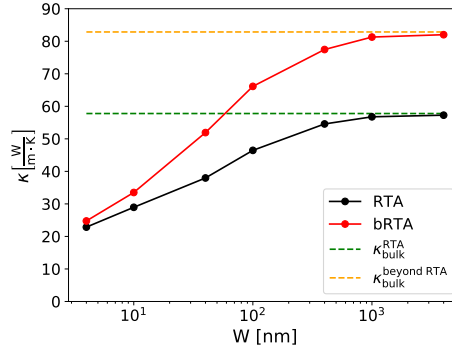


Figure 6.14.: Fitted thermal conductivity as a function of ZZ nanoribbon width for RTA (black) and bRTA (red) MC calculations. RTA (green) and beyond RTA (orange) bulk values are given for reference.

keeping with the fact that differences between the RTA and bRTA solutions are the largest in the middle of the bar (see Fig. 6.19), spectral decompositions of the

6. BTE-Barna: thermal simulation of devices based on 2D materials

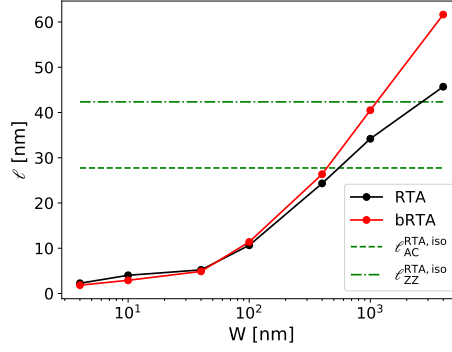


Figure 6.15.: Fitted non-local distance ℓ as a function of ZZ nanoribbon width for RTA (black) and bRTA (red) MC calculations. RTA bulk values of ℓ calculated using Sendra et. al.'s formula [143] are given for reference (green).

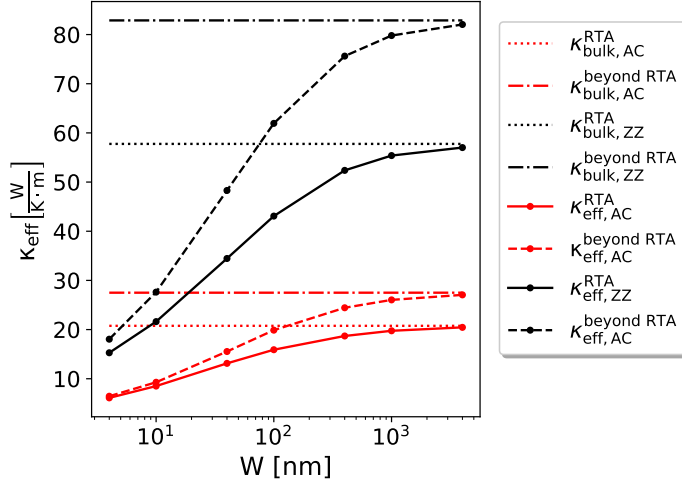


Figure 6.16.: Effective thermal conductivity for AC and ZZ nanoribbons of different widths at 300 K obtained through the direct (RTA) and iterative (beyond the RTA) solution of the linearized-PBTE. Bulk values are provided as reference.

deviational temperature deviate the most at the middle as opposed to the edges. They also vanish with time as both tend to the same temperature profile [see Figs.

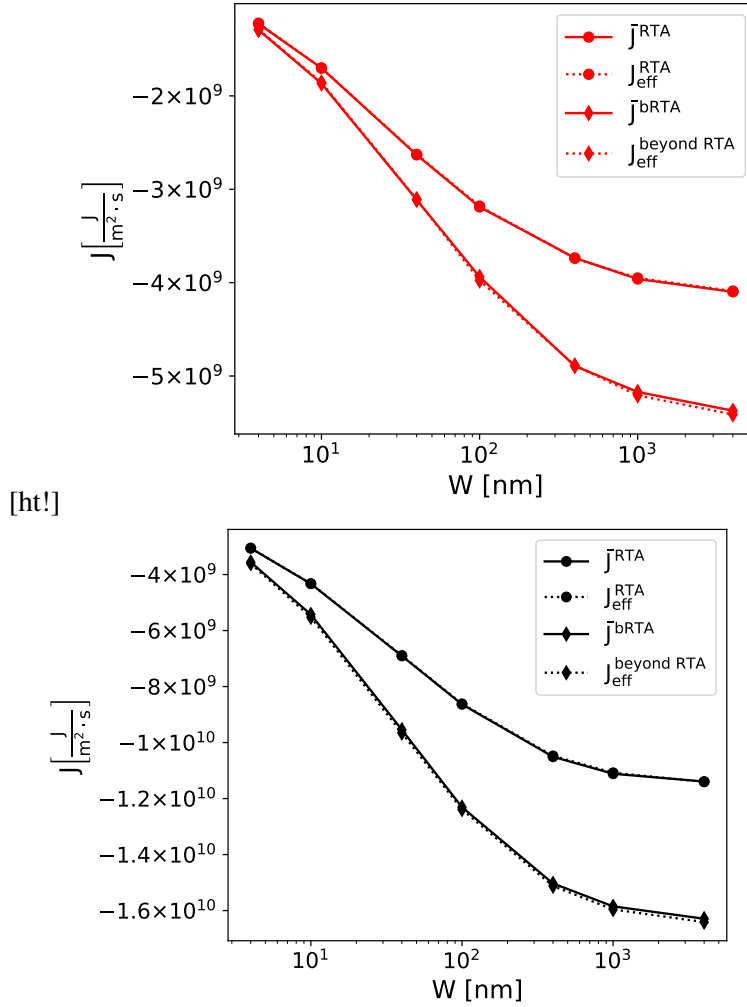


Figure 6.17.: Comparison between effective RTA and beyond RTA heat fluxes for AC (top) and ZZ (bottom) nanoribbons and the respective Monte Carlo obtained fluxes for a 0.2 K nm^{-1} gradient in the unbound direction.

6.21(a)-6.21(d)]. Moreover, from the spectral decomposition it can also be seen that differences are more prominent at low frequencies, corresponding to phonons with longer intrinsic lifetimes (see Fig. 6.20), which indicates that the decay of

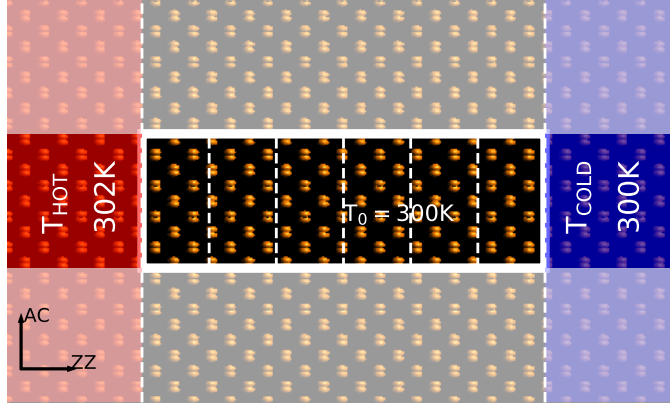


Figure 6.18.: Sketch of phosphorene heating simulation in ZZ direction. Periodic boundary conditions are depicted with off-color boxes.

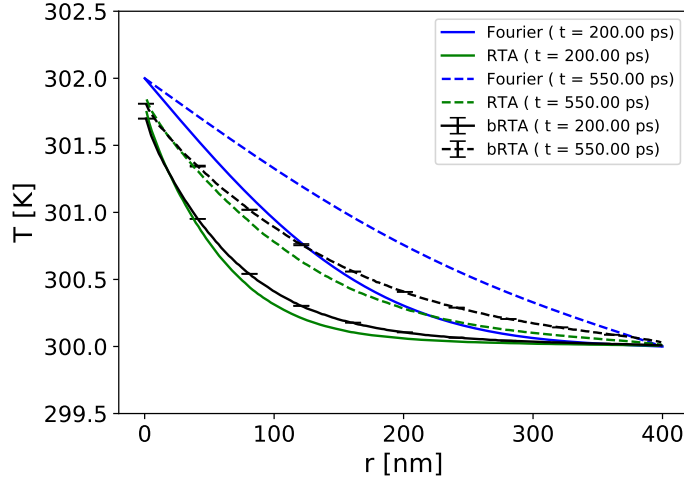


Figure 6.19.: Temperature profiles obtained with the RTA (green), bRTA (black) and Fourier (blue) approaches as functions of position for a ZZ-phosphorene bar at 200 ps (solid) and 550 ps (dashed).

such modes is clearly much more overestimated than for high-frequency ones. This explains the large disparity between the RTA and bRTA conductivities. It

is therefore advisable to resort to the bRTA method for modeling fast/short heat dynamics, for example when studying heat dissipation in state-of-the-art electronic devices, as less sophisticated approximations fail to describe it accurately.

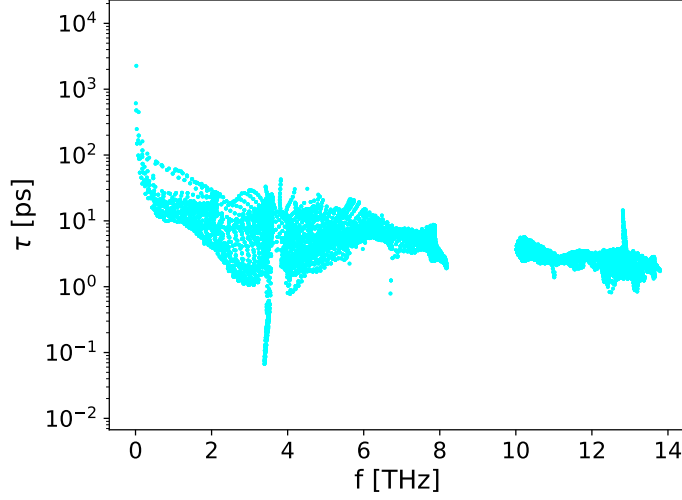


Figure 6.20.: Bulk-phosphorene lifetimes as function of frequency at 300 K.

6.6.1.3. *Finite device examples*

As previously mentioned, being able to predict thermal transport in complex devices and geometries is of key importance. To this end, we show examples for more complex systems, either because they have geometrical elements which are difficult to model computationally, such a wedge geometry (see Fig. 6.22), or because they present interesting elements from a simulator capability point of view such as more than two terminals, which is a common experimental setup.

Steady-state temperature profiles and heat fluxes for the wedge-like geometry within and beyond the RTA for two different configurations, depending on which terminal is put at 301 K (the one at the top or the one at the bottom) while the

6. BTE-Barna: thermal simulation of devices based on 2D materials

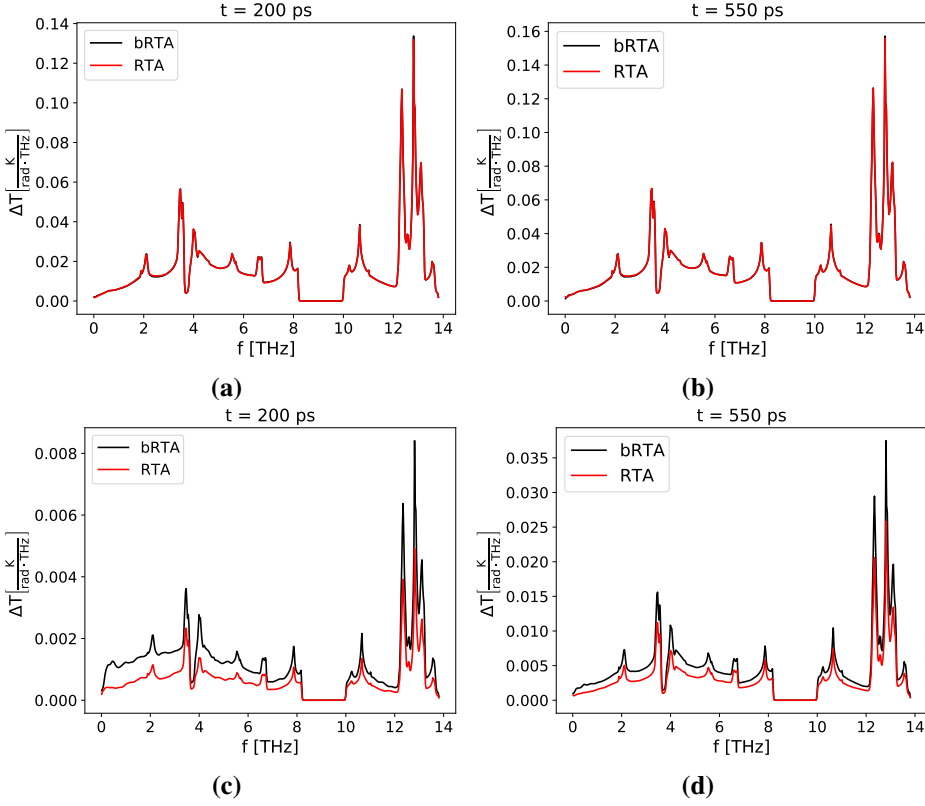


Figure 6.21.: RTA (red) and bRTA (black) spectral decomposed temperature deviations for 400 nm ZZ-phosphorene bar at 15 nm (a and b) and 203 nm (c and d) from the hot edge, at times 200 ps and 550 ps.

other is kept at the reference temperature of 300 K, can be seen at Figs. 6.23 and 6.24 respectively. Similar asymmetric devices are used as thermal rectifiers, but we cannot expect to detect rectification here because this model is based on the bulk spectrum and therefore does not account for phenomena such as device-reservoir interactions or size-dependent vibrational spectra [278, 279]. Moreover, it should be noted that thermal differences used here are too small for any sign of thermal rectification to be significant over statistical noise [278], or to

activate the rectification mechanism based on different temperature-dependent behavior [278, 280, 281]. Higher thermal differences are however unattainable with the current implementation as the error introduced by the linearization of the collision operator would be too high.

The heat fluxes and temperature profiles for the multiterminal structure (Fig. 6.25) are presented in Figs. 6.26 and 6.27, showing the capability of our simulator to properly account for several sources/drains (isothermal reservoirs). Indeed, for the bRTA case, there is even an additional population of phonons due to the initial conditions, as the initial temperature profile was set to the RTA estimate in order to accelerate its convergence to the steady-state.

6.6.2. Results: Example of material junction

Finally, to show the capability of our improved RTA simulator to describe devices with different materials, we present the temperature profile (Fig. 6.28) in a finite device structure composed by graphene on one half and h-BN encapsulated graphene on the other half (see Fig. 6.29). The first-principles data needed for this calculation were obtained from Ref. [282] in the case of graphene, where those properties had been calculated on a $80 \times 80 \times 1$ \mathbf{q} -mesh with a broadening parameter of 1 and a conventional thickness of 0.345 nm [178]. Regarding h-BN encapsulated graphene, the required first-principles data were obtained using density functional theory using Perdew-Burke-Ernzerhof functional [64] plus the D3 [72, 283] correction to energy due to van der Waals interactions between layers as implemented in VASP [197–199] with a Γ -centered \mathbf{k} -mesh of $7 \times 7 \times 1$ points for minimization, and using Phonopy [161] and thirdorder.py [46] with a supercell of $7 \times 7 \times 1$ to obtain second and third order interatomic force constants, respectively. The phonon properties of h-BN-encapsulated graphene were calculated using a $40 \times 40 \times 1$ Γ -centered \mathbf{q} -mesh with a broadening parameter

6. *BTE-Barna: thermal simulation of devices based on 2D materials*

of 1 and setting the stack thickness to 1.001 nm [178, 284, 285].

6. *BTE-Barna*: thermal simulation of devices based on 2D materials

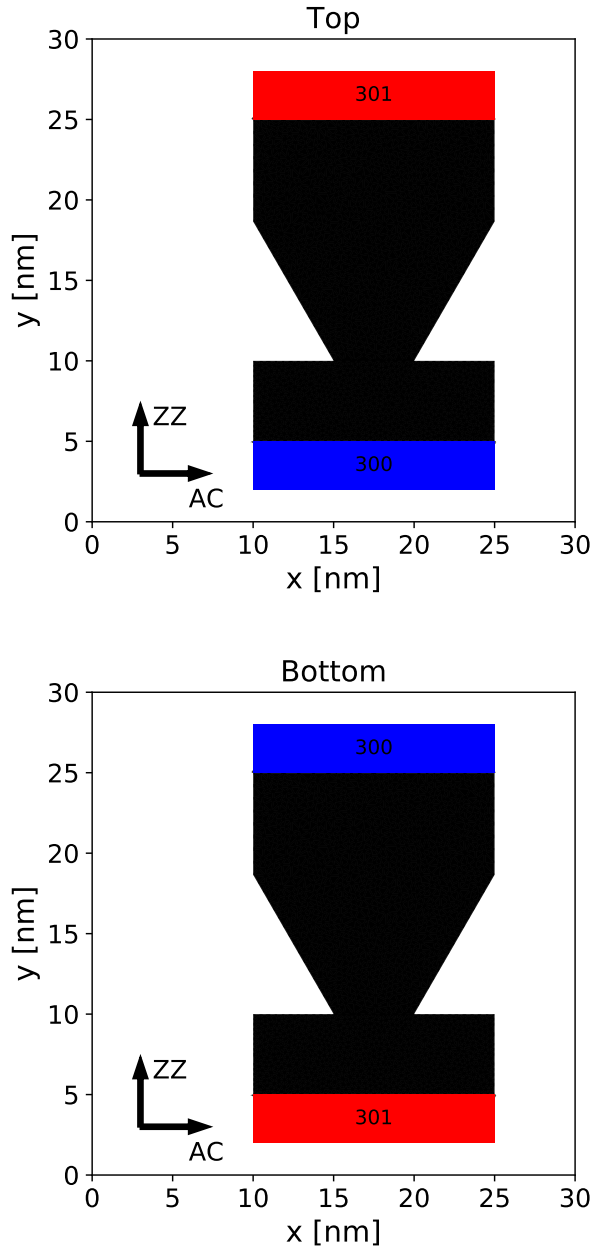


Figure 6.22.: Phosphorene wedge-like geometry with hot reservoir at the top or at the bottom.

6. *BTE-Barna: thermal simulation of devices based on 2D materials*

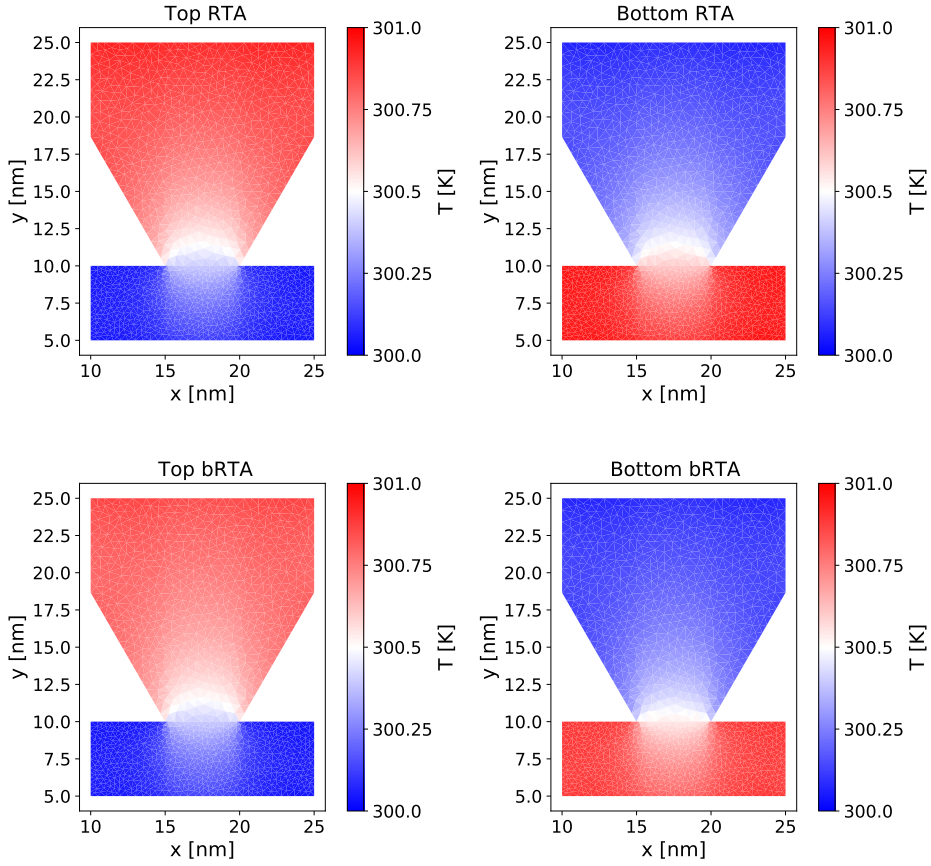


Figure 6.23.: RTA and beyond RTA temperature profiles for Fig. 6.22 configurations at steady-state.

6. *BTE-Barna: thermal simulation of devices based on 2D materials*

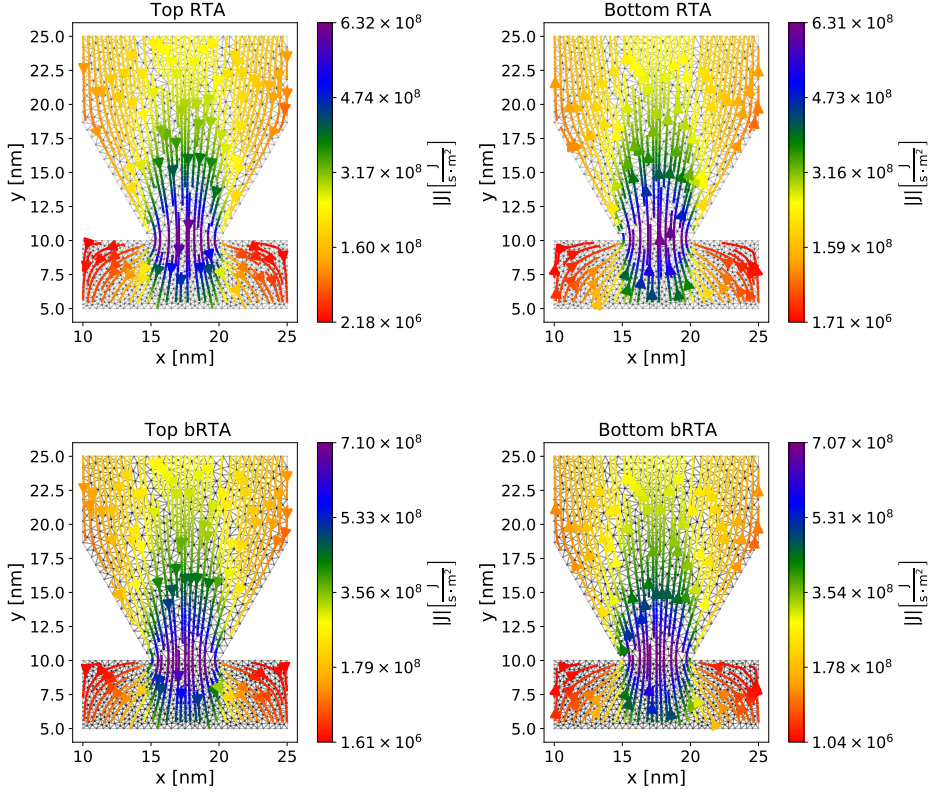


Figure 6.24.: Steady-state RTA and beyond-RTA heat fluxes for the configurations depicted in Fig. 6.22.

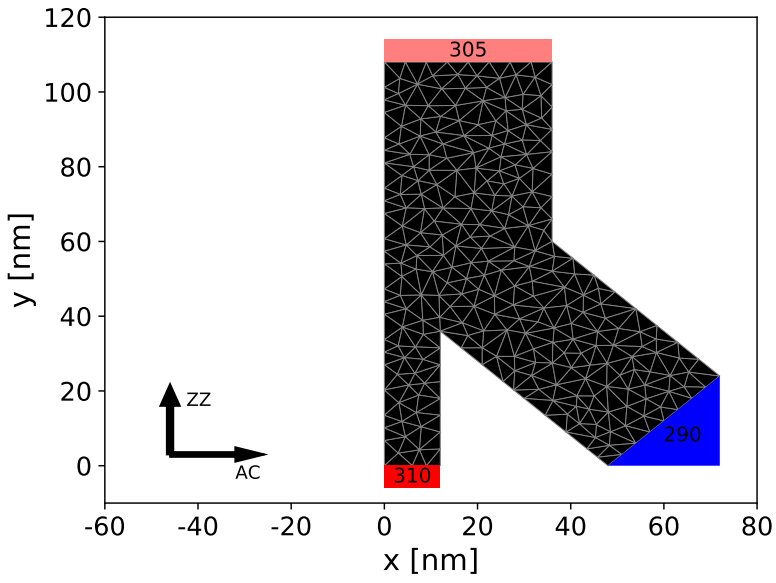


Figure 6.25.: Example phosphorene structure with multiple terminals (isothermal reservoirs) at 310 K, 305 K and 290 K.

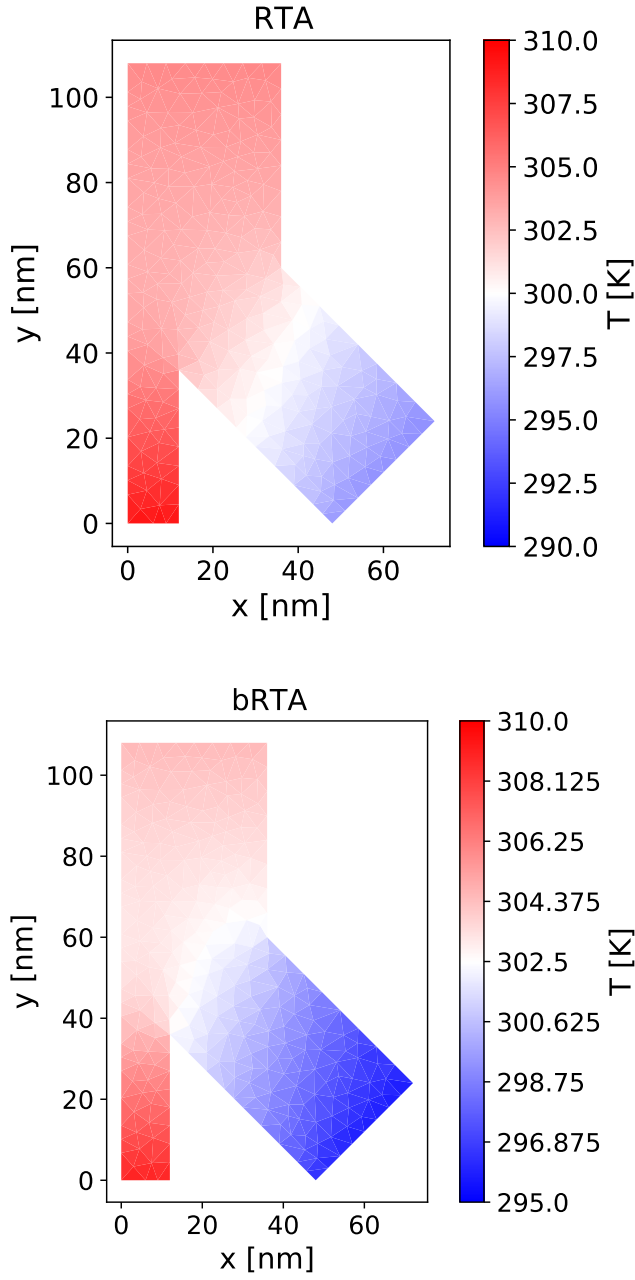


Figure 6.26.: Steady-state RTA and beyond-RTA temperature profiles for the configuration depicted in Fig. 6.25.

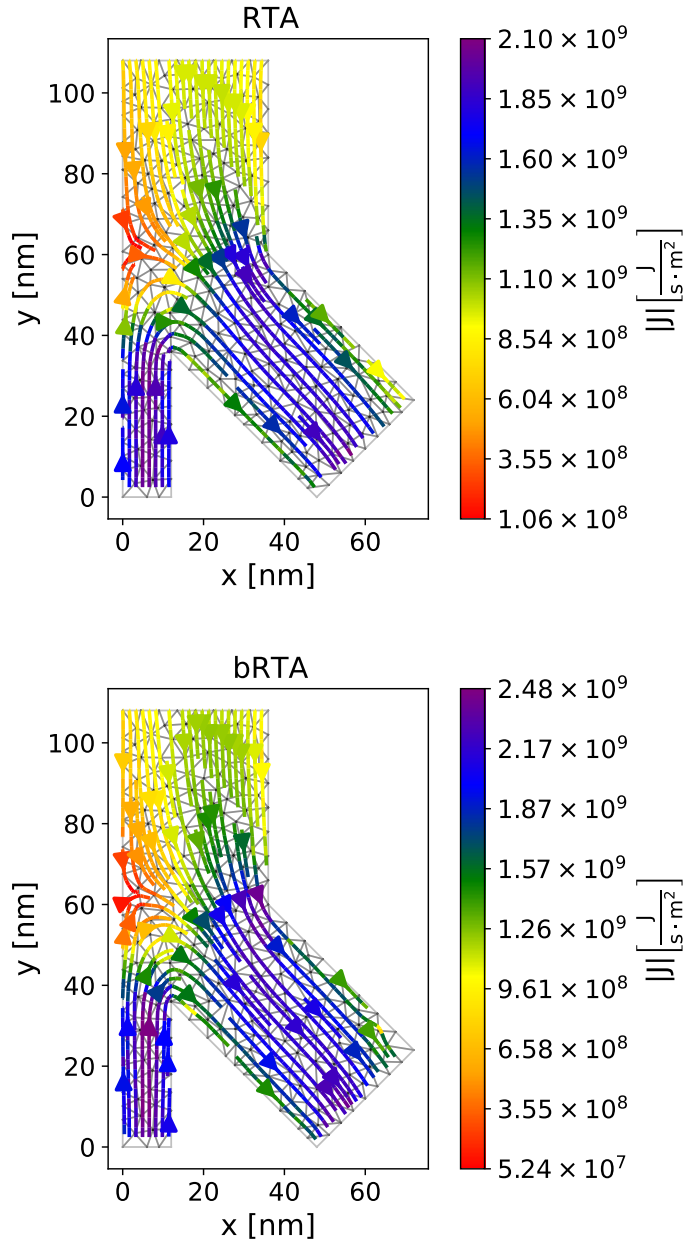


Figure 6.27.: Steady-state RTA and beyond-RTA heat fluxes for the configuration depicted in Fig. 6.25.

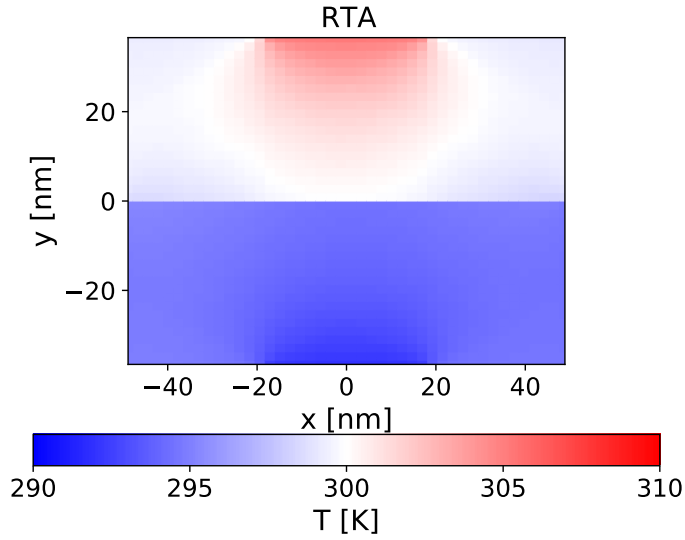


Figure 6.28.: Steady-state RTA temperature profile for the configuration in Fig. 6.29.

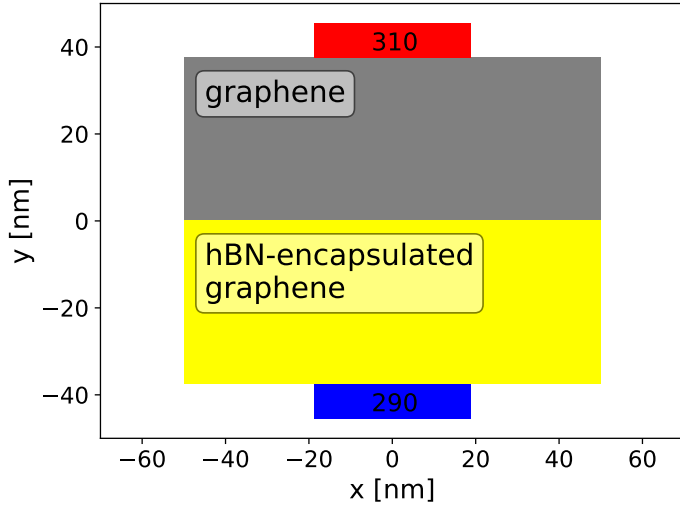


Figure 6.29.: Structure containing a junction between graphene and hBN-encapsulated graphene and two isothermal boundaries at 290 K (blue) and 310 K (red).

6.7. Summary and conclusions

In this Chapter we have presented BTE-Barna, a software package that extends the almaBTE package to calculate the thermal properties of devices and systems based on 2D materials. We have showcased the new capabilities with an extensive set of tests and examples. For instance, the package was used to highlight the differences in the heat flux profile for the case of Poiseuille flow in a nanoribbon, for the case of RTA and beyond the RTA. Amid all new features the most relevant are:

1. The iterative solver has been extended to provide the effective conductivity for nanoribbons (and nanowires in the case of 3D materials).
2. A highly efficient RTA Monte Carlo simulator for the computation of the steady-state properties based on the one included in almaBTE has been implemented. In contrast with the original implementation, this new one can address finite and/or periodic 2D systems and their heterojunctions under the effect of thermal gradients and isothermal reservoirs. Moreover, it now provides information for transient to steady-state for finite systems. It also enables RTA Monte Carlo simulations of 2D systems with complex geometries, including non-uniform cross-sections.
3. A beyond-RTA Monte Carlo simulator for 2D systems was implemented to provide an accurate description for those cases in which RTA fails. This innovation, in particular, has required the implementation of a completely different Monte Carlo formalism in a much more efficient way than had previously been achieved.

This package is published as a fork of almaBTE and is freely available to download at <https://github.com/sousaw/BTE-Barna>. Overall, we expect BTE-Barna to provide a new set of tools for design and prediction of thermal transport/management in 2D based devices and systems.

CHAPTER 7

Hydrodynamic signatures in thermal transport in devices based on 2D materials from first-principles

This Chapter reproduces to a great extent the contents of [Raya-Moreno, M., Carrete, J., Cartoixà, X. (2022). Hydrodynamic signatures in thermal transport in devices based on 2D materials: an ab initio study. arXiv preprint arXiv:2203.05293.], which has been submitted for publication to Physical Review B.

As extensively discussed in Chapter 3, the classical approach to heat transport is the Fourier’s law. However, as detailed in Section 3.1.1, Fourier’s law is known to break down in small systems and short timescales, with several experimental examples available [34–38]. Such erroneous descriptions have their origin in the shortcomings of Fourier’s law, namely the infinite velocity of heat propagation and the lack of non-local effects. The inclusion of these two effects into the theory makes heat acquire characteristics of a viscous fluid, which are describable via additional hydrodynamic (Navier-Stokes-like) terms (see Subsection 3.1.1.1).

As discussed in Section 3.2, in the case of semiconductors, where phonons

7. Hydrodynamic signatures in devices based on 2D materials

are the main heat carriers, it is possible to obtain an accurate description of thermal transport, including non-Fourier features, by solving the Peierls-Boltzmann transport equation (PBTE) with the appropriate boundary conditions [39, 40] (see Subsection 6.6.1.1 for practical examples of non-Fourier behavior, i.e. Poiseuille flux). Despite its advantages in terms of precision and transferability when combined with first-principles data (see Subsection 3.2.6), the solution of the PBTE, for devices and/or structures of interest for heat management or thermoelectric applications, is rather complex and expensive (see Chapters 4 and 6 to get an insight of the complexity for the MC algorithms solving the PBTE and their practical implementation, respectively). Moreover, the overall complexity of the PBTE makes it hard to obtain an intuitive and clear physical picture of heat transport phenomena [132, 133].

In this context, beyond-Fourier mesoscopic models (i.e., the ones that not only describe the classical diffusive regime of Fourier's law, but other important transport regimes in the nanoscale, such as the ballistic and hydrodynamic ones) are essential for a fast, simple, and physically intuitive description of thermal transport at the micro/nanoscale [133]. Among all available mesoscopic equations, the hydrodynamic equation (see Section 3.1.1.1) stands out as a promising candidate since it can be directly derived from the BTE, so that a microscopic physical description of its variables might be obtained, enabling their calculation with *ab initio* methods for accurate simulations [143, 286].

Two clear signatures of hydrodynamic behavior are the formation of heat flux vortices and the appearance of non-monotonic temperature profiles in non-trivial sample geometries. Such hydrodynamic features have also been predicted to appear in the context of electronic transport for graphene [287], and recent works have also predicted the existence of thermal vortices in nanoporous silicon [288] and graphene-based devices [289, 290], though the used methodology was, in these cases, based on fitted parameters or models instead of a full microscopic

7. Hydrodynamic signatures in devices based on 2D materials

ab-initio-based description. This has been improved in the recent work of Guo *et al.* [104], where they predicted vorticity in graphene-based devices based on Callaway’s model [99] informed with *ab initio* scattering rates. However, despite the increase in the accuracy with respect to the gray model in Ref. [290] or the relaxation time approximation (RTA), Callaway’s model is known to yield thermal conductivities with, at best, a 30% error [103, 104] at room temperature in the case of graphene. Although the accuracy of Callaway’s model can be improved by a more careful analysis of umklapp scattering in thermal resistivity [103, 105], reducing the error to 3%, such improvement is not guaranteed *a priori*. For instance, in the case of black phosphorous the error in the zigzag thermal conductivity, even with such a correction, is of 15% [103]. This lack of systematic predictability together with other theoretical drawbacks, like the requirement to differentiate between normal and umklapp processes—a distinction that some authors find arbitrary [101, 102]—makes it necessary to go beyond and make use of the full linearized scattering operator for an accurate, predictive description of hydrodynamics in both real and reciprocal space. Although few scarce examples of such a step can be found in the literature [178, 291, 292], none of them discussed any complex geometries in which vorticity or non-monotonic temperature profiles appear. Consequently, this raises the question of to what extent simpler non-systematic approaches to the scattering operator, like Callaway’s or the RTA, can properly describe such features, and how their use compares to the exact linearized collision operator.

In this Chapter, we study hydrodynamic signatures in graphene and phosphorene-based nanodevices at room temperature by solving the PBTE via energy-based deviational Monte Carlo (MC) techniques with a full linearized scattering operator where the scattering rates are obtained from first principles, using the BTE-Barna code described in the previous Chapter. We discuss the accuracy and effect on those hydrodynamic features of using non-systematic approaches

7. Hydrodynamic signatures in devices based on 2D materials

to the scattering operator, namely the relaxation time approximation, in comparison to the most accurate full linearized operator. We also provide insight into the mechanisms originating those features, and we show that the key factor in vortex appearance is the vertical separation between the heat source and drain, regardless of the relative importance of normal vs. resistive scattering. Finally, we complement our results with solutions of the hydrodynamic equation for a better understanding of some size effects as well as studying signatures below the MC statistical noise.

This Chapter is structured as follows: after briefly discussing hydrodynamics in Section 7.1, we detail the applied methodology for the heat fluxes and thermal profiles calculation in Section 7.2, and we present the bulk properties, cumulative curves and a discussion of the expected hydrodynamic features in Section 7.3. The results for devices are provided in Sec. 7.4, both for thinner (Subsection 7.4.1) and wider ballistic devices (Subsection 7.4.2). The summary and conclusions of this Chapter are given in Section 7.5.

7.1. Hydrodynamics and 2D materials: the role of normal and umklapp processes

The steady-state hydrodynamics equation of heat transport is given by the steady-state version of Eq. 3.4,

$$\mathbf{J} = -\kappa \nabla T + \ell^2 \nabla^2 \mathbf{J}, \quad (7.1)$$

where we recall that \mathbf{J} is the heat flux, κ is the thermal conductivity tensor, T is the temperature and ℓ is a non-local length tensor, which is related to the distance in which phonon distribution can conserve its inertia even under the effect of intrinsic scattering.

As discussed in Section 3.1.1, one of the earliest derivations of this hydro-

7. Hydrodynamic signatures in devices based on 2D materials

dynamic equation for heat transport was by Guyer and Krumhansl (GK) [138]. However, because of the assumption made in its supposition—i.e. normal (\mathcal{N}) processes dominance over all other scattering mechanisms, namely umklapp (\mathcal{U}) and extrinsic (\mathcal{E}), which includes boundary and/or interface scattering—the hydrodynamic features are only possible when these processes dominate [132, 139, 140, 289].

This last condition, namely $\mathcal{N} \gg (\mathcal{U}, \mathcal{E})$, has been customarily associated with the failure of the RTA, as in such a case most of the processes are not directly resistive but indirectly so through population redistribution, which makes the RTA ansatz inappropriate. Consequently, as noted in Subsection 3.1.1.1, in 2D materials, in which the RTA has been observed to provide a poor description of thermal properties [139, 147], hydrodynamic features should be stronger than for other materials [139, 289].

We found it worth recalling that the role of \mathcal{U} and \mathcal{N} processes in phonon hydrodynamics is much more intricate than the widespread belief that \mathcal{N} processes must dominate. Indeed, it is a sufficient but not necessary condition (see Subsection 3.1.1.1). Moreover, such a distinction has several conceptual flaws discussed in Subsection 2.2.1.1. On this basis, most modern hydrodynamic theories do not rely on the \mathcal{N} dominance or on the classification of three-phonon processes into \mathcal{N} and \mathcal{U} [143], generalizing the hydrodynamic regime to all kind of materials, including but not limited to materials like room-temperature silicon in which intrinsic resistive scattering is the dominant mechanism [143], i.e. out of the range of applicability of the Guyer-Krumhansl (classical) hydrodynamics.

Taking into consideration everything mentioned here, we have selected graphene and phosphorene for our study. The former was chosen because, in addition to it being the prototypical 2D material, several works [287, 289] have already predicted current vortices in both electronic and thermal transport. On the other hand, the latter was chosen in view of its excellent electronic properties [264],

7. Hydrodynamic signatures in devices based on 2D materials

which have positioned it as a principal actor in the extension of Moore's law down to atomic sizes [268], thus making a proper description of heat transport, including hydrodynamics, essential for the developing of phosphorene-based devices.

7.2. Methodology

Previous works have predicted electrical current vortices and negative nonlocal resistance in 2D materials (graphene) when finite sources are injecting heat/electrons [287, 289, 290]. A sketch of those geometries, henceforth called Levitov configurations, is depicted in Fig. 7.1. The dimensions of the studied Levitov configurations were selected to investigate all possible regimes; to that end, a mean free path (λ_α) and a non-local length (ℓ) have been computed to provide an approximate idea of the limiting sizes of each transport regime. The mean free path is defined as

$$\lambda_\alpha \equiv ([\kappa^{\text{SG}}]^{-1} \kappa^{\text{RTA}})_{\alpha\alpha}. \quad (7.2)$$

Here α indicates a Cartesian component, κ^{RTA} is the RTA thermal conductivity tensor and κ^{SG} is the small-grain thermal conductivity tensor defined as [46]

$$\kappa^{\text{SG}} = \frac{1}{k_B T^2 V_{uc}} \sum_{\sigma} n_{\sigma}^0 (n_{\sigma}^0 + 1) \frac{\hbar \omega_{\sigma}}{|\mathbf{v}_{\sigma}|} \mathbf{v}_{\sigma} \otimes \mathbf{v}_{\sigma}, \quad (7.3)$$

where k_B is the Boltzmann constant, V_{uc} is the volume of the unit cell, σ is a phonon mode, n_{σ}^0 is the Bose-Einstein distribution for mode σ , \hbar is the reduced Planck constant, ω_{σ} is the phonon frequency and v_{σ} is the phonon group velocity. In addition, the non-local length (ℓ) within the RTA and for isotropic materials,

7. Hydrodynamic signatures in devices based on 2D materials

$\ell_{\text{iso}}^{\text{RTA}}$, can be calculated using Eq. 3.17:

$$\ell_{\text{iso}}^{\text{RTA}} = \frac{1}{5} \frac{\int_{BZ} \hbar q_i v_i^2 \tau_i^2 \frac{\partial n_i^0}{\partial T} di}{\int_{BZ} \hbar q_i v_i \frac{\partial n_i^0}{\partial T} di}, \quad (3.17)$$

where q_i is the wave vector of the i mode in the first Brillouin Zone.

Additionally, we also provide the thermal conductivity as it is an essential quantity in the hydrodynamic equation. Cumulative quantities were also computed as a mean to obtain a deeper understanding of size effects in these configurations [40].

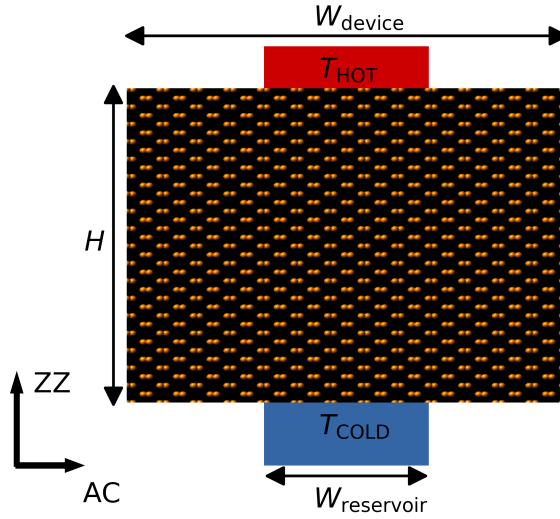


Figure 7.1.: Sketch of a Levitov configuration with characteristic lengths H , $W_{\text{reservoir}}$ and W_{device} indicated. The transport axis, armchair (AC) and zigzag (ZZ), for phosphorene case are given as reference.

7. Hydrodynamic signatures in devices based on 2D materials

Heat flux and temperature profiles for several Levitov configurations are obtained through the PBTE solution. Owing to the high complexity of the Levitov geometry, we use the efficient, energy-based deviational Monte Carlo approach (see Section 4.2) to solve the PBTE under the RTA and beyond (bRTA), implemented in BTE-Barna [293] (see Chapter 6) to solve the PBTE.

Atomic positions, harmonic and anharmonic interatomic force constants (IFCs), needed to compute the basic phonon properties (i.e.: group velocities, lifetimes, frequencies) and the propagator [178, 293] required for the PBTE Monte Carlo solvers, were computed as indicated in the previous Chapter, for both phosphorene (see Subsection 6.5) and graphene (see Section 6.6.2).

Finally, to efficiently investigate some dimensional limits and other features as the existence of vortices with magnitudes well below statistical noise caused by the intrinsic scattering algorithms [171, 293], we solved Eq. (7.1) using the finite elements package FEniCS [294, 295], with its parameters extracted from cumulative curves. To detail, the used mesh for such calculations was a rectangular one, with a spacing of 1 nm for the phosphorene simulations and 3 nm for the graphene one. Regarding the boundary conditions, a non-slip condition was chosen owing to its simplicity although we notice from previous MC results that there is a non-negligible flux in the boundaries [293].

7.3. Bulk properties and size effects

In their work, Shang *et al.* [289] proposed two different mechanisms as the origin of thermal vortices. For small systems, in the ballistic regime, the source would be the combination of elastic boundary scattering plus the phase of phonons but not hydrodynamics per se. On the other hand, for larger devices, they concluded that vorticity is due to \mathcal{N} -scattering dominance together with boundary conditions (finite sources injecting the heat into the system).

7. Hydrodynamic signatures in devices based on 2D materials

To get an idea of the interplay between the device dimensions and its transport regime, we have calculated the bulk non-local length and mean free path for graphene and phosphorene at room temperature (see Table 7.1). Additionally, we also provide the thermal conductivity because of its importance for heat hydrodynamics, with very good agreement with other theoretical calculations and experimental values. Although the non-local lengths and mean free paths offer a general idea of transport regime limits, they fail to provide insight on how system boundaries partially suppress the macroscopic thermal properties (i.e. κ and ℓ), as longer-mean-free-path phonons do not fully contribute to these macroscopic variables [39]. The last is especially important as it modifies ℓ , which is one of the quantities determining the transport regime. While it would be possible to obtain the effective macroscopic quantities for given geometries via averaging [40], the overall complexity of the Levitov configuration makes such a task unfeasible. On the other hand, even though, as noted by Li *et al.* [40], mean free path cumulative functions do not hold accurate predictive power, they are a useful tool to interpret size effects on transport variables. To that end, we provide the cumulative thermal conductivity and non-local length as a function of phonon mean free path (see Figs. 7.2 and 7.3).

It should be noted that the theoretical formulas used to obtain the $\ell_{\text{iso}}^{\text{RTA}}$ values are derived under the assumption of isotropy and are therefore expected to be useful only as approximations in the phosphorene case. Regarding ℓ values beyond the RTA, we expect them to be higher overall as in the RTA all processes are incorrectly deemed as directly resistive [143, 293]. Notwithstanding this, in the case of graphene the dominance over $\ell_{\text{iso}}^{\text{RTA}}$ of low-frequency ZA-modes in the neighborhood of Γ with extremely large mean free paths (of the order of 4 mm)—to the point that when suppressed the $\ell_{\text{iso}}^{\text{RTA}}$ gets reduced from 53.9 μm to 43.5 nm—makes the qualitative prediction of the beyond-RTA- ℓ behavior much more complicated, as the proper description of scattering operator would highly

7. Hydrodynamic signatures in devices based on 2D materials

Table 7.1.: Calculated κ , ℓ and λ for bulk graphene and bulk phosphorene at 300 K. The experimental values of κ and values of other theoretical calculations are also provided.

	κ^{RTA} $\left(\frac{\text{W}}{\text{m}\cdot\text{K}}\right)$	$\kappa^{\text{beyond RTA}}$ $\left(\frac{\text{W}}{\text{m}\cdot\text{K}}\right)$	κ^{ref} $\left(\frac{\text{W}}{\text{m}\cdot\text{K}}\right)$	$\ell_{\text{iso}}^{\text{RTA}}$ (nm)	λ (nm)
Graphene	1.17×10^3	4.20×10^3	$(4.84\text{-}5.30) \times 10^3$ ^a $(3.08\text{-}5.15) \times 10^3$ ^b	5.39×10^4 (43.5 [†])	169
Phosphorene (AC)	20.8	27.5	23.9 ^c 35.5 ^d 22.0 ^e	27.7	20.2
Phosphorene (ZZ)	57.8	82.9	82.1 ^c 108 ^d 63.2 ^e	42.3	33.5

[†] this value corresponds to the $\ell_{\text{iso}}^{\text{RTA}}$ calculation without including low frequency ZA modes in the neighborhood of Γ with λ around 4.2 nm.

^a Experimental κ obtained from Ref. [296].

^b Experimental κ obtained from Ref. [297].

^c First-principles calculated κ obtained from Ref. [272]. κ is rescaled to take into account differences in assumed thickness.

^d First-principles calculated κ obtained from Ref. [273]. κ is rescaled to take into account differences in assumed thickness.

^e First-principles calculated κ obtained from Ref. [269].

affect those ZA-modes. This is not surprising, as the RTA is known to fail in predicting graphene's thermal properties [139]. For instance, in our case the RTA predicts the κ to be only 27% of the fully converged value.

Regarding device dimensions, in the phosphorene case we expect hydrodynamic features to be observable out of the (quasi)ballistic regime, as the mean

7. Hydrodynamic signatures in devices based on 2D materials

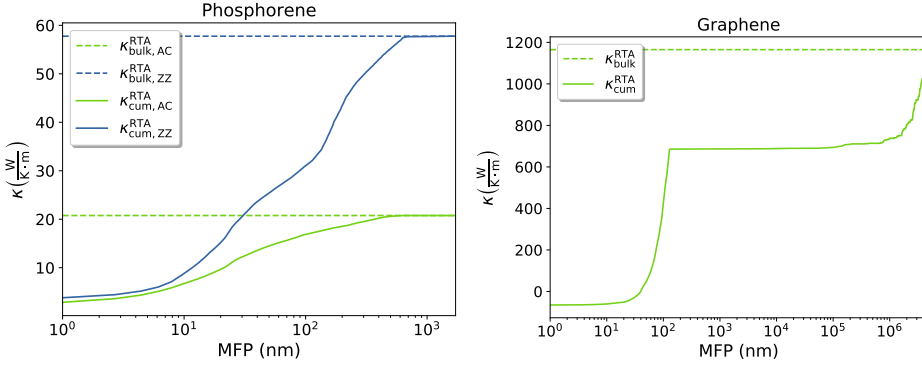


Figure 7.2.: Cumulative κ^{RTA} for phosphorene (left) and graphene (right) with respect to mean free path at 300 K. Bulk values are provided as reference. These values have been computed in a denser \mathbf{q} -mesh, namely $300 \times 300 \times 1$ ($480 \times 480 \times 1$) for phosphorene (graphene), through a cubic spline interpolation from the finer mesh to remove nonphysical artifacts.

free path is a bit longer than the non-local length, the true value of which is expected to be larger than the one in Table 7.1 [293]. The latter suggests that phosphorene is a highly hydrodynamic material at the nanoscale, as the phonon distribution is capable of keeping its inertia even under the effect of significant intrinsic scattering. The case of graphene is somewhat more complex, as the major contribution to thermal variables, especially the non-local length, comes from the low-frequency ZA modes in the neighborhood of Γ with extremely large mean free paths. At the nanoscale, the contribution of these modes to thermal conductivity or non-local length becomes negligible because a large suppression factor due to boundary scattering—see Eq. (14) in Ref. [46]—, thus lowering the non-local length to 43.5 nm. Hence for graphene nanodevices, since that non-local length is smaller than λ , one would only expect hydrodynamics within the (quasi)ballistic regime.

7. Hydrodynamic signatures in devices based on 2D materials

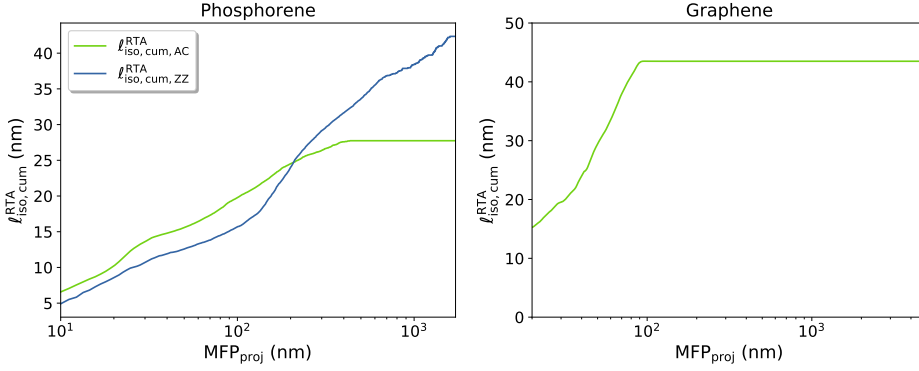


Figure 7.3.: Cumulative $\ell_{\text{iso}}^{\text{RTA}}$ for phosphorene (left) and graphene (right) with respect to projected mean free path at 300 K. The graphene cumulative function has been restricted to small λ as almost all the contribution to bulk values comes from modes with λ around 4.2 nm. These values have been computed in a denser \mathbf{q} -mesh, namely $300 \times 300 \times 1$ ($480 \times 480 \times 1$) for phosphorene (graphene), through a cubic spline interpolation from the finer mesh to remove nonphysical artifacts.

7.4. Results

Before presenting the results of our simulations, we find it worth commenting on the hydrodynamic signatures we have analyzed. Although the hydrodynamic regime presents several characteristic features, based on previous results [287, 289, 290] we have focused our study on flux vortices and negative thermal resistance regions, namely regions in which the flux propagates in the same direction as the thermal gradient. None of those features can be easily described using Fourier's law unless one relies on complex models allowing for a position-dependent non-diagonal and non-definite-positive κ -tensor. However, these features arise naturally in hydrodynamics (see Eq. 7.1) without using those complex and sometimes unphysical models, just unique and diagonal κ and ℓ tensors.

7. Hydrodynamic signatures in devices based on 2D materials

Furthermore, we also find it worth providing a summary of the characteristics of all the devices presented in this Section with an indication of the transport regime they are expected to be found on (see Fig. 7.4 and Table 7.2). In the next Subsections, we discuss the transition from ballistic to non-ballistic regimes together with hydrodynamic to diffusive or Fourier regimes and their crossovers. Additionally, we provide insight on the effect of the source sizes with respect to device width. Finally, we use the graphene wider devices to obtain information regarding the formation of the hydrodynamic features.

7.4.1. Quasiballistic devices

Here, we provide the thermal profile ¹ and heat flux for phosphorene and graphene-based Levitov configurations well inside quasiballistic regime (see Figs. 7.5 and 7.6), i.e. $H < \lambda$, for within and beyond the RTA.

All temperature profiles show a small linear variation of temperature between the reservoirs (i.e. $x = 0$), with abrupt changes near the reservoirs. Such a feature confirms that our devices are in the quasiballistic regime [170]. This statement is further supported by heat flux profiles, in which the small differences in fluxes between the bRTA and RTA indicate the dominance of boundary scattering (as this mechanism is not dependent on the approach used to describe intrinsic scattering) thus devices are in the quasiballistic regime [139, 140].

Regarding the hydrodynamic signatures, we can observe two flux vortices for all devices. Moreover, by combining flux and thermal profiles, we observe zones of negative thermal resistance at both sides of the reservoirs (see hot (cold) regions at both sides of cold (hot) reservoirs with the heat flux going downwards in

¹In this and all the subsequent plots the color scale of the temperature profiles is slightly non-linear in the vicinity of 300 K to highlight the negative resistivity zones

7. Hydrodynamic signatures in devices based on 2D materials

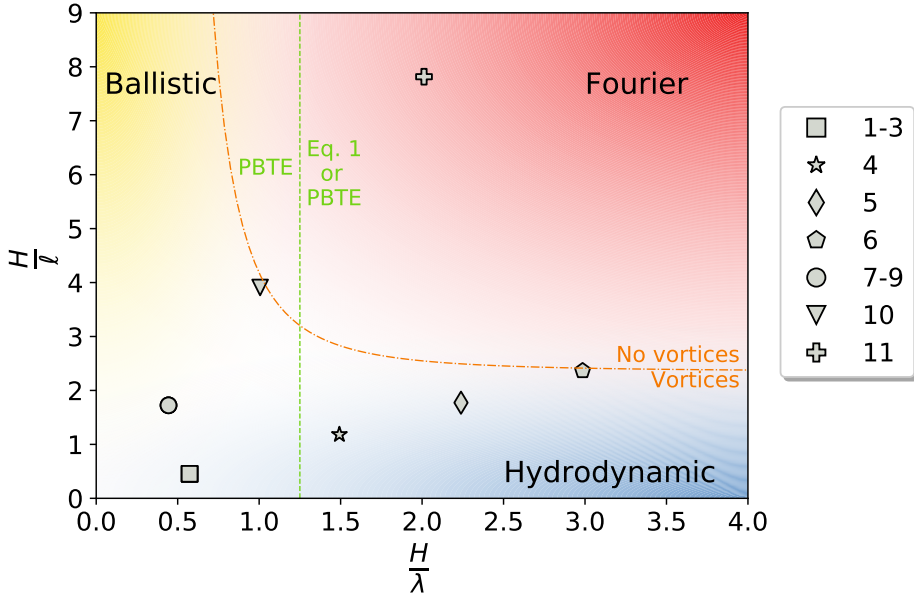


Figure 7.4.: Ballistic and hydrodynamic regime scores at 300 K for all the different Levitin structures studied in this work (see Table 7.2 for the id. reference). The transport regime for the given scores is indicated with the background color—i.e. Fourier (red), hydrodynamic (blue) or ballistic (yellow)—with gradient zones representing a transition between the different regimes. The green dashed line gives an idea of the crossover between ballistic and regimes for which Eq. 7.1 can provide a more quantitative prediction; namely regions without strong ballistic features which are describable through the PTBE but also the hydrodynamic equation. The orange dashed line provides an approximate idea of for which scores we expect vortices to be possible for acceptable values of pipe-flow score (i.e. < 0.5).

Figs. 7.5 and 7.6). Thus, all our (quasi)ballistic devices are in the hydrodynamic regime, even in the absence of \mathcal{N} processes, in opposition to more classical hydrodynamic theories.

Finally, the observable differences between graphene and phosphorene, especially for heat fluxes, which are as expected of higher values in graphene, are easily understood by noting the higher group velocities and lower scattering rates

7. Hydrodynamic signatures in devices based on 2D materials

Table 7.2.: Configuration id., material (P: phosphorene and G: graphene), characteristic sizes and figure references to all the different Levitov structures studied in this work. To illustrate the expected regimes of each device we provide ballistic ($\frac{H}{\lambda}$) and hydrodynamic ($\frac{H}{\ell}$) regime scores at 300 K, with lower values representing to be well inside the respective regime. Boldface in ballistic and hydrodynamic scores indicates that, within the RTA, such device is well inside in that respective transport regime. Additionally, we provide a pipe-flow score ($\frac{W_{\text{reservoir}}}{W_{\text{device}}}$), meaning 0 point sources and 1 a pipe like structure, so that for higher values vorticity is not allowed as in this limit one recovers a Poiseuille-like flow.

Id. #	Material	$W_{\text{reservoir}}$ (nm)	W_{device} (nm)	H (nm)	$\frac{H}{\lambda}^{\dagger}$	$\frac{H}{\ell}^{\dagger}$	$\frac{W_{\text{reservoir}}}{W_{\text{device}}}$	Figs.
1	P	25.0	160	19.2	0.573	0.454	0.156	7.5,7.8(a)
2	P	25.0	320	19.2	0.573	0.454	0.078	7.8(b)
3	P	25.0	46.0	19.2	0.573	0.454	0.543	7.11
4	P	25.0	160	50.0	1.492	1.182	0.156	7.14,7.17(a)
5	P	25.0	160	75.0	2.239	1.773	0.156	7.15,7.17(b)
6	P	25.0	160	100	2.985	2.364	0.156	7.16,7.17(c)
7	G	37.5	375	75.0	0.444	1.724	0.100	7.6,7.12
8	G	37.5	750	75.0	0.444	1.724	0.050	7.10
9	G	37.5	3750	75.0	0.444	1.724	0.010	7.13
10	G	37.5	375	170	1.006	3.908	0.100	7.18
11	G	37.5	375	340	2.012	7.816	0.100	7.19

[†] For phosphorene devices the scores are calculated using the ZZ values of ℓ and λ , as it is the leading direction of thermal transport.

of graphene when compared to the phosphorene ones. Moreover, the asymmetric vortices found in phosphorene have their root in the material anisotropy.

On top of that, and taking into account the role of boundary scattering on vortex formation pointed out by Shang *et al.* [289], we also provide the PBTE solution

7. Hydrodynamic signatures in devices based on 2D materials

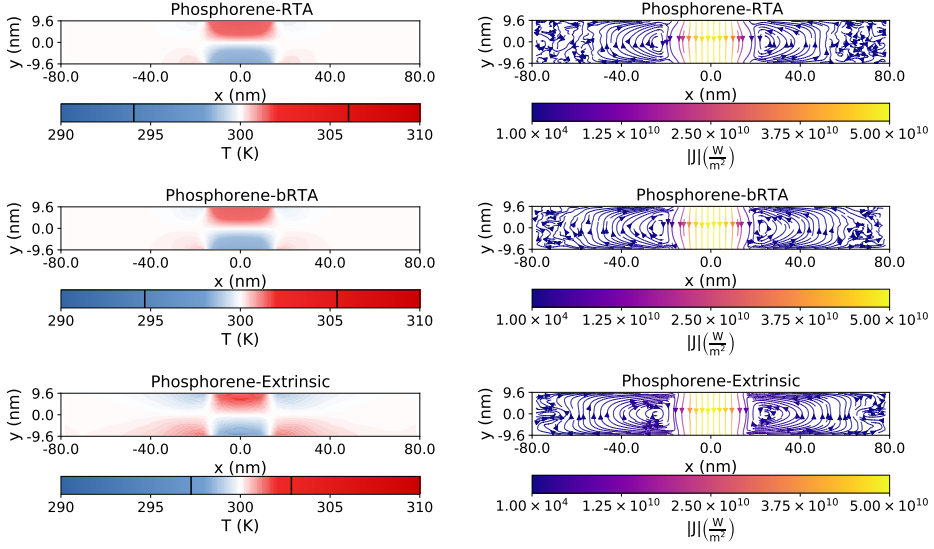


Figure 7.5.: The RTA (top), bRTA (middle) and extrinsic (bottom) steady-state thermal profiles (left) and heat fluxes (right) for a ballistic phosphorene-based Levitov configuration with $W_{\text{reservoir}} = 25$ nm, $W_{\text{device}} = 160$ nm and $H = 19.2$ nm, $T_{\text{HOT}} = 310$ K and $T_{\text{COLD}} = 290$ K. The black bars at the color-bars of temperature profiles indicate the highest and the lowest temperature found in device.

without intrinsic scattering (i.e. three-phonon and isotopic scattering), henceforth referred to as extrinsic (see the bottom panels of Figs. 7.5 and 7.6). From those results, it is clear that the boundary scattering is the only mechanism leading to vortex formation, as the other proposed contributing factor, the phase of phonons, is disregarded by the PBTE [298]. This last statement agrees with Zhang *et al.*'s observations [290]: if allowed by boundary scattering, i.e. system geometry, vortices will form, being protected from destruction by the absence or scarcity of intrinsic resistive scattering processes. Furthermore, phosphorene extrinsic results show a curious feature, two secondary vortices, which are found neither in the RTA nor in bRTA results. We need to stress that the flux magnitude of such secondary vortices is well below— $\sim 10^4$ times smaller than the maximum,

7. Hydrodynamic signatures in devices based on 2D materials

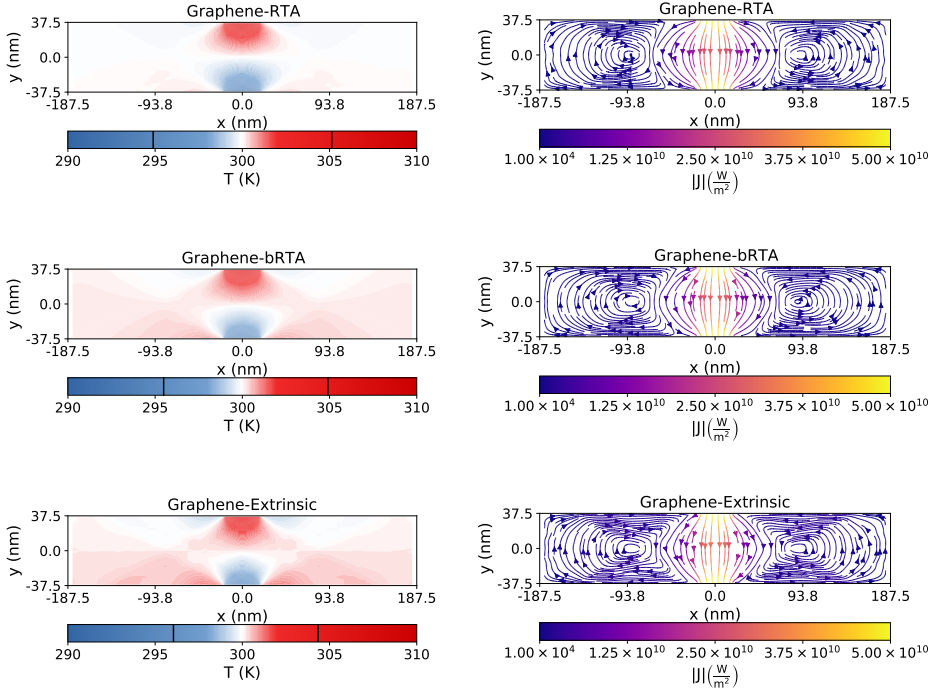


Figure 7.6.: The RTA (top), bRTA (middle) and extrinsic (bottom) steady-state thermal profiles (left) and heat fluxes (right) for a ballistic graphene-based Levitov configuration with $W_{\text{reservoir}} = 37.5$ nm, $W_{\text{device}} = 375$ nm and $H = 75$ nm, $T_{\text{HOT}} = 310$ K and $T_{\text{COLD}} = 290$ K. The black bars at the colorbars of temperature profiles indicate the highest and the lowest temperature found in device.

see Fig. 7.7—the error introduced by the scattering algorithms [171], so the observed flux in that area for the RTA and bRTA is nothing but noise-masked flux. To check for the existence of those secondary vortices, we resorted to the hydrodynamic equation using the cumulative quantities for the given device dimension as equation parameters; the result is given in Fig. 7.8(a).

Although there exist differences between this solution of the hydrodynamic equation and the MC simulations, those can be attributed to the facts that cu-

7. Hydrodynamic signatures in devices based on 2D materials

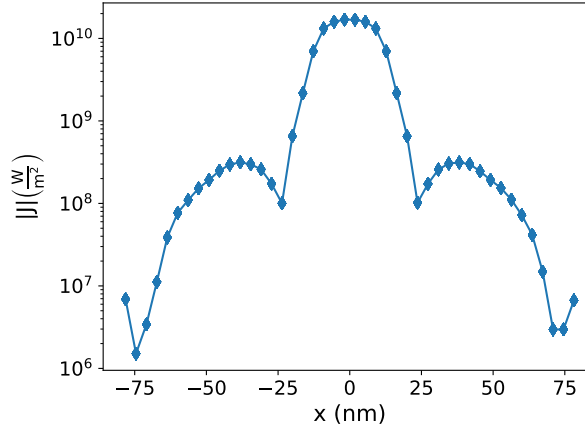


Figure 7.7.: Cut of heat flux magnitude at extrinsic case of Fig. 7.5 for $y=0$ nm as function of x .

mulative variables only capture the qualitative effects of size and that Eq. 7.1 does not capture ballistic effects present in the device. Moreover, we recall that the calculation of the ℓ values used here was conducted under the assumption of isotropy. Notwithstanding all these differences, this result together with extrinsic simulation strongly suggests the presence of additional vortices hidden by noise in Fig. 7.5.

We also provide evidence of the existence of ternary and higher order vortices by solving the hydrodynamic equation for a wider phosphorene device (see Fig. 7.8(b)). Interestingly, we observe from those results that each vortex is approximately 100 times smaller in magnitude than the previous one (see Fig. 7.9) in line with MC simulation (Fig. 7.7). We note that the noise at both lateral edges of the larger phosphorene device is due to the finite numerical precision in the simulations. Additionally, we complement those results with the hydrodynamic equation solutions for a larger graphene device (see Fig. 7.10), showing that the train of vortices is a general solution, and not a particular solution of phosphorene due to its properties. Indeed, the observation of a vortex train in wider devices

7. Hydrodynamic signatures in devices based on 2D materials

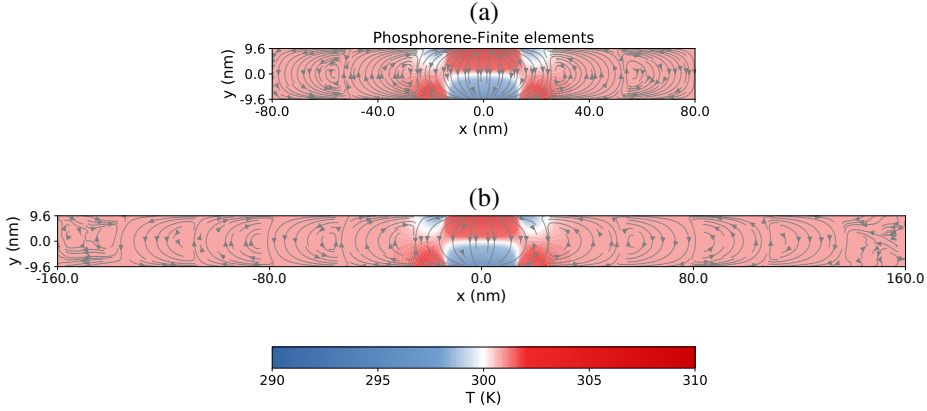


Figure 7.8.: The finite elements solution of the hydrodynamic equation for two phosphorene-based Levitov configurations with $W_{\text{reservoir}} = 25$ nm, $W_{\text{device}} = 160$ nm (a) / 320 nm (b) and $H = 19.2$ nm, $T_{\text{HOT}} = 310$ K, $T_{\text{COLD}} = 290$ K, $\kappa_{AC} = 10.47$ W m⁻¹ K⁻¹ (a) / 11.72 W m⁻¹ K⁻¹ (b), $\kappa_{ZZ} = 17.15$ W m⁻¹ K⁻¹ (a) / 21.58 W m⁻¹ K⁻¹ (b), $\ell_{AC} = 10.81$ nm (a) / 13.30 nm (b), and $\ell_{ZZ} = 9.04$ nm (a) / 11.60 nm (b). The temperature profile is given in a blue-red colormap together with the heat flux isolines (gray).

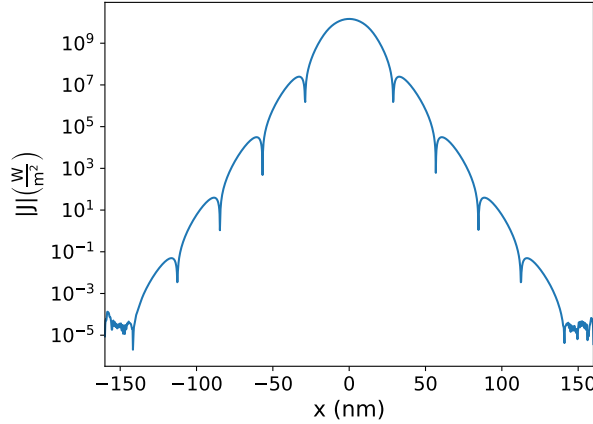


Figure 7.9.: Cut of heat flux magnitude at Fig. 7.8(b) for $y = 0$ nm as function of x .

7. Hydrodynamic signatures in devices based on 2D materials

($W_{\text{device}} \gg \lambda, W_{\text{reservoir}}$) provides further information about the mechanism behind vorticity, suggesting that boundary scattering over lateral walls plays a secondary role in vortex generation at most.

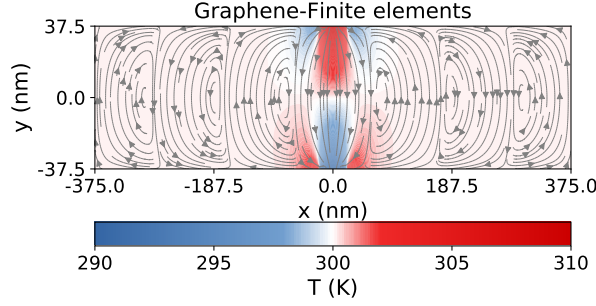


Figure 7.10.: The finite elements solution of the hydrodynamic equation for a graphene-based Levitov configuration with $W_{\text{reservoir}} = 37.5$ nm, $W_{\text{device}} = 750$ nm and $H = 75$ nm, $T_{\text{HOT}} = 310$ K, $T_{\text{COLD}} = 290$ K, $\kappa = 374.08$ W m⁻¹ K⁻¹, and $\ell = 34.73$ nm. The temperature profile is given in a blue-red colormap together with the heat flux isolines (gray).

In addition to providing information about the mechanism behind the vortex formation, the similarity between the RTA and bRTA fluxes suggests that because of boundary scattering dominance in the (quasi)ballistic regime, a proper description of the intrinsic scattering operator might be unnecessary to obtain a correct qualitative behavior of the flux. This contrasts with the findings in Ref. [293], in which different values of non-local length, the defining parameter of vorticity, for the RTA and bRTA were found in nanoribbons of sizes similar to those found in our devices. In view of such discrepancies, we investigated the existence of limiting cases, namely those cases in which a small difference in ℓ might lead to different vorticity. In Fig. 7.11 we can see an example of such a limiting case for phosphorene, confirming the importance of a proper treatment of scattering even in the quasiballistic regime for a proper description of vortices. There, it can be observed that while in the RTA there are four different vortices, in the bRTA case

7. Hydrodynamic signatures in devices based on 2D materials

there are still two different vortices. Moreover, those results also show vortex damping due to the lateral wall, demonstrating that a minimum distance between lateral walls and the reservoir ends is necessary for vortices to form [290]. This is not surprising, as in the limit of thermal reservoirs occupying all top and bottom edges one must recover a Poiseuille flow.

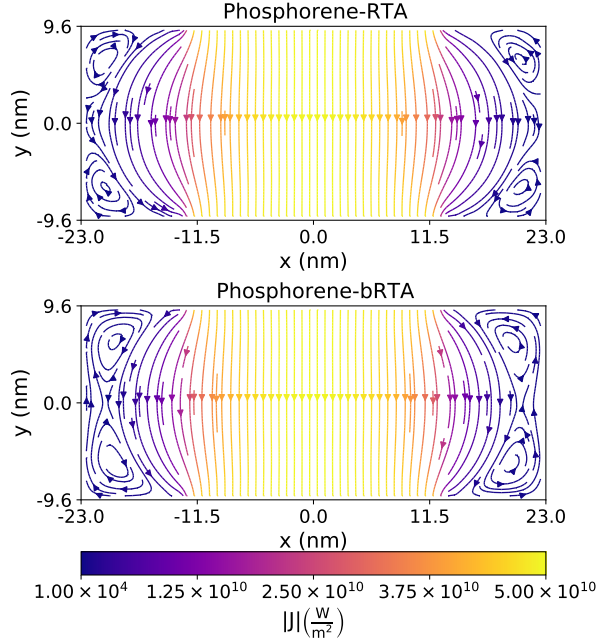


Figure 7.11.: The RTA (top) and bRTA (bottom) steady-state heat fluxes for a limiting case phosphorene-based Levitov configuration with $W_{\text{reservoir}} = 25$ nm, $W_{\text{device}} = 46$ nm and $H = 19.2$ nm, $T_{\text{HOT}} = 310$ K and $T_{\text{COLD}} = 290$ K.

7. Hydrodynamic signatures in devices based on 2D materials

7.4.1.1. Vortex formation

To obtain a better understanding about how boundary scattering creates vortices, we look into how they are formed. For that purpose, we provide temporal snapshots showing the vortex formation within the bRTA framework, starting from a graphene-based Levitov configuration with $W_{\text{reservoir}} = 37.5$ nm, $W_{\text{device}} = 375$ nm and $H = 75$ nm, $T_{\text{HOT}} = 310$ K and $T_{\text{COLD}} = 290$ K, initially at 300 K in Fig. 7.12.

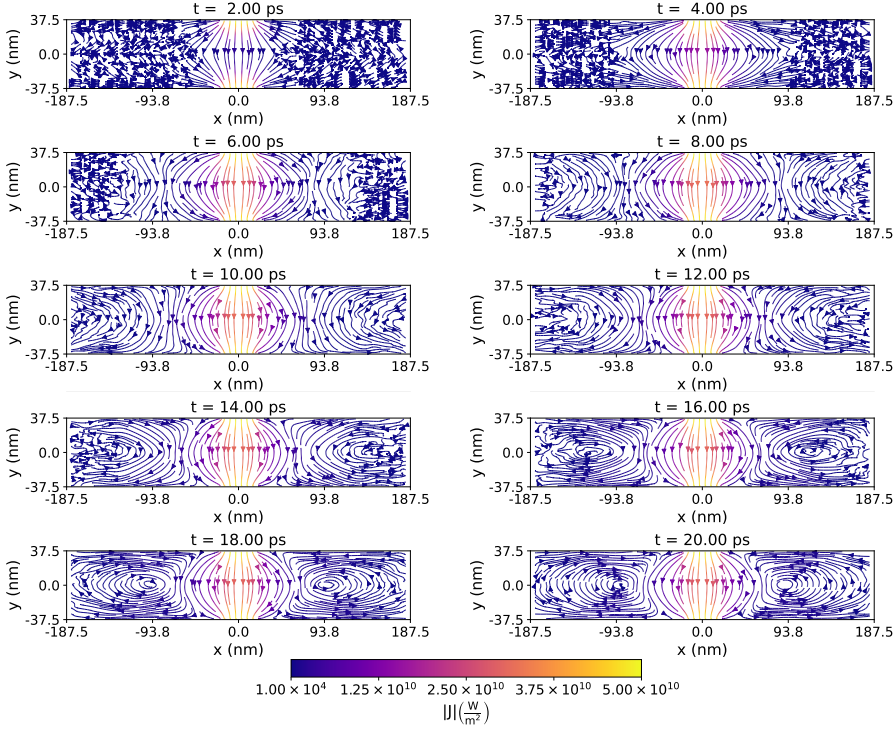


Figure 7.12.: The bRTA heat flux at different times for a graphene-based Levitov configuration with $W_{\text{reservoir}} = 37.5$ nm, $W_{\text{device}} = 375$ nm and $H = 75$ nm, $T_{\text{HOT}} = 310$ K and $T_{\text{COLD}} = 290$ K, initially at 300 K.

These results show that the formation of vortices begins at the sources, and

7. Hydrodynamic signatures in devices based on 2D materials

how they advance with time towards the lateral edges until their closure. In further detail, the phonons arrive at the opposite vertical wall and slide laterally along it until they are stopped by boundary scattering, or collide with the lateral walls, closing the vortex in both cases. In the former, we recall that walls act as phonon sources due to diffusive scattering, and thus they reemit a small part of those incident phonons, which again slide laterally along the edges until they are stopped by edge friction or the collision with the lateral wall forming in that way additional vortices.

Thus, such behavior supports the importance of top and bottom boundary scattering, as for larger devices vortices can start forming before a significant number of phonons can scatter at lateral borders. This latter statement is further confirmed by larger device simulations in which no phonon arrived at a lateral wall but the vortices are formed (see Fig. 7.13).

7.4.2. Non-ballistic devices

Here we provide results for less ballistic devices than those of the previous section, i.e. $H \gtrsim \lambda$. As aforementioned, owing to the differences in the mean free path and non-local length between graphene and phosphorene, we expect both to show rather distinct vorticity.

7.4.2.1. Phosphorene

Devices out of the ballistic regime are in principle much more interesting in the case of phosphorene, as the non-local length is slightly larger than the mean free path, therefore allowing for hydrodynamic features outside the ballistic regime. Moreover, based on the fit of ℓ to Monte Carlo results found in Ref. [293], we expect its value to be larger than the calculated one, thus allowing for vortices

7. Hydrodynamic signatures in devices based on 2D materials

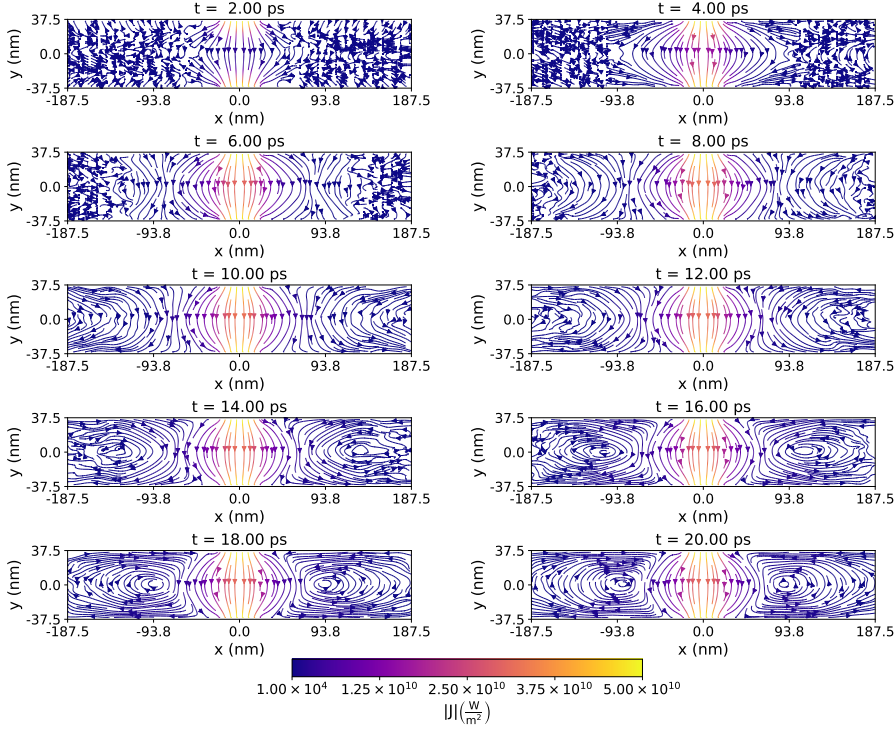


Figure 7.13.: The BRTA heat flux at different times for a large graphene-based Levitov configuration with $W_{\text{reservoir}} = 37.5 \text{ nm}$, $W_{\text{device}} = 3.75 \mu\text{m}$ and $H = 75 \text{ nm}$, $T_{\text{HOT}} = 310 \text{ K}$ and $T_{\text{COLD}} = 290 \text{ K}$, initially at 300 K . Only the central part of the device is depicted as most of the device is empty of phonons.

and negative thermal resistances in devices with H larger than what would be expected from the results in Table 7.1.

Because of this, we have simulated three different heights: 50, 75, and 100 nm, the RTA and bRTA steady-state heat fluxes of which are shown in Figs. 7.14-7.16. These results are to be compared to the extrinsic-only solution for the same set of heights (see the extrinsic cases at the bottom of Figs 7.14-7.16) to highlight the effect of intrinsic scattering on the steady-state properties. Additionally, we

7. Hydrodynamic signatures in devices based on 2D materials

provide the bRTA thermal profiles for all heights in Figs. 7.17(a)-7.17(c). In smaller devices, we observe that device geometry allows for the formation of two vortices (see the extrinsic case at the bottom of Fig. 7.14), which are present even when intrinsic scattering is added. Interestingly, if we set aside the expected magnitude differences between all the treatments of the scattering operator, we can observe (Fig. 7.14) subtle differences in the vortex profiles. While within the extrinsic treatment we can see two clean vortices, the addition of intrinsic scattering through the RTA causes those vortices to start dissipating at the device's corners. However, the proper treatment of scattering leads to slightly different alterations, as such dissipation of vorticity is less pronounced, while the RTA incipient fracture of principal vortices into two becomes clearer in the bRTA case. Therefore, the full linearized scattering operator is necessary to obtain an appropriate description of vorticity.

The 75 and 100 nm results (see Figs. 7.15 and 7.16) further support this latter statement. In both cases vorticity is geometrically permitted (see the extrinsic cases at the bottom of Figs 7.15 and 7.16) but suppressed in the RTA case, which shows an almost perfect diffusive profile, especially for the 100 nm device. On the other hand, the correct description of the scattering operator allows the vortices to survive in both cases. This fact is nothing but a consequence of the RTA deeming all three-phonon processes as resistive, which translates into lower ℓ values. Indeed, we expect the flux direction to be qualitatively similar for devices much larger than ℓ , as they tend to have diffusive profiles—i.e. profiles compatible with Fourier's law—in which the only difference between the RTA and bRTA is the flux magnitude due to the thermal conductivity differences.

Regarding thermal resistance, we can observe a low-magnitude negative resistance, when compared to ballistic devices, for the 50 device (Figs. 7.14 and 7.17(a)), and even a lower one in the 75 nm one (Figs. 7.15 and 7.17(b)). For the larger device (i.e. 100 nm, Figs. 7.16 and 7.17(c)) no significant negative thermal

7. Hydrodynamic signatures in devices based on 2D materials

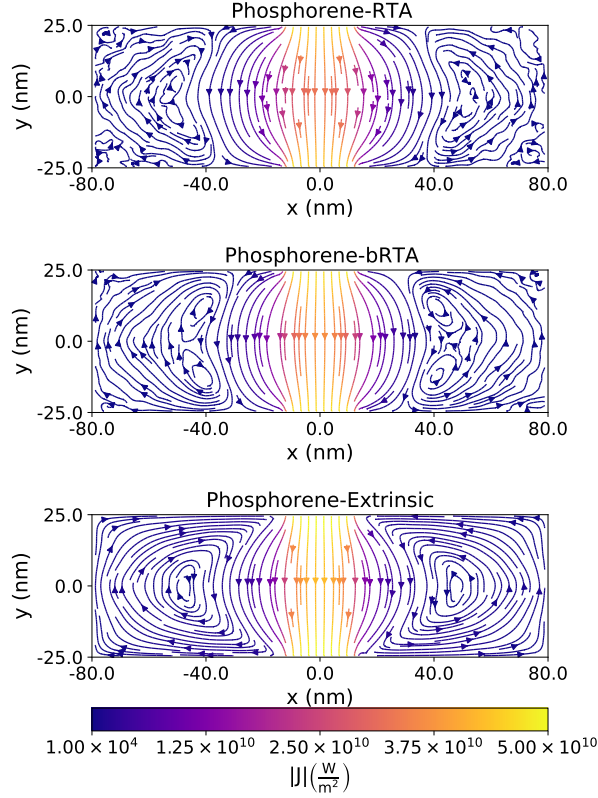


Figure 7.14.: The RTA (top), bRTA (middle) steady-state, and extrinsic (bottom) heat fluxes for phosphorene-based Levitov configuration with $W_{\text{reservoir}} = 25$ nm, $W_{\text{device}} = 160$ nm and $H = 50$ nm, $T_{\text{HOT}} = 310$ K and $T_{\text{COLD}} = 290$ K.

resistance is observed, indicating (in line with the flux results) a weakening of hydrodynamic regime with increasing H . This is a consequence of the phonon distribution losing its inertia—i.e. preventing the effect of boundary scattering—while traveling due to intrinsic resistive scattering, up until the point that for larger distances (H) it is completely lost before arriving to the opposite side, and thus one arrives at the Fourier’s diffusive regime.

7. Hydrodynamic signatures in devices based on 2D materials

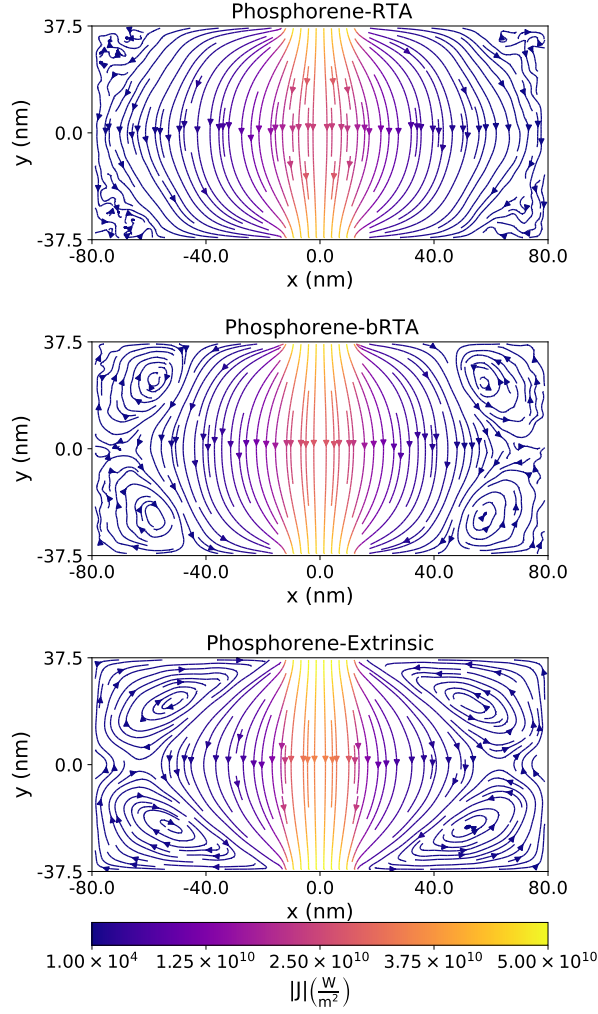


Figure 7.15.: The RTA (top), bRTA (middle) steady-state, and extrinsic (bottom) heat fluxes for phosphorene-based Levitov configuration with $W_{\text{reservoir}} = 25 \text{ nm}$, $W_{\text{device}} = 160 \text{ nm}$ and $H = 75 \text{ nm}$, $T_{\text{HOT}} = 310 \text{ K}$ and $T_{\text{COLD}} = 290 \text{ K}$.

7. Hydrodynamic signatures in devices based on 2D materials

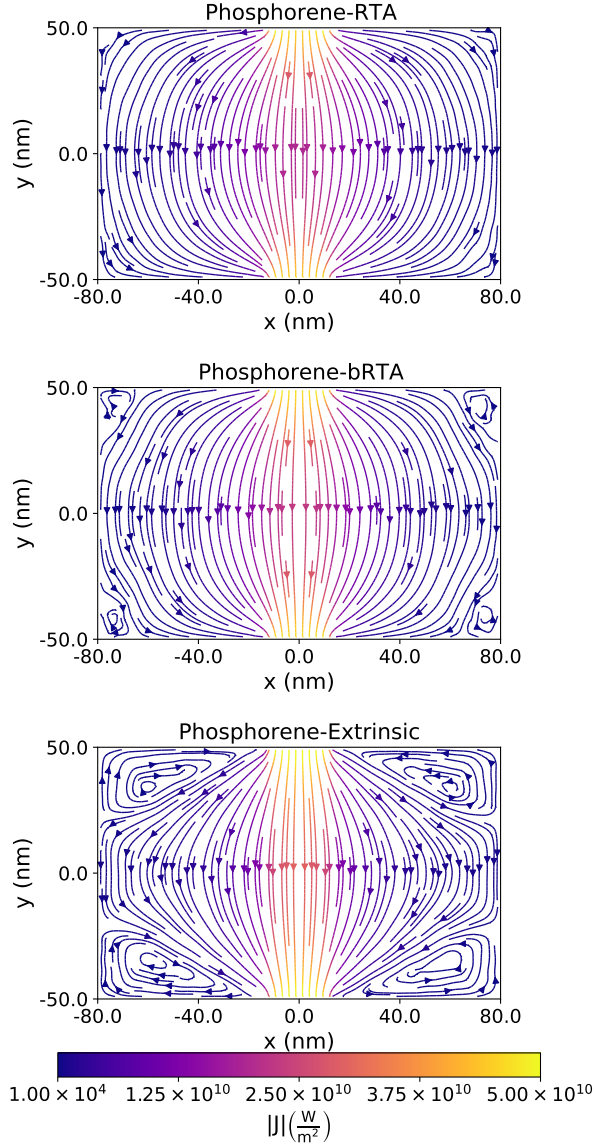


Figure 7.16.: The RTA (top), bRTA (middle) steady-state, and extrinsic (bottom) heat fluxes for phosphorene-based Levitov configuration with $W_{\text{reservoir}} = 25$ nm, $W_{\text{device}} = 160$ nm and $H = 100$ nm, $T_{\text{HOT}} = 310$ K and $T_{\text{COLD}} = 290$ K.

7. Hydrodynamic signatures in devices based on 2D materials

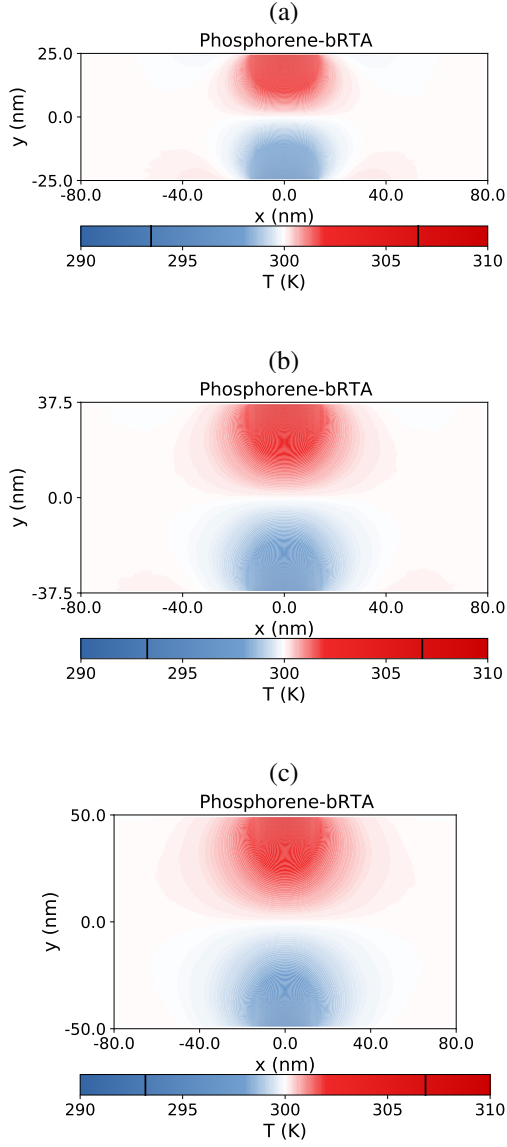


Figure 7.17.: The bRTA steady-state temperature profile for several phosphorene-based Levitov configurations with $W_{\text{reservoir}} = 25$ nm, $W_{\text{device}} = 160$ nm and $H = 50$ nm (a) / 75 nm (b) / 100 nm (c), $T_{\text{HOT}} = 310$ K and $T_{\text{COLD}} = 290$ K. The black bars at the colorbars of temperature profiles, indicate the highest and the lowest temperature found in device.

7.4.2.2. Graphene

The graphene RTA and bRTA steady-state heat fluxes are depicted in Fig. 7.18, showing a clear diffusive (Fourier-like) profile in the RTA case. In contrast, some vorticity can be observed in the bRTA results, indicating a clear underestimation of non-local length—i.e. the ability of the distribution to keep its inertia—because of the RTA limitations. Therefore, it is indeed possible to have some small vorticity out of the ballistic regime. When incrementing the height, we observe that vortices cannot form even without intrinsic scattering (see the extrinsic case at the bottom of Fig. 7.19) although some non-local effects appear in the flux, namely the curvature of the isolines near the corners of the extrinsic case in Fig. 7.19. However, such hydrodynamic effects are not present neither in the RTA nor bRTA (see the top and middle panels of Fig. 7.19) due to the intrinsic scattering effect (i.e. $\ell \ll H$), showing both a Fourier-like profile.

7. Hydrodynamic signatures in devices based on 2D materials

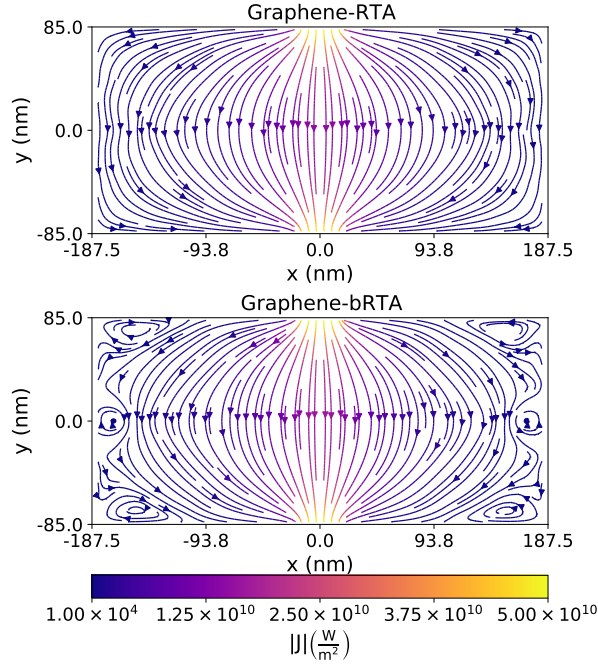


Figure 7.18.: The RTA (top) and bRTA (bottom) steady-state heat fluxes for graphene-based Levitov configuration with $W_{\text{reservoir}} = 37.5 \text{ nm}$, $W_{\text{device}} = 375 \text{ nm}$ and $H = 170 \text{ nm}$, $T_{\text{HOT}} = 310 \text{ K}$ and $T_{\text{COLD}} = 290 \text{ K}$.

7. Hydrodynamic signatures in devices based on 2D materials

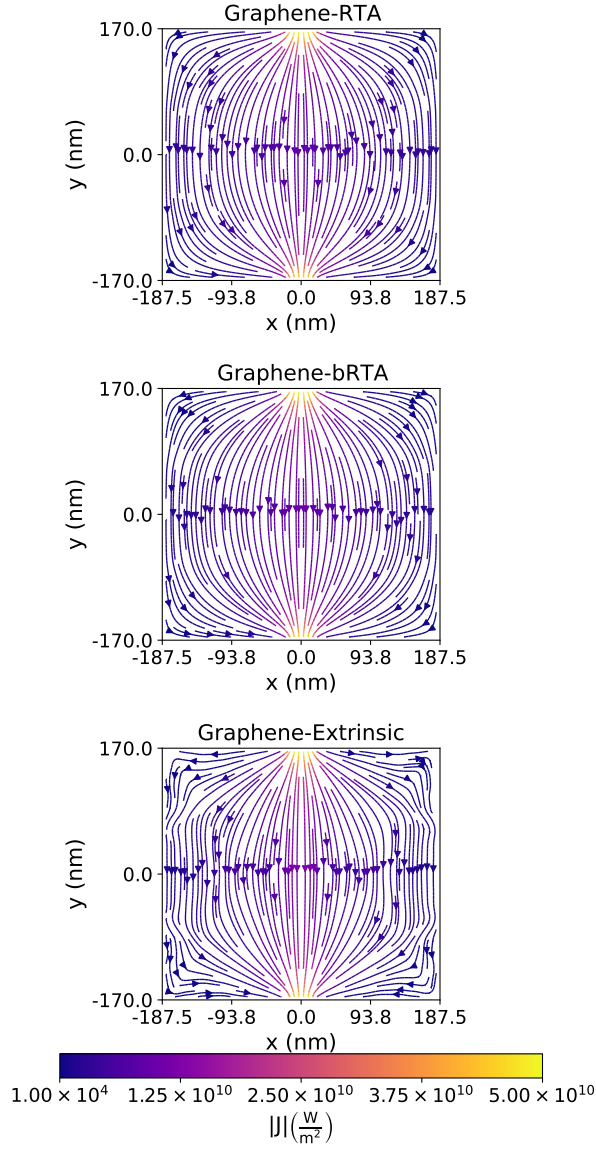


Figure 7.19.: The RTA (top), bRTA (middle) and extrinsic (bottom) steady-state heat fluxes for graphene-based Levitov configuration with $W_{\text{reservoir}} = 37.5$ nm, $W_{\text{device}} = 375$ nm and $H = 340$ nm, $T_{\text{HOT}} = 310$ K and $T_{\text{COLD}} = 290$ K.

7.5. Summary and conclusions

In this Chapter, we have presented Monte Carlo simulations of phonon transport with a full linearized *ab initio* scattering operator, leading to the manifestation of hydrodynamic signatures such as vorticity and non-monotonic temperature profiles in planar graphene and phosphorene device geometries. We find such signatures at room temperature in quasiballistic and non-ballistic regimes, in contradiction with the predictions of classical hydrodynamic models, which required a predominance of normal scattering, but in agreement with more recent and generalized models which find the signatures even when all scattering is resistive. In contrast to previous observations, we demonstrate that there is a shared mechanism among all transport regimes originating the hydrodynamic signatures, namely boundary scattering. Indeed, we show that in our devices, undergoing vertical transport, boundary scattering at horizontal edges is the leading mechanism behind vortex formation, proving through the solution of the hydrodynamic equation that an increment in the horizontal dimension only leads to the formation of more convection cells instead of vortex (hydrodynamics) destruction. We have illustrated the critical importance of the device dimensions, especially the distance between sources and the opposite horizontal walls (i.e. the ones causing the vortices), in determining the presence or absence of hydrodynamic effects, opposite to previous considerations based only on the relative importance of normal vs. resistive scattering. Moreover, we have demonstrated that having a proper description of the intrinsic scattering using the full linearized scattering operator will, through more accurate values of ℓ , result in qualitative consequences, showing that the RTA can lead to an incorrect number of vortices or no vorticity at all in cases where it should be present.

Finally, based on our calculations, we point out that experimental observation of hydrodynamic signatures at room temperature would be favored by choosing a

7. Hydrodynamic signatures in devices based on 2D materials

small graphene sample under 100 nm in height, a finite source and sink as narrow as possible and a device width at least three times larger than the source/sink widths.

Conclusions

In this thesis, we have investigated using first principles the thermal properties of nanoscale-emerging crystal phases found in nanowires. Moreover, we present a new software package, BTE-Barna, containing iterative and Monte Carlo solvers of the Peierls-Boltzmann transport equation for two-dimensional-based devices, and a practical example of their application to study thermal hydrodynamic features from an *ab initio* perspective. The main contributions of this work are summarized in the following points:

- The lattice thermal conductivity for cubic and hexagonal phases of several semiconductors has been calculated using first principles. The differences in κ between both phases are explained. Indeed, for binary semiconductors, we found that classical conditions for a high κ are incapable of explaining such differences. Therefore, we focused our analysis on two quantities that directly contribute to the three-phonon scattering rate and contain all the classical conditions: the anharmonicity, which we find to be always higher in the cubic phase; and the accessible phase space, which is higher for the hexagonal one. Based on such observation we developed a methodology to predict which phase is the most conductive, where other more qualitative approaches fail.

Conclusions

- We have also presented the lattice thermal conductivity for several nanowires made of cubic and hexagonal phases for those semiconductors, showing the effect of boundary scattering on $\kappa_{\text{hex}}/\kappa_{\text{cub}}$. Moreover, we find that such systems might be of interest for complex phononic and thermoelectric applications/systems (e.g. telescopic nanowires) due to their ability to tune such a rate over a great range, especially in the case of AIs, by simply modifying their diameter.
- We have presented a new software package, BTE-Barna, extending the capabilities of almaBTE to tackle nanodevices based on 2D materials, as well as nanowires. Specifically, we have implemented an iterative steady-state solver to provide the effective conductivity of nanoribbons and nanowires. Moreover, we have implemented a highly efficient RTA Monte Carlo simulator for the computation of the steady-state properties based on the one included in almaBTE, so that it can now tackle finite and/or periodic 2D systems and their heterojunctions under the effect of thermal gradients and isothermal reservoirs, while providing information from the transient to steady-state. Finally, we have implemented a beyond-RTA Monte Carlo simulator for 2D systems to provide an accurate description for those cases in which the RTA fails.
- We have studied the thermal hydrodynamic signatures (i.e. heat flux vortices and negative thermal resistance regions) in graphene and phosphorene-based nanodevices at room temperature using BTE-Barna MC solvers. This last is a considerable improvement with respect to previous studies, in which the used methodology was based on fitted parameters or models instead of a full microscopic *ab-initio*-based description. Moreover, we have provided insight into the mechanisms originating those hydrodynamic features, relating this last point to the non-local lengths and mean free paths. Additionally, we have complemented our results with solutions of

Conclusions

the hydrodynamic equation using finite elements for a better understanding of some size effects as well as studying signatures below the MC statistical noise, for instance, demonstrating the existence of several convection cells.

The work here presented may be extended by:

- Extending the iterative solver to solve the coupled electron-phonon BTE focusing on the solution of the electron-phonon-BTE for highly symmetric systems with confinement, namely nanoribbons and nanowires, via suppression factors. This way the enhancement of thermoelectric properties due to confinement could be studied from a fully first-principles perspective.
- Including four-phonon processes into the BTE-Barna to improve the accuracy of the simulations in the high-temperature regime.
- Extending the MC formalism and solvers to couple electronic and phononic systems for non-degenerate semiconductors.

APPENDIX A

Description of the BTE–Barna executables, inputs, and outputs

A.1. kappa_Tsweep_nanos

The calculation of the effective thermal conductivity κ_{nano} for nanowires and nanoribbons at both the RTA and beyond RTA levels is implemented in the `kappa_Tsweep_nanos` executable. The executable parameters are the same as for `kappa_Tsweep` but with an additional parameter to control the number of TBB threads in which the recalculation and symmetrization will take place.

```
kappa_Tsweep_nanos input.xml Nthreads
```

Regarding input files, it uses the same format as `kappa_Tsweep` but with some additions:

```
<system name="nanoribbon" L="500.0"/>  
<AnharmonicIFC name="FORCE_CONSTANTS_3RD"  
scalebroad="1.0"/>
```

A. Description of the *BTE-Barna* executables, inputs, and outputs

1. `system/name` [string]: Indicates the type of nanosystem. Accepted values: `nanowires` and `nanoribbons`.
2. `system/L` [double,units(nm)]: limiting length of the system, radius for nanowires and width for nanoribbons.
3. `AnharmonicIFC/name` [string]: path to file containing third-order force constants. Only needed for beyond calculations.
4. `AnharmonicIFC/scalebroad` [double]: broadening parameter for adaptive smearing. Only needed for beyond-RTA calculations.

Finally `kappa_Tsweep_nanos` will produce a csv output file (`{h5filename}_{systemname}_L_{L}_{u}_{Tmin}_{Tmax}.Tsweep`) with the following format

$$\begin{array}{ccc}
 T[K], & \kappa_{\text{nano}}^{\text{RTA}} \left[\frac{W}{\text{m} \cdot \text{K}} \right], & \kappa_{\text{nano}}^{\text{beyond RTA}} \left[\frac{W}{\text{m} \cdot \text{K}} \right] \\
 T_0, & \kappa_{\text{nano}}^{\text{RTA}}(T_0), & \kappa_{\text{nano}}^{\text{beyondRTA}}(T_0) \\
 T_1, & \kappa_{\text{nano}}^{\text{RTA}}(T_1), & \kappa_{\text{nano}}^{\text{beyondRTA}}(T_1) \\
 \vdots, & \vdots, & \vdots \\
 T_n, & \kappa_{\text{nano}}^{\text{RTA}}(T_n), & \kappa_{\text{nano}}^{\text{beyondRTA}}(T_n)
 \end{array}$$

where u is the transport direction.

A.2. Monte Carlo simulators and analyzers: inputs, outputs and executables

A.2.1. Geometry files

As noted in Chapter 6, the implementation of the MC algorithms divides the real space into computational boxes defined by the user as convex hulls if points.

A. Description of the *BTE-Barna* executables, inputs, and outputs

This choice allows for the use of external routines taking care of the correct surface tessellation. Moreover, it allows for complex geometries as porous or wedge-like geometries. Files containing geometries are given in XML format. Here, we provide a toy example to show geometry file input format and describe its capabilities:

```
<Geometry>
  <number_of_boxes Ngeom="4"/>
  <Box>
    <MaterialID name="black_P"/>
    <boxid id="0"/>
    <Vertices dim="2" npoints="4">
      6.0 6.0
      6.0 7.0
      7.0 6.0
      7.0 7.0
    </Vertices>
    <initCnd Teq="300." Tinit="301.0"/>
  </Box>
  <Box>
    <MaterialID name="black_P"/>
    <boxid id="1"/>
    <Vertices dim="2" npoints="4">
      6.0 6.0
      6.0 7.0
      5.0 6.0
      5.0 7.0
    </Vertices>
    <initCnd Teq="300."/>
    <Translate_to id="2">
      1.0 0.0 0.0
    </Translate_to>
  </Box>
  <Box>
    <MaterialID name="black_P"/>
    <boxid id="2"/>
    <Vertices dim="2" npoints="4">
      8.0 6.0
      8.0 7.0
```

A. Description of the *BTE-Barna* executables, inputs, and outputs

```

        7.0 6.0
        7.0 7.0
    </Vertices>
    <initCnd Teq="300."/>
    <Translate_to id="1">
    -1.0 0.0 0.0
    </Translate_to>
</Box>
<Box>
    <MaterialID name="black_P"/>
    <boxid id="3"/>
    <Vertices dim="2" npoints="4">
        5.0 6.0
        5.0 5.0
        8.0 6.0
        8.0 5.0
    </Vertices>
    <initCnd Teq="303.0"/>
    <Reservoir/>
</Box>
</Geometry>
```

We now list all possible parameters in geometry files:

1. number_of_boxes/Ngeom [integer]: Indicates the number of boxes.
2. Box/MaterialID/name [string]: Box material
3. Box/Vertices/dim [integer]: system dimension (Accepted values: 2).
4. Box/Vertices/npoints [integer]: number of vertices.
5. Box/Vertices [double, array(dim,npoints),units(nm)]: Box vertices (NOTE: they need to form a convex hull).
6. Box/initCnd/Teq [double,units(K)]: Reference temperature.
7. Box/initCnd/Tinit [double,optional,units(K)]: Temperature to initialize the box population out of reference (default: Teq). RTA simulator ignores this.
8. Box/Reservoir : if present it indicates that the box is an isothermal reservoir.

A. Description of the *BTE-Barna* executables, inputs, and outputs

9. Box/Translate_to/id [int]: It indicates that any particle entering that box is translated to “id” box.
10. Box/Translate_to [double,array(1,3),units(nm)]: Translation vector applied to any particle entering that box.

A.2.2. RTAMC2D

The RTAMC2D executable implements the general RTA algorithm of Section 4.6 and the specialization described in Subsection 4.6.2 to obtain the steady-state for periodic structures under a thermal gradient. It has as command line inputs:

RTAMC2D input.xml N_{threads} [N_{runs}]

1. input.xml [string]: xml file containing the input.
2. N_{threads} [integer]: number of TBB threads for simulation.
3. N_{runs} [integer,optional]: number of repetitions to be done, to prevent table creation and data loading (default: 1).

A.2.2.1. input.xml

We provide now another toy example of input.xml files together with an explanation of its variables:

```
<RTA_MC2d>
  <geometry file="grta01.xml"/>
  <gradient x="0.2" y="0.0"/>
  <convergence energy="-1.0" flux="-1.0"/>
  <time dt="0.5" maxtime="100000"/>
  <material name="black_P" database="black_monolayer_50_50_1.h5"
    thickness="0.5" T0="300.0"/>
  <material name="biblack_P" database="biblack_50_50_1.h5"
    thickness="1.0" T0="300.0"/>
```

A. Description of the BTE-Barna executables, inputs, and outputs

```
<layer material="black_P" layer_name="black_bare"
  atoms="0 1 2 3"/>
<layer material="biblack_P" layer_name="black_mid"
  atoms="0 1 2 3"/>
<layer material="biblack_P" layer_name="black_alone"
  atoms="4 5 6 7"/>
<layers_connection layer_A="black_mid" layer_B="black_bare"/>
<particles N="10000000"/>
<ballistic/>
<spectral>
  <resolution ticks="500">
  <location bin="0">
<spectral/>
</RTA_MC2d>
```

1. geometry_file [string]: XML file containing geometry data.
2. gradient/x [double,units(K/nm)]: x-component of homogeneous thermal gradient applied to all boxes (NOTE: requires y-component and activates the specialized algorithm to obtain steady-state for extended systems).
3. gradient/y [double,units(K/nm)]: y-component of homogeneous thermal gradient applied to all boxes (NOTE: requires x-component and activates the specialized algorithm to obtain steady-state for extended systems).
4. convergence/energy [double,optional]: if given, the loop of the specialized algorithm to obtain steady-state for extended systems with an applied thermal gradient is broken when relative difference in deviational energy density is lower than this threshold (default: -1.0).
5. convergence/flux [double,optional]: if given, the loop of the specialized algorithm to obtain steady-state for extended systems with an applied thermal gradient is broken when relative differences of heat fluxes are lower than this threshold (default: -1.0).
6. time/dt [double,units(ps)]: spacing for mesh in time.

A. Description of the *BTE-Barna* executables, inputs, and outputs

7. time/maxtime [double,units(ps)]: Maximum time for particles.
8. material/name [string]: material id.
9. material/database [string]: path to almaBTE's database containing phonon properties.
10. material/thickness [double,units(nm)]: real thickness in z-direction, used to correct DFT lattice vector in z-direction.
11. material/T0 [double,units(K)]: reference temperature of whole system (NOTE: it must be the same for all materials).
12. particles/N [integer]: Number of particles to be simulated (NOTE: be aware that even numbers are required for specialized algorithm to obtain steady-state for extended systems with an applied thermal gradient in order for sources not to add energy into the system).
13. spectral/resolution/ticks [integer,optional]: Number of divisions for spectral decomposition of fluxes and deviational temperature.
14. spectral/location/bin [integer,optional]: Box id in which spectral decomposition is calculated.
15. layer/material [string,optional]: name of material in which layer is localized. This is for LDMM.
16. layer/layer_name [string,optional]: name of layer. This is for LDMM.
17. layer/atoms [int,optional]: identity of atoms in the layer (follows the order of POSCAR). This is for LDMM.
18. layers_connection/layer_A [string,optional]: name of layer connected with layer_B (of same entry). There can be multiple entries of layer_connection if more than one connection is present. This is for LDMM.
19. layers_connection/layer_B [string,optional]: name of layer connected with layer_A (of same entry). This is for LDMM.

A. Description of the BTE-Barna executables, inputs, and outputs

20. ballistic [optional]: if given, intrinsic scattering is deactivated.

A.2.2.2. Output files

In the case of specialized algorithm to obtain steady-state for periodic structures under thermal gradient a file called `steady_state_T0K_run_irun.csv`, where $T0$ is the reference temperature and *irun* is the simulation id within the N_{runs} . This file contains in csv format the following:

$$\begin{aligned} &T_0, T_1, \quad \dots, T_{Nboxes} \\ &J_{x,0}, J_{x,1}, \quad \dots, J_{x,Nboxes} \\ &J_{y,0}, J_{y,1}, \quad \dots, J_{y,Nboxes} \end{aligned}$$

Additionally, if spectral decomposition is activated four files will be generated per selected box:

1. `steady_deltaT_omega_ibox_T0K_run_irun.csv`: contains the frequency grid in the first column and the deviational temperature per frequency in second one.

$$\begin{aligned} &\omega_0, \quad \omega_1, \quad \dots, \quad \omega_{Nticks} \\ &\Delta T_0, \quad \Delta T_1, \quad \dots, \quad \Delta T_{Nticks} \end{aligned}$$

2. `steady_jx_omega_ibox_T0K_run_irun.csv`: analogous to temperature file, but with heat flux $[J/(m^2s)]$ in x-direction.
3. `steady_jy_omega_ibox_T0K_run_irun.csv`: analogous to temperature file, but with heat flux $[J/(m^2s)]$ in y-direction.
4. `steady_fd_q_ibox_T0K_run_irun.csv`: contains the \mathbf{q}_x and \mathbf{q}_y grid in the first and second rows, respectively, and the deviational phonon

A. Description of the *BTE-Barna* executables, inputs, and outputs

population per \mathbf{q} -point in the following one.

$$\begin{aligned} & \# \mathbf{q}_{x,0}, \mathbf{q}_{x,1}, \quad \dots, \mathbf{q}_{x,N_q-1} \\ & \# \mathbf{q}_{y,0}, \mathbf{q}_{y,1}, \quad \dots, \mathbf{q}_{y,N_q-1} \\ & f^d(\mathbf{q}_0), f^d(\mathbf{q}_1), \quad \dots, f^d(\mathbf{q}_{N_q-1}) \end{aligned}$$

On the other hand, the general algorithm produces three output files per run:

1. `temperature_T0K_run_irun.csv`: contains the temperature in K per boxes (column) at given times (rows). First column of each row gives the middle point of the time bin.
2. `jxT0K_run_irun.csv`: analogous to temperature file, but with heat flux $[J/(m^2s)]$ in x-direction.
3. `jyT0K_run_irun.csv`: analogous to temperature file, but with heat flux $[J/(m^2s)]$ in y-direction.

plus four additional files per selected box if spectral decomposition is conducted:

1. `deltaT_omega_ibox_T0K_run_irun.csv`: contains the frequency grid in the first column and the deviational temperature per frequency in at each time step in the following ones.

$$\begin{array}{ccccc} -1, & \omega_0, & \omega_1, & \dots, & \omega_{N_{ticks}} \\ t_0, & \Delta T_0(t_0), & \Delta T_1(t_0), & \dots, & \Delta T_{N_{ticks}}(t_0) \\ t_1, & \Delta T_0(t_1), & \Delta T_1(t_1), & \dots, & \Delta T_{N_{ticks}}(t_1) \\ \vdots & \vdots & \vdots & \ddots & \vdots \\ t_f, & \Delta T_0(t_f), & \Delta T_1(t_f), & \dots, & \Delta T_{N_{ticks}}(t_f) \end{array}$$

where t_i is the middle point of each time grid bin.

2. `jx_omega_ibox_T0K_run_irun.csv`: analogous to temperature file, but with heat flux $[J/(m^2s)]$ in x-direction.

A. Description of the *BTE-Barna* executables, inputs, and outputs

3. `jy_omega_ibox_T0K_run_irun.csv`: analogous to temperature file, but with heat flux $[J/(m^2s)]$ in y-direction.
4. `fd_q_ibox_T0K_run_irun.csv`: contains the q_x and q_y grid in the first and second rows, respectively, and the deviational phonon population per q -point at each time step in the following ones.

$$\begin{array}{cccc}
 \#q_{x,0}, & q_{x,1}, & \dots, & q_{x,N_q-1} \\
 \#q_{y,0}, & q_{y,1}, & \dots, & q_{y,N_q-1} \\
 \\
 t_1, & f^d(q_0, t_1), & \dots, & f^d(q_{N_q-1}, t_1) \\
 \vdots & \vdots & \ddots & \vdots \\
 t_f, & f^d(q_0, t_f), & \dots, & f^d(q_{N_q-1}, t_f)
 \end{array}$$

A.2.3. PropagatorBuilder

The `PropagatorBuilder` executable implements the building of the B -matrix and subsequent $P(\Delta t)$ calculation using the Krylov subspace method (see Subsection 6.4.2). It has as command line inputs:

```
[mpi] PropagatorBuilder database.h5 IFC3 T
      Δt Nthreads
```

1. `database.h5` [string]: almaBTE's database for that material.
2. `IFC3` [string]: third-order force constants file in sparse format [46].
3. `T` [double,units(K)]: reference temperature.
4. `Δt` [double, units(ps)]: time step for propagator calculation.
5. `Nthreads` [integer]: number of TBB threads to be used in the simulation.

It generates two binaries as outputs:

`materialname_Na_Nb_1_TK_Δtps.B.eigen.bin` and

A. Description of the *BTE-Barna* executables, inputs, and outputs

`materialname_NaNb_1_TK_Δtps.P.eigen.bin`, which contain the B and $P(\Delta t)$ matrices, respectively.

A.2.4. **beRTAMC2D**

The `beRTAMC2D` executable implements the `bRTA` algorithm. The code uses the same geometrical routines than `RTAMC2D` code, built on top of `boost::geometry` library [251]. The computational intensive parts of the algorithm are parallelized using `oneTBB` [299] (multithreading), namely the ballistic evolution, the scattering algorithm, the building of the particle histogram, and the particle cancellation.

Before detailing the inputs and outputs of the executable we find worth to recall/mention the main differences with respect to the code implemented in `RTAMC2D`. Besides scattering and sampling, the main differences between both implementations are:

1. Initial temperature: It allows for initial temperatures different to the reference one (see).
2. Free flight: t_{flight} is defined as $\min\{\Delta t, t_b\}$ being Δt the time step used for $P(\Delta t)$ calculation.
3. Interface scattering: It is not implemented.
4. Boundary scattering: Particles reaching the boundaries are used to calculate the boundary temperature via cubic spline interpolation of the flux in the boundary. Then, the interpolated temperature is used to create the distribution from which particles are randomly drawn during the time step (see Subsection 4.2.2.2).
5. Multiple reference temperatures: It allows for more than a single reference temperature.

A. Description of the *BTE-Barna* executables, inputs, and outputs

Moreover, the histogram of particles is saved at each time step, enabling the calculation of frequency- and mode-resolved properties. Writing to disk is handled by a dedicated thread and performed in a sparse format using the MessagePack library [300].

A.2.4.1. Line command inputs

The code has the following command line inputs:

```
beRTAMC2D input.xml Nthreads
```

1. `input.xml` [string]: xml file containing the input.
2. `Nthreads` [integer]: number of TBB threads to be used in the simulation.

A.2.4.2. *input.xml*

We provide now another toy example of `input.xml` files together with an explanation of its variables:

```
<beRTAMC2D>
  <geometry file="grta01.xml"/>
  <gradient x="0.2" y="0.0"/>
  <time dt="0.5" maxtime="100000"/>
  <material name="black_P" database="black_monolayer_50_50_1.h5"
    thickness="0.5">
    <propagator T="300" file="bP.P.eigen.bin"/>
  </material>
  <Eff Ed="4.0e-26" particles="3600" Tmax="301.0" Tmin="299.0"/>
</beRTAMC2D>
```

1. `geometry_file` [string]: XML file containing geometry data.
2. `gradient/x` [double,units(K/nm)]: x-component of homogeneous thermal gradient applied to all boxes (NOTE: requires y-component).

A. Description of the BTE-Barna executables, inputs, and outputs

3. gradient/y [double,units(K/nm)]: y-component of homogeneous thermal gradient applied to all boxes (NOTE: requires x-component).
4. time/dt [double,units(ps)]: time step.
5. time/maxtime [double,units(ps)]: Maximum time for simulation.
6. material/name [string]: material id.
7. material/database [string]: path to almaBTE's database containing phonon properties.
8. material/thickness [double,units(nm)]: real thickness in z-direction, used to correct DFT lattice vector in z-direction.
9. material/propagator/T [double,units(K)]: reference temperature used to calculate the propagator.
10. material/propagator/file [string]: path to propagator matrix binary.
11. Eeff/particles [integer]: division of energy guess, the calculation of the guess is done individually per box and the minimum value is selected. Not needed if Eeff/Ed is provided.
12. Eeff/Tmin [double,units(K)]: minimum temperature used to calculate the deviational energy per particle. Not needed if Eeff/Ed is provided.
13. Eeff/Tmax [double,units(K)]: maximum temperature used to calculate the deviational energy per particle. Not needed if Eeff/Ed is provided.
14. Eeff/Ed [double,units(J)]: deviational energy per particle, it is not needed if Eeff/particles, Eeff/Tmin and Eeff/Tmax are provided. (NOTE: the RTAMC2D calculated value for same system and initial conditions is a proper value).
15. RTA [optional]: if given, the RTA is used for scattering.

A. Description of the *BTE-Barna* executables, inputs, and outputs

A.2.4.3. *Outputs: standard output*

Simulation data is dumped to standard output, with lines without physical information starting with #. Data for lines with physical information is structured as follows:

$$istep\ t\ N_{particles}\ \rho_0^d\ J_{x,0}\ J_{y,0}\ \dots\ \rho_{N-1}^d\ J_{x,N-1}\ J_{y,N-1},$$

with *istep* being the MC loop steep, and the energy density and fluxes are given for the N boxes forming the system. All quantities are given in SI except for time which is given in ps.

A.2.4.4. *Outputs: properties.msgpack.bin*

The particle distribution per box and time step is dumped in sparse binary format in `properties.msgpack.bin` using using MessagePack library [300]. Each time step information in the file starts by a `std::size_t` value ($size_{block}$) followed by # indicating the number of characters comprising the block. Blocks are comprised of arrays of $3 + 2N_{boxes}$ elements, with the three first ones being: time (double), deviational energy per particle (double) and one array with the T_{ref} for all boxes. This is followed by a structure for each box composed of an `std::size_t` indicating the number of non-zero elements in the distribution function vector and one array containing non-zero pairs (except in the case of empty boxes in which a dummy one is created) of an `std::size_t` indicating the phonon mode and one integer containing the number of net particles in that mode with its sign indicating if they are positive or negative particles.

This file can be processed with `dist_reader` executable to obtain the spectral decomposition of the deviational temperature and heat flux at selected boxes and times.

A.2.5. `dist_reader`

The `dist_reader` executable allows the extraction of spectral resolved quantities in both space and time, using the `beRTAMC2D` outputs. It has as command line inputs:

```
dist_reader input.xml properties.msgpack.bin
```

1. `input.xml` [string]: xml file containing the input.
2. `properties.msgpack.bin` [string]: file containing distribution function at given times as produced by `beRTAMC2D`.

it will provide the spectral decomposition of the deviational temperature as well as those of fluxes, with the same format as `RTAMC2D` spectral decomposition files, but with time column referring to the instantaneous time rather than the middle of time bin.

A.2.5.1. *input.xml*

`input.xml` is the same as in the case of `beRTAMC2D`, with the following extra terms:

1. `spectral/resolution/ticks` [integer]: Number of divisions for spectral decomposition of fluxes and deviational temperature.
2. `spectral/time/t` [double]: Times at which the spectral decomposition will be calculated. It can be used more than one time
3. `spectral/location/bin` [integer]: Box id in which spectral decomposition is calculated. It can be used more than one time.

A. Description of the BTE-Barna executables, inputs, and outputs

A.2.5.2. Output files

Spectral decomposition of temperature is printed in `deltaT_omega_BoxID.csv` and fluxes in `jx_omega_BoxID.csv` and `jy_omega_BoxID.csv`. The **q**-resolved deviational phonon distribution function is printed in `fd_BoxID.csv`. Data format is the same of the RTA spectral decomposed and **q**-resolved quantities, but this time with t indicating the instantaneous time and not the middle of time bin.

Bibliography

- [1] G. E. Moore, “*Cramming More Components onto Integrated Circuits*”, *Electronics* **38**, 114–117 (1965).
- [2] A. L. Moore and L. Shi, “*Emerging challenges and materials for thermal management of electronics*”, *Mater. Today* **17**, 163–174 (2014).
- [3] E. Pop, S. Sinha, and K. Goodson, “*Heat Generation and Transport in Nanometer-Scale Transistors*”, *Proc. IEEE* **94**, 1587–1601 (2006).
- [4] E. Macii, “*Ultra low-power electronics and design*”, Springer (2004).
- [5] P. R. Panda, B. Silpa, A. Shrivastava, and K. Gummidipudi, “*Power-efficient system design*”, Springer Science & Business Media (2010).
- [6] P. E. Ross, “*Why cpu frequency stalled*”, *IEEE Spectr.* **45**, 72 (2008).
- [7] “*Ministerio para la Transición Ecológica y el Reto Demográfico: Centrales Nucleares en España*”, <https://energia.gob.es/nuclear/Centrales/Espana/Paginas/CentralesEspana.aspx>, Accessed: 2022-04-05.

Bibliography

- [8] M. Chhowalla, D. Jena, and H. Zhang, “*Two-dimensional semiconductors for transistors*”, *Nat. Rev. Mater.* **1**, 16052 (2016).
- [9] D. Akinwande, N. Petrone, and J. Hone, “*Two-dimensional flexible nano-electronics*”, *Nat. Commun.* **5**, 5678 (2014).
- [10] J. Jiang, K. Parto, W. Cao, and K. Banerjee, “*Ultimate Monolithic-3D Integration With 2D Mater.: Rationale, Prospects, and Challenges*”, *IEEE J. Electron Devices Soc.* **7**, 878–887 (2019).
- [11] “*50 Years of Microprocessor Trend Data (K. Rupp)*”, <https://github.com/karlrupp/microprocessor-trend-data>, Accessed: 2022-04-05.
- [12] A. Danowitz, K. Kelley, J. Mao, J. P. Stevenson, and M. Horowitz, “*CPU DB: recording microprocessor history*”, *Commun. ACM* **55**, 55–63 (2012).
- [13] “*SPECint 2006*”, <https://www.spec.org/cpu2006/CINT2006/>, Accessed: 2022-04-05.
- [14] “*SPEC CPU@2017*”, <https://www.spec.org/cpu2017/>, Accessed: 2022-04-05.
- [15] A. J. Minnich, M. S. Dresselhaus, Z. F. Ren, and G. Chen, “*Bulk nanostructured thermoelectric materials: current research and future prospects*”, *Energy Environ. Sci.* **2**, 466–479 (2009).
- [16] M. Maldovan, “*Sound and heat revolutions in phononics*”, *Nature* **503**, 209–217 (2013).
- [17] A. Shakouri, “*Recent Developments in Semiconductor Thermoelectric Physics and Materials*”, *Annu. Rev. Mater. Res.* **41**, 399–431 (2011).

Bibliography

- [18] G. A. Slack, “*New Materials and Performance Limits for Thermoelectric Cooling*”, in: D.M. Rowe , ed., “*CRC Handbook of Thermoelectrics*”, CRC Press (Boca Raton, 1995).
- [19] M. G. Kanatzidis, “*Nanostructured Thermoelectrics: The New Paradigm?*”, Chem. Mater. **22**, 648–659 (2010).
- [20] M. Mattila, T. Hakkarainen, H. Lipsanen, H. Jiang, and E. I. Kauppinen, “*Catalyst-free growth of In(As)P nanowires on silicon*”, Appl. Phys. Lett. **89**, 063119 (2006).
- [21] S. Paiman, Q. Gao, H. H. Tan, C. Jagadish, K. Pemasiri, M. Montazeri, H. E. Jackson, L. M. Smith, J. M. Yarrison-Rice, X. Zhang, and J. Zou, “*The effect of V/III ratio and catalyst particle size on the crystal structure and optical properties of InP nanowires*”, Nanotechnology **20**, 225606 (2009).
- [22] F. J. Lopez, U. Givan, J. G. Connell, and L. J. Lauhon, “*Silicon Nanowire Polytypes: Identification by Raman Spectroscopy, Generation Mechanism, and Misfit Strain in Homostructures*”, ACS Nano **5**, 8958–8966 (2011).
- [23] H. I. T. Hauge, M. A. Verheijen, S. Conesa-Boj, T. Etzelstorfer, M. Watzinger, D. Kriegner, I. Zardo, C. Fasolato, F. Capitani, P. Postorino, S. Kölling, A. Li, S. Assali, J. Stangl, and E. P. A. M. Bakkers, “*Hexagonal Silicon Realized*”, Nano Lett. **15**, 5855–5860 (2015).
- [24] J. Tang, J.-L. Maurice, F. Fossard, I. Florea, W. Chen, E. V. Johnson, M. Foldyna, L. Yu, and P. Roca i Cabarrocas, “*Natural occurrence of the diamond hexagonal structure in silicon nanowires grown by a plasma-assisted vapour–liquid–solid method*”, Nanoscale **9**, 8113–8118 (2017).

Bibliography

- [25] K. Hiruma, M. Yazawa, T. Katsuyama, K. Ogawa, K. Haraguchi, M. Koguchi, and H. Kakibayashi, “*Growth and optical properties of nanometer-scale GaAs and InAs whiskers*”, J. Appl. Phys. **77**, 447–462 (1995).
- [26] P. Caroff, K. A. Dick, J. Johansson, M. E. Messing, K. Deppert, and L. Samuelson, “*Controlled polytypic and twin-plane superlattices in III–V nanowires*”, Nat. Nanotechnol. **4**, 50 (2009).
- [27] M. Tchernycheva, J. C. Harmand, G. Patriarche, L. Travers, and G. E. Cirilin, “*Temperature conditions for GaAs nanowire formation by Au-assisted molecular beam epitaxy*”, Nanotechnology **17**, 4025 (2006).
- [28] I. Zardo, S. Conesa-Boj, F. Peiro, J. R. Morante, J. Arbiol, E. Uccelli, G. Abstreiter, and A. Fontcuberta i Morral, “*Raman spectroscopy of wurtzite and zinc-blende GaAs nanowires: Polarization dependence, selection rules, and strain effects*”, Phys. Rev. B **80**, 245324 (2009).
- [29] S. Assali, I. Zardo, S. Plissard, D. Kriegner, M. A. Verheijen, G. Bauer, A. Meijerink, A. Belabbes, F. Bechstedt, J. E. M. Haverkort, and E. P. A. M. Bakkers, “*Direct Band Gap Wurtzite Gallium Phosphide Nanowires*”, Nano Lett. **13**, 1559–1563 (2013).
- [30] A. Berg, S. Lehmann, N. Vainorius, A. Gustafsson, M.-E. Pistol, L. R. Wallenberg, L. Samuelson, and M. T. Borgström, “*Growth and characterization of wurtzite GaP nanowires with control over axial and radial growth by use of HCl in-situ etching*”, J. Cryst. Growth **386**, 47–51 (2014).

Bibliography

- [31] T. Li, J. Song, X. Zhao, Z. Yang, G. Pastel, S. Xu, C. Jia, J. Dai, C. Chen, A. Gong, F. Jiang, Y. Yao, T. Fan, B. Yang, L. Wågberg, R. Yang, and L. Hu, “*Anisotropic, lightweight, strong, and super thermally insulating nanowood with naturally aligned nanocellulose*”, *Sci. Adv.* **4**, eaar3724 (2018).
- [32] J. Fourier, “*Théorie analytique de la chaleur*”, Chez Firmin Didot, père et fils (1822).
- [33] A. Sellitto, V. A. Cimmelli, and D. Jou, “*Mesosopic theories of heat transport in nanosystems*”, Springer (2016).
- [34] R. B. Wilson and D. G. Cahill, “*Anisotropic failure of Fourier theory in time-domain thermoreflectance experiments*”, *Nat. Commun.* **5**, 5075 (2014).
- [35] A. Ziabari, P. Torres, B. Vermeersch, Y. Xuan, X. Cartoixa, A. Torelló, J.-H. Bahk, Y. R. Koh, M. Parsa, P. D. Ye, F. X. Alvarez, and A. Shakouri, “*Full-field thermal imaging of quasiballistic crosstalk reduction in nanoscale devices*”, *Nat. Commun.* **9**, 255 (2018).
- [36] A. Beardo, M. G. Hennessy, L. Sendra, J. Camacho, T. G. Myers, J. Bafaluy, and F. X. Alvarez, “*Phonon hydrodynamics in frequency-domain thermoreflectance experiments*”, *Phys. Rev. B* **101**, 075303 (2020).
- [37] J. A. Johnson, A. A. Maznev, J. Cuffe, J. K. Eliason, A. J. Minnich, T. Kehoe, C. M. S. Torres, G. Chen, and K. A. Nelson, “*Direct Measurement of Room-Temperature Nondiffusive Thermal Transport Over Micron Distances in a Silicon Membrane*”, *Phys. Rev. Lett.* **110**, 025901 (2013).

Bibliography

- [38] P. Torres, A. Ziabari, A. Torelló, J. Bafaluy, J. Camacho, X. Cartoixà, A. Shakouri, and F. X. Alvarez, “*Emergence of hydrodynamic heat transport in semiconductors at the nanoscale*”, Phys. Rev. Materials **2**, 076001 (2018).
- [39] J. M. Ziman, “*Electrons and phonons: the theory of transport phenomena in solids*”, Oxford university press (2001).
- [40] W. Li, L. Lindsay, D. A. Broido, D. A. Stewart, and N. Mingo, “*Thermal conductivity of bulk and nanowire $Mg_2Si_xSn_{1-x}$ alloys from first principles*”, Phys. Rev. B **86**, 174307 (2012).
- [41] M. Omini and A. Sparavigna, “*An iterative approach to the phonon Boltzmann equation in the theory of thermal conductivity*”, Phys. B: Condens. Matter **212**, 101–112 (1995).
- [42] M. Omini and A. Sparavigna, “*Beyond the isotropic-model approximation in the theory of thermal conductivity*”, Phys. Rev. B **53**, 9064–9073 (1996).
- [43] M. Raya-Moreno, H. Aramberri, J. A. Seijas-Bellido, X. Cartoixà, and R. Rurali, “*Thermal conductivity of hexagonal Si and hexagonal Si nanowires from first-principles*”, Appl. Phys. Lett. **111**, 032107 (2017).
- [44] A. Ward, D. A. Broido, D. A. Stewart, and G. Deinzer, “*Ab initio theory of the lattice thermal conductivity in diamond*”, Phys. Rev. B **80**, 125203 (2009).
- [45] L. Lindsay, D. A. Broido, and T. L. Reinecke, “*Ab initio thermal transport in compound semiconductors*”, Phys. Rev. B **87**, 165201 (2013).
- [46] W. Li, J. Carrete, N. A. Katcho, and N. Mingo, “*ShengBTE: A solver of the Boltzmann transport equation for phonons*”, Comput. Phys. Commun. **185**, 1747–1758 (2014).

Bibliography

- [47] J. Carrete, B. Vermeersch, A. Katre, A. van Roekeghem, T. Wang, G. K. Madsen, and N. Mingo, “*almaBTE : A solver of the space–time dependent Boltzmann transport equation for phonons in structured materials*”, Comput. Phys. Commun. **220**, 351–362 (2017).
- [48] A. Togo, L. Chaput, and I. Tanaka, “*Distributions of phonon lifetimes in Brillouin zones*”, Phys. Rev. B **91**, 094306 (2015).
- [49] F. Giustino, “*Materials modelling using density functional theory: properties and predictions*”, Oxford University Press (2014).
- [50] M. Born and R. Oppenheimer, “*Zur Quantentheorie der Molekeln*”, Ann. Phys. (Berl.) **389**, 457–484 (1927).
- [51] R. M. Martin, “*Electronic structure: basic theory and practical methods*”, Cambridge university press (2020).
- [52] C. J. Cramer, “*Essentials of computational chemistry: theories and models*”, John Wiley & Sons (2004).
- [53] P. Hohenberg and W. Kohn, “*Inhomogeneous Electron Gas*”, Phys. Rev. **136**, B864–B871 (1964).
- [54] W. Kohn and L. J. Sham, “*Self-Consistent Equations Including Exchange and Correlation Effects*”, Phys. Rev. **140**, A1133–A1138 (1965).
- [55] W. Kohn and P. Vashishta, “*General Density Functional Theory*”, in: S. Lundqvist and N. March , eds., “*Theory of the Inhomogeneous Electron Gas*”, Springer Science & Business Media (1983) , Ch. 2 pp. 79-148.
- [56] G. P. Srivastava, “*The physics of phonons*”, Taylor & Francis (1990).

Bibliography

- [57] M. Lüders, A. Ernst, W. Temmerman, Z. Szotek, and P. Durham, “*Ab initio angle-resolved photoemission in multiple-scattering formulation*”, J. Condens. Matter Phys. **13**, 8587 (2001).
- [58] W. Kohn, “*Nobel Lecture: Electronic structure of matter—wave functions and density functionals*”, Rev. Mod. Phys. **71**, 1253–1266 (1999).
- [59] J. P. Perdew and A. Zunger, “*Self-interaction correction to density-functional approximations for many-electron systems*”, Phys. Rev. B **23**, 5048–5079 (1981).
- [60] D. M. Ceperley and B. J. Alder, “*Ground State of the Electron Gas by a Stochastic Method*”, Phys. Rev. Lett. **45**, 566–569 (1980).
- [61] J. P. Perdew and Y. Wang, “*Accurate and simple analytic representation of the electron-gas correlation energy*”, Phys. Rev. B **45**, 13244–13249 (1992).
- [62] S. H. Vosko, L. Wilk, and M. Nusair, “*Accurate spin-dependent electron liquid correlation energies for local spin density calculations: a critical analysis*”, Can. J. Phys. **58**, 1200–1211 (1980).
- [63] J. P. Perdew, “*Accurate Density Functional for the Energy: Real-Space Cutoff of the Gradient Expansion for the Exchange Hole*”, Phys. Rev. Lett. **55**, 1665–1668 (1985).
- [64] J. P. Perdew, K. Burke, and M. Ernzerhof, “*Generalized Gradient Approximation Made Simple*”, Phys. Rev. Lett. **77**, 3865–3868 (1996).
- [65] A. Zee, “*Group theory in a nutshell for physicists*”, Princeton University Press (2016).

Bibliography

- [66] M. S. Dresselhaus, G. Dresselhaus, and A. Jorio, “*Group theory: application to the physics of condensed matter*”, Springer Science & Business Media (2007).
- [67] D. Wallace, “*Thermodynamics of Crystals*”, John Wiley & Sons (1998).
- [68] S. Grimme, “*Density functional theory with London dispersion corrections*”, Wiley Interdisciplinary Reviews: Computational Molecular Science **1**, 211–228 (2011).
- [69] K. Berland, V. R. Cooper, K. Lee, E. Schröder, T. Thonhauser, P. Hyldgaard, and B. I. Lundqvist, “*van der Waals forces in density functional theory: a review of the vdW-DF method*”, Reports on Progress in Physics **78**, 066501 (2015).
- [70] M. Stöhr, T. Van Voorhis, and A. Tkatchenko, “*Theory and practice of modeling van der Waals interactions in electronic-structure calculations*”, Chem. Soc. Rev. **48**, 4118–4154 (2019).
- [71] S. Grimme, “*Semiempirical GGA-type density functional constructed with a long-range dispersion correction*”, J. Comput. Chem. **27**, 1787–1799 (2006).
- [72] S. Grimme, J. Antony, S. Ehrlich, and H. Krieg, “*A consistent and accurate ab initio parametrization of density functional dispersion correction (DFT-D) for the 94 elements H-Pu*”, J. Chem. Phys. **132**, 154104 (2010).
- [73] M. Dion, H. Rydberg, E. Schröder, D. C. Langreth, and B. I. Lundqvist, “*Van der Waals Density Functional for General Geometries*”, Phys. Rev. Lett. **92**, 246401 (2004).
- [74] O. A. Vydrov and T. Van Voorhis, “*Nonlocal van der Waals Density Functional Made Simple*”, Phys. Rev. Lett. **103**, 063004 (2009).

Bibliography

- [75] K. Lee, D. Murray, L. Kong, B. I. Lundqvist, and D. C. Langreth, “*Higher-accuracy van der Waals density functional*”, Phys. Rev. B **82**, 081101 (2010).
- [76] O. A. Vydrov and T. Van Voorhis, “*Nonlocal van der Waals density functional: The simpler the better*”, J. Chem. Phys. **133**, 244103 (2010).
- [77] D. J. Singh and L. Nordstrom, “*Planewaves, Pseudopotentials, and the LAPW method*”, Springer Science & Business Media (2006).
- [78] S. Baroni, S. de Gironcoli, A. Dal Corso, and P. Giannozzi, “*Phonons and related crystal properties from density-functional perturbation theory*”, Rev. Mod. Phys. **73**, 515–562 (2001).
- [79] P. Bendt and A. Zunger, “*Simultaneous Relaxation of Nuclear Geometries and Electric Charge Densities in Electronic Structure Theories*”, Phys. Rev. Lett. **50**, 1684–1688 (1983).
- [80] J. Ihm, A. Zunger, and M. L. Cohen, “*Momentum-space formalism for the total energy of solids*”, J. Phys. C: Solid State Phys. **12**, 4409–4422 (1979).
- [81] X. Gonze and J.-P. Vigneron, “*Density-functional approach to nonlinear-response coefficients of solids*”, Phys. Rev. B **39**, 13120–13128 (1989).
- [82] Y. Wang, S.-L. Shang, H. Fang, Z.-K. Liu, and L.-Q. Chen, “*First-principles calculations of lattice dynamics and thermal properties of polar solids*”, NPJ Comput. Mater. **2**, 1–10 (2016).
- [83] X. Gonze, “*Perturbation expansion of variational principles at arbitrary order*”, Phys. Rev. A **52**, 1086–1095 (1995).

Bibliography

- [84] X. Gonze, “*First-principles responses of solids to atomic displacements and homogeneous electric fields: Implementation of a conjugate-gradient algorithm*”, Phys. Rev. B **55**, 10337–10354 (1997).
- [85] X. Gonze and C. Lee, “*Dynamical matrices, Born effective charges, dielectric permittivity tensors, and interatomic force constants from density-functional perturbation theory*”, Phys. Rev. B **55**, 10355–10368 (1997).
- [86] T. T. Heikkilä, “*The Physics of Nanoelectronics: Transport and Fluctuation Phenomena at Low Temperatures*”, Oxford University Press (Oxford, 2013).
- [87] M. Lundstrom, “*Fundamentals of carrier transport*”, Cambridge University Press (2000).
- [88] T. Sohler, M. Gibertini, M. Calandra, F. Mauri, and N. Marzari, “*Breakdown of Optical Phonons’ Splitting in Two-Dimensional Materials*”, Nano Lett. **17**, 3758–3763 (2017).
- [89] M. D. Luca, X. Cartoixa, D. I. Indolese, J. Martín-Sánchez, K. Watanabe, T. Taniguchi, C. Schönenberger, R. Trotta, R. Rurali, and I. Zardo, “*Experimental demonstration of the suppression of optical phonon splitting in 2D materials by Raman spectroscopy*”, 2D Mater. **7**, 035017 (2020).
- [90] U. Rössler, “*Solid state theory: an introduction*”, Springer Science & Business Media (2009).
- [91] D. Ferry, “*Quantum mechanics: an introduction for device physicists and electrical engineers*”, CRC Press (2020).
- [92] R. E. Peierls and R. S. Peierls, “*Quantum theory of solids*”, Oxford University Press (1955).

Bibliography

- [93] N. W. Ashcroft and N. D. Mermin, “*Solid state physics*”, Harcourt College Publishers (1976).
- [94] G. Kresse, J. Furthmüller, and J. Hafner, “*Ab initio Force Constant Approach to Phonon Dispersion Relations of Diamond and Graphite*”, EPL **32**, 729–734 (1995).
- [95] L. T. Kong, “*Phonon dispersion measured directly from molecular dynamics simulations*”, Comput. Phys. Commun. **182**, 2201–2207 (2011).
- [96] L. T. Kong, G. Bartels, C. Campaña, C. Denniston, and M. H. Müser, “*Implementation of Green’s function molecular dynamics: An extension to LAMMPS*”, Comput. Phys. Commun. **180**, 1004–1010 (2009).
- [97] M. T. Dove and M. T. Dove, “*Introduction to lattice dynamics*”, Cambridge university press (1993).
- [98] A. Warda, *First principles theory of the lattice thermal conductivity of semiconductors*, PhD thesis, Boston College (Chestnut Hill, Massachusetts, 2009).
- [99] J. Callaway, “*Model for Lattice Thermal Conductivity at Low Temperatures*”, Phys. Rev. **113**, 1046–1051 (1959).
- [100] R. Peierls, “*Zur kinetischen theorie der wärmeleitung in kristallen*”, Ann. Phys. (Berl.) **395**, 1055–1101 (1929).
- [101] P. L. Taylor and O. Heinonen, “*A Quantum Approach to Condensed Matter Physics*”, Cambridge University Press (2002).
- [102] A. A. Maznev and O. B. Wright, “*Demystifying umklapp vs normal scattering in lattice thermal conductivity*”, Am. J. Phys. **82**, 1062–1066 (2014).

Bibliography

- [103] Z. Ding, J. Zhou, B. Song, M. Li, T.-H. Liu, and G. Chen, “*Umklapp scattering is not necessarily resistive*”, Phys. Rev. B **98**, 180302 (2018).
- [104] Y. Guo, Z. Zhang, M. Nomura, S. Volz, and M. Wang, “*Phonon vortex dynamics in graphene ribbon by solving Boltzmann transport equation with ab initio scattering rates*”, Int. J. Heat Mass Transf. **169**, 120981 (2021).
- [105] Y. Guo, Z. Zhang, M. Bescond, S. Xiong, M. Wang, M. Nomura, and S. Volz, “*Size effect on phonon hydrodynamics in graphite microstructures and nanostructures*”, Phys. Rev. B **104**, 075450 (2021).
- [106] L. D. Landau and E. M. Lifshitz, “*Course of theoretical physics: Physical Kinetics*”, Pergamon P. (1981).
- [107] S. L. Shindé and G. P. Srivastava, “*Length-scale dependent phonon interactions*”, Springer (2014).
- [108] D. A. Broido, A. Ward, and N. Mingo, “*Lattice thermal conductivity of silicon from empirical interatomic potentials*”, Phys. Rev. B **72**, 014308 (2005).
- [109] O. Jepson and O. Anderson, “*The electronic structure of h.c.p. Ytterbium*”, Solid State Commun. **9**, 1763–1767 (1971).
- [110] M. Kawamura, Y. Gohda, and S. Tsuneyuki, “*Improved tetrahedron method for the Brillouin-zone integration applicable to response functions*”, Phys. Rev. B **89**, 094515 (2014).
- [111] P. Giannozzi, O. Andreussi, T. Brumme, O. Bunau, M. B. Nardelli, M. Calandra, R. Car, C. Cavazzoni, D. Ceresoli, *et al.*, “*Advanced capabilities for materials modelling with Quantum ESPRESSO*”, J. Condens. Matter Phys. **29**, 465901 (2017).

Bibliography

- [112] P. E. Blöchl, O. Jepsen, and O. K. Andersen, “*Improved tetrahedron method for Brillouin-zone integrations*”, Phys. Rev. B **49**, 16223–16233 (1994).
- [113] J. R. Yates, X. Wang, D. Vanderbilt, and I. Souza, “*Spectral and Fermi surface properties from Wannier interpolation*”, Phys. Rev. B **75**, 195121 (2007).
- [114] A. Togo, L. Chaput, I. Tanaka, and G. Hug, “*First-principles phonon calculations of thermal expansion in Ti_3SiC_2 , Ti_3AlC_2 , and Ti_3GeC_2* ”, Phys. Rev. B **81**, 174301 (2010).
- [115] T. Feng, X. Yang, and X. Ruan, “*Phonon anharmonic frequency shift induced by four-phonon scattering calculated from first principles*”, J. Appl. Phys. **124**, 145101 (2018).
- [116] L. Paulatto, F. Mauri, and M. Lazzeri, “*Anharmonic properties from a generalized third-order ab initio approach: Theory and applications to graphite and graphene*”, Phys. Rev. B **87**, 214303 (2013).
- [117] C. H. Lee and C. K. Gan, “*Anharmonic interatomic force constants and thermal conductivity from Grüneisen parameters: An application to graphene*”, Phys. Rev. B **96**, 035105 (2017).
- [118] G. Deinzer, M. Schmitt, A. P. Mayer, and D. Strauch, “*Intrinsic lifetimes and anharmonic frequency shifts of long-wavelength optical phonons in polar crystals*”, Phys. Rev. B **69**, 014304 (2004).
- [119] G. Fugallo, B. Rousseau, and M. Lazzeri, “*Infrared reflectance, transmittance, and emittance spectra of MgO from first principles*”, Phys. Rev. B **98**, 184307 (2018).

Bibliography

- [120] G. Fugallo, M. Lazzeri, L. Paulatto, and F. Mauri, “*Ab initio variational approach for evaluating lattice thermal conductivity*”, Phys. Rev. B **88**, 045430 (2013).
- [121] S.-I. Tamura, “*Isotope scattering of dispersive phonons in Ge*”, Phys. Rev. B **27**, 858–866 (1983).
- [122] M. Arrigoni, J. Carrete, N. Mingo, and G. K. H. Madsen, “*First-principles quantitative prediction of the lattice thermal conductivity in random semiconductor alloys: The role of force-constant disorder*”, Phys. Rev. B **98**, 115205 (2018).
- [123] H. R. Seyf, L. Yates, T. L. Bougher, S. Graham, B. A. Cola, T. Detchprohm, M.-H. Ji, J. Kim, R. Dupuis, W. Lv, and A. Henry, “*Rethinking phonons: The issue of disorder*”, NPJ Comput. Mater. **3**, 49 (2017).
- [124] F. D. Santiago, M. Raya-Moreno, Á. Miranda, M. Cruz-Irisson, X. Cartoixà, and R. Rurali, “*Tunable thermal conductivity of ternary alloy semiconductors from first-principles*”, J. Phys. D: Appl. Phys. **54**, 335302 (2021).
- [125] T. Borca-Tasciuc, D. W. Song, J. R. Meyer, I. Vurgaftman, M.-J. Yang, B. Z. Noshov, L. J. Whitman, H. Lee, R. U. Martinelli, G. W. Turner, M. J. Manfra, and G. Chen, “*Thermal conductivity of $\text{AlAs}_{0.07}\text{Sb}_{0.93}$ and $\text{Al}_{0.9}\text{Ga}_{0.1}\text{As}_{0.07}\text{Sb}_{0.93}$ alloys and $(\text{AlAs})_I/(\text{AlSb})_{1I}$ digital-alloy superlattices*”, J. Appl. Phys. **92**, 4994–4998 (2002).
- [126] W. Liu and A. A. Balandin, “*Thermal conduction in $\text{Al}_x\text{Ga}_{1-x}\text{N}$ alloys and thin films*”, J. Appl. Phys. **97**, 073710 (2005).
- [127] F. Giustino, “*Electron-phonon interactions from first principles*”, Rev. Mod. Phys. **89**, 015003 (2017).

Bibliography

- [128] S. Poncé, E. Margine, C. Verdi, and F. Giustino, “*EPW: Electron–phonon coupling, transport and superconducting properties using maximally localized Wannier functions*”, *Comput. Phys. Commun.* **209**, 116–133 (2016).
- [129] C. Verdi and F. Giustino, “*Fröhlich Electron-Phonon Vertex from First Principles*”, *Phys. Rev. Lett.* **115**, 176401 (2015).
- [130] T. Deng, G. Wu, W. Shi, Z. M. Wong, J.-S. Wang, and S.-W. Yang, “*Ab initio dipolar electron-phonon interactions in two-dimensional materials*”, *Phys. Rev. B* **103**, 075410 (2021).
- [131] D. G. Cahill, P. V. Braun, G. Chen, D. R. Clarke, S. Fan, K. E. Goodson, P. Keblinski, W. P. King, G. D. Mahan, A. Majumdar, H. J. Maris, S. R. Phillpot, E. Pop, and L. Shi, “*Nanoscale thermal transport. II. 2003–2012*”, *Appl. Phys. Rev.* **1**, 011305 (2014).
- [132] Y. Guo and M. Wang, “*Phonon hydrodynamics and its applications in nanoscale heat transport*”, *Phys. Rep.* **595**, 1–44 (2015).
- [133] Y. Guo and M. Wang, “*Phonon hydrodynamics for nanoscale heat transport at ordinary temperatures*”, *Phys. Rev. B* **97**, 035421 (2018).
- [134] F. X. Alvarez, J. Casas-Vázquez, and D. Jou, “*Robustness of the nonequilibrium entropy related to the Maxwell-Cattaneo heat equation*”, *Phys. Rev. E* **77**, 031110 (2008).
- [135] C. Cattaneo, “*Sulla conduzione del calore*”, *Atti Sem. Mat. Fis. Univ. Modena* **3**, 83–101 (1948).
- [136] R. A. Guyer and J. A. Krumhansl, “*Thermal Conductivity, Second Sound, and Phonon Hydrodynamic Phenomena in Nonmetallic Crystals*”, *Phys. Rev.* **148**, 778–788 (1966).

Bibliography

- [137] A. Sellitto, I. Carlomagno, and D. Jou, “*Two-dimensional phonon hydrodynamics in narrow strips*”, Proc. R. Soc. A: Math. Phys. Eng. Sci. **471**, 20150376 (2015).
- [138] R. A. Guyer and J. A. Krumhansl, “*Solution of the Linearized Phonon Boltzmann Equation*”, Phys. Rev. **148**, 766–778 (1966).
- [139] A. Cepellotti, G. Fugallo, L. Paulatto, M. Lazzeri, F. Mauri, and N. Marzari, “*Phonon hydrodynamics in two-dimensional materials*”, Nat. Commun. **6**, 6400 (2015).
- [140] G. Chen, “*Non-Fourier phonon heat conduction at the microscale and nanoscale*”, Nat. Rev. Phys. **3**, 555–569 (2021).
- [141] M. Simoncelli, N. Marzari, and A. Cepellotti, “*Generalization of Fourier’s Law into Viscous Heat Equations*”, Phys. Rev. X **10**, 011019 (2020).
- [142] A. Cepellotti and N. Marzari, “*Thermal Transport in Crystals as a Kinetic Theory of Relaxons*”, Phys. Rev. X **6**, 041013 (2016).
- [143] L. Sendra, A. Beardo, P. Torres, J. Bafaluy, F. X. Alvarez, and J. Camacho, “*Derivation of a hydrodynamic heat equation from the phonon Boltzmann equation for general semiconductors*”, Phys. Rev. B **103**, L140301 (2021).
- [144] G. Chen, “*Nanoscale energy transport and conversion: a parallel treatment of electrons, molecules, phonons, and photons*”, Oxford university press (2005).
- [145] M. Simoncelli, N. Marzari, and F. Mauri, “*Unified theory of thermal transport in crystals and glasses*”, Nat. Phys. **15**, 809–813 (2019).
- [146] M. Simoncelli, *Thermal transport beyond Fourier, and beyond Boltzmann*, PhD thesis, EPFL (Lausanne, Switzerland, 2021).

Bibliography

- [147] L. Lindsay, A. Katre, A. Cepellotti, and N. Mingo, “*Perspective on ab initio phonon thermal transport*”, J. Appl. Phys. **126**, 050902 (2019).
- [148] D. J. Ecsedy and P. G. Klemens, “*Thermal resistivity of dielectric crystals due to four-phonon processes and optical modes*”, Phys. Rev. B **15**, 5957–5962 (1977).
- [149] T. Feng and X. Ruan, “*Quantum mechanical prediction of four-phonon scattering rates and reduced thermal conductivity of solids*”, Phys. Rev. B **93**, 045202 (2016).
- [150] T. Feng, L. Lindsay, and X. Ruan, “*Four-phonon scattering significantly reduces intrinsic thermal conductivity of solids*”, Phys. Rev. B **96**, 161201 (2017).
- [151] C. De Tomas, A. Cantarero, A. Lopeandia, and F. Alvarez, “*From kinetic to collective behavior in thermal transport on semiconductors and semiconductor nanostructures*”, J. Appl. Phys. **115**, 164314 (2014).
- [152] A. Cepellotti and N. Marzari, “*Thermal Transport in Crystals as a Kinetic Theory of Relaxons*”, Phys. Rev. X **6**, 041013 (2016).
- [153] L. Chaput, “*Direct Solution to the Linearized Phonon Boltzmann Equation*”, Phys. Rev. Lett. **110**, 265506 (2013).
- [154] Z. Wang and N. Mingo, “*Absence of Casimir regime in two-dimensional nanoribbon phonon conduction*”, Appl. Phys. Lett. **99**, 101903 (2011).
- [155] H. Casimir, “*Note on the conduction of heat in crystals*”, Physica **5**, 495–500 (1938).
- [156] A. R. Hutson, “*Piezoelectric Scattering and Phonon Drag in ZnO and CdS*”, J. Appl. Phys. **32**, 2287–2292 (1961).

Bibliography

- [157] J. Sadhu, H. Tian, J. Ma, B. Azeredo, J. Kim, K. Balasundaram, C. Zhang, X. Li, P. M. Ferreira, and S. Sinha, “*Quenched Phonon Drag in Silicon Nanowires Reveals Significant Effect in the Bulk at Room Temperature*”, Nano Lett. **15**, 3159–3165 (2015).
- [158] N. H. Protik and D. A. Broido, “*Coupled transport of phonons and carriers in semiconductors: A case study of n-doped GaAs*”, Phys. Rev. B **101**, 075202 (2020).
- [159] F. F. M. Sabatti, S. M. Goodnick, and M. Saraniti, “*Particle-Based Modeling of Electron–Phonon Interactions*”, J. Heat Transfer **142**, 012402 (2019).
- [160] M. Mohamed, Z. Aksamija, W. Vitale, F. Hassan, K.-H. Park, and U. Ravaioli, “*A Conjoined Electron and Thermal Transport Study of Thermal Degradation Induced During Normal Operation of Multigate Transistors*”, IEEE Trans. Electron Devices **61**, 976–983 (2014).
- [161] A. Togo and I. Tanaka, “*First principles phonon calculations in materials science*”, Scr. Mater. **108**, 1–5 (2015).
- [162] Z. Han, X. Yang, W. Li, T. Feng, and X. Ruan, “*FourPhonon: An extension module to ShengBTE for computing four-phonon scattering rates and thermal conductivity*”, Comput. Phys. Commun. **270**, 108179 (2022).
- [163] N. H. Protik, C. Li, M. Pruneda, D. Broido, and P. Ordejón, “*The elphbolt ab initio solver for the coupled electron-phonon Boltzmann transport equations*”, NPJ Comput. Mater. **8**, 28 (2022).
- [164] P. Torres, F. X. Alvarez, X. Cartoixà, and R. Rurali, “*Thermal conductivity and phonon hydrodynamics in transition metal dichalcogenides from first-principles*”, 2D Mater. **6**, 035002 (2019).

Bibliography

- [165] C. Melis, R. Dettori, S. Vandermeulen, and L. Colombo, “*Calculating thermal conductivity in a transient conduction regime: theory and implementation*”, Eur. Phys. J. B **87**, 96 (2014).
- [166] S. Stackhouse, L. Stixrude, and B. B. Karki, “*Thermal Conductivity of Periclase (MgO) from First Principles*”, Phys. Rev. Lett. **104**, 208501 (2010).
- [167] A. Marcolongo, P. Umari, and S. Baroni, “*Microscopic theory and quantum simulation of atomic heat transport*”, Nat. Phys. **12**, 80–84 (2016).
- [168] R. B. Peterson, “*Direct Simulation of Phonon-Mediated Heat Transfer in a Debye Crystal*”, J. Heat Transfer **116**, 815–822 (1994).
- [169] D. Lacroix, K. Joulain, and D. Lemonnier, “*Monte Carlo transient phonon transport in silicon and germanium at nanoscales*”, Phys. Rev. B **72**, 064305 (2005).
- [170] S. Mei, L. N. Maurer, Z. Aksamija, and I. Knezevic, “*Full-dispersion Monte Carlo simulation of phonon transport in micron-sized graphene nanoribbons*”, J. Appl. Phys. **116**, 164307 (2014).
- [171] J.-P. M. Péraud, C. D. Landon, and N. G. Hadjiconstantinou, “*Monte Carlo methods for solving the Boltzmann transport equation*”, Annu. Rev. Heat Transf. **17**, 205-265 (2014).
- [172] Y. Chen, D. Li, J. R. Lukes, and A. Majumdar, “*Monte Carlo Simulation of Silicon Nanowire Thermal Conductivity*”, J. Heat Transfer **127**, 1129–1137 (2005).
- [173] F. F. M. Sabatti, S. M. Goodnick, and M. Saraniti, “*Simulation of Phonon Transport in Semiconductors Using a Population-Dependent Many-Body Cellular Monte Carlo Approach*”, J. Heat Transfer **139**, 032002 (2016).

Bibliography

- [174] N. G. Hadjiconstantinou, G. A. Radtke, and L. L. Baker, “*On Variance-Reduced Simulations of the Boltzmann Transport Equation for Small-Scale Heat Transfer Applications*”, J. Heat Transfer **132**, 112401 (2010).
- [175] J.-P. M. Péraud and N. G. Hadjiconstantinou, “*Efficient simulation of multidimensional phonon transport using energy-based variance-reduced Monte Carlo formulations*”, Phys. Rev. B **84**, 205331 (2011).
- [176] J.-P. M. Péraud and N. G. Hadjiconstantinou, “*An alternative approach to efficient simulation of micro/nanoscale phonon transport*”, Appl. Phys. Lett. **101**, 153114 (2012).
- [177] C. D. Landon, *A deviational Monte Carlo formulation of ab initio phonon transport and its application to the study of kinetic effects in graphene ribbons*, PhD thesis, Massachusetts Institute of Technology (Cambridge, Massachusetts, 2014).
- [178] C. Landon and N. Hadjiconstantinou, “*Deviational simulation of phonon transport in graphene ribbons with ab initio scattering*”, J. Appl. Phys. **116**, 163502 (2014).
- [179] E. T. Swartz and R. O. Pohl, “*Thermal boundary resistance*”, Rev. Mod. Phys. **61**, 605–668 (1989).
- [180] W. Little, “*The transport of heat between dissimilar solids at low temperatures*”, Can. J. Phys. **37**, 334–349 (1959).
- [181] J. Larroque, P. Dollfus, and J. Saint-Martin, “*Phonon transmission at Si/Ge and polytypic Ge interfaces using full-band mismatch based models*”, J. Appl. Phys. **123**, 025702 (2018).

Bibliography

- [182] P. Reddy, K. Castelino, and A. Majumdar, “*Diffuse mismatch model of thermal boundary conductance using exact phonon dispersion*”, Appl. Phys. Lett. **87**, 211908 (2005).
- [183] P. E. Hopkins, “*Multiple phonon processes contributing to inelastic scattering during thermal boundary conductance at solid interfaces*”, J. Appl. Phys. **106**, 013528 (2009).
- [184] J. Carrete, M. López-Suárez, M. Raya-Moreno, A. S. Bochkarev, M. Royo, G. K. H. Madsen, X. Cartoixa, N. Mingo, and R. Rurali, “*Phonon transport across crystal-phase interfaces and twin boundaries in semiconducting nanowires*”, Nanoscale **11**, 16007–16016 (2019).
- [185] N. Roberts and D. Walker, “*A review of thermal rectification observations and models in solid materials*”, Int. J. Therm. Sci. **50**, 648–662 (2011).
- [186] J. Randrianalisoa and D. Baillis, “*Monte Carlo simulation of cross-plane thermal conductivity of nanostructured porous silicon films*”, J. Appl. Phys. **103**, 053502 (2008).
- [187] J. Randrianalisoa and D. Baillis, “*Monte Carlo Simulation of Steady-State Microscale Phonon Heat Transport*”, J. Heat Transf. **130**, 072404 (2008).
- [188] C.-Y. Yeh, Z. W. Lu, S. Froyen, and A. Zunger, “*Zinc-blende-wurtzite polytypism in semiconductors*”, Phys. Rev. B **46**, 10086–10097 (1992).
- [189] T. Akiyama, K. Sano, K. Nakamura, and T. Ito, “*An Empirical Potential Approach to Wurtzite–Zinc-Blende Polytypism in Group III–V Semiconductor Nanowires*”, Jpn. J. Appl. Phys. **45**, L275 (2006).
- [190] W. Li and N. Mingo, “*Thermal conductivity of bulk and nanowire InAs, AlN, and BeO polymorphs from first principles*”, J. Appl. Phys. **114**, 183505 (2013).

Bibliography

- [191] S. Mukhopadhyay, L. Lindsay, and D. S. Parker, “*Optic phonon bandwidth and lattice thermal conductivity: The case of Li_2X ($\text{X} = \text{O}, \text{S}, \text{Se}, \text{Te}$)*”, Phys. Rev. B **93**, 224301 (2016).
- [192] G. Slack, “*Nonmetallic crystals with high thermal conductivity*”, J. Phys. Chem. Solids **34**, 321–335 (1973).
- [193] L. Lindsay, D. A. Broido, and T. L. Reinecke, “*First-Principles Determination of Ultrahigh Thermal Conductivity of Boron Arsenide: A Competitor for Diamond?*”, Phys. Rev. Lett. **111**, 025901 (2013).
- [194] C. Frondel and U. B. Marvin, “*Lonsdaleite, a Hexagonal Polymorph of Diamond*”, Nature **214**, 587–589 (1967).
- [195] M. Raya-Moreno, R. Rurali, and X. Cartoixà, “*Thermal conductivity for III-V and II-VI semiconductor wurtzite and zinc-blende polytypes: The role of anharmonicity and phase space*”, Phys. Rev. Materials **3**, 084607 (2019).
- [196] G. Giorgi, M. Amato, S. Ossicini, X. Cartoixà, E. Canadell, and R. Rurali, “*Doping of III-V Arsenide and Phosphide Wurtzite Semiconductors*”, J. Phys. Chem. C **124**, 27203–27212 (2020).
- [197] G. Kresse and J. Hafner, “*Ab initio molecular dynamics for liquid metals*”, Phys. Rev. B **47**, 558–561 (1993).
- [198] G. Kresse and J. Hafner, “*Ab initio molecular-dynamics simulation of the liquid-metal–amorphous-semiconductor transition in germanium*”, Phys. Rev. B **49**, 14251–14269 (1994).
- [199] G. Kresse and J. Furthmüller, “*Efficiency of ab-initio total energy calculations for metals and semiconductors using a plane-wave basis set*”, Comput. Mater. Sci. **6**, 15–50 (1996).

Bibliography

- [200] G. Kresse and J. Furthmüller, “*Efficient iterative schemes for ab initio total-energy calculations using a plane-wave basis set*”, Phys. Rev. B **54**, 11169–11186 (1996).
- [201] P. E. Blöchl, “*Projector augmented-wave method*”, Phys. Rev. B **50**, 17953–17979 (1994).
- [202] G. Kresse and D. Joubert, “*From ultrasoft pseudopotentials to the projector augmented-wave method*”, Phys. Rev. B **59**, 1758–1775 (1999).
- [203] Y. Wang, J. J. Wang, W. Y. Wang, Z. G. Mei, S. L. Shang, L. Q. Chen, and Z. K. Liu, “*A mixed-space approach to first-principles calculations of phonon frequencies for polar materials*”, J. Phys.: Condens. Matter **22**, 202201 (2010).
- [204] G. Ortiz, I. Souza, and R. M. Martin, “*Exchange-Correlation Hole in Polarized Insulators: Implications for the Microscopic Functional Theory of Dielectrics*”, Phys. Rev. Lett. **80**, 353–356 (1998).
- [205] S. Narasimhan and S. de Gironcoli, “*Ab initio calculation of the thermal properties of Cu: Performance of the LDA and GGA*”, Phys. Rev. B **65**, 064302 (2002).
- [206] M. Arrigoni and G. K. Madsen, “*Comparing the performance of LDA and GGA functionals in predicting the lattice thermal conductivity of III-V semiconductor materials in the zincblende structure: The cases of AlAs and BAs*”, Comput. Mater. Sci. **156**, 354–360 (2019).
- [207] H. Neumann, “*J. H. Edgar (ed.). Properties of Group III Nitrides. (EMIS Datareviews Series No. 11). INSPEC, The Institution of Electrical Engineers, London 1994. 302 Seiten, 121 Abbildungen, 77 Tabellen. ISBN 0–85296–818–3*”, Cryst. Res. Technol. **30**, 910 .

Bibliography

- [208] S. Funk, A. Li, D. Ercolani, M. Gemmi, L. Sorba, and I. Zardo, “*Crystal Phase Induced Bandgap Modifications in AlAs Nanowires Probed by Resonant Raman Spectroscopy*”, ACS Nano **7**, 1400–1407 (2013).
- [209] T. Azuhata, T. Sota, and K. Suzuki, “*Second-order Raman spectra and lattice dynamics in AlAs*”, J. Phys.: Condens. Matter **7**, 1949 (1995).
- [210] A. Tabata, R. Enderlein, J. R. Leite, S. W. da Silva, J. C. Galzerani, D. Schikora, M. Kloidt, and K. Lischka, “*Comparative Raman studies of cubic and hexagonal GaN epitaxial layers*”, J. Appl. Phys. **79**, 4137–4140 (1996).
- [211] “*Gallium phosphide (GaP) phonon frequencies and wavenumbers*”, in: O. Madelung, U. Rössler, and M. Schulz, eds., “*Group IV Elements, IV-IV and III-V Compounds. Part a - Lattice Properties*”, Springer Berlin Heidelberg (Berlin, Heidelberg, 2001) pp. 1–7.
- [212] D. Strauch and B. Dorner, “*Phonon dispersion in GaAs*”, J. Phys.: Condens. Matter **2**, 1457 (1990).
- [213] E. G. Gadret, M. M. de Lima, J. R. Madureira, T. Chiamonte, M. A. Cotta, F. Iikawa, and A. Cantarero, “*Optical phonon modes of wurtzite InP*”, Appl. Phys. Lett. **102**, 122101 (2013).
- [214] P. H. Borchers, G. F. Alfrey, A. D. B. Woods, and D. H. Saunderson, “*Phonon dispersion curves in indium phosphide*”, J. Phys. C **8**, 2022 (1975).
- [215] I. Zardo, S. Yazji, N. Hörmann, S. Hertenberger, S. Funk, S. Mangialardo, S. Morkötter, G. Koblmüller, P. Postorino, and G. Abstreiter, “*EI(A) Electronic Band Gap in Wurtzite InAs Nanowires Studied by Resonant Raman Scattering*”, Nano Lett. **13**, 3011–3016 (2013).

Bibliography

- [216] R. Carles, N. Saint-Cricq, J. B. Renucci, M. A. Renucci, and A. Zwick, “*Second-order Raman scattering in InAs*”, Phys. Rev. B **22**, 4804–4815 (1980).
- [217] P. Teredesai, F. Deepak, A. Govindaraj, A. Sood, and C. Rao, “*A Raman study of CdSe and ZnSe nanostructures.*”, J. Nanosci. Nanotechnol. **2**, 495–498 (2002).
- [218] B. Hennion, F. Moussa, G. Pepy, and K. Kunc, “*Normal modes of vibrations in ZnSe*”, Phys. Lett. A **36**, 376–378 (1971).
- [219] D. Zhao, X. Qian, X. Gu, S. A. Jajja, and R. Yang, “*Measurement Techniques for Thermal Conductivity and Interfacial Thermal Conductance of Bulk and Thin Film Materials*”, J. Electron. Packag. **138**, 040802 (2016).
- [220] L. Shindé and J. S. Goela, “*High thermal conductivity materials*”, Springer (Berlin, 2006).
- [221] M. Karim, D. Cameron, and M. Hashmi, “*Characterization of mixed-phase BN thin films deposited by plasma CVD*”, Surf. Coat. Technol. **60**, 502–505 (1993).
- [222] C. B. Samantaray and R. N. Singh, “*Review of synthesis and properties of cubic boron nitride (c-BN) thin films*”, Int. Mater. Rev. **50**, 313–344 (2005).
- [223] M. A. Afromowitz, “*Thermal conductivity of $Ga_{1-x}Al_xAs$ alloys*”, J. Appl. Phys. **44**, 1292–1294 (1973).
- [224] H. Shibata, Y. Waseda, H. Ohta, K. Kiyomi, K. Shimoyama, K. Fujito, H. Nagaoka, Y. Kagamitani, R. Simura, and T. Fukuda, “*High Thermal Conductivity of Gallium Nitride (GaN) Crystals Grown by HVPE Process*”, Mater. Trans., JIM **48**, 2782–2786 (2007).

Bibliography

- [225] A. Jeżowski, O. Churiukova, J. Mucha, T. Suski, I. A. Obukhov, and B. A. Danilchenko, “*Thermal conductivity of heavily doped bulk crystals GaN:O. Free carriers contribution*”, Mater. Res. Express **2**, 085902 (2015).
- [226] E. Richter, M. Gründer, B. Schineller, F. Brunner, U. Zeimer, C. Netzel, M. Weyers, and G. Tränkle, “*GaN boules grown by high rate HVPE*”, Phys. Status Solidi C **8**, 1450–1454 (2011).
- [227] H. Shibata, Y. Waseda, K. Shimoyama, K. Kiyomi, and H. Nagaoka , “*Gallium nitride-based material and method of manufacturing the same*”, U.S. Patent No. US 2009/0081110 A1 (14 September 2009).
- [228] E. F. Steigmeier and I. Kudman, “*Acoustical-Optical Phonon Scattering in Ge, Si, and III-V Compounds*”, Phys. Rev. **141**, 767–774 (1966).
- [229] M. Neuberger, “*Handbook of Electronic Materials Volume 2: III-V Semiconducting Compounds*”, IFI/Plenum (New York, 1971).
- [230] S. Sze and K. Ng, “*Appendix G Properties of Si and GaAs*”, in: “*Physics of Semiconductor Devices*”, Wiley-Blackwell (2006), Ch. pp. 790–790.
- [231] E. F. Steigmeier and I. Kudman, “*Thermal Conductivity of III-V Compounds at High Temperatures*”, Phys. Rev. **132**, 508–512 (1963).
- [232] “*Zinc selenide (ZnSe) thermoelectric power, thermal conductivity*”, in: O. Madelung, U. Rössler, and M. Schulz , eds., “*II-VI and I-VII Compounds; Semimagnetic Compounds*”, Springer Berlin Heidelberg (Berlin, Heidelberg, 1999) pp. 1–5.
- [233] G. A. Slack, “*The Thermal Conductivity of Nonmetallic Crystals*”, Solid State Phys. **34**, 1–71 (1979).
- [234] M. Roufosse and P. G. Klemens, “*Thermal Conductivity of Complex Dielectric Crystals*”, Phys. Rev. B **7**, 5379–5386 (1973).

Bibliography

- [235] L. Lindsay and D. A. Broido, “*Three-phonon phase space and lattice thermal conductivity in semiconductors*”, J. Phys. Condens. Matter **20**, 165209 (2008).
- [236] D. Li, Y. Wu, P. Kim, L. Shi, P. Yang, and A. Majumdar, “*Thermal conductivity of individual silicon nanowires*”, Appl. Phys. Lett. **83**, 2934–2936 (2003).
- [237] J. Wu, B. M. Borg, D. Jacobsson, K. A. Dick, and L.-E. Wernersson, “*Control of composition and morphology in InGaAs nanowires grown by metalorganic vapor phase epitaxy*”, J. Cryst. Growth **383**, 158–165 (2013).
- [238] J. Lähnemann, M. O. Hill, J. Herranz, O. Marquardt, G. Gao, A. Al Hassan, A. Davtyan, S. O. Hruszkewycz, M. V. Holt, C. Huang, I. Calvo-Almazán, U. Jahn, U. Pietsch, L. J. Lauhon, and L. Geelhaar, “*Correlated Nanoscale Analysis of the Emission from Wurtzite versus Zincblende (In,Ga)As/GaAs Nanowire Core–Shell Quantum Wells*”, Nano Lett. **19**, 4448–4457 (2019).
- [239] F. Glas, J.-C. Harmand, and G. Patriarche, “*Why Does Wurtzite Form in Nanowires of III-V Zinc Blende Semiconductors?*”, Phys. Rev. Lett. **99**, 146101 (2007).
- [240] N. Mingo, “*Green’s function methods for phonon transport through nano-contacts*”, in: S. Volz , ed., “*Thermal nanosystems and nanomaterials*”, Springer (2009) , Ch. 3 pp. 63-94.
- [241] Z.-Y. Ong, “*Tutorial: Concepts and numerical techniques for modeling individual phonon transmission at interfaces*”, J. Appl. Phys. **124**, 151101 (2018).

Bibliography

- [242] P. A. Khomyakov, G. Brocks, V. Karpan, M. Zwierzycki, and P. J. Kelly, “*Conductance calculations for quantum wires and interfaces: Mode matching and Green’s functions*”, Phys. Rev. B **72**, 035450 (2005).
- [243] P. Vashishta, R. K. Kalia, J. P. Rino, and I. Ebbsjö, “*Interaction potential for SiO₂: A molecular-dynamics study of structural correlations*”, Phys. Rev. B **41**, 12197–12209 (1990).
- [244] P. Vashishta, R. K. Kalia, A. Nakano, and J. P. Rino, “*Interaction potential for silicon carbide: A molecular dynamics study of elastic constants and vibrational density of states for crystalline and amorphous silicon carbide*”, J. Appl. Phys. **101**, 103515 (2007).
- [245] C. I. Ribeiro-Silva, J. P. Rino, L. G V. Gonçalves, and A. Picinin, “*An effective interaction potential for gallium phosphide*”, J. Condens. Matter Phys. **23**, 055801 (2011).
- [246] P. S. Branicio, J. P. Rino, C. K. Gan, and H. Tsuzuki, “*Interaction potential for indium phosphide: a molecular dynamics and first-principles study of the elastic constants, generalized stacking fault and surface energies*”, J. Condens. Matter Phys. **21**, 095002 (2009).
- [247] C. A. Polanco and L. Lindsay, “*Phonon thermal conductance across GaN-AlN interfaces from first principles*”, Phys. Rev. B **99**, 075202 (2019).
- [248] R. Rurali, L. Colombo, X. Cartoixa, Ø. Wilhelmsen, T. T. Trinh, D. Bedeaux, and S. Kjelstrup, “*Heat transport through a solid–solid junction: the interface as an autonomous thermodynamic system*”, Phys. Chem. Chem. Phys. **18**, 13741–13745 (2016).
- [249] P. A. Knight, D. Ruiz, and B. Uçar, “*A Symmetry Preserving Algorithm for Matrix Scaling*”, SIAM J. Matrix Anal. Appl. **35**, 931–955 (2014).

Bibliography

- [250] “Eigen3”, <https://eigen.tuxfamily.org>, Accessed: 2021-04-30.
- [251] “Boost Geometry”, https://www.boost.org/doc/libs/1_70_0/libs/geometry/doc/html/index.html, Accessed: 2021-04-30.
- [252] W. Xu, G. Zhang, and B. Li, “*Interfacial thermal resistance and thermal rectification between suspended and encased single layer graphene*”, J. Appl. Phys. **116**, 134303 (2014).
- [253] X.-K. Chen, M. Pang, T. Chen, D. Du, and K.-Q. Chen, “*Thermal Rectification in Asymmetric Graphene/Hexagonal Boron Nitride van der Waals Heterostructures*”, ACS Appl. Mater. Interfaces **12**, 15517–15526 (2020).
- [254] A. Neumaier, “*Rundungsfehleranalyse einiger Verfahren zur Summation endlicher Summen*”, ZAMM-Z. Angew. Math. Me. **54**, 39–51 (1974).
- [255] C. Moler and C. Van Loan, “*Nineteen Dubious Ways to Compute the Exponential of a Matrix, Twenty-Five Years Later*”, SIAM Rev. **45**, 3–49 (2003).
- [256] N. J. Higham, “*The Scaling and Squaring Method for the Matrix Exponential Revisited*”, SIAM Rev. **51**, 747–764 (2009).
- [257] “Eigen3 Exponential Matrix”, https://eigen.tuxfamily.org/dox/unsupported/group__MatrixFunctions__Module.html#matrixbase_exp, Accessed: 2021-04-30.
- [258] W. E. Arnoldi, “*The principle of minimized iterations in the solution of the matrix eigenvalue problem*”, Q. Appl. Math. **9**, 17–29 (1951).
- [259] C. Wasshuber, *About single-electron devices and circuits*, PhD thesis, Technische Univ. Wien (Vienna, Austria, 1997).

Bibliography

- [260] Y. Saad, “*Analysis of Some Krylov Subspace Approximations to the Matrix Exponential Operator*”, SIAM J. Numer. Anal. **29**, 209–228 (1992).
- [261] Q. H. Wang, K. Kalantar-Zadeh, A. Kis, J. N. Coleman, and M. S. Strano, “*Electronics and optoelectronics of two-dimensional transition metal dichalcogenides*”, Nat. Nanotechnol. **7**, 699–712 (2012).
- [262] F. Schwierz, “*Graphene transistors*”, Nat. Nanotechnol. **5**, 487 (2010).
- [263] S. Chen, S. Kim, W. Chen, J. Yuan, R. Bashir, J. Lou, A. M. van der Zande, and W. P. King, “*Monolayer MoS₂ Nanoribbon Transistors Fabricated by Scanning Probe Lithography*”, Nano Lett. **19**, 2092–2098 (2019).
- [264] N. Haratipour, S. Namgung, S.-H. Oh, and S. J. Koester, “*Fundamental Limits on the Subthreshold Slope in Schottky Source/Drain Black Phosphorus Field-Effect Transistors*”, ACS Nano **10**, 3791–3800 (2016).
- [265] X. Luo, Y. Rahbariagh, J. C. M. Hwang, H. Liu, Y. Du, and P. D. Ye, “*Temporal and Thermal Stability of Al₂O₃-Passivated Phosphorene MOSFETs*”, IEEE Electron Device Lett. **35**, 1314–1316 (2014).
- [266] L. Li, Y. Yu, G. J. Ye, Q. Ge, X. Ou, H. Wu, D. Feng, X. H. Chen, and Y. Zhang, “*Black phosphorus field-effect transistors*”, Nat. Nanotechnol. **9**, 372–377 (2014).
- [267] P. Wu, D. Reis, X. S. Hu, and J. Appenzeller, “*Two-dimensional transistors with reconfigurable polarities for secure circuits*”, Nat. Electron. **4**, 45–53 (2021).
- [268] H. Ilatikhameneh, T. Ameen, B. Novakovic, Y. Tan, G. Klimeck, and R. Rahman, “*Saving Moore’s Law Down To 1 nm Channels With Anisotropic Effective Mass*”, Sci. Rep. **6**, 31501 (2016).

Bibliography

- [269] B. Smith, B. Vermeersch, J. Carrete, E. Ou, J. Kim, N. Mingo, D. Ak-inwande, and L. Shi, “*Temperature and Thickness Dependences of the Anisotropic In-Plane Thermal Conductivity of Black Phosphorus*”, Adv. Mater. **29**, 1603756 (2017).
- [270] J. Carrete, W. Li, L. Lindsay, D. A. Broido, L. J. Gallego, and N. Mingo, “*Physically founded phonon dispersions of few-layer materials and the case of borophene*”, Mater. Res. Lett. **4**, 204–211 (2016).
- [271] A. Castellanos-Gomez, L. Vicarelli, E. Prada, J. O. Island, K. L. Narasimha-Acharya, S. I. Blanter, D. J. Groenendijk, M. Buscema, G. A. Steele, J. V. Alvarez, H. W. Zandbergen, J. J. Palacios, and H. S. J. der van Zant, “*Isolation and characterization of few-layer black phosphorus*”, 2D Mater. **1**, 025001 (2014).
- [272] L. Zhu, G. Zhang, and B. Li, “*Coexistence of size-dependent and size-independent thermal conductivities in phosphorene*”, Phys. Rev. B **90**, 214302 (2014).
- [273] A. Jain and A. J. H. McGaughey, “*Strongly anisotropic in-plane thermal transport in single-layer black phosphorene*”, Sci. Rep. **5**, 8501 (2015).
- [274] S. Lee, D. Broido, K. Esfarjani, and G. Chen, “*Hydrodynamic phonon transport in suspended graphene*”, Nat. Commun. **6**, 6290 (2015).
- [275] K. Bernstein, R. K. Cavin, W. Porod, A. Seabaugh, and J. Welser, “*Device and Architecture Outlook for Beyond CMOS Switches*”, Proc. IEEE **98**, 2169–2184 (2010).
- [276] A. J. Minnich, G. Chen, S. Mansoor, and B. S. Yilbas, “*Quasiballistic heat transfer studied using the frequency-dependent Boltzmann transport equation*”, Phys. Rev. B **84**, 235207 (2011).

Bibliography

- [277] B. Vermeersch, J. Carrete, N. Mingo, and A. Shakouri, “*Superdiffusive heat conduction in semiconductor alloys. I. Theoretical foundations*”, Phys. Rev. B **91**, 085202 (2015).
- [278] Y. Wang, A. Vallabhaneni, J. Hu, B. Qiu, Y. P. Chen, and X. Ruan, “*Phonon Lateral Confinement Enables Thermal Rectification in Asymmetric Single-Material Nanostructures*”, Nano Lett. **14**, 592–596 (2014).
- [279] J. Lee, V. Varshney, A. K. Roy, J. B. Ferguson, and B. L. Farmer, “*Thermal Rectification in Three-Dimensional Asymmetric Nanostructure*”, Nano Lett. **12**, 3491–3496 (2012).
- [280] C. Dames, “*Solid-State Thermal Rectification With Existing Bulk Materials*”, J. Heat Transfer **131**, 061301 (2009).
- [281] X. Cartoixa, L. Colombo, and R. Rurali, “*Thermal Rectification by Design in Telescopic Si Nanowires*”, Nano Lett. **15**, 8255–8259 (2015).
- [282] “*almaBTE database*”, <https://almabte.bitbucket.io/database/>, Accessed: 2021-09-30.
- [283] S. Grimme, S. Ehrlich, and L. Goerigk, “*Effect of the damping function in dispersion corrected density functional theory*”, J. Comput. Chem. **32**, 1456–1465 (2011).
- [284] R. S. Pease, “*An X-ray study of boron nitride*”, Acta Crystallogr. **5**, 356–361 (1952).
- [285] D. Golla, K. Chattrakun, K. Watanabe, T. Taniguchi, B. J. LeRoy, and A. Sandhu, “*Optical thickness determination of hexagonal boron nitride flakes*”, Appl. Phys. Lett. **102**, 161906 (2013).

Bibliography

- [286] P. Torres Alvarez, *Thermal Transport in Semiconductors: First Principles and Phonon Hydrodynamics*, PhD thesis, Universitat Autònoma de Barcelona (Bellaterra, Spain, 2018).
- [287] L. Levitov and G. Falkovich, “*Electron viscosity, current vortices and negative nonlocal resistance in graphene*”, Nat. Phys. **12**, 672–676 (2016).
- [288] C. Zhang, Z. Guo, and S. Chen, “*An implicit kinetic scheme for multiscale heat transfer problem accounting for phonon dispersion and polarization*”, Int. J. Heat Mass Transf. **130**, 1366–1376 (2019).
- [289] M.-Y. Shang, C. Zhang, Z. Guo, and J.-T. Lü, “*Heat vortex in hydrodynamic phonon transport of two-dimensional materials*”, Sci. Rep. **10**, 8272 (2020).
- [290] C. Zhang, S. Chen, and Z. Guo, “*Heat vortices of ballistic and hydrodynamic phonon transport in two-dimensional materials*”, Int. J. Heat Mass Transf. **176**, 121282 (2021).
- [291] X. Li and S. Lee, “*Role of hydrodynamic viscosity on phonon transport in suspended graphene*”, Phys. Rev. B **97**, 094309 (2018).
- [292] X. Li and S. Lee, “*Crossover of ballistic, hydrodynamic, and diffusive phonon transport in suspended graphene*”, Phys. Rev. B **99**, 085202 (2019).
- [293] M. Raya-Moreno, X. Cartoixà, and J. Carrete, “*BTE-Barna: An extension of almaBTE for thermal simulation of devices based on 2D materials*”, arXiv preprint arXiv:2202.00505v2 (2022).
- [294] A. Logg, K.-A. Mardal, and G. Wells, “*Automated solution of differential equations by the finite element method: The FEniCS book*”, Springer Science & Business Media (2012).

Bibliography

- [295] M. Alnæs, J. Blechta, J. Hake, A. Johansson, B. Kehlet, A. Logg, C. Richardson, J. Ring, M. E. Rognes, and G. N. Wells, “*The FEniCS project version 1.5*”, Arch. Num. Soft. **3**, 100 (2015).
- [296] A. A. Balandin, S. Ghosh, W. Bao, I. Calizo, D. Teweldebrhan, F. Miao, and C. N. Lau, “*Superior thermal conductivity of single-layer graphene*”, Nano Lett. **8**, 902–907 (2008).
- [297] S. Ghosh, I. Calizo, D. Teweldebrhan, E. P. Pokatilov, D. L. Nika, A. A. Balandin, W. Bao, F. Miao, and C. N. Lau, “*Extremely high thermal conductivity of graphene: Prospects for thermal management applications in nanoelectronic circuits*”, Appl. Phys. Lett. **92**, 151911 (2008).
- [298] Z. Zhang, Y. Guo, M. Bescond, J. Chen, M. Nomura, and S. Volz, “*Coherent thermal transport in nano-phononic crystals: An overview*”, APL Mater. **9**, 081102 (2021).
- [299] “*Intel oneTBB*”, <https://github.com/oneapi-src/oneTBB>, Accessed: 2021-09-30.
- [300] “*MessagePack*”, <https://msgpack.org/>, Accessed: 2021-04-30.